SYNTHESES AND STRUCTURAL CHARACTERIZATION OF NEW XENON(II) COMPOUNDS AND THE USE OF A XENON(II) CATION AS AN OXIDANT FOR THE PREPARATION OF HALOGENATED CARBOCATIONS

To my wife,

Nathasha K. Moran

For her constant love and support throughout

my graduate studies

SYNTHESES AND STRUCTURAL CHARACTERIZATION OF NEW XENON(II) COMPOUNDS AND THE USE OF A XENON(II) CATION AS AN OXIDANT FOR THE PREPARATION OF HALOGENATED CARBOCATIONS

By

MATTHEW D. MORAN

A Thesis

Submitted to the School of Graduate Studies

in Partial Fulfillment of the Requirements

for the Degree

Doctor of Philosophy

McMaster University

DOCTOR OF PHILOSOPHY — McMaster University

(Chemistry) — Hamilton, Ontario

TITLE: SYNTHESES AND STRUCTURAL CHARACTERIZATION OF NEW XENON(II) COMPOUNDS AND THE USE OF A XENON(II) CATION FOR THE PREPARATION OF HALOGENATED CARBOCATIONS

AUTHOR: Matthew D. Moran, B.A.Sc. (McMaster University)

SUPERVISOR: Professor Gary J. Schrobilgen

NUMBER OF PAGES: 313, xxv

ABSTRACT

The chemistry of Xe(II) has been significantly extended to include the first examples of a neutral Xe(II) oxide fluoride species, $O(XeF)_2$, as well as the first nitrate derivative of Xe(II), $FXeONO_2$. Until recently, neutral oxide fluorides were known for all formal oxidation states of xenon except Xe(II). The synthesis of the missing oxide fluoride of Xe(II), $O(XeF)_2$, has been accomplished by reaction of the $[FXeOXeFXeF][AsF_6]$ salt with NOF and characterized by NMR spectroscopy in CH_3CN solution at –78 °C and by Raman spectroscopy. Reaction of NO_2F with $[FXeOXeFXeF][AsF_6]$ has provided the first structurally characterized noble-gas nitrate, $FXeONO_2$, which slowly decomposes (–78 °C) to $XeF_2 \cdot N_2O_4$. X-ray crystal structures have been determined for $FXeONO_2$, $XeF_2 \cdot N_2O_4$, and $XeF_2 \cdot HNO_3$. The preparation of the $XeONO_2^+$ cation was attempted by the reaction of $FXeONO_2$ with AsF_5 at –78 °C, but was not directly observed. It is presumed that the cation initially forms, but rapidly decomposes to give Xe, O_2, and $[NO_2][AsF_6]$.

The salt, $[XeOTeF_5][Sb(OTeF_5)_6]$, is a strong, low-temperature oxidant capable of oxidizing halomethanes in SO_2ClF solvent at –78 °C. The CCl_3^+ and CBr_3^+ cations have been synthesized by oxidation of CCl_4 and CBr_4, respectively. The CBr_3^+ cation reacts with $BrOTeF_5$, produced in the initial redox reaction, to give $CBr(OTeF_5)_2^+$, $C(OTeF_5)_3^+$, and Br_2. The $XeOTeF_5^+$ cation also reacts with $BrOTeF_5$ to give the $Br(OTeF_5)_2^+$ cation. The X-ray crystal structures of $[CCl_3][Sb(OTeF_5)_6]$, $[CBr_3][Sb(OTeF_5)_6] \cdot SO_2ClF$, and

$[C(OTeF_5)_3][Sb(OTeF_5)_6]\cdot 3SO_2ClF$ have been determined and show that the carbocations are trigonal planar about the central atom.

Reactions of chlorofluoro- and bromofluoromethanes with $[XeOTeF_5][Sb(OTeF_5)_6]$ have also been investigated in SO_2ClF solvent by ^{13}C and ^{19}F NMR spectroscopy at –80 °C. The $CFCl_2^+$ and $CFCl(OTeF_5)^+$ cations are among the carbocations that have been obtained by reactions of $CFCl_3$ and CF_2Cl_2 with $XeOTeF_5^+$. The CF_2Br^+ cation is an intermediate in the reaction of $XeOTeF_5^+$ with CF_2Br_2, undergoing rapid halogen exchange with CF_2Br_2 to form $CFBr_2^+$ and CF_3Br. The $CFBr_2^+$ cation undergoes further halogen exchange over several hours to form the CBr_3^+ cation and CF_3Br. Although the highly electrophilic CF_3^+ cation has not been isolated by the reaction of CF_3Br with $XeOTeF_5^+$, ^{13}C and ^{19}F NMR spectroscopy indicates the CF_3^+ cation reacts with $BrOTeF_5$ to form $F_3CBrOTeF_5^+$ and/or abstracts an $OTeF_5$ group from the $Sb(OTeF_5)_6^-$ anion to yield CF_3OTeF_5 and, ultimately, $[SbBr_4][Sb(OTeF_5)_6]$.

The synthesis of $C(OTeF_5)_4$ has been accomplished by reaction of CBr_4 with $BrOTeF_5$ in SO_2ClF solution, and has been fully characterized by NMR spectroscopy, Raman spectroscopy, and single-crystal X-ray diffraction, and its geometric parameters have been compared with those of the isoelectronic $B(OTeF_5)_4^-$ anion in order to assess the symmetry of the $E(OTe)_4^{-/0}$ (E = B, C) subgroup.

ACKNOWLEDGEMENTS

I wish to thank Professor Gary J. Schrobilgen for providing me with two interesting and exciting avenues of research, as well as for his guidance, enthusiasm, support, patience, and confidence in me.

I would also like to thank the other members of my supervisory committee, Professors Ronald J. Gillespie and Ignacio Vargas-Baca, for their insights and interest in my research projects.

A heartfelt thanks to Dr. Hélène P. A. Mercier for her expertise, advice, and encouragement throughout the course of this work, as well as for the numerous hours spent in helping solve various crystal structures, tabulating data, and writing contributions for our publications together.

I am also very grateful to Dr. Bernard E. Pointner as my primary mentor in learning the day-to-day operations of the laboratory, his off-color humor, his insatiable appetite (i.e., KFC eating contests), and for his friendship. Also special thanks to Dr. Neil Vasdev, Dr. Karsten Koppe, Dr. John F. Lehmann, and Dr. Adrienne A. Pedrech for their expertise, advice, support, and friendship during my first years of graduate school.

I am also grateful to Gregory L. Smith (a.k.a. "Smitty"), Gregory J. Bahun, Lindsay S. Cahill, and Matthew C. Parrott for useful discussions, good times, keeping me sane during the waning years of my graduate career, and for their friendship.

Thanks to other past and present members of the Schrobilgen research group, namely Rezwan Ashique, Babak Behnam-Azad, David Brock, Hugh "Hughferd" Elliott, Michael Hughes, and Dr. Kazuhiko Matumoto.

For their help in their respective fields, I would like to thank Dr. Reijo Suontamo (computational chemistry, University of Jyväskylä), Dr. Jim Britten (X-ray crystallographic facilities), Dr. Don Hughes (NMR facilities), and Michael Palme (Chemistry Glassblowing Shop).

I would like to acknowledge the Natural Science and Engineering Council (NSERC) for both PGS-A (two year) and PGS-D (two year) scholarships, the Ontario Ministry of Training and Education (OGS) for a one-year scholarship, and the Department of Chemistry at McMaster University for their financial support.

Finally, I would like to thank my wife, Natasha Moran, for her unwavering love, support, and confidence in my abilities during my entire tenure as a graduate student. As well, special thanks to my parents, Gordon and Margaret-Ann, and my in-laws, Peter and Eileen, for both their emotional and financial support throughout.

PREFACE

The following Chapters have been published, in part or in whole, by the American Chemical Society (ACS). All experimental work was conducted by the author. All computational work was conducted by the author alone, or in conjunction with Dr. Reijo Suontamo, Department of Chemistry, University of Jyväskylä, Jyväskylä, Finland.

Chapter 5: Mercier, H. P. A.; Moran, M. D.; Sanders, J. C. P.; Schrobilgen, G. J.; Suontamo, R. J. *Inorg. Chem.* **2005**, *44*, 49-60.

Chpater 6: Mercier, H. P. A.; Moran, M. D.; Schrobilgen, G. J.; Steinberg, C.; Suontamo, R. J. *J. Am. Chem. Soc.* **2004**, *126*, 5533-5548.

Chapter 7: Mercier, H. P. A.; Moran, M. D.; Schrobilgen, G. J. In *Recent Developments in Carbocation and Onium Ion Chemistry*; Laali, K. K., Ed.; American Chemical Society; Washington, DC, 2007; Volume 965, Chapter 19, pp 394-427.

Chapter 8: Moran, M. D.; Mercier, H. P. A.; Schrobilgen, G. J. *Inorg. Chem.* **2007**, *46*, 5034-5045.

LIST OF ABBREVIATIONS AND SYMBOLS

General

BDH	British Drug Houses
SAE	Society of Automotive Engineers
ax	axial
eq	equatorial
CCD	charge-coupled device
FT	Fourier transform
FEP	perfluoroethylene/perfluoropropylene copolymer
IR	infrared
Kel-F	chlorotrifluoroethylene polymer
PTFE	tetrafluoroethylene polymer
VSEPR	valence shell electron pair repulsion
N.A.	natural abundance (isotopic)
DSC	Differential Scanning Calorimetry

Raman Spectroscopy

$\Delta\nu$	frequency
cm^{-1}	wavenumber
n	stretching mode
d	in-plane bend
ρ_w	wagging mode

ρ_r	rocking mode
ρ_t	twisting mode
o.o.p.	out-of-plane
i.p.	in-plane

Nuclear Magnetic Resonance Spectroscopy

NMR	nuclear magnetic resonance
ppm	parts per million
δ	chemical shift
I	nuclear spin quantum number
J	scalar coupling constant, in Hz
Hz	Hertz, or cycles per second
FID	free induction decay
SF	spectral frequency
SW	sweep width
TD	time domain
PW	pulse width
$\Delta\nu_{1/2}$	line width at half height
WF	width factor

X-ray Crystallography

$a, b, c, \alpha, \beta, \gamma$	unit cell parameters

V	unit cell volume
λ	wavelength
Z	molecules per unit cell
V_m	molecular volume (V/Z)
mol. wt.	molecular weight
ρ	density
μ	absorption coefficient
F	structure factor
R_1	conventional agreement index
w	overall weight parameter
wR_2	weighted agreement index

Computational and Thermochemical

ELF	electron localization fuction
DFT	density functional theory
CCSD(T)	couple cluster, with single and double substitutions and non-iterative triplet excitations
MP2	Møller-Plesset, second order perturbation
HF	Hartree-Fock
RLC	relative large core
ECP	effective core potential
NBO	natural bond orbital/natural bond order
GIAO	Gauge-Independent Atomic Orbital

HOMO	highest occupied molecular orbital
LUMO	lowest unoccupied molecular orbital
ΔH^{o}	standard enthalpy of reaction
ΔH_{f}^{o}	standard enthalpy of formation
ΔG^{o}	standard free energy of reaction
ΔG_{f}^{o}	standard free energy of formation

TABLE OF CONTENTS

page

LIST OF TABLES

LIST OF FIGURES

CHAPTER 1

INTRODUCTION

1.1. Noble-Gas Chemistry

The chemistry of the noble gases has been actively pursued since the discovery of noble gas reactivity by Neil Bartlett.[1] When Bartlett discovered that platinum (VI) hexafluoride, PtF_6, was able to oxidize molecular oxygen, O_2, to O_2^+,[1] it became evident that PtF_6 should also have the potential to oxidize xenon gas, since xenon and molecular oxygen have similar ionization potentials (12.13 eV and 12.2 eV, respectively). Bartlett demonstrated that xenon gas was readily oxidized by PtF_6 at room temperature (eq 1.1) to

$$Xe_{(g)} + PtF_{6\,(g)} \longrightarrow [Xe][PtF_6]_{(s)} \qquad (1.1)$$

yield an orange-yellow solid, which was then formulated as $[Xe][PtF_6]$. Later, Bartlett[2] reported that the reaction between xenon and PtF_6 yielded a mixture of $[XeF][PtF_6]$ and $[XeF][Pt_2F_{11}]$, however, he maintains that a pale yellow solid resulting from the reaction of a stoichiometric mixture of Xe and PtF_6 is indeed $[Xe][PtF_6]$, which is more properly formulated as $[XeF][PtF_5]$. The synthesis of a stable xenon compound quickly led to other examples of xenon compounds, such as XeF_2,[3] as well as to compounds of krypton[4-6] and radon in trace amounts.[7] While a compound of argon, HArF, has been stabilized in a solid argon matrix at very low temperature (7.5 K) and studied by infrared spectroscopy,[8,9] no long-lived argon species has been synthesized to date, nor has a radon

compound been sythesized in macroscopic amounts. Thus, the only two Group 18 elements which exhibit extensive chemistries are krypton and xenon. Xenon has the most extensive chemistry of all the noble gases, exhibiting oxidation states of 0, +½, +2, +4, +6, and +8, which are stabilized by bonds to electronegative atoms such as fluorine, oxygen, and chlorine, as well as by ligands bonded through oxygen, carbon, and nitrogen. A number of comprehensive reviews covering the chemistry of the noble gases are available,[10-16] as well as historical accounts of the events leading to the discovery of noble gas reactivity and its impact on modern chemistry.[17,18]

1.2. Xenon(II) Chemistry

The compounds of xenon in the +2 oxidation state are the most widely studied of the noble gases, and are ultimately derived from xenon difluoride, XeF_2. Several synthetic routes to XeF_2 are known, with the most convenient, high-yield synthesis being the direct combination of the elements at high temperature (~300 °C) and high pressure in the presence of an excess of Xe (eq 1.2).[19,20] The compound exists as a white, crystalline

$$Xe + F_2 \longrightarrow XeF_2 \qquad (1.2)$$

solid that is stable at room temperature (ΔH_f° = –333 kJ mol^{-1}),[21] and exhibits strong oxidant behavior.

The reactivity of XeF_2 has been extensively explored, resulting in Xe–O, Xe–C, Xe–N, and Xe–Cl bonded species. Derivatives of xenon(II) are typically prepared by

fluoride ion abstraction from XeF_2, and by metathesis (ligand exchange) reactions involving XeF_2 and a suitable ligand transfer reagent or strong protic acid.

1.2.1. Fluoride Ion Donor Properties of XeF_2

Xenon difluoride reacts with strong fluoride acceptors such as AsF_5 and SbF_5 to form XeF^+ and $F(XeF)_2^+$ salts (eq 1.3–1.5).[22-24] The XeF^+ cation interacts strongly with

$$XeF_2 + MF_5 \longrightarrow [XeF][MF_6] \ (M = As, Sb) \quad (1.3)$$

$$XeF_2 + 2MF_5 \longrightarrow [XeF][M_2F_{11}] \ (M = As, Sb) \quad (1.4)$$

$$XeF_2 + [XeF][MF_6] \longrightarrow [F(XeF)_2][MF_6] \ (M = As, Sb) \quad (1.5)$$

the anion by means of a fluorine bridge between xenon and a fluorine of the counterion,[24] while the $F(XeF)_2^+$ cation is only weakly bridged to the counterion. The latter cation can be regarded as a fluoride ion bridged to two XeF^+ cations, forming a symmetric, planar, V-shaped cation having C_{2v} symmetry (Structure I).[23] The $F(XeF)_2^+$ cation also exhibits

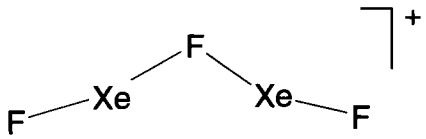

I

slightly bent bond angles about the xenon atom.[23] Fluorine bridge formation attests to the strong Lewis acid character of the XeF^+ cation.[13]

The ionic character of the Xe---F interaction in the $[XeF][MF_6]$ salts is dependent on the ability of the MF_6^- anion to partially donate a fluoride ion to the XeF^+ cation. Decreasing the fluoride ion donor strength of the anion (increasing the Lewis acidity of the Lewis acid fluoride) leads to more ionic Xe---F bridge interactions. For example, the weaker fluoride ion donor properties of $Sb_2F_{11}^-$, relative to AsF_6^-, leads to a more ionic interaction between the bridging Xe---F in $[XeF][Sb_2F_{11}]$ (Xe---F distance, 2.35(4) Å) than in $[XeF][AsF_6]$ (Xe---F distance, 2.12(5) Å).[25] Because these bonds are not purely ionic, they are significantly shorter than the sum of the xenon and fluorine van der Walls radii (3.63 Å).[26] Weaker fluoride ion donor properties also result in shorter, more covalent terminal Xe–F_t bonds for $[XeF][Sb_2F_{11}]$ (1.84(1) Å)[24] than for $[XeF][AsF_6]$ (1.873(6) Å).[25] A simple valence bond description for $[XeF][MF_6]$ accounts for the behavior of the F_t–Xe bond of XeF^+ salts. The interaction can be represented in terms of three competing resonance structures which serve to describe the so-called 3c-2e hypervalent bonding in their structures (Structures II, III and IV). As the interaction

$$\underset{\text{II}}{F\text{–}Xe^+\ F\text{–}MF_5^-} \leftrightarrow \underset{\text{III}}{F\text{–}Xe^+\ F^-\ MF_5} \leftrightarrow \underset{\text{IV}}{F^-\ {}^+Xe\text{–}F\ MF_5}$$

between xenon and the bridged fluorine becomes more ionic in character (Structure III), the bridging fluorine donates less electron density to $F–Xe^+$, increasing the bond order between xenon and the terminal fluorine. Conversely, a more covalent interaction between xenon and the bridge fluorine (Structure IV) donates more electron density to $F–Xe^+$, decreasing the bond order between xenon and the terminal fluorine.

1.2.2. Metathetical Reactions Involving XeF_2

Xenon difluoride forms several derivatives of the type F–Xe–L and L–Xe–L. The main synthetic approach to these species involves fluoride ion replacement with the conjugate base of a strong, oxidatively resistant, monoprotic acid (eq 1.6 and 1.7). The criteria for a ligand that is suitable for stabilizing for xenon(II) are: (1) the ligand must

$$XeF_2 + HL \longrightarrow FXeL + HF \quad (1.6)$$

$$XeF_2 + 2HL \longrightarrow XeL_2 + 2HF \quad (1.7)$$

possess a high effective group electronegativity, (2) the ligand must exist as a moderate to strong monoprotic acid, (3) the deprotonated monoprotic acid (anion) should be stable and form stable salts with alkali metals, and (4) the least electronegative element of the ligand should be in its highest oxidation state. The last criterion ensures that the ligand will be oxidatively resistant towards XeF_2. Several strong monoprotic acids, including $HOSO_2F$,[27,28] $HOTeF_5$,[29,30] $HOSeF_5$,[31] $HOClO_3$,[28] $HOSO_2CF_3$,[32] $HOC(O)CF_3$,[33] and $HN(SO_2F)_2$,[34] match these criteria and have been successfully employed in HF displacement reactions with XeF_2. The monosubstituted derivatives can further be converted to the XeL^+ cations by fluoride ion abstraction using an appropriate Lewis acid (eq 1.8 and 1.9). The neutral compounds are significantly less stable than XeF_2, and

$$FXeL + MF_5 \longrightarrow [XeL][MF_6] \ (M = As, Sb) \quad (1.8)$$

$$FXeL + 2MF_5 \longrightarrow [XeL][M_2F_{11}] \ (M = As, Sb) \quad (1.9)$$

decompose to give peroxide species (eq 1.10 and 1.11), as is the case for $Xe(OChF_5)_2$.[31]

$$Xe(OChF_5)_2 \longrightarrow Xe + F_5ChO{-}OChF_5 \ (Ch = Se, Te) \quad (1.10)$$

$$FXeOChF_5 \longrightarrow XeF_2 + Xe + F_5ChO{-}OChF_5 \ (Ch = Se, Te) \quad (1.11)$$

In addition to metathesis reactions involving a strong protic acid, boron-based ligand transfer reagents of the form BL_3 (L = $OTeF_5$,[35] C_6F_5,[36] XC_6F_4,[36] where X = 3-F, 4-F, 3-CF_3, 4-CF_3) have led to the preparation of Xe–O and Xe–C bonded derivatives as exemplified in eq 1.12 and 1.13.

$$3XeF_2 + 2B(OTeF_5)_3 \longrightarrow 3Xe(OTeF_5)_2 + 2BF_3 \quad (1.12)$$

$$XeF_2 + B(C_6F_5)_3 \longrightarrow [XeC_6F_5][(C_6F_5)_nBF_{4-n}] \ (n = 0–4) \quad (1.13)$$

Finally, $OIOF_4$ [37] and $OP(O)F_2$ [38] derivatives of XeF_2 have been prepared by insertion into the Xe–F bond of XeF_2 using the oxide fluorides IO_2F_3 and $P_2O_3F_4$, respectively (eq 1.14 and 1.15). Reactions using these dehydrofluorinated compounds are

$$XeF_2 + IO_2F_3 \longrightarrow FXeOIOF_4 \quad (1.14)$$

$$XeF_2 + P_2O_3F_4 \longrightarrow FXeOPOF_2 + POF_3 \quad (1.15)$$

desirable because no HF is formed, which could back react with the derivative of interest by reprotonating the ligand. Also, $OIOF_4$ derivatives have been prepared by an acid displacement of $HOTeF_5$ from of the xenon(II) derivative, $Xe(OTeF_5)_2$, using the stronger protic acid, $HOIOF_4$, to give $Xe(OIOF_4)_2$ (eq 1.16).[37]

$$Xe(OTeF_5)_2 + 2HOIOF_4 \longrightarrow Xe(OIOF_4)_2 + 2\,HOTeF_5 \quad (1.16)$$

1.2.3. The Lewis Acid Properties of the XeF^+ Cation

The XeF^+ cation, apart from its potential as a strong oxidizer, acts as a Lewis acid towards oxidatively resistant bases such as nitriles, pyridines, diazenes, and triazenes in HF or BrF_5 solvents (eq 1.17–1.20). The strong Lewis acidity of XeF^+ is further

$$[XeF][AsF_6] + CH_3CN \longrightarrow [CH_3CN—XeF][AsF_6] \quad (1.17)$$

$$[XeF][AsF_6] + C_5F_5N \longrightarrow [C_5F_5N—XeF][AsF_6] \quad (1.18)$$

$$[XeF][AsF_6] + o\text{-}, p\text{-}C_4F_4N_2 \longrightarrow [C_4F_4NN—XeF][AsF_6] \quad (1.19)$$

$$[XeF][AsF_6] + s\text{-}C_3F_3N_3 \longrightarrow [C_3F_3N_2N—XeF][AsF_6] \quad (1.20)$$

demonstrated by its ability to form the dinuclear $F(XeF)_2^+$ cation, and does so in preference to bridging to MF_6^- (eq 1.5).

1.2.4. Complexes of XeF_2

Complexes of xenon difluoride can be divided into two classes, those that form interactions with weak to moderate Lewis acids through the fluorine atom, and those that interact with electronegative atoms through the xenon atom. There are many examples of the former, where Lewis acids such as XeF_4, $XeOF_4$, IF_5, and XeF_5^+ form $XeF_2{\cdot}XeF_4$,[39] $XeF_2{\cdot}XeOF_4$,[40] $XeF_2{\cdot}IF_5$,[41] and $nXeF_2{\cdot}m[XeF_5][AsF_6]$ (n = 1, 2; m = 1, 2),[42] respectively. Xenon difluoride also forms adducts with the weak fluoride ion acceptor MOF_4 (M = W, Mo) to give $XeF_2{\cdot}MOF_4$, $XeF_2{\cdot}2MOF_4$, and $XeF_2{\cdot}n MoOF_4$.[43,44] In these cases the

F–Xe–F---Mo linkage is non-labile on the NMR time scale at suitably low temperatures. Similarly, the series of $[A^{x}(XeF_2)_n][(MF_6)_x]$ salts (A = La, Nd, Sm, Eu, Gd, Dy, Ho, Er, Pr, Tb, Mg, Ca, Sr, Ba, Cd, Pb; x = 1, 2, 3; n = 2, 2.5, 3, 4, 5, 9; M = As, Sb, Bi) have been investigated,[45-52] where XeF_2 is adducted to a metal cation through one fluorine atom. There are currently no reports of XeF_2 complexes that involve hydrogen bonding to, or weak dipole-dipole interactions with, lighter main group compounds.

1.2.5. Spectroscopic Characterization of XeF_2 Complexes

Apart from single crystal X-ray diffraction, spectroscopic techniques such as Raman spectroscopy and multi-NMR spectroscopy have proven useful in characterizing the environment of XeF_2 in a variety of molecular adducts. Adduct formation involving XeF_2 can occur symmetrically, as shown in the crystal structures of $XeF_2{\cdot}XeOF_4$ and $XeF_2{\cdot}2[XeF_5][AsF_6]$, preserving the center of symmetry at xenon in XeF_2 and gives rise to a single symmetric XeF_2 stretch in the Raman spectra of these adducts. Adduct formation can also occur in an asymmetric fashion, destroying the center of symmetry at xenon of XeF_2. This gives rise to two bands to high and low frequency of pure XeF_2 (498 cm^{-1}) in the Raman spectrum, as illustrated by $XeF_2{\cdot}MOF_4$ (M = Mo, W). Similarly, the series of $[A^{x}(XeF_2)_n][(MF_6)_x]$ (vide supra) salts possess linear distortions that give rise to Xe–F stretching modes at high frequency (514 to 584 cm^{-1}) and low frequency (411 to 463 cm^{-1}). Many of the X-ray crystal structures determined for these complexes show that the two Xe–F bond lengths of the XeF_2 moiety are significantly different within $\pm 3\sigma$, in agreement with the vibrational frequencies.

While it is expected that the asymmetric stretch of XeF_2 (555 cm^{-1})[53] would be observable in the Raman spectrum upon breaking the center of symmetry of the XeF_2 molecule, it has not been observed thus far for these complexes. Instead, the symmetric and asymmetric stretching modes of XeF_2 are replaced with terminal and bridging Xe–F stretches, which are coupled with one another. The strength of this coupling is directly related to the strength of the interaction between XeF_2 and the Lewis acid center.

1.3. Xenon(II) Oxide Fluorides

The syntheses of xenon oxide fluorides of Xe(IV) and Xe(VI) have been accomplished by various methods,[54-63] the most convenient being by the controlled hydrolyses of XeF_4 and XeF_6 in HF solution according to eq 1.21–1.23.[64,65] More

$$XeF_4 + H_2O \xrightarrow{HF} XeOF_2 + 2HF \quad (1.21)$$

$$XeF_6 + H_2O \xrightarrow{HF} XeOF_4 + 2HF \quad (1.22)$$

$$XeOF_4 + H_2O \xrightarrow{HF} XeO_2F_2 + 2HF \quad (1.23)$$

recently, an improved synthesis of $XeOF_2$ has been reported. Controlled hydrolysis of XeF_4 by H_2O in CH_3CN solvent yields $XeOF_2 \cdot CH_3CN$ in essentially quantitative yield.[66] Adducted CH_3CN can be removed at low temperature under dynamic vacuum to give pure $XeOF_2$. Although several neutral and ionic xenon oxide fluorides are known for Xe(IV) and Xe(VI), as well as neutral oxide fluorides for Xe(VIII) (Table 1.1), only one species, $FXeOXeFXeF^+$,[67] but no neutral oxide fluoride, has been reported for Xe(II).

Table 1.1. Known Fluoro- and Oxofluoro-Cations and Anions of Xenon, Their Parent Compounds, and Geometries

	Parent Compound	Structure[a]	Cation(s)	Structure[a]	Anion(s)	Structure[a]
Xe(II)	XeF_2	(linear, $D_{\infty h}$)	XeF^+	(linear, $C_{\infty v}$)		
			$FXe{-}{-}{-}F{-}{-}{-}XeF^+$	(V-shape, C_{2v})[b]		
	FXeOXeF[c]	(V-shape, C_{2v})	$FXeOXeFXeF^+$	(bent chain, C_s)		
Xe(IV)	XeF_4	(square plane, D_{4h})	XeF_3^+	(T-shape, C_{2v})	XeF_5^-	(pentagonal planar, D_{5h})
	$XeOF_2$	(T-shape, C_{2v})			$XeOF_3^-$	(planar, C_{2v})
Xe(VI)	XeF_6	(monocapped octahedron, C_{3v})	XeF_5^+ $F_5Xe{-}{-}{-}F{-}{-}{-}XeF_5^+$ [a]	(square pyramid, C_{4v})	XeF_7^- XeF_8^{2-}	(monocapped octahedron, C_{3v}) (square antiprism, D_{4d})
	$XeOF_4$	(square pyramid, C_{4v})	$XeOF_3^+$	(disphenoid, C_s)	$XeOF_5^-$ $(XeOF_4)_3F^-$ [e]	(pentagonal pyramid, C_{5v})[d]
	XeO_2F_2	(disphenoid, C_{2v})	XeO_2F^+ $FO_2Xe{-}{-}{-}F{-}{-}{-}XeO_2F^+$ [b]	(trigonal pyramid, C_{2v})	$XeO_2F_3^-$	(square pyramid, C_s)
	XeO_3	(trigonal pyramid, C_{3v})			XeO_3F^-	f
Xe(VIII)	XeO_2F_4	(pseudooctahedron, D_{4h})[g]				
	XeO_3F_2	(trigonal bipyramid, D_{3h})			$XeO_3F_3^-$	(pseudooctahedron, facial arrangement, C_{3v})
	XeO_4	(tetrahedron, T_d)			$XeO_4F_2^{2-}$	(distorted octahedron, mixture of isomers cis (C_{2v}) and trans (D_{4h}))

Table 1.1. (continued...)

[a] Point group symmetries are given in parentheses. [b] Cations that are mononuclear in xenon and the F_5Xe---F---XeF_5^+ ($Xe_2F_{11}^+$) cation interact with their fluoroanions through one or more fluorine bridges. Details of the structure and fluorine bridging in the FO_2Xe---F---XeO_2F^+ ($Xe_2O_4F_3^+$) cation are unknown, but the Xe---F---Xe arrangement is assumed to be bent as in the FXe---F---XeF^+ ($Xe_2F_3^+$) and $Xe_2F_{11}^+$ cations. The $Xe_2F_3^+$ cation forms no fluorine bridges with its fluoroanion. The XeF_5 groups in $Xe_2F_{11}^+$ have essentially square pyramidal geometries. [c] This work. [d] Point symmetry determined by vibrational spectroscopy. [e] Three $XeOF_4$ molecules, having essentially square pyramidal geometries, are coordinated through the xenon atoms to a single fluoride ion to give a trigonal pyramidal arrangement about the fluoride ion. [f] The structure consists of open polymeric chains, $(XeO_3F^-)_n$, with two fluorine bridges to each xenon atom. [g] Predicted geometry.

While $XeOF_4$ is a thermodynamically stable liquid (estimated ΔH_f^o, –25 kJ mol^{-1}),[68] the other neutral oxide fluorides are themodynamically unstable. The Xe(IV) oxide fluoride, $XeOF_2$, is known to undergo redox decomposition, eliminating molecular oxygen (eq 1.24),[64] or by disproportionation into XeF_2 and Xe_2OF_2 (eq 1.25). The XeO_2F_2 molecule

$$XeOF_2 \longrightarrow XeF_2 + \tfrac{1}{2}O_2 \quad (1.24)$$

$$2XeOF_2 \longrightarrow XeF_2 + Xe_2OF_2 \quad (1.25)$$

is an endothermic solid (estimated ΔH_f^o, 234 kJ mol^{-1}).[68] Except for the $XeOF_3^-$ anion, all anionic and cationic xenon oxide fluorides that have been reported are derived from neutral Xe(VI) oxide fluorides. Dinuclear μ-$F(XeO_2F)_2^+$, trinuclear $F(XeOF_4)_3^-$, and polymeric $(XeO_3F^-)_n$ xenon oxide fluoride species have also been prepared and possess fluorine-bridged xenon centers.

1.4. The XeL^+ (L = F, $OSeF_5$, $OTeF_5$) Cations and $M(OTeF_5)_6^-$ (M = As, Sb, Bi) Anions; General Background

The electronegativity of the pentafluoroorthotellurate group, $OTeF_5$, is comparable to that of fluorine in its ability to stabilize a variety of noble-gas species.[69,70] Derivatives of the $OTeF_5$ group are known for the +2, +4, and +6 oxidation states of xenon,[29,30,71-76] as well as for the +2 oxidation state of krypton.[77] The $OTeF_5$ analogue of the well-known XeF^+ cation, $XeOTeF_5^+$, was first obtained as the AsF_6^- salt by reaction of $FXeOTeF_5$ with AsF_5.[71] The $[XeOTeF_5][Sb_2F_{11}]$ salt was subsequently synthesized

from $[XeOTeF_5][AsF_6]$ by AsF_5 displacement in liquid SbF_5,[8] and the $XeOTeF_5^+$ cation has been characterized in solution by ^{19}F, ^{125}Te, and ^{129}Xe NMR spectroscopy in SbF_5 solvent,[76] and in the solid state by Raman spectroscopy of $[XeOTeF_5][AsF_6]$ [71,72,75] and $[XeOTeF_5][Sb_2F_{11}]$.[76] The X-ray crystal structure of $[XeOTeF_5][AsF_6]$ shows that the unsaturated primary coordination sphere of $XeOTeF_5^+$, like that of XeF^+, renders it a Lewis acid that interacts with the AsF_6^- anion by means of a fluorine bridge. The resulting Xe---F cation-anion distance (2.24(3) Å)[75] is significantly less than the sum of xenon and fluorine van der Waals radii (3.63 Å)[26] and similar to that in $[XeF][AsF_6]$ (2.208(3) Å)[78] and $[XeOSeF_5][AsF_6]$ (2.31(4) Å).[75]

No solid state structural data currently exists for salts of the XeF^+ or $XeOTeF_5^+$ cations in which either XeF^+ or $XeOTeF_5^+$, or any other noble-gas cation, may be regarded as "devoid" of interactions with their counter anions. Likely candidates for anions that may prove to be weakly coordinating with respect to XeF^+ and $XeOTeF_5^+$ are members of the oxidatively resistant $M(OTeF_5)_6^-$ (M = As, Sb, Bi) anion series.[35] The latter anions effectively disperse a single negative charge over 30 fluorine atoms rather than over six fluorine atoms as in their MF_6^- analogues. In addition to their low basicities, the high effective group electronegativity of the $OTeF_5$ ligand and its steric requirements in these hexa-coordinate anions may be expected to make the electron lone pairs of the linking oxygen atoms less accessible to attack by strong electrophiles. The $Sb(OTeF_5)_6^-$ anion has been shown to resist attack by the strongly oxidizing $SbCl_4^+$ and $SbBr_4^+$ cations,[79] leading to the X-ray crystal structure determinations of their $Sb(OTeF_5)_6^-$ salts.

The $XeOTeF_5^+$ cation is of considerable interest because of its use synthetically for generating main-group cationic species by oxidative elimination of a halogen ligand bonded to the main-group element (see Chapters 6 and 7).[80] Until now generation of cationic species of the main-group element using xenon cations has been limited to XeF^+ [81-88] and $C_6F_5Xe^+$ [89,90] (see Section 1.5).

1.5. Synthetic Applications of Noble-Gas Salts

Although the noble-gas cations are stronger oxidants than their parent neutral compounds, their oxidant properties have not been exploited to a significant extent in synthetic contexts. Among the xenon cations, XeF^+ has been the most exploited synthetically.[81] It has been used in HF solvent to synthesize (precursors given in square brackets) a variety of monofluorosulfonium cations such as R_2SF^+ [R_2S; R = H, Cl, CN, C_6F_5, CF_3, CH_3], $RR'SF^+$ [RR'S; R = CH_3, CF_3 and R' = H] and $(R_2C)_2SSF^+$ [$(R_2CS)_2$; R = CF_3, Cl] as their MF_6^- (M = As, Sb) salts.[81] The reaction of XeF^+ with H_2O in anhydrous HF has been reported to give the H_2OF^+ cation,[91] but this work has been shown to be erroneous, instead giving rise to the $FXeOXeFXeF^+$ cation.[67] In group 15, $PnCl_3$ (Pn = P, As) have been fluorinated in HF solvent by XeF^+ to give the corresponding $PnFCl_3^+$ cations as their AsF_6^- salts.[81,82] Nitrosyl fluoride, NOF, also reacts in HF with XeF^+ to form the ONF_2^+ cation.[83] The only reports of synthetic applications to group 17 chemistry are of the Cl_3^+ [84] and Br_5^+ [85] cations generated in HF by reaction of $[XeF][MF_6]$ with Cl_2 and Br_2. The previously known Br_3^+ cation has also been prepared by this route.[85] The XeF^+ cation has also been shown to oxidize Xe in SbF_5 in the

presence of low concentrations of HF[88] to give the previously known $Xe_2^{+\cdot}$ radical cation.[86,87] The $C_6F_5Xe^+$ cation is considerably less electrophilic than the XeF^+ cation.[92] Thus far, $C_6F_5Xe^+$ has been shown to arylate pentafluorophenyl derivatives of several main-group elements; $(C_6F_5)_3As$, $(C_6F_5)_3P$, $(C_6F_5)_2S$, C_6F_5I, and C_6F_5Br to give $(C_6F_5)_4As^+$,[89] $(C_6F_5)_4P^+$,[93] $(C_6F_5)_3S^+$,[90] $(C_6F_5)_2I^+$,[90] and $(C_6F_5)_2Br^+$,[90] respectively. No synthetic applications of the remaining higher oxidation state xenon cations have been reported thus far. The KrF^+ and $F(KrF)_2^+$ cations are well-established superoxidant species capable of oxidizing NF_3 to NF_4^+,[94] BrF_5 to BrF_6^+,[95,96] TcO_2F_3 to $TcOF_5$,[97,98] and O_2 to O_2^+ [5] (reference 16 and references therein should be consulted for further examples). The aforementioned reactions involving krypton fluorocations were carried out in oxidatively resistant solvent media such as anhydrous HF. Similarly, synthetic chemistry involving the use of XeF^+ as an oxidant has been solely reliant upon the superacid, anhydrous HF, as the solvent medium.

1.6. Purpose and Scope of the Present Work

The objectives of the present work are three-fold: (1) to extend the chemistry of the oxide fluorides of xenon, (2) to extend the known derivatives of Xe(II) to include a nitrate species, and (3) to apply Xe(II) cations to the syntheses of new main-group cations.

The syntheses of all the neutral oxide fluorides of Xe(IV), Xe(VI), and Xe(VIII) have been reported, but no neutral oxide fluorides of Xe(II) have been prepared to date. A major goal of this work is to extend the chemistry of the known oxide fluorides of xenon

by synthesizing FXeOXeF (hereafter referred to as $O(XeF)_2$) and structurally characterize it. The preparation of this compound would complete the list of known neutral oxide fluorides of xenon.

Many oxygen-bound ligands have been found to form stable compounds with Xe(II), but no confirmed synthesis or structural characterization of a noble-gas nitrate, ONO_2, has been reported. Two prior reports have suggested the formation of $FXeONO_2$ [99,100] and $Xe(ONO_2)_2$,[99] but neither study attempted to provide spectroscopic evidence or made attempts to isolate $FXeONO_2$ or $Xe(ONO_2)_2$. Attempts to synthesize and characterize the nitrate derivatives, $FXeONO_2$ and $Xe(ONO_2)_2$, was another major goal of the research undertaken in this Thesis.

The third major objective of this research was to extend the chemistry of strongly electrophilic main-group cations by use of a strong oxidant noble-gas cation as a synthon. A prior body of work has utilized XeF^+ and $XeC_6F_5^+$ to generate main-group cations by direct oxidation of the central atom (see Section 1.5). This approach, however, suffers from one or two major drawbacks: (1) it relies on the protic, superacidic medium, HF, to solubilize XeF^+, which, in turn, reacts with the substrate of interest, and (2) it involves oxidative addition of F or C_6F_5 to the substrate. A major goal of this Thesis was to generate other main-group cations using the strongly oxidizing noble-gas salt, $[XeOTeF_5][Sb(OTeF_5)_6]$, which is highly soluble at low temperature in the non-protic, weakly basic solvent SO_2ClF. The intent was to generate halomethyl cations by oxidative removal of a ligand, such as chlorine, bromine, or iodine, from the carbon center, rather than by oxidation and concerted ligation of the central atom. Prior to this work, the

halomethyl cations CX_3^+ (X = Cl, Br, I) had only been characterized in the gas phase by ion cyclotron resonance (ICR) mass spectrometry, or as long-lived species by NMR spectroscopy in SO_2ClF solution, or by infrared spectroscopy in the case of CCl_3^+ (see Chapter 6). Also, during the course of the Thesis, the CI_3^+ cation has been characterized by X-ray crystallography as the $[CI_3][Al(OC(CF_3)_3)_3]$ salt.[101] As such, the structural determination of the remaining perhalomethyl cations, CX_3^+ (X = F, Cl, Br) as well as obtaining spectroscopic evidence for long-lived, mixed chlorofluoromethyl cations, CFX_2^+ and CF_2X^+ (X = Cl, Br), was a major goal in the present work.

CHAPTER 2

EXPERIMENTAL SECTION

2.1. Standard Techniques

2.1.1. Dry Box and Vacuum Line Techniques

The compounds used and prepared during the course of this work were moisture- and temperature-sensitive, and were handled under rigorously anhydrous conditions on glass and metal vacuum line systems or in an inert atmosphere (N_2 gas) dry box (Vacuum Atmospheres Model DLX, oxygen and moisture <0.1 ppm) equipped with a glass cryowell. Preparative work inside the dry box requiring low temperatures was accomplished using a metal Dewar filled with 4.5 mm copper-plated spheres that had previously been cooled to ca. –140 °C in the glass cryowell (–196 °C) of the dry box.

Preparative work involving volatile fluorides that attack glass (e.g. HF) were carried out on metal vacuum lines constructed primarily from 316 stainless steel and nickel and fitted with 316 stainless steel valves (Autoclave Engineers, Inc., Figure 2.1). Pressures were measured at ambient temperatures using MKS Model PDR-5B pressure transducers having wetted surfaces constructed of Inconel. The pressure transducer possessed a range of 0–1150 Torr, which was accurate to ±0.5 Torr.

Reactions that did not involve transfer of materials that attack glass were carried out on Pyrex glass vacuum lines equipped with grease-free 6-mm J. Young PTFE/glass

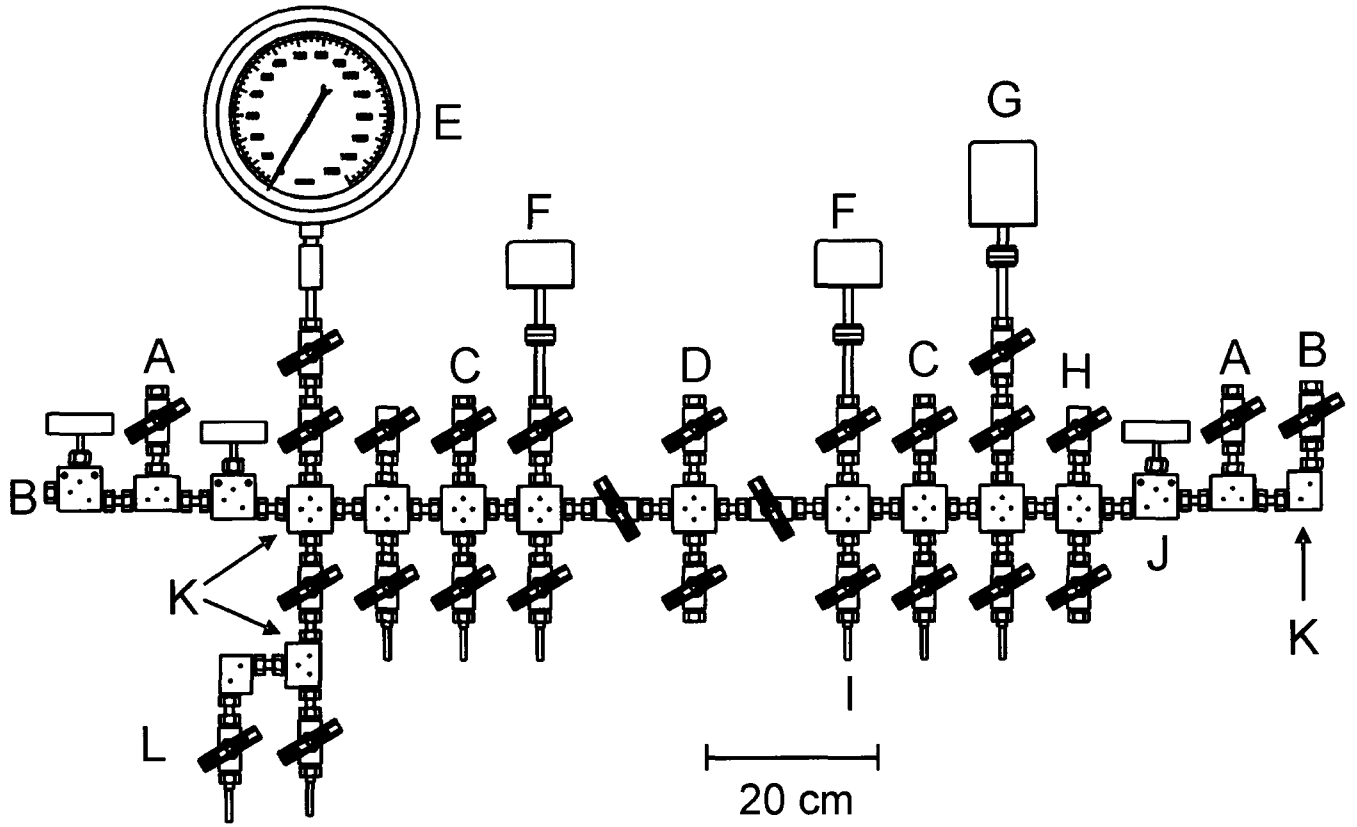

Figure 2.1. The metal vacuum line used in the manipulation of corrosive materials. (A) Outlet to liquid nitrogen and soda lime traps followed by a two-stage direct-drive rotary vacuum pump (Edwards E2M8) – roughing vacuum. (B) Outlet to soda lime and liquid nitrogen traps followed by a two-stage direct-drive rotary vacuum pump (Edwards E2M8) – high vacuum. (C) Dry N_2 inlets. (D) F_2 inlet. (E) Bourdon pressure gauge (0–1500 Torr). (F) MKS Model PDR-5B pressure transducers (0–1000 Torr). (G) MKS Model PDR-5B pressure transducer (0–10 Torr). (H) Ultra-high-purity argon inlet. (I) ¼-in. o.d. ($^1/_8$-in. i.d.) nickel reaction vessel port. (J) High-pressure stainless steel valve (Autoclave Engineers). (K) 316 stainless steel X-, T-, and L-connections employing $^3/_8$-in. o.d. ($^1/_8$-in. i.d.) threaded nickel tubing. (L) Submanifold for NOF/NO_2F transfer.

stopcocks outfitted with PTFE barrels (Figure 2.2). Pressures inside the glass manifold were monitored using a mercury manometer.

Vacuum on the glass vacuum lines (ca. 10^{-3}–10^{-4} Torr) was accomplished using Edwards two-stage internal vane E2M8 direct-drive vacuum pumps. Vacuum was maintained on the metal line using two E2M8 vacuum pumps; the first, a roughing pump, was used primarily for the removal of volatile fluoride and oxide fluoride compounds. The rough pump was used to pump reactive, volatile fluorine compounds through a fluoride/fluorine trap consisting of a stainless steel tube (ca. 60 cm, 15 cm dia.) packed with soda lime absorbent (Fisher Scientific, 4–8 mesh), followed by a final trapping procedure, utilizing a glass liquid nitrogen trap to remove CO_2 and water formed by reaction of fluoride materials with soda lime and other volatile materials that were unreactive towards soda lime. The second vacuum pump provided the high vacuum (ca. 10^{-4} Torr) source for the manifold and was fitted with a glass liquid nitrogen trap.

2.1.2. Preparative Apparatus and Sample Vessels

All synthetic work was carried out in reactors constructed from lengths of ¼-in. and ⅜-in. o.d. FEP tubing which were heat-sealed at one end and heat-flared (45° SAE) at the other. The tubing was connected to Kel-F valves, encased in aluminum housings, using brass flare fittings. All vessels were then connected to a glass vacuum line using Cajon fittings and were rigorously dried by pumping (a minimum of 6 h) under dynamic vacuum. Vessels were then connected to the metal vacuum line using a PTFE Swagelok union and passivated with ca. 1000 Torr of F_2 for ca. 12 h. Once passivated, vessels were

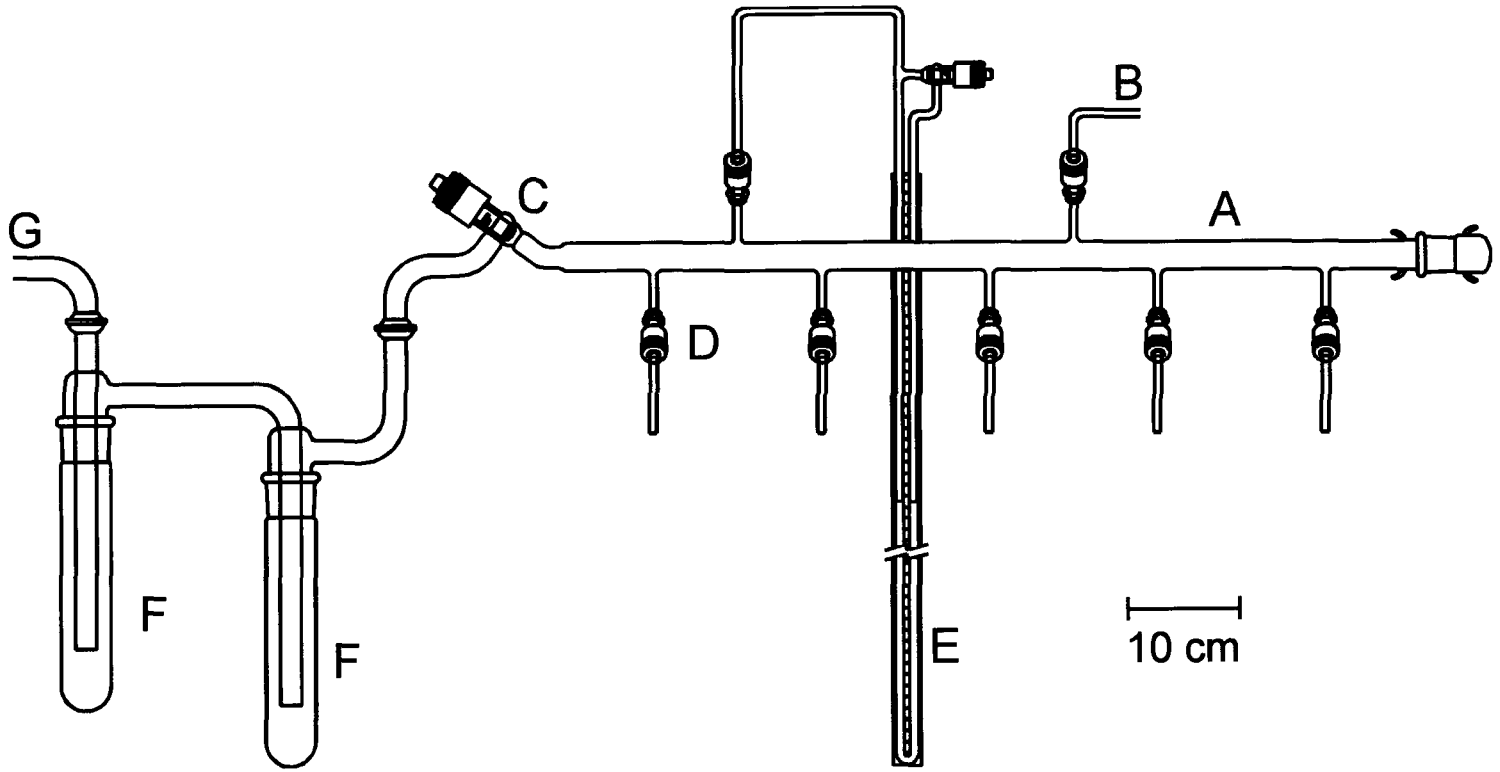

Figure 2.2. Glass vacuum line used for the manipulation of non-corrosive volatile materials. (A) Main vacuum manifold. (B) Dry N_2 inlet. (C) 15-mm greaseless J-Young valve with PTFE barrel. (D) 6-mm greaseless J-Young valve with PTFE barrel. (E) Mercury manometer. (F) Liquid N_2 cold trap. (G) Outlet to vacuum pump.

evacuated under dynamic vacuum to remove all volatile impurities and back-filled with dry N_2 (ca. 1000 Torr) prior to use. Similarly, connections made to a metal vacuum line were dried under dynamic vacuum and passivated with F_2 gas overnight. Connections made to a glass vacuum line were dried under dynamic vacuum overnight.

Nuclear magnetic resonance spectra were acquired using tubes prepared from ¼-in. and 9-mm o.d. FEP tubing. The 9-mm o.d. FEP NMR samples were constructed from lengths of ⅜-in. o.d. FEP by reducing their diameter in a heated brass cylindrical die using mechanical pressure. One end of each tube was heat-sealed using the end of a heated thin-walled 10-mm o.d. glass NMR tube, while the other end was fused to ca. 5 cm of ¼-in. o.d. thick-walled tubing. The end was subsequently heat-flared (45° SAE) for connection to a Kel-F valve. Prior to acquisition of the NMR data the sample tubes were heat-sealed under dynamic vacuum using a nichrome wire resistance furnace of appropriate diameter. Otherwise, NMR samples were prepared in 5-mm o.d. thin wall precision glass NMR tubes (Wilmad) fused to ¼-in. o.d. lengths of glass tubing which were in turn attached to 4-mm J. Young PTFE/glass stopcocks by use of ¼-in. stainless steel Cajon Ultratorr unions fitted with Viton O-rings. The NMR tubes were then vacuum-dried for 8–12 h before use.

Low-temperature Raman spectra of solids (ca. –160 °C) were recorded on samples prepared in both thin-walled ¼-in. and ⅜-in. FEP tubing, as well as 5-mm o.d. glass tubes fused to ¼-in. o.d. lengths of glass tubing which were in turn attached to 4-mm J. Young PTFE/glass stopcocks by use of ¼-in. stainless steel Cajon Ultratorr unions fitted with Viton O-rings.

All connections to vacuum lines were made using thick-walled ¼-in. FEP tubing in conjunction with either a ¼-in. PTFE Swagelok connector outfitted with PTFE compression fittings (ferrules) or ¼-in. stainless steel Cajon Ultra-Torr connectors outfitted with stainless steel compression fittings and Viton rubber O-rings.

2.2. Preparation and Purification of Starting Materials

2.2.1. Sources and Purification of N_2, Ar, F_2, Xe, O_2, O_3, NO, and NO_2

House nitrogen gas was generated by boiling off liquid nitrogen (Air Liquide) and was further dried through a freshly regenerated bed of type 4Å molecular sieves. High purity argon gas (VitalAire), also employed for the back pressuring of reaction vessels, was used without further purification. Technical grade fluorine gas (Air Products) and Xe (Air Products, 99.995%) were used without further purification, unless high purity fluorine gas was required (see Section 2.2.4). High purity oxygen gas (Aire Liquide) was used without further purification. Ozone, O_3, was generated by a Welsback T-408 ozonator using high-purity O_2. Nitrogen oxide, NO (Matheson, >99%) was purified by condensing commercial NO into a 30-mL nickel can at –196 °C, followed by warming to –120 °C using an ethanol slush, and condensing the NO gas into the reaction vessel at –196 °C. Nitrogen dioxide, NO_2 (Matheson, >99.5%), was purified by pressurizing the glass vessel, fitted with a 4-mm J. Young PTFE/glass stopcock, with high-purity O_2, followed by several freeze-pump-thaw cycles at –196 °C.

2.2.2. Purification of Anhydrous HF, SO_2ClF, and CH_3CN

Anhydrous hydrogen fluoride, HF (Harshaw Chemical Co.), was purified by addition of ca. 5 atm of fluorine gas to a commercial HF sample contained in a nickel can for a period of ca. one month prior to use, converting residual water to HF and O_2. The HF was then distilled into a Kel-F storage vessel equipped with a Kel-F valve and stored at room temperature for future use. Transfer of HF was accomplished by vacuum distillation from the Kel-F storage vessel, on a metal vacuum line, through connections constructed from FEP, as shown in Figure 2.3.

Sulfuryl chloride fluoride (Allied Chemical Co., Baker and Adams Division, >90%, ca. 100 g crude material) was purified by fractional distillation through two FEP U-tube traps cooled to –78 and –90 °C, respectively, effectively removing the inert impurity SO_2F_2. The remaining SO_2ClF was then condensed into an FEP U-tube containing ca. 80 g of SbF_5 at –78 °C and slowly warmed to room temperature with vigorous mixing to remove SO_2, which is known to rapidly reduce xenon(II) species. The purified SO_2ClF was then transferred to an FEP U-tube cooled to –78 °C and containing dried KF. Again, the mixture was slowly warmed to room temperature with vigorous mixing and allowed to stand with periodic mixing at room temperature for ca. 2 h to remove any residual HF. The sample was again cooled to –78 °C and condensed into a 1.25-in. FEP reaction vessel containing XeF_2 (1.7 g) for 24 h to ensure all impurities with reducing properties (i.e., SO_2) were removed. Finally, the liquid was distilled by dynamic pumping at –78 °C into a glass vessel, outfitted with a 6-mm J. Young all-glass stopcock,

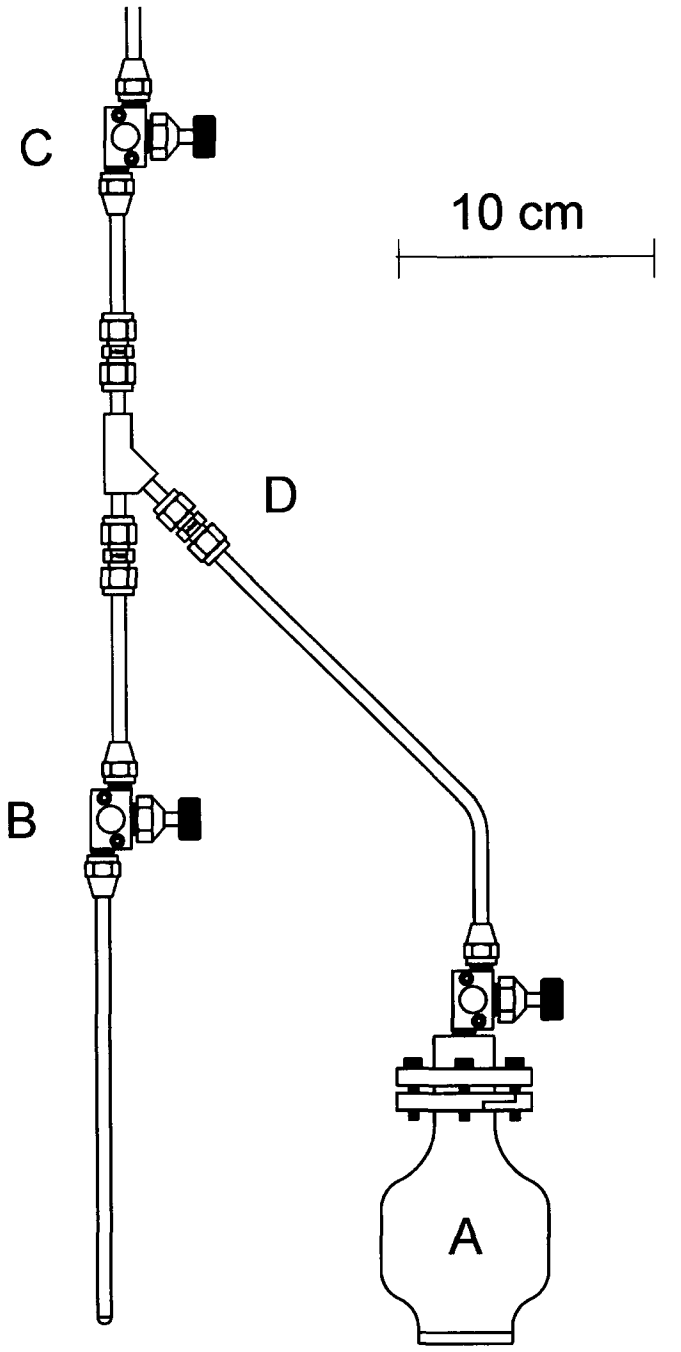

Figure 2.3. Hydrogen fluoride distillation apparatus. (A) Kel-F storage vessel containing HF. (B) FEP reaction vessel fitted with a Kel-F valve. (C) Kel-F valve connected to vacuum manifold. (D) Kel-F Y-connection with Teflon Swagelok unions.

over a bed of dry KF. The purity of the sample was assessed by ^{1}H, ^{17}O, and ^{19}F NMR spectroscopy of a neat sample recorded at –80 °C, in which only trace amounts of SO_2F_2 (2.2%) were found. Transfers were performed using a glass vacuum line by vacuum distillation of SO_2ClF through a sub-manifold comprised of a Y-shaped glass connection to the reaction vessel (Figure 2.4). The sample was stored at room temperature until used.

Acetonitrile (Caledon, HPLC Grade) was purified according to the literature method,[102] and was transferred under vacuum using a glass vacuum line and a glass Y-piece.

2.2.3. Natural Abundance and Isotopically-enriched Water, H_2O, $H_2{}^{17}O$, and $H_2{}^{18}O$

Natural abundance water (Caledon, HPLC grade) was used without further purification. Oxygen-17 enriched water (^{16}O, 35.4%; ^{17}O, 21.9%; ^{18}O, 42.7%) and ^{18}O-enriched water (99.99%) were obtained from the Bureau de Rayonnements Ionisants, Saclay, France, and used without further purification.

2.2.4. NOF, NO_2F, and $^{15}NO_2F$

Nitrosyl fluoride, NOF, was prepared by reaction of NO and F_2 in a 30-mL nickel can. Pure NO gas (ca. 833 Torr, 0.0905 mol) was measured using a 2-L nickel can and was condensed into a 30-mL reaction can at –196 °C. After transfer, the line was pumped to remove any residual material. Fluorine gas was then condensed into an intermediate 30-mL can at –196 °C. The can was then warmed to –183 °C using a liquid oxygen bath and F_2, free of non-volatile contaminants (i.e., HF, CF_4, OF_2, and/or NF_3), was allowed

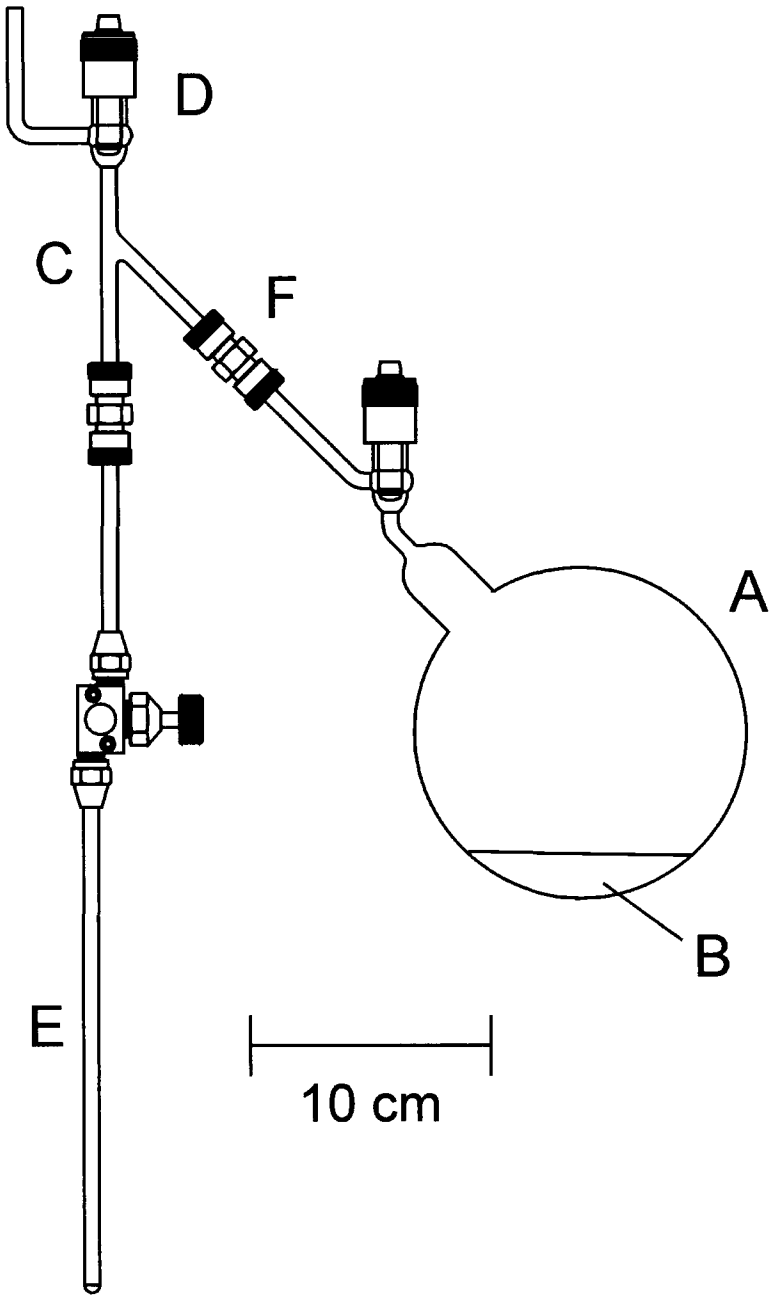

Figure 2.4. Apparatus used for the vacuum transfer of SO_2ClF solvent. (A) 250-mL glass vessel equipped with a 4-mm J. Young all-glass stopcock. (B) Bed of dry, powdered KF. (C) Glass Y-connector. (D) 6-mm J. Yound PTFE/glass valve. (E) FEP reaction vessel fitted with a Kel-F valve. (F) Stainless steel Cajon Ultratorr Union.

into the line and 2-L can. The purified F_2 (384 Torr, 0.0417 mol) was then condensed into the reaction can cooled to –196 °C. The reaction vessel was then closed and allowed to warm slowly to room temperature. After ca. 1 h at room temperature, the vessel was again cooled to –196 °C and the residual F_2 was removed under dynamic vacuum. The procedure was repeated a second time to give a combined yield of 8.63 g (0.1762 mol). Trace amounts of NO_2F (2.2%) and NOF_3 (0.85%) were estimated by recording the ^{19}F NMR spectrum of the liquid product at –80 °C. A fluorine-passivated submanifold, constructed from 316 stainless steel and nickel and dedicated to the transfer of NOF (and NO_2F, vide infra; Figure 2.1), was passivated with NOF prior to transfer to a reaction vessel. The success of the passivation was determined by a visual check of the color of the NOF/NO_2F condensed into an auxillary tube (see Section 2.3.1).

Nitryl fluoride, NO_2F, was prepared by reaction of NO_2 and F_2 in a 30-mL nickel can in a manner similar to that used for the preparation of NOF. Purified NO_2 (12 g) was vacuum distilled into a ½-in. o.d. FEP tube that was fused to a 5-cm length of ¼-in. o.d. FEP tubing fitted with a Kel-F valve. Approximately 3 g of NO_2 was reacted with excess F_2 to generate NO_2F for passivation of the nickel can. The crude NO_2F was then removed, and the remaining NO_2 was reacted with a slight excess of purified F_2 in two steps. The amount of NOF impurity was 2.5% as determined by ^{19}F NMR spectroscopy of the liquid product at –80 °C. Subsequent use of NO_2F involved the passivation of a fluorine-passivated submanifold (vide supra) with NO_2F prior to distillation into a reaction vessel.

The preparation of $^{15}NO_2F$ is an improved version of the published method.[103] In a one-step preparation, $Na^{15}NO_2$ (0.5080 g, 7.258 mmol) was added to a nickel reactor (ca. 10 mL) inside the dry box. The vessel was attached to the metal vacuum line, where all connections were dried under vacuum and passivated with F_2 overnight. Excess F_2 (8.915 mmol) was condensed onto the solid at –196 °C. The valve was then closed and the mixture warmed to –78 °C, where the vigorous release of gaseous CO_2 from the surrounding dry ice/acetone bath indicated the reaction was taking place. The reactor was allowed to warm slowly to room temperature overnight. The reactor was then cooled to –196 °C, and excess F_2 was slowly removed under dynamic vacuum. The ^{19}F NMR spectrum of the neat liquid product at –80 °C showed an NOF impurity (8.1% by integration).

2.2.5. AsF_3, AsF_5, SbF_3, and XeF_2

Arsenic trifluoride (containing ca. 9 mol% HF as shown by ^{19}F NMR spectroscopy), was purified by condensing crude AsF_3 into a 2-L nickel can preloaded with an 8-fold molar excess of dry NaF, and was allowed to stand at room temperature for a period of ca. 24 h, during which time it was frequently agitated.

Arsenic pentafluoride was prepared as previously described[104,105] by direct fluorination of purified AsF_3 with purified F_2 in a nickel can. The AsF_5 was used from the reaction can without further purification.

Antimony trifluoride, SbF_3 (Aldrich, 98%), was purified by vacuum sublimation (350–400 °C) and stored in the dry box prior to use.

Xenon difluoride was prepared according to the literature method[104] and stored in a Kel-F tube inside a dry box prior to use.

2.2.6. NaF, $NaNO_2$ and $Na^{15}NO_2$

Sodium fluoride, NaF (J. T. Baker Chemical Co., 99%) and natural abundance (BDH Chemical, 97%) and ^{15}N-enriched (Isotec, 98+%) $NaNO_2$ were dried by dynamically pumping the powders under vacuum at 250–300 °C and 150 °C, respectively, in glass drying tubes employing greased connections and J-Young PTFE/glass stopcocks for a period of 3 days. The freshly dried salts were then stored inside the dry box prior to use.

2.2.7. HNO_3 and N_2O_5

Anhydrous HNO_3 was prepared from red-fuming (90%) HNO_3 (Fischer Scientific Co.) by drying the later over 30% fuming sulfuric acid, followed by distillation under dynamic vacuum at room temperature into a reactor at –196 °C. Nitrogen pentoxide was synthesized from HNO_3 and P_4O_{10} and purified with ozone, O_3, according to the literature method.[106]

2.2.8. CCl_4, CBr_4, Freon-11 ($CFCl_3$), Freon-12 (CF_2Cl_2), Freon-13 (CF_3Cl), Freon-12B2 (CF_2Br_2), and Freon-13B1 (CF_3Br)

Carbon tetrachloride, CCl_4, (Aldrich) was dried for several days over CaH_2 and distilled into a glass vessel fitted with a 4-mm J. Young PTFE/glass stopcock prior to use. Carbon tetrabromide, CBr_4 (Aldrich), was purified by sublimation under dynamic

vacuum and stored in a dry box prior to use. Freon-11, Freon-12, and Freon-12B2 (Matheson) were dried over P_4O_{10} for several days and distilled into glass vessels fitted with 4-mm J. Young PTFE/glass stopcocks. Freon-13 (Matheson) was distilled into a stainless steel reactor fitted with a stainless steel valve over a bed of dry P_4O_{10} and stored at room temperature. Freon-13B1 (Matheson) was used without further purification.

2.2.9. $[H_3O][AsF_6]$, $[H_3{}^{17}O][AsF_6]$, and $[H_3{}^{18}O][AsF_6]$

Natural abundance, ^{17}O-, and ^{18}O- enriched $[H_3O][AsF_6]$ salts were prepared as described in the literature.[107] In a typical preparation, water, 0.17401 g (9.6590 mmol), was transferred into a 5-mm o.d. FEP weighing tube inside the dry box, and the entire weighing tube was inserted into a $^3/_8$-in. o.d. FEP reaction vessel fitted with a Kel-F valve. Anhydrous hydrogen fluoride was then distilled into the FEP reactor at –196 °C to a depth of ca. 6.5 cm, i.e. until the level of HF was above the level of the weighing tube containing H_2O. The mixture was allowed to warm to room temperature and was thoroughly agitated. The metal vacuum line was evacuated and passivated twice with AsF_5. A slight excess of arsenic pentafluoride (9598 Torr in a 19.7-mL volume; 1.64 g, 9.65 mmol), was then condensed onto the reaction mixture at –196 °C. The reaction mixture was warmed to –78 °C to effect dissolution of AsF_5 in the HF solution, immediately affording a white precipitate of $[H_3O][AsF_6]$. The reaction mixture was allowed to warm to room temperature and was agitated for ca. 10 min. to dissolve the product, forming a clear, colorless solution. The reaction vessel was then cooled to –78 °C and connected to the glass line through an intermediate FEP U-tube trap cooled to

–196 °C. The HF solvent and any unreacted AsF_5 were pumped off over a period of ca. 5 h at –78 °C, and subsequently pumped on at room temperature for an additional 1 h. The ^{17}O- and ^{18}O-enriched samples of $[H_3O][AsF_6]$ were prepared in the same manner as the natural abundance sample. The purities of the salts were verified by low-temperature Raman spectroscopy.

2.2.10. $[Xe_3OF_3][AsF_6]$, $[Xe_3{}^{17}OF_3][AsF_6]$, and $[Xe_3{}^{18}OF_3][AsF_6]$

Inside the dry box, 0.05996 g (0.2884 mmol) of $[H_3O][AsF_6]$ was transferred to a ¼-in. o.d. FEP h-shaped reactor fitted with a Kel-F valve. Anhydrous HF was then distilled (ca. 0.5 mL) into the reaction vessel at –196 °C. The cold vessel was returned to the dry box through the cryowell cold port and maintained at –140 °C. Xenon difluoride, 0.04731 g (0.2795 mmol), was added to the frozen mixture. The frozen sample was removed from the dry box and connected to a glass vacuum line through an FEP U-tube trap cooled to –196 °C. The vessel was warmed to –50 °C and agitated for ca. 10 min. until all the XeF_2 had dissolved. Formation of an orange-red crystalline precipitate under a light orange solution occurred immediately. The sample was allowed to stand for ca. 1 h, after which time the solution had become clear and colorless above the orange-red precipitate. The HF solvent was decanted into the side arm which had been cooled to –78 °C. The HF in the side arm was warmed to room temperature and back-distilled onto the sample at –78 °C in order to remove any further $[F(XeF)_2][AsF_6]$ impurity or unreacted starting material. The process was repeated a total of three times. The side arm was then cooled to –196 °C and heat-sealed off under dynamic vacuum. The sample was

back-filled with dry N_2 at –78 °C and stored at –78 °C. The purity of $[Xe_3OF_3][AsF_6]$ and absence of XeF2, $[H_3O][AsF_6]$, and $[F(XeF)_2][AsF_6]$ were verified by low-temperature Raman spectroscopy.

Samples of $[Xe_3{}^{17}OF_3][AsF_6]$ and $[Xe_3{}^{18}OF_3][AsF_6]$ were prepared in a similar manner to that used for $[Xe_3OF_3][AsF_6]$. The preparation of the ^{17}O-enriched compound was carried out on a larger scale using a 9-mm o.d. FEP tube fused to a ¼-in. o.d. FEP h-shaped reactor, and fitted with a Kel-F valve. In the dry box, 0.1069 g (0.63147 mmol) of XeF_2 was transferred to 0.12527 g (0.59935 mmol) of $[H_3{}^{17}O][AsF_6]$ in HF which was cooled to ca. –140 °C. The reaction was carried out at –50 °C, yielding a red-orange crystalline precipitate. The ^{18}O-enriched compound was prepared in a ¼-in. o.d. FEP h-shaped reactor fitted with a Kel-F valve. In the dry box, 0.13212 g (0.78045 mmol) of XeF_2 was transferred to 0.13875 g (0.66411 mmol) of $[H_3{}^{18}O][AsF_6]$ in HF and cooled to ca. –140 °C. The reaction was also carried out at –50 °C and yielded red-orange crystals. The purities of both compounds were checked by low-temperature Raman spectroscopy.

2.2.11. $HOTeF_5$, $B(OTeF_5)_3$, $Sb(OTeF_5)_3$, and $Xe(OTeF_5)_2$

Pentafluoroorthotelluric acid, $HOTeF_5$, was prepared by reaction of $Te(OH)_6$ (BDH Chemical, >99.5%) with H_2SO_4 and NaF (to generate HSO_3F in situ) as described elsewhere.[108]

The compound, $B(OTeF_5)_3$, was prepared by reaction of BCl_3 (Matheson) and $HOTeF_5$ according to the literature method,[109] and stored in a ½-in. o.d. FEP tube equipped with an FEP plug inside the dry box.

The compound, $Sb(OTeF_5)_3$, was prepared by reaction of SbF_3 and $B(OTeF_5)_3$ by the literature method,[110] and stored in a ¼-in. o.d. FEP tube fitted with an FEP plug inside the dry box.

The compound, $Xe(OTeF_5)_2$, was prepared by reaction of XeF_2 and $B(OTeF_5)_3$ as described in the literature,[35] and stored in at –78 °C in a ½-in. o.d. FEP vessel fused to a ca. 4-cm length of ¼-in. o.d. FEP tube fitted with a Whitey ORM2 stainless steel valve under an atmosphere of dry N_2 gas.

2.3. Syntheses of $O(XeF)_2$, $^{17}O(XeF)_2$, and $^{18}O(XeF)_2$

A sample of $[Xe_3OF_3][AsF_6]$ in a ¼-in. o.d. FEP tube fitted with a Kel-F valve was connected to a metal vacuum line through an h-shaped FEP connection that was, in turn, connected to an empty ¼-in. o.d. auxiliary FEP tube fitted with a Kel-F valve. Nitrosyl fluoride was condensed into the auxiliary tube at –196 °C. The solid NOF was colorless, consistent with the absence of N_2O_3. A small amount of NOF was then condensed into the top of the reaction vessel at –196 °C. The solid NOF was warmed to –78 °C whereupon it melted and reacted with $[Xe_3OF_3][AsF_6]$ to form a bright yellow solid over the red-orange solid precipitate. The sample was titrated with NOF at –78 °C until the orange-red color of $[Xe_3OF_3][AsF_6]$ was no longer evident, resulting in a faint blue-coloured solid suspension in colorless NOF. Excess NOF was then removed under dynamic vacuum at –78 °C, yielding a pale yellow solid.

The ^{17}O- and ^{18}O-enriched samples of $O(XeF)_2$ were prepared from $[Xe_3{}^{17}OF_3][AsF_6]$ and $[Xe_3{}^{18}OF_3][AsF_6]$, respectively, in a manner similar to that used for the preparation of natural abundance $O(XeF)_2$.

2.4. Preparation of $FXeONO_2$, $FXe^{18}ONO_2$, and $FXeO^{15}NO_2$

A sample of $[Xe_3OF_3][AsF_6]$ (or $[Xe_3{}^{18}OF_3][AsF_6]$) in a ¼-in. o.d. FEP reactor fitted with a Kel-F valve, an auxiliary ¼-in. o.d. FEP reactor, and a nickel vessel containing NO_2F (or $^{15}NO_2F$) were attached to a 3-way ¼-in. o.d. FEP connector by means of brass compression fittings or ¼-in. stainless steel Cajon Ultratorr unions fitted with Viton O-rings. All connections and the auxiliary tube were passivated with F_2 for several hours. The NO_2F sample, cooled to –78 °C, was condensed into the auxiliary tube (ca. 0.5 mL) at –196 °C and sealed, followed by warming to –78 °C to visually check the purity of the sample (N_2O_3 is an intense blue color at low concentrations in liquid NO_2F) and to control the amount added to $[Xe_3OF_3][AsF_6]$. The NO_2F in the auxiliary tube (–78 °C) was then condensed onto the $[Xe_3OF_3][AsF_6]$ at –196 °C. The reactor was then warmed to –50 °C, where, after 5 h, the magenta solid slowly changed to a white suspension in excess NO_2F solution. Excess NO_2F was removed under vacuum at –110 °C to yield a white, microcrystalline solid corresponding to a mixture of $FXeONO_2$, XeF_2, and $[NO_2][AsF_6]$.

2.5. Preparation of $XeF_2 \cdot HNO_3$

Inside the dry box, XeF_2 (0.14063g, 0.83070 mmol) was added to a ¼-in. o.d. FEP reactor fitted with a Kel-F valve. Sulfuryl chloride fluoride (ca. 1.5 mL) was then condensed onto the sample at −196 °C, followed by condensation of HNO_3 (0.10469 g, 1.66141 mmol) onto the frozen mixture at −196 °C. The mixture was warmed to −30 °C and agitated for 1 h, after which the solvent was removed under vacuum at −78 °C to give a colorless, microcrystalline $XeF_2 \cdot HNO_3$.

2.6. Preparation of $XeF_2 \cdot N_2O_4$

Xenon difluoride (0.1510 g, 0.8920 mmol) was added to a ¼-in. o.d. FEP reactor fitted with a Kel-F valve inside the dry box. Liquid N_2O_4 was then condensed onto the sample at −78 °C (ca. 1.5 mL) and pressurized with 1 atm. of dry nitrogen. The reactor was warmed to 10 °C to effect dissolution, and initially gave a yellow-brown solution. Cooling to −10 °C caused the adduct to precipitate from the solution as a colorless solid. Formation of the adduct was verified by low-temperature (−160 °C) Raman spectroscopy of the compound under a frozen N_2O_4 solution.

2.7. Synthesis of $[XeOTeF_5][Sb(OTeF_5)_6] \cdot SO_2ClF$

CAUTION! The oxidative aggressiveness of $[XeOTeF_5][Sb(OTeF_5)_6] \cdot SO_2ClF$ is manifested by the ability of the dry salt and its SO_2ClF solutions to oxidize and crack the bodies of the Kel-F valves used in the synthesis and handling of this compound should they come into contact with their wetted surfaces. In a typical synthesis, 0.49654 g

(0.5929 mmol) of $Sb(OTeF_5)_3$ and 0.72192 g (1.1864 mmol) of $Xe(OTeF_5)_2$ were weighed out and added to a 25-cm long ¼-in. o.d. FEP reaction vessel maintained at –120 °C inside a dry box. The reaction vessel was removed cold from the dry box and immediately placed inside a –78 °C bath and connected to a glass vacuum line, where SO_2ClF solvent (ca. 3 mL) was condensed into the reaction vessel under static vacuum at –196 °C. The reactor was warmed to –20 °C, whereupon the reactants dissolved to give a colorless solution and the reaction proceeded with the liberation of xenon gas to give an intense yellow solution of $[XeOTeF_5][Sb(OTeF_5)_6]$. The reaction vessel was periodically cooled to –78 °C and opened to the vacuum line manifold to remove xenon gas. After 3 h at –20 °C, the reactor was warmed to 0 °C for several minutes to ensure that the reaction was complete. The solvent was then removed under vacuum at –78 °C to yield a pale yellow powder and was then pumped at 0 °C for ca. 30 min to give $[XeOTeF_5][Sb(OTeF_5)_6]\cdot SO_2ClF$. The purity of the sample was confirmed by low-temperature (–160 °C) Raman spectroscopy and in SO_2ClF solution by ^{17}O, ^{19}F, ^{121}Sb, ^{125}Te, and ^{129}Xe NMR spectroscopy (see Chapter 5).

2.8. Preparation of $[CX_3][Sb(OTeF_5)_6]$ (X = Cl, Br, $OTeF_5$)

Stoichiometric amounts of solid $[XeOTeF_5][Sb(OTeF_5)_6]$ (0.04134 g, 0.0215 mmol), cooled to –120 °C, and CBr_4 (0.01091 g, 0.0329 mmol) were weighed into an NMR tube, also cooled to –120 °C, in the dry box and immediately transferred to a glass vacuum line, where 0.4–0.5 mL of SO_2ClF was vacuum distilled onto the mixture at –78 °C. To enhance the yield of $[C(OTeF_5)_3][Sb(OTeF_5)_6]$, $BrOTeF_5$ was condensed onto the

sample of $[CBr_3][Sb(OTeF_5)_6]$ in a 3:1 mole ratio based on initial amounts of $[XeOTeF_5][Sb(OTeF_5)_6]$ and CBr_4, and allowed to react at –20 °C for ca. 3 h (see Chapter 6). In the case of CCl_4 (270 torr, 0.00337 g, 0.0219 mmol), SO_2ClF was vacuum distilled onto $[XeOTeF_5][Sb(OTeF_5)_6]$ (0.04152 g, 0.02159 mmol), followed by condensation of CCl_4 onto the mixture at –196 °C.

2.9. Preparation of $[Br(OTeF_5)_2][Sb(OTeF_5)_6]$

Inside the dry box, $[XeOTeF_5][Sb(OTeF_5)_6]$ (0.10124 g, 0.05264 mmol) was transferred at –120 °C to an NMR sample tube kept at the same temperature. The sample was removed from the dry box, immediately placed in a –78 °C bath, and connected to a glass vacuum line. After drying the connection under dynamic vacuum, 0.4–0.5 mL of SO_2ClF was condensed onto the sample under static vacuum at –78 °C. A stoichiometric excess of $BrOTeF_5$ (0.02347 g, 0.0737 mmol) was then vacuum distilled into the tube at –196 °C.

2.10. Preparation of $[CFX_2][Sb(OTeF_5)_6]$ and $[F_3C–Br–OTeF_5][Sb(OTeF_5)_6]$ (X = Cl, Br)

In the dry box, stoichiometric amounts of solid $[XeOTeF_5][Sb(OTeF_5)_6]$ (ca. 0.02 mmol), cooled to –120 °C, were weighed into 5-mm o.d. glass NMR tubes (Wilmad) kept at the same temperature. The samples were then transferred to a glass vacuum line, where 0.4–0.5 mL of SO_2ClF was vacuum distilled onto the mixture at –78 °C (vide supra). The $CFCl_3$ (ca. 0.02 mmol) or CF_2Br_2 (ca. 0.04 mmol) were vacuum distilled onto the mixture

at –196 °C to produce $[CFCl_2][Sb(OTeF_5)_6]$ and $[CFBr_2][Sb(OTeF_5)_6]$, respectively. Similarly, CF_3Br (ca. 0.02 mmol) was condensed onto the mixture at –196 °C to afford the$[F_3C–Br–OTeF_5][Sb(OTeF_5)_6]$ salt. All reactions were left for 1–2 h at –78 °C to allow the reaction to reach completion.

2.11. Preparation of Natural Abundance and ^{13}C-enriched $C(OTeF_5)_4$

On a glass vacuum line, $BrOTeF_5$ (0.3908 g, 1.227 mmol) was condensed into a pre-weighed glass vessel fitted with a 4-mm J. Young PTFE/glass stopcock at –196 °C under static vacuum. Inside the dry box, CBr_4 (0.1015 g, 0.3061 mmol) was added to a ¼-in. o.d. FEP reaction vessel fitted with a Kel-F valve. The reaction vessel was removed from the dry box and connected to a glass vacuum line, where SO_2ClF solvent (ca. 1.5 mL) was condensed onto CBr_4 under static vacuum at –78 °C, followed by condensation of $BrOTeF_5$ onto the sample under static vacuum at –196 °C. Warming to –78 °C under autogeneous pressure resulted in a vigourous reaction which was indicated by rapid boiling of the solvent and a color change from a bright ruby red solution to a dull red-brown solution of Br_2 and a white precipitate. The reaction mixture was warmed to 0 °C after 1 h, at which point the white precipitate dissolved. Removal of SO_2ClF (–78 °C) and Br_2 (0 °C) under dynamic vacuum yielded white, microcrystalline $C(OTeF_5)_4$ in nearly quantitative yield. The product sublimed slowly at room temperature under static vacuum, and melted at 33.6 °C as determined by DSC (see Chapter 8). Carbon-13 enriched $C(OTeF_5)_4$ was prepared in a similar manner by reaction of 0.4232 g (1.3286 mmol) of $BrOTeF_5$ with 0.1104 g (0.3319 mmol) of 99% ^{13}C-enriched CBr_4 in SO_2ClF.

2.12. Preparation of $[N(CH_3)_4][B(OTeF_5)_4]$

The salt, $[N(CH_3)_4][B(OTeF_5)_4]$, was prepared by reaction of equimolar amounts of $[N(CH_3)_4][OTeF_5]$ and $B(OTeF_5)_3$ in CH_2Cl_2 using a procedure similar to that used for the preparation of $[N(n\text{-}Bu)_4][B(OTeF_5)_4]$.[111]

2.13. X-ray Crystallography

2.13.1. Crystal Growth

A large majority of the crystals grown for structure determination by X-ray crystallography were grown in the low-temperature crystal growing apparatus depicted in Figure 2.5.

2.13.1.1. Attempted Crystal Growth of $O(XeF)_2$

Several attempts were made to grow crystals of $O(XeF)_2$ from CH_3CN solution at low temperatures. However, complete dissolution could only be achieved at temperatures ranging from –15 to –25 °C. Prolonged times at this temperature (ca. 2–3 h) failed to yield crystalline material, and further cooling failed to produce any solid material, indicative of decomposition which is commensurate with the solid-state decomposition temperature. When the solution was rapidly cooled to –30 °C or below crystals immediately formed, but detonated upon drying under vacuum at –42 °C, with the emission of blue light. Attempts to mount crystals grown quickly at –35 °C and slightly wetted with CH_3CN gave a diffraction pattern, but no unit cell could be determined, presumably because the fast crystal growth yielded microcrystalline material rather than

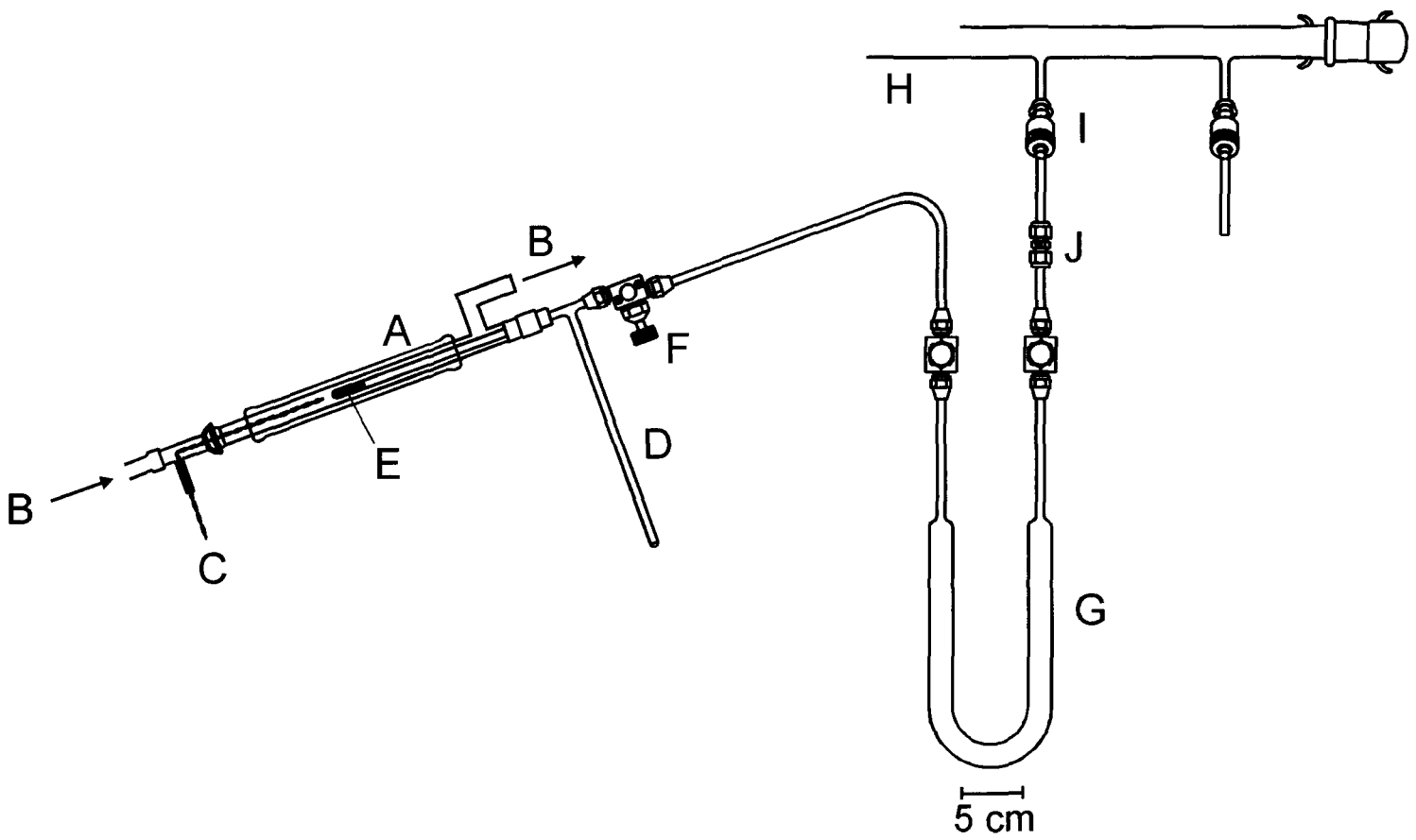

Figure 2.5. Low-temperature crystal growing apparatus. (A) Glass-jacketed dewar. (B) Nitrogen cold flow. (C) Thermocouple lead. (D) T-shaped FEP reaction vessel with side arm. (E) Sample region. (F) Kel-F valve. (G) FEP U-trap. (H) Vacuum manifold. (I) Greaseless J-Young valve with PTFE barrel. (J) PTFE Swagelok or stainless steel Cajon Ultra-Torr connector.

single crystals.

2.13.1.2. $FXeONO_2$

Sulfuryl chloride fluoride (ca. 1.5 mL) was distilled onto a mixture of $FXeONO_2$, XeF_2, and $[NO_2][AsF_6]$ at –78 °C that had been synthesized in situ in one arm of a ¼-in. o.d. FEP T-shaped reactor fitted with a Kel-F valve. The reactor was pressurized with ca. 1 atm. of dry nitrogen and warmed to –30 °C, effecting partial dissolution of the white solid mixture. The arm containing the solution was inclined at ca. 5° from horizontal inside the glass dewar of a crystal growing apparatus that had been previously adjusted to –35 °C. Over 2–3 h colorless plates formed at –35 °C. The temperature was lowered over a period of 3–4 h to –50 °C, allowing for more complete crystallization. The crystals were isolated by decanting the solvent under dry nitrogen into the side arm of the FEP vessel, which was immersed in a dry ice/acetone bath, followed by evacuation and drying of the crystalline product under dynamic vacuum at –80 °C before the side arm containing the supernatant was removed by heat sealing it off at –196 °C. A crystal having the dimensions 0.22 × 0.16 × 0.04 mm was selected for low-temperature X-ray structure determination.

2.13.1.3. $XeF_2 \cdot HNO_3$

Sulfuryl chloride fluoride (ca. 1.5 mL) was distilled onto a sample of solid $XeF_2 \cdot HNO_3$ at –196 °C that had been synthesized in one arm of a ¼-in. o.d. FEP T-shaped reactor fitted with a Kel-F valve. The reactor was warmed to –30 °C to effect

dissolution; after a few minutes of intense mixing the adduct dissolved to give a clear, colorless solution. The arm containing the solution was inclined at ca. 5° from horizontal inside the glass dewar of a crystal growing apparatus that had been previously adjusted to –40 °C to prevent decomposition. After ca. 15 min clear, colorless plates had begun to grow on the walls of the reactor. Over the course of 7 h, the temperature was lowered to –60 °C after which time a large quantity of crystals had grown. The supernatant was decanted at –70 °C into the side arm of the reactor, which was cooled in a dry ice/acetone bath. The sample was dried under dynamic vacuum at –80 °C before heat sealing off the side arm of the reactor at –196 °C. A crystal having the dimensions 0.20 × 0.13 × 0.04 mm was selected for low-temperature X-ray structure determination.

2.13.1.4. $XeF_2 \cdot N_2O_4$

A solution of $XeF_2 \cdot N_2O_4$ in liquid N_2O_4 was prepared in a ¼-in. o.d. FEP T-shaped reactor fitted with a Kel-F valve. The arm containing the solution was inclined at ca. 5° from horizontal inside the glass dewar of a crystal growing apparatus that had been previously adjusted to 3 °C. Initially long needles of XeF_2 formed. Upon cooling to –3 °C plates began to form on the needles over a period of 1 h. Over a period of an additional 6 h more plates formed, after which time the N_2O_4 was decanted under dry nitrogen into the side arm of the FEP vessel at –80 °C. The crystals were dried under dynamic vacuum at –10 °C before heat sealing off the side arm containing the supernatant at –196 °C. A crystal having the dimensions 0.16 × 0.08 × 0.04 mm was selected for low-temperature X-ray structure determination.

2.13.1.5. $[XeOTeF_5][Sb(OTeF_5)_6]\cdot SO_2ClF$

Inside the dry box, ca. 0.2 g of $[XeOTeF_5][Sb(OTeF_5)_6]\cdot SO_2ClF$ at –120 °C was transferred to a T-shaped ¼-in. o.d. FEP reactor kept at the same temperature, and dissolved in the minimum amount (ca. 0.5 mL) of SO_2ClF. Crystals were grown by slow cooling of the reaction mixture from –50 to –80 °C over a period of 2 days inside the vertical arm of the reaction vessel. Pale yellow, block-shaped crystals were isolated by decanting the solvent into the horizontal arm at –80 °C, followed by drying under dynamic vacuum at the same temperature. The side arm was then heat sealed off at –196 °C.

2.13.1.6. $[CCl_3][Sb(OTeF_5)_6]$, $[CBr_3][Sb(OTeF_5)_6]\cdot SO_2ClF$ and $[C(OTeF_5)_3][Sb(OTeF_5)_6]\cdot 3SO_2ClF$

Crystals of $[CCl_3][Sb(OTeF_5)_6]$ were obtained by reaction of ca. 0.2 g of $[XeOTeF_5][Sb(OTeF_5)_6]$ and a two-fold excess of CCl_4 in 1.5 mL of SO_2ClF inside a T-shaped ¼-in. o.d. FEP reaction vessel. Colorless crystals were grown by slow cooling of the reaction mixture from –20 to –50 °C over a period of 6 h inside the vertical arm of the reaction vessel. Colorless, plate-shaped crystals were isolated by decanting the solvent into the horizontal arm (–80 °C), drying the crystals under dynamic vacuum at –78 °C, and heat sealing the side arm off at –196 °C. Crystals of $[CBr_3][Sb(OTeF_5)_6]\cdot SO_2ClF$ (pale yellow), $[C(OTeF_5)_3][Sb(OTeF_5)_6]\cdot 3SO_2ClF$ (colorless) and Br_2 (red brown) crystals were grown and isolated in a manner similar to that described for

$[CCl_3][Sb(OTeF_5)_6]$. Bromine produced in the reaction was identified by determination of the unit cell parameters[112,113] at –173 °C for a crystal selected from the bulk sample.

2.13.1.7. Attempted Crystal Growths of $[CFCl_2][Sb(OTeF_5)_6]$ and $[F_3C–Br–OTeF_5][Sb(OTeF_5)_6]$

Attempts were made to grow crystals of $[CFCl_2][Sb(OTeF_5)_6]$ by reaction of ca. 0.2 g of $[XeOTeF_5][Sb(OTeF_5)_6]$ and a stoichiometric amount of $CFCl_3$ in 1.5 mL of SO_2ClF inside a T-shaped ¼-in. o.d. FEP reaction vessel. Although a white precipitate formed during reaction at –78 °C, attempts to grow crystals by redissolution at –30 °C and cooling between –30 to –50 °C over a period of 6 h inside the vertical arm of the reaction vessel failed, indicating that the salt is not stable above –30 °C. Similar attempts to grow crystals below –50 °C yielded a white film that was unsuitable for X-ray diffraction. Similar attempts to grow crystals of $[F_3C–Br–OTeF_5][Sb(OTeF_5)_6]$ also failed, giving a white, microcrystalline solid over three days between –50 to –60 °C. On the trough the crystals were found to transform to a powder easily when manupulated and thus were unsuitable for X-ray diffraction.

2.13.1.8. Attempted Crystal Growth of $[CFBr_2][Sb(OTeF_5)_6]$; Crystal Growth of $[SbBr_4][Sb(OTeF_5)_6]\cdot SO_2ClF$

Attempts were made to grow $[CFBr_2][Sb(OTeF_5)_6]$ crystals between –40 to –50 °C over several hours inside the vertical arm of the reaction vessel. Colorless, plate-shaped crystals were isolated by decanting the solvent into the horizontal arm, followed

by drying under dynamic vacuum at –78 °C. However, X-ray crystallography indicated that the crystals were $[SbBr_4][Sb(OTeF_5)_6]\cdot SO_2ClF$, indicating that the sample had reacted further (see Chapter 7).

2.13.1.9. $C(OTeF_5)_4$

Approximately 0.2 g of $C(OTeF_5)_4$ was transferred inside a dry box by means of a solid syringe into a 10-mm o.d. glass tube fused to a ¼-in. o.d. length of glass tubing which was, in turn, connected to a 4-mm J. Young PTFE/glass stopcock using a ¼-in. 316 stainless steel Swagelok Ultratorr union with Viton O-rings. The vessel was then removed from the dry box and connected to a glass vacuum line, where it was flame sealed under dynamic vacuum at –196 °C. Large, colorless crystals were grown by sublimation over a period of ca. 1 week at ambient temperatures, after which time the glass tube was returned to the dry box where it was cut open. Several crystals were selected under a microscope attached to the dry box and heat sealed inside 0.1–0.4 mm glass Lindemann capillaries and stored at room temperature prior to mounting on the diffractometer. The crystal used in this study was a block having the dimensions 0.45 × 0.35 × 0.30 mm.

2.13.1.10. $N(CH_3)_4][B(OTeF_5)_4]$

Approximately 0.2 g of compound was transferred into a T-shaped ¼-in. o.d. FEP reaction vessel. Methylene chloride was then condensed onto the salt under static vacuum at –196 °C (ca. 1.5 mL). The salt was dissolved at 50 °C, and crystals were grown by

slow cooling of the solution from 50 °C to room temperature over a period of 6 h inside the vertical arm of the reaction vessel. Colorless, needle-shaped crystals were isolated by decanting the solvent into the horizontal arm (–80 °C), drying the crystals under dynamic vacuum at –20 °C, and heat sealing the side arm off at –196 °C. The crystal of $[N(CH_3)_4][B(OTeF_5)_4]$ used for this study was a needle having the dimensions 0.18 × 0.05 × 0.04 mm.

2.13.2. Low-Temperature Crystal Mounting

Because most of the samples investigated in this work were thermally unstable and/or moisture sensitive, all of the samples investigated (except for $C(OTeF_5)_4$, vide supra) were mounted at low temperature using the apparatus depicted in Figures 2.6 and 2.7. The reaction vessels containing the samples were first cut open below the Kel-F valve under a flow of dry argon gas, using an inverted glass funnel, while maintaining the sample at –78 °C. The sample was then quickly dumped into to the aluminum trough of the crystal mounting apparatus under a stream of dry argon, precooled (–100 ± 3 °C) by the regulated passage of dry nitrogen gas flow through a 5-L dewar filled with liquid N_2 (Figures 2.6 and 2.7). The temperature inside the trough was measured using a copper-constantan thermocouple positioned in the sample region of the trough. Using an additional glass sleeve, which was fitted into a concentric position around the silvered cold-flow dewar, an ambient nitrogen gas flow was slowly passed through the sleeve in order to maintain a laminar flow, thereby reducing atmospheric moisture build up in the trough. Crystals were then selected using a stereo-zoom microscope and mounted on a

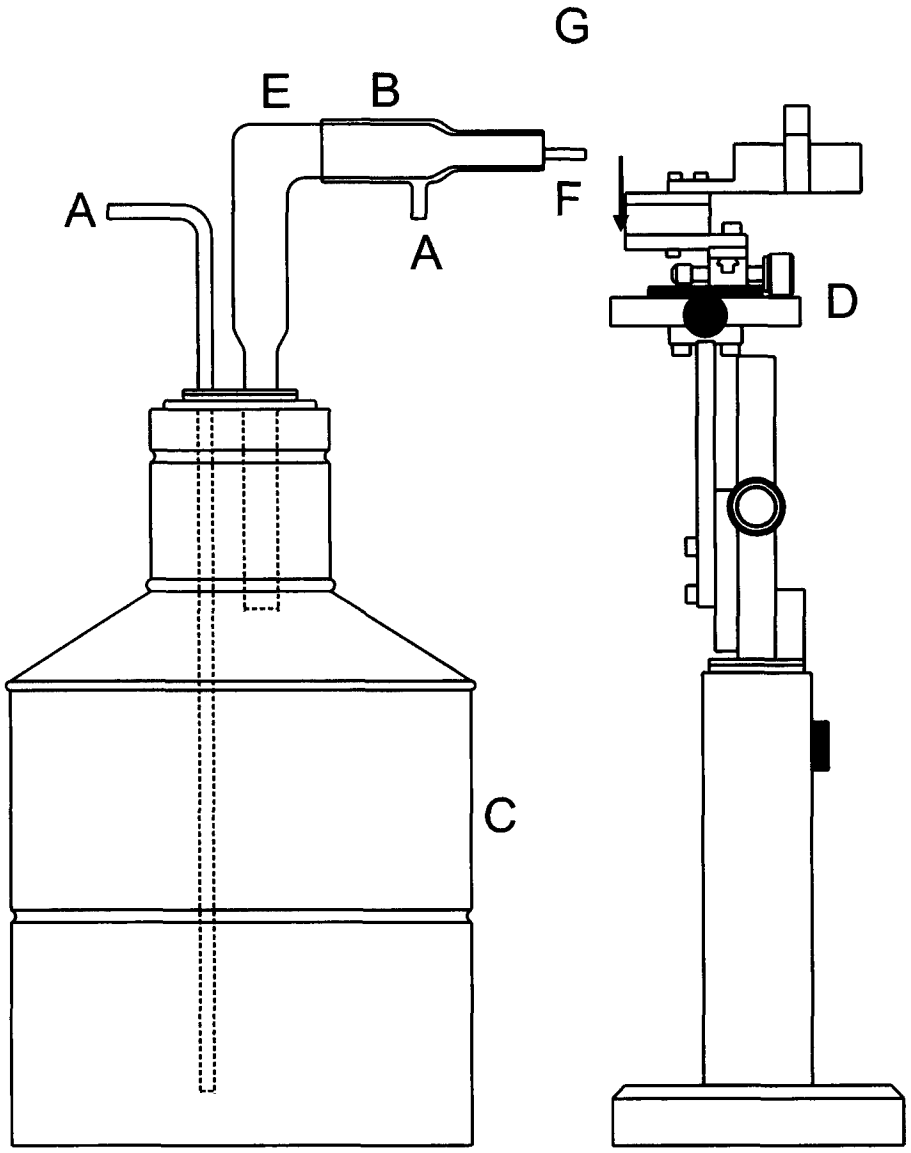

Figure 2.6. Low-temperature crystal mounting apparatus. (A) Nitrogen inlet. (B) Glass sleeve for ambient nitrogen flow. (C) Liquid N_2 dewar. (D) Adjustable support stage. (E) Silvered dewar (glass). (F) Aluminum trough. (G) Stereo-zoom microscope.

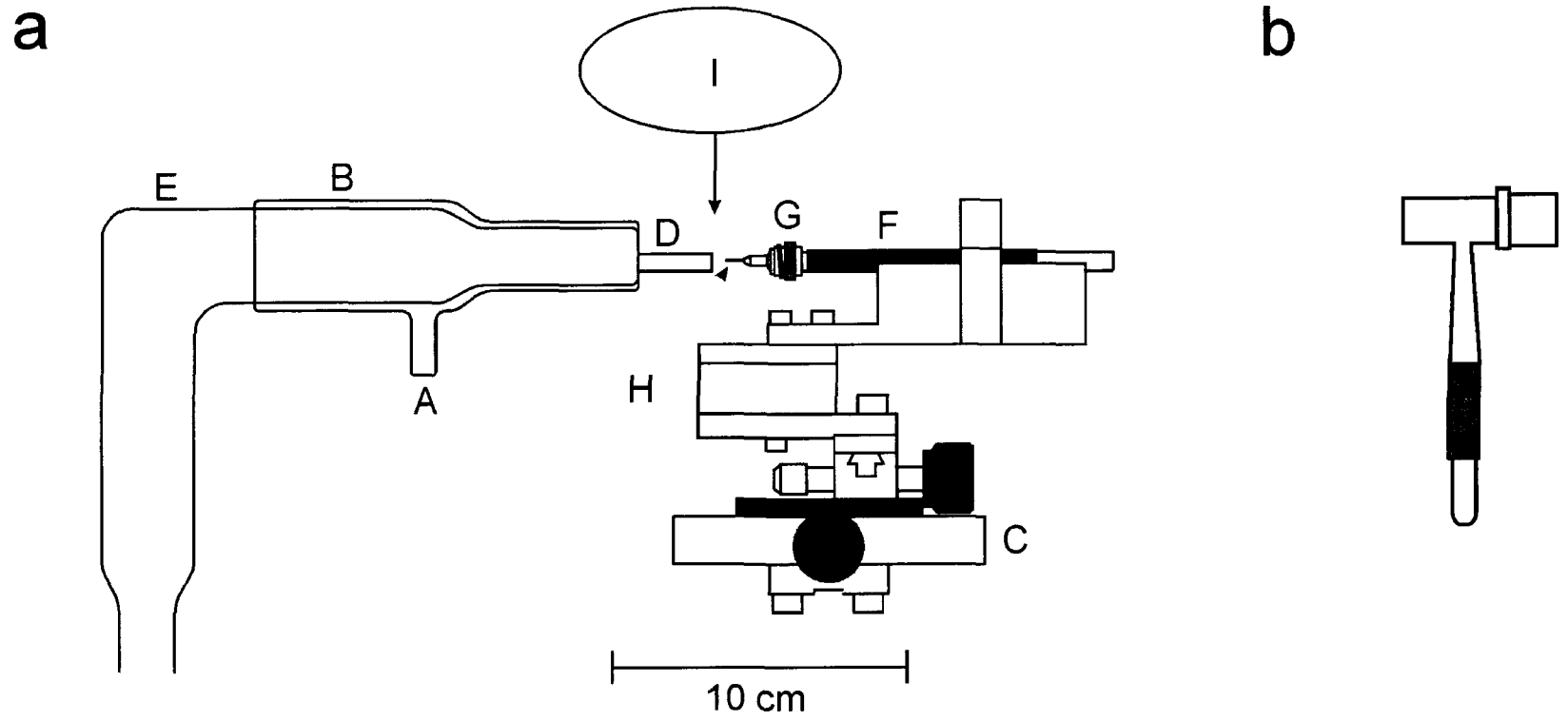

Figure 2.7. (a) Enlarged view of the crystal mounting apparatus; (A) Ambient nitrogen gas flow inlet. (B) Glass sleeve for ambient nitrogen gas flow. (C) Adjustable support stage. (D) Aluminum trough. (E) Silvered glass jacketed dewar. (F) Magnetic-tipped wand affixed to (G) the magnetic-based copper pin-fibre assembly. (H) Glass fibre. (I) Stereo-zoom microscope. (b) A set of cryotongs employed in the transfer of the copper pin-fibre assembly with adhered crystal from the support stage to the goniometer head.

glass fibre (0.05 to 0.1-mm o.d.) using perfluorinated polyether oil (Ausimont Inc., Fomblin Z15 or Z25) which served as an adhesive upon freezing at low temperature. The glass fibre was previously mounted with epoxy cement to a copper pin fitted to a magnetic base and affixed to the end of a magnetic wand (Hampton Research). The magnetic wand could be fastened to an adjustable support stage such that samples could be inspected under the stereo-zoom microscope once affixed to the glass fibre. The mounted crystal and magnetic pin were quickly (ca. 5 s) transferred from the crystal mounting apparatus to the magnetic mount of the goniometer by means of cryotongs (Hampton Research) which were precooled in liquid N_2 prior to use. The crystals were maintained at low temperature on the goniometer head by a cold N_2 gas flow provided by a Molecular Structure Corporation cryostat system.

2.13.3. Collection, Reduction, Refinement, and Solution of X-ray Crystallographic Data

All crystallographic data acquired during the course of this Thesis were collected using two different diffractometers: (1) a Siemens P4 diffractometer and (2) a Bruker SMART APEX II diffractometer. Both instruments were equipped with an Oxford Cryosystems low-temperature accessory that provided a stream of cold, gaseous N_2 for low-temperature data collection, and controlled by a Cryostream Controller 700 (Oxford Cryosystems).

The Siemens diffractometer was equipped with a Siemens 1K CCD area detector controlled by SMART[114] and a rotating anode (molybdenum) emitting Kα radiation

monochromated (λ = 0.71073 Å) by a graphite crystal. Diffraction data collection (typically at –173 °C) consisted of a full φ-rotation at $\chi = 0^{\circ}$ using 0.3° (1040 + 30) frames, followed by a series of short (80 frames) ω scans at various φ and χ settings to fill the gaps. The crystal-to-detector distance was 4.970–5.000 cm, and the data collection was carried out in a 512 × 512 pixel mode using 2 × 2 pixel binning. Processing of the raw data was completed using SAINT+,[115] which applied Lorentz and polarization corrections to three-dimensionally integrated diffraction spots.

The Bruker SMART APEX II diffractometer was equipped with an APEX II 4K CCD area detector and a 3-axis goniometer, controlled by the APEX2 Graphical User Interface (GUI) software,[116] and a sealed tube X-ray source (Mo target) emitting Kα radiation monochromated (λ = 0.71073 Å) by a graphite crystal. Diffraction data collection was typically at –173 °C consisted of a full φ-rotation at a fixed $\chi = 54.74^{\circ}$ with 0.36° (1010) frames, followed by a series of short (250 frames) ω scans at various φ settings to fill the gaps. The crystal-to-detector distance was 4.969–4.999 cm, and the data collection was carried out in a 512 × 512 pixel mode using 2 × 2 pixel binning. Processing of the raw data was completed using the APEX2 GUI software,[116] which applied Lorentz and polarization corrections to three-dimensionally integrated diffraction spots.

The program SADABS[117,118] was used for the scaling of diffraction data, the application of a decay correction, and an empirical absorption correction based on the intensity ratios of redundant reflections. The XPREP[119,120] program was used to confirm the unit cell dimensions and the crystal lattices. The solutions were obtained by direct

methods, which located the positions of the atoms (including hydrogen) defining the structural units. The final refinement was obtained by introducing anisotropic thermal parameters and the recommended weightings for all atoms except hydrogen. The maximum electron densities in the final difference Fourier map were located near the heavy atoms. All calculations were performed using the SHELXTL package[120] for the structure determination, solution refinement, and for the molecular graphics.

2.14. Raman Spectroscopy

All Raman spectra were recorded on a Bruker RFS 100 Fourier transform Raman spectrometer employing a quartz beam splitter and a liquid-nitrogen cooled Ge diode detector. The 1064-nm line of a Nd-YAG laser was used for excitation with a laser spot of <0.1 mm at the sample and configured such that only the 180°-backscattered radiation was detected. The scanner velocity was 5 kHz and the wavelength range was 5894 to 10394 cm^{-1} relative to the laser line at 9394 cm^{-1}, resulting in a spectral range of 3501 to –999 cm^{-1}. Fourier transformations were processed using a Blackman Harris 4-term apodization and a zero-filling factor of 2. Typical acquisitions involved ca. 300–500 scans at 1.0 cm^{-1} resolution for strongly scattering samples and 1000–1800 scans at 1.0 cm^{-1} for weakly scattering samples. Low-temperature spectra were acquired using a R495 low-temperature accessory which provided temperatures ranging from –40 to –160 °C with an estimated error of ±1 °C.

2.15. Nuclear Magnetic Resonance Spectroscopy

High-field nuclear magnetic resonance spectra were recorded unlocked (field drift < 0.1 Hz h^{-1}) on a Bruker DRX-500 (11.744 T) spectrometer in conjunction with a Silicon Graphics Indy workstation using XWINNMR. The spectrometer was equipped with a Bruker 5-mm broad band inverse probe or a 10-mm broad band probe. Low-temperature spectra were acquired using a cold nitrogen gas flow and a variable temperature controller (BV-T 2000). The ^{1}H, ^{13}C, ^{15}N, ^{17}O, ^{19}F, ^{125}Te, and ^{129}Xe were referenced externally at 30 °C using neat samples of TMS (^{1}H and ^{13}C), CH_3NO_2, H_2O, $CFCl_3$, $Te(CH_3)_2$, and $XeOF_4$, respectively.

A summary of typical spectroscopic parameters used for the spectra acquired for this Thesis are provided in Table 2.1. In some cases, gaussian rather than exponential multiplication was used to process the FID, and is dealt with in the relevant discussions. Spectral simulations were performed using the program MEXICO.[121]

2.16. Differential Scanning Calorimetry

Differential scanning calorimetry was performed on a TA Instruments DSC 2910 modulated differential scanning calorimeter to determine the phase transition temperatures of $C(OTeF_5)_4$. Inside the dry box, 0.00869 g of $C(OTeF_5)_4$ was loaded into a preweighed cold-welded aluminium pan inside the dry box. The pan was closed by a pierced aluminium lid and weighed again to obtain the mass of the compound by difference. The temperature was reduced from 25 to −125 °C at a rate of −15 °C min^{-1}, and then increased to 125 °C at a rate of 15 °C min^{-1}. An identical run was repeated on

Table 2.1. Summary of Typical Spectroscopic Parameters Used for NMR Spectroscopy

Acquisition Parameter[a]	^{1}H	^{13}C	^{14}N	^{17}O	^{19}F	^{125}Te	^{129}Xe
B_o = 11.744 T							
SF (MHz)	500.130	125.758	36.141	67.800	470.592	157.869	138.857
TD (K)	32	32	16	32	64	128	32
SW (kHz)	7	29	29	44	25 to 100	94	100
Hz/pt	0.207	0.885	1.765	1.350	0.380	0.721	3.051
PW (μs)	2.5	6.0	6.0	10.0	2.5	5.3	12.2
RD (s)	2.5	2 to 5	0.05	0.01	0.1	0.1	0.1
NS	100	10000	100,000	100,0000	500 to 5000	50000	100,000
B_o = 14.095 T							
SF (MHz)		150.903					
TD (K)		64					
SW (kHz)		36					
Hz/pt		0.55					
PW (μs)		13.8					
RD (s)		2					
NS		25000					

[a] The abbreviations denote: B_o, applied magnetic field; SF, spectral frequency; TD, time domain; SW, sweep width; PW, pulse width; RD, relaxation delay; NS, number of scans.

the same sample, where the absence of discernable transitions indicated that sample decomposition and/or reaction with the aluminium sample container had occurred.

2.17. Electronic Structure Calculations

2.17.1. Calculations of Optimized Geometries, Vibrational Frequencies, Atomic Charges, Atomic Valencies and Natural Bond Orders

Calculations presented in Chapters 3, 5, and 6 were carried out in collaboration with Dr. Reijo J. Suontamo, Department of Chemistry, University of Jyväskylä, Jyväskylä, Finland. All calculations were performed using the Gaussian 98 [122] or Gaussian 03 [123] software packages. Geometries were fully optimized using Hartree-Fock (HF), density functional theory (SVWN, SVWN5, PBEPBE, and PBE1PBE) and Møller-Plesset (MP2) methods using DZVP, Stuttgart RLC ECP, and/or (SDB-)cc-pVTZ and aug-cc-pVTZ(-PP) basis sets. Basis sets were obtained online (http://gnode2.pnl.gov/bse/portal). Fundamental vibrational frequencies were calculated along with Raman intensities. Natural Bond Order (NBO) analyeses[124-127] were obtained for the optimized local minima. Calculations of chemical shifts and coupling constants were carried out using the Gauge-Independant Atomic Orbital Method (GIAO).[128-131] Vibrational motions for mode assignments were visualized with the aid of the program GaussView.[132]

2.17.2. Electron Localization Function (ELF) Calculations

Electron localization functions discussed in Chapters 3 and 5 were performed by Dr. Reijo J. Suontamo. The calculations were carried out using the TopMod software package.[133]

CHAPTER 3

A NEUTRAL OXIDE FLUORIDE OF XENON(II): SYNTHESIS AND CHARACTERIZATION OF $O(XeF)_2$ AND A COMPUTATIONAL STUDY OF $O(NgF)_2$ AND $F(NgF)_2^+$ (Ng = Kr, Xe)

3.1. Introduction

A general treatment of the oxide fluorides of xenon is provided in the Introduction (see Chapter 1). The discovery of the first cationic Xe(II) oxide fluoride, $FXeOXeFXeF^+$,[67,134] occurred during a reinvestigation of the reported protonated hypofluorous acid cation, H_2OF^+.[91] Experiments designed to repeat this work gave, instead, $[Xe_3OF_3][MF_6]$ (M = As, Sb) salts.[67]

No systematic studies exist for the preparation of a neutral oxide fluoride of Xe(II) by hydrolysis of XeF_2, and it has been reported that acidic and neutral solutions of XeF_2 are stable for short periods of time, and decompose to give Xe, O_2, and HF.[11] The discovery the $FXeOXeFXeF^+$ cation has provided a synthetic route to $O(XeF)_2$. The present work describes the synthesis of $O(XeF)_2$ from $[Xe_3OF_3][AsF_6]$, and the spectroscopic characterization of the first neutral oxide fluoride of xenon.

3.2. Results and Discussion

3.2.1. Synthesis and Reactivity of $O(XeF)_2$

The crystal structures of both $Xe_3OF_3^+$ salts have been obtained in which the cation is comprised of a FXeOXe---FXeF zig-zag chain. The long contact (2.510(8) Å, As; 2.508(7) Å, Sb) between xenon and the bridging fluorine atom suggests that XeF_2

may be readily displaced from $Xe_3OF_3^+$ by a suitable oxidatively resistant base according to eq 3.1, where M = K or NO.

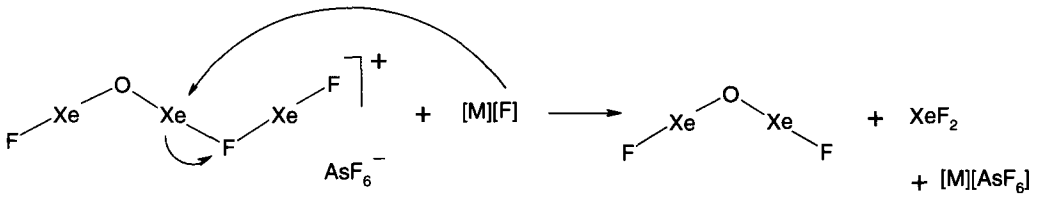

(3.1)

Reaction of the magenta-colored solid $[Xe_3OF_3][AsF_6]$ with liquid NOF at −78 °C afforded a pale blue-colored solid/liquid mixture, which yielded a pale yellow solid upon removal of excess NOF under dynamic vacuum at −78 °C (eq 3.2). The blue color

$$[Xe_3OF_3][AsF_6] + NOF \longrightarrow O(XeF)_2 + XeF_2 + [NO][AsF_6] \qquad (3.2)$$

Presumably arose from traces of N_2O_3.[135] The product mixture was found to be stable indefinitely at temperatures at or below −30 °C.

Because an excess of NOF was used to react with $[Xe_3OF_3][AsF_6]$, products from the reaction of $[Xe_3OF_3][AsF_6]$ with the NO_2F impurity (ca. 3%) in the NOF sample could be observed by ^{17}O, ^{19}F, and ^{129}Xe NMR spectroscopy ($FXeONO_2$, see Chapter 4) and in the solid state by low-temperature Raman spectroscopy ($XeF_2 \cdot N_2O_4$, see Chapter 4). In addition to the known side products, three peaks in the Raman spectrum at 416.5, 406.6, and 180.7 cm^{-1} could not be assigned, but were suggestive of an exclusively Xe–O bound molecule (see Sections 3.2.4 and 3.2.5).

Syntheses that employed ^{17}O-enriched (^{16}O, 35.4%; ^{17}O, 21.9%; ^{18}O, 42.7%) and ^{18}O-enriched (99.99%) $[Xe_3{}^*OF_3][AsF_6]$ confirmed the results derived from the natural

abundance reaction, but further demonstrated that the enriched oxygen from $Xe_3{}^*OF_3{}^+$ is not retained solely in the $^*O(XeF)_2$ product, as suggested by the concerted pathway in eq 3.1. Rather, peaks assignable to the N^*O^+ cation and the $XeF_2{\cdot}N_2O_3{}^*O$ adduct, as well as to $^{16}O(XeF)_2$ in the case of the ^{18}O-enriched compound, were observed by Raman spectroscopy (see Sections 3.2.4 and 3.2.5). Oxygen isotope scrambling was also observed in CH_3CN solution by NMR spectroscopy. Although the resonance arising from $^{17}O(XeF)_2$ was expected to be more intense than that of the other oxygen-containing products, the natural abundance and $^{17/18}O$-enriched oxygen atoms are randomly scrambled in solution. Thus, the resonances in the ^{17}O NMR spectrum appear equivalent in intensity to those of the natural abundance products (see Section 3.2.3). Furthermore, there are unassigned peaks at 416.5, 406.6, and 180.7 cm^{-1}, attributed to an $(XeO)_n$ polymer (vide infra), which shifted by 7.0, 3.4, and 0.0 cm^{-1}, respectively, in the Raman spectrum of the ^{18}O-enriched product. The enrichment studies thus indicate that the $FXeOXeFXeF^+$ cation does not react with NOF as proposed in eq 3.1, but rather may react in a manner analogous to the reaction of the $FXeOXeFXeF^+$ cation with NO_2F (see Chapter 4), proceeding through FXeONO as an intermediate (eq 3.3). This reaction pathway accounts for the formation of $XeF_2{\cdot}N_2O_3{}^*O$, $XeF_2{\cdot}N_2O_4$, and $(XeO)_n$ according to eq 3.4–3.6.

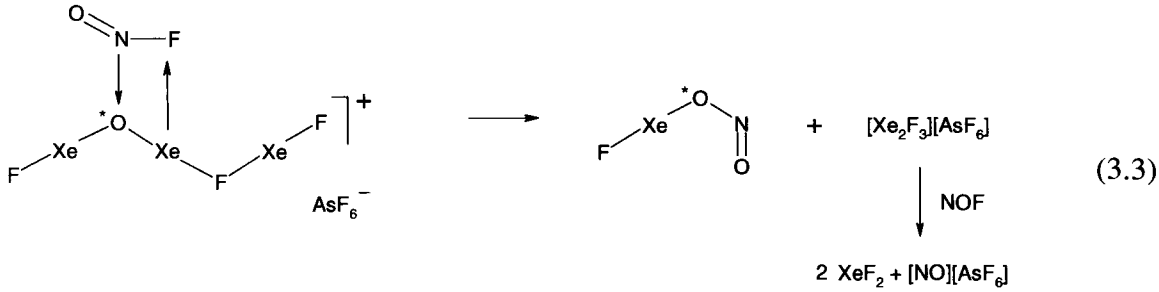

(3.3)

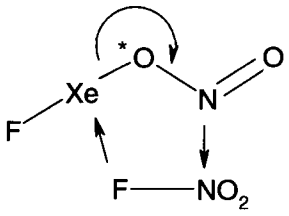

$$\longrightarrow \quad XeF_2 \cdot N_2O_3{}^{\cdot}O \tag{3.4}$$

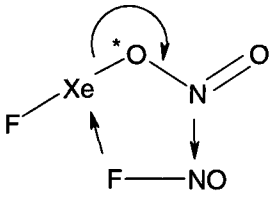

$$\longrightarrow \quad XeF_2 + N_2O_2{}^{\cdot}O \xrightarrow[-\ NO \text{ or } N^{\cdot}O]{\text{dyn. vacuum}} \begin{matrix} XeF_2 \cdot N_2O_4 \\ \text{or } XeF_2 \cdot N_2O_3{}^{\cdot}O \end{matrix} \tag{3.5}$$

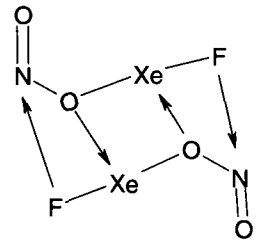

$$\longrightarrow$$

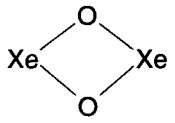

$$+ 2\ NOF \qquad \xrightarrow{+\ n\ FXeONO} \quad (XeO)_{n-1} + n\ NOF \tag{3.6}$$

The proposed reaction pathways account for the color of the reaction medium (vide supra), which is caused by a small amount of the intense blue N_2O_3. In addition, the formation of the proposed $(XeO)_n$ oligomer accounts for the two intense Raman bands observed in the Xe–O stretching region of the Raman spectrum, and the concomitant shifts in the Raman spectrum of the ^{18}O-substituted product (see Sections 3.2.4 and 3.2.5).

The formation of $O(XeF)_2$, according to eq 3.7 and 3.8, is apparently favored, but

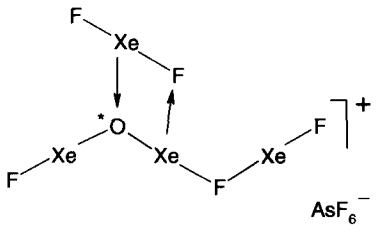

$$\longrightarrow$$

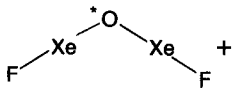

$$+ \quad [Xe_2F_3][AsF_6] \tag{3.7}$$

$$\downarrow NOF$$

$$2\ XeF_2 + [NO][AsF_6]$$

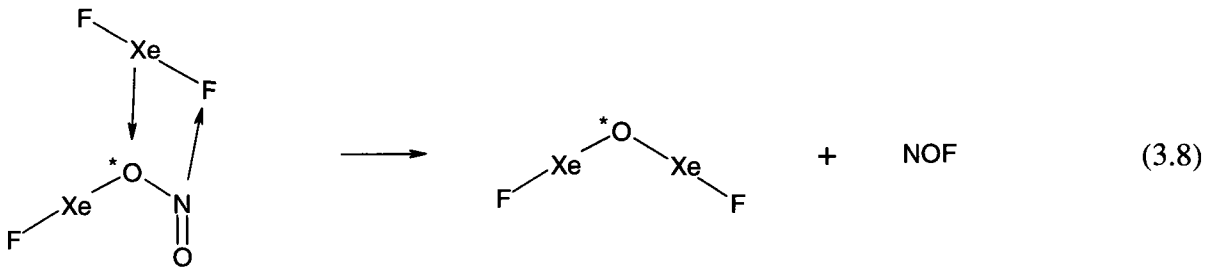

(3.8)

it is also possible for FXe*ONO to undergo intramolecular rearrangement (eq 3.9), or to undergo a bimolecular reaction (eq 3.10). The barrier to rearrangement was calculated to

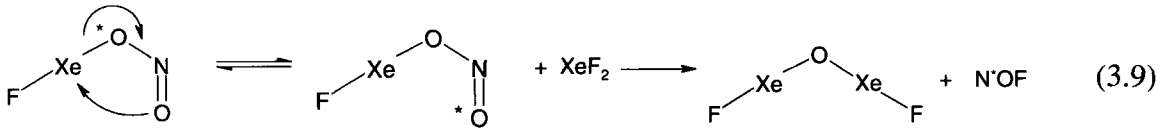

(3.9)

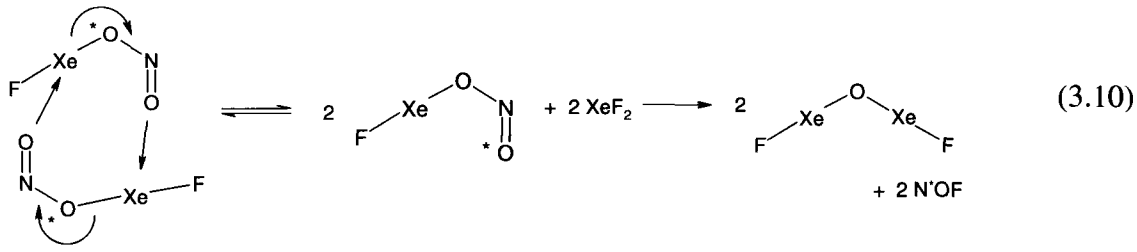

(3.10)

be +2.85 kJ mol^{-1} (SVWN/(SDB-)cc-pVTZ), thus it is plausible that FXeON*O arises as a result of this rearrangement (see Section 3.2.5). The subsequent reaction of FXeON*O with XeF_2 accounts for the observation of both $^{16}O(XeF)_2$ and $[N^*O][AsF_6]$ in the Raman spectra of $^{18}O(XeF)_2$.

The displacement of XeF_2 from $Xe_3OF_3^+$ was attempted in HF solvent using KF as the fluoride ion donor (eq 3.11). Although XeF_2 is likely displaced, it is probable that

$$[Xe_3OF_3][AsF_6] + [K][F] \xrightarrow{HF} O(XeF)_2 + XeF_2 + [K][AsF_6] \qquad (3.11)$$

the resulting $O(XeF)_2$ immediately undergoes solvolysis in HF to yield XeF_2 and H_3O^+ according to eq 3.12–3.14, with the overall reaction given by eq 3.15 (species in parentheses are inferred and were not directly observed), as determined by ^1H, ^{17}O, ^{19}F,

$$O(XeF)_2 + HF \longrightarrow (FXeOH) + XeF_2 \qquad (3.12)$$

$$[FXeOH] + HF \longrightarrow (H_2O) + XeF_2 \qquad (3.13)$$

$$(H_2O) + HF \longrightarrow [H_3O][F] \qquad (3.14)$$

$$O(XeF)_2 + 3\,HF \longrightarrow [H_3O][F] + 2XeF_2 \qquad (3.15)$$

and ^{129}Xe NMR spectroscopy at –80 °C. The formation of the proposed FXeOH intermediate is rapid on the NMR time scale, thus neither $O(XeF)_2$ nor FXeOH were observed by low-temperature ^{19}F NMR spectroscopy.

In order to further elucidate the products obtained from the decomposition of $O(XeF)_2$, two experiments were performed, where (1) the solid was warmed step-wise between –30 and 10 °C, with constant monitoring by low-temperature Raman spectroscopy, and (2) by the low-temperature (–78 °C) reaction of $O(XeF)_2$ with anhydrous HF, followed by removal of excess HF by dynamic vacuum at the same temperature and characterization of the products by low-temperature Raman spectroscopy. In the former case, very slow decomposition occurred between –25 and 5 °C over 6 hours, with complete decomposition occurring over 4 h at 10 °C, while reaction with HF was rapid at –78 °C. In both cases, the product was orange in color. The

products of both reactions could not be identified by Raman spectroscopy, but the spectra of both products were found to be very similar, indicating that the proton from HF in the latter decomposition is not incorporated into the decomposition products (see Appendix A).

3.2.2. Attempted Synthesis of [FXeOXe][AsF_6]

The preparation of [FXeOXe][AsF_6] was attempted by reaction of $O(XeF)_2$ with liquid AsF_5 at −78 °C according to eq 3.16. However, only [XeF][AsF_6] and unreacted

$$O(XeF)_2 + AsF_5 \longrightarrow [FXeOXe][AsF_6] \qquad (3.16)$$

$O(XeF)_2$ were observed, indicating that only the XeF_2 present in the system reacts with AsF_5. No bands were attributable to the $FXeOXe^+$ cation,[67] with the most notable absences being the bands calculated at 573 cm^{-1} for the $\nu(Xe–F) - \nu(Xe_t–O)$ mode and at 534 cm^{-1} for the $\nu(Xe_t–O) + \nu(Xe–F)$ mode, which are expected to be the most intense.

3.2.3 NMR Spectroscopy

3.2.3.1. Solution Structural Characterization of Natural Abundance and ^{17}O-enriched $O(XeF)_2$ by ^{17}O, ^{19}F, and ^{129}Xe NMR Spectroscopy

The identification of the title compound hinges on its characterization in CH_3CN solvent by direct observation of its natural abundance spin-½ nuclides, ^{19}F and ^{129}Xe. Key experimental and simulated ^{19}F and ^{129}Xe NMR spectra are depicted in Figures 3.1a and 3.1b, where xenon is represented as Ω to denote that the spin system is heteronuclear. A

listing of the natural abundance isotopomers and their associate spin-spin coupling paths that give rise to the component subspectra that account for the NMR spectra are provided Figure 3.2. The ^{17}O NMR spectra are depicted in Figure 3.3. The chemical shifts, δ, and spin-spin coupling constants, J, are summarized in Table 3.1, where the fractional isotopomeric abundances are derived in Table 3.2. The number of observed environments and the multiplet patterns are consistent with an $O(XeF)_2$ molecule having C_{2v} point symmetry. The geometry deduced from the NMR solution study is supported by computational studies (see Section 3.2.5).

The major species XeF_2 (^{19}F, singlet, −179.1 ppm; ^{129}Xe, triplet, −1783 ppm; $^1J(^{19}F-^{129}Xe)$, 5646 Hz), the AsF_6^- anion (^{19}F, 1:1:1:1 multiplet, −64.8 ppm), and the NO^+ cation (^{17}O, singlet, 610 ppm), and the minor species N_2O_4 (^{17}O, singlet, 420 ppm), the NO_2^+ cation (^{17}O, singlet, 420 ppm), and $FXeONO_2$ (^{19}F, singlet, −135.1 ppm; ^{129}Xe, doublet, −1897 ppm; ^{17}O, singlet, 454 ppm for the two terminal oxygen atoms and 383 ppm for the bridging oxygen atom; $^1J(^{19}F-^{129}Xe)$, 5467 Hz) were identified by their known NMR parameters (N_2O_4 and NO_2^+ were found to overlap in the ^{17}O NMR spectrum, see Figure 3.3). In additon, the ^{17}O, ^{19}F, and ^{129}Xe NMR spectra (−40 °C) of the yellow CH_3CN solution revealed intense new resonances that were assigned to the $O(XeF)_2$ molecule as discussed below.

3.2.3.2. Solution Structure Determination of $O(XeF)_2$

The solution structure of $O(XeF)_2$ was confirmed by use of the spectral simulation program MEXICO,[121] and NMR chemical shifts and coupling constants have been

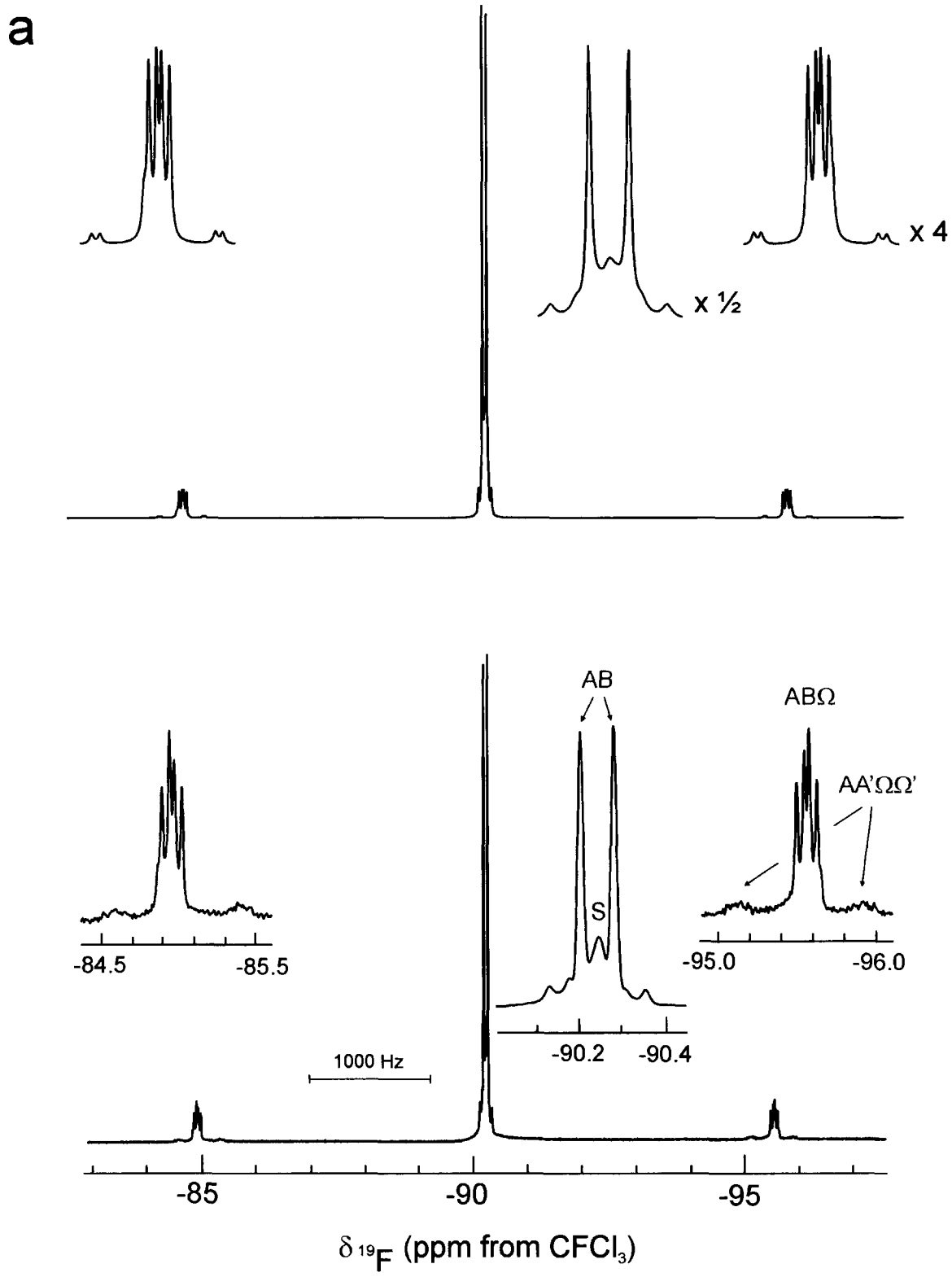
a
x 4
x ½
AB
ABΩ
AA'ΩΩ'
S
-84.5
-85.5
-90.2
-90.4
-95.0
-96.0
1000 Hz
-85
-90
-95
δ 19F (ppm from CFCl3)

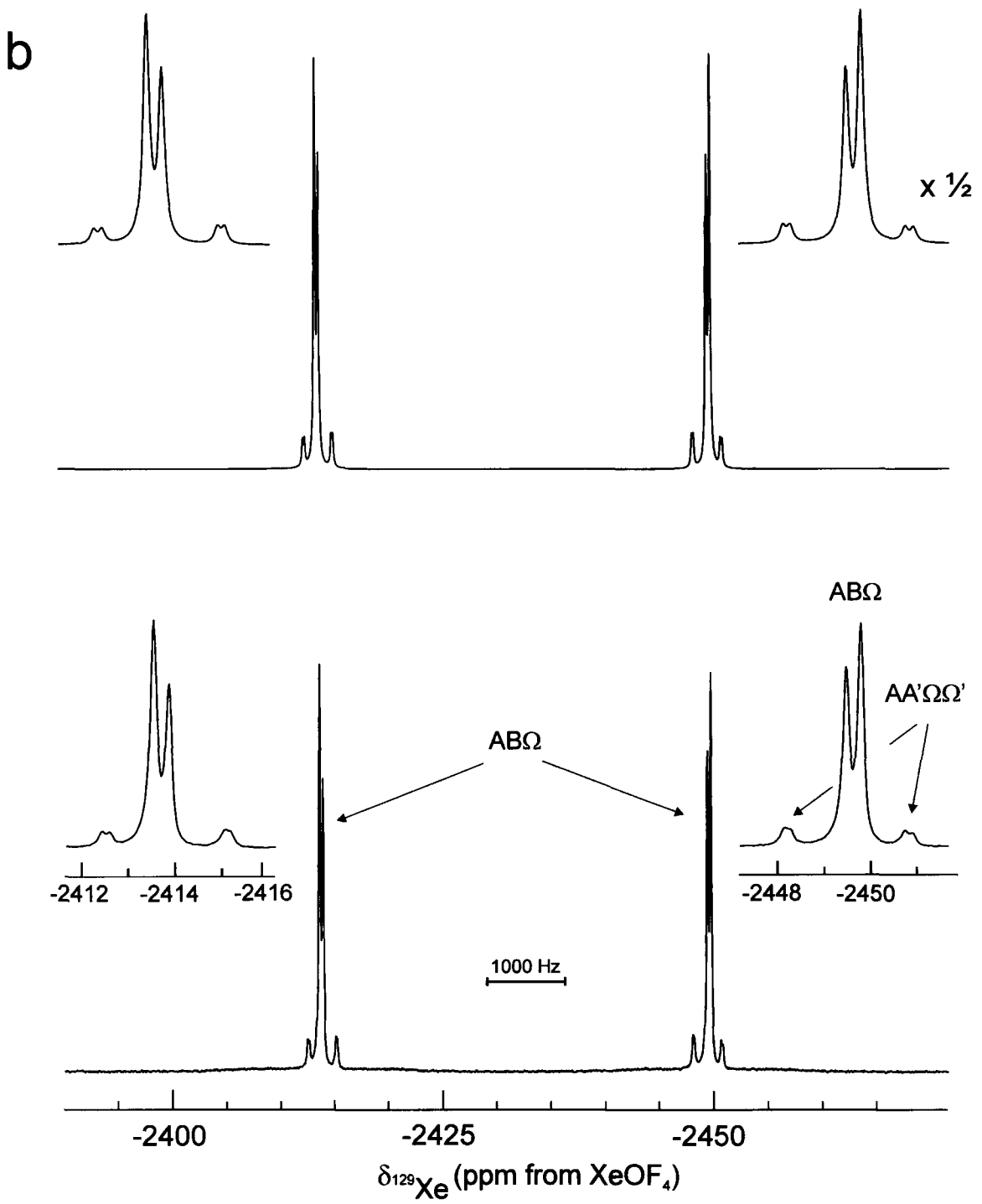

Figure 3.1. The calculated (upper trace) and experimental (lower trace) (a) ^{19}F and (b) ^{129}Xe NMR spectra of $O(XeF)_2$ in CH_3CN at –40 °C. Symbols denote ^{19}F (A, B) and ^{129}Xe (Ω) nuclei, respectively.

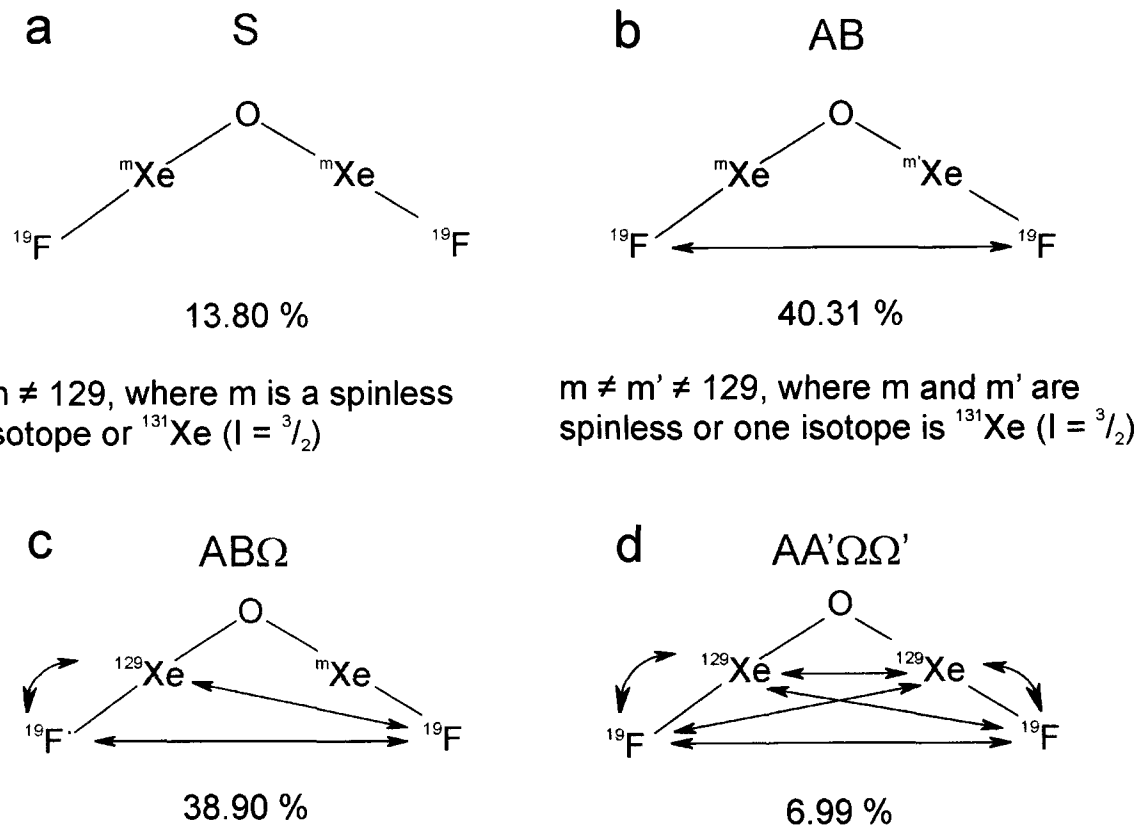

Figure 3.2. Schematic of the coupling paths that arise from the four ^{19}F and two ^{129}Xe NMR subspectra that occurs for natural abundance $O(XeF)_2$. The ^{131}Xe–^{19}F and ^{131}Xe–^{129}Xe spin-spin couplings are quadrupole collapsed.

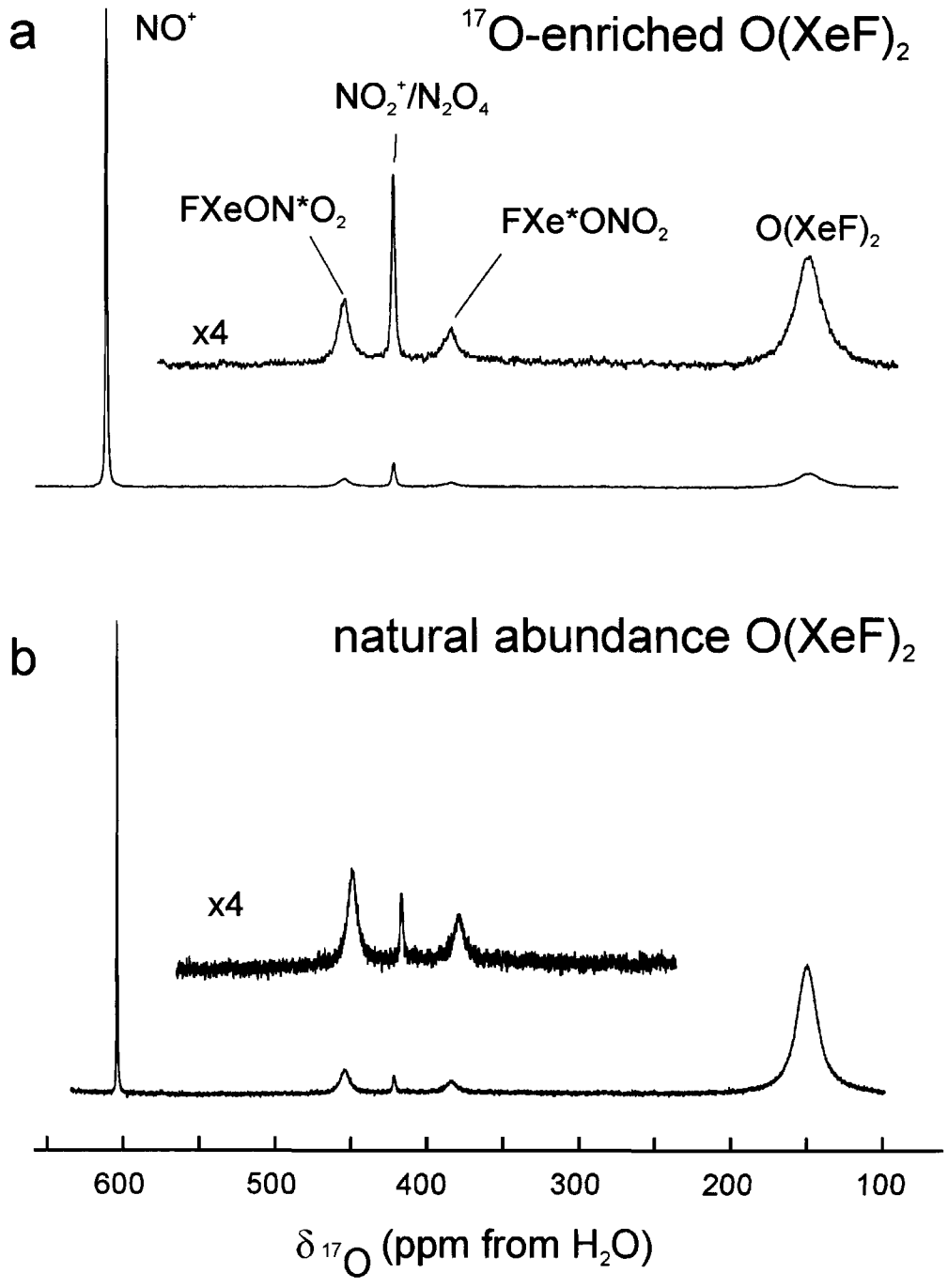

Figure 3.3. The ^{17}O NMR spectra of: (a) ^{17}O-enriched (21.9 %) $O(XeF)_2$ and (b) natural abundance $O(XeF)_2$ in CH_3CN solution at –40 °C.

Table 3.1. Natural Abundance Isotopomers and Subspectra Comprising the ^{19}F and ^{129}Xe NMR Spectra of $O(XeF)_2$, Including Experimental and Calculated[a] Chemical Shifts and Coupling Constants

spin, Xe_1[b]	spin, Xe_2[b]	isotopomer fractional abundance[c]	^{19}F spectrum $\delta(^{19}F)$, ppm	^{19}F spectrum multiplicity	^{129}Xe spectrum $\delta(^{129}Xe)$, ppm	^{129}Xe spectrum multiplicity	coupling constants, J (Hz)
m	m	0.1380	−90.251[d] (−54.1)	S			
m	m′	0.4031	−90.210 (F_A)[e] −90.286 (F_B)[e]	AB			$^4J(^{19}F_A–^{19}F_B)$, < 1[d] (−80.5)
129	m	0.3890	−90.210 (F_A)[e] −90.286 (F_B)[e]	ABΩ	−2437.5 (−2324.7)	ABΩ	$^1J(^{19}F–^{129}Xe)$, 4997.8[d,f] (−5106.6) $^3J(^{19}F–^{129}Xe)$, 46.7[d] (−80.5)
129	129	0.699	−90.248[d]	AA′ΩΩ′	−2437.5 (−2324.7)	AA′ΩΩ′	$^1J(^{19}F–^{129}Xe)$, 4997.8[d,f] (−5106.6) $^2J(^{129}Xe–^{129}Xe)$, 364.7[e] (401.7) $^3J(^{19}F–^{129}Xe)$, 46.7[e] (−75.4) $^4J(^{19}F_A–^{19}F_B)$, 23.3[e] (−80.5)

[a] PBE1PBE/DZVP, calculated chemical shifts and coupling constants appear in parentheses. [b] The symbols m and m′ represent all spinless isotopes of xenon, as well as xenon-131; the $^{131}Xe–^{19}F$ and $^{131}Xe–^{129}Xe$ spin-spin couplings are quadrupole collapsed. [c] See Table 3.2 for a detailed listing of isotopomers, xenon isotopic abundances, isotopomer probabilities, and the relative weghtings of their corresponding spin systems, their probabilities, and their fractions. [d] Estimated using spectral simulation software, MEXICO. [e] Directly measured from the ^{19}F NMR spectrum. [f] A value of 5027.8 Hz was used for simulation of the ^{19}F spectrum.

Table 3.2. Percentage Abundance of All Isotopes of Xenon and the Percentage of Each Isotopomeric Subspectra

isotope	natural abundance (%)
^{124}Xe	0.09
^{126}Xe	0.09
^{128}Xe	1.92
^{129}Xe	26.44
^{130}Xe	4.08
^{131}Xe	21.18
^{132}Xe	26.89
^{134}Xe	10.44
^{136}Xe	8.87

spin system	isotope, Xe_1	isotope, Xe_2	probability[a]	sum
AA′ΩΩ′	129	129	0.0699	0.0699
	129	124	0.00047592	
	129	126	0.00047592	
	129	128	0.01015296	
	129	130	0.02157504	
ABΩ	129	131	0.11199984	0.3890
	129	132	0.14219412	
	129	134	0.05520672	
	129	136	0.04690456	
	124	126	0.00000162	
	124	128	0.00003456	
	124	130	0.00007344	
	124	131	0.00038124	
	124	132	0.00048402	
	124	134	0.00018792	
AB	124	136	0.00015966	0.4031
	126	128	0.00003456	
	126	130	0.00007344	
	126	131	0.00038124	
	126	132	0.00048402	
	126	134	0.00018792	
	126	136	0.00015966	

Table 3.2. (continued...)

AB	128	130	0.00156672	0.4031
	128	131	0.00813312	
	128	132	0.01031424	
	128	134	0.00400896	
	128	136	0.00340608	
	130	131	0.01728288	
	130	132	0.02194224	
	130	134	0.00851904	
	130	136	0.00723792	
	131	132	0.11390604	
	131	134	0.04422384	
	131	136	0.03757332	
	132	134	0.05614632	
	132	136	0.04770286	
	134	136	0.01852056	
S	124	124	0.00000081	0.1380
	126	126	0.00000081	
	128	128	0.00036864	
	130	130	0.00166464	
	131	131	0.04485924	
	132	132	0.07230721	
	134	134	0.01089936	
	136	136	0.00786769	
			Σ	1.0000

[a] The probability of each isotopomer is the square of the abundance when $Xe_1 = Xe_2$, or the product of the abundances of Xe_1 and Xe_2 when multiplied by 2 ($Xe_1 \neq Xe_2$).

calculated using GIAO at the PBE1PBE/DZVP level of theory (Table 3.1 and 3.3). The spectral simulations (Figures 3.1a and 3.1b) are in excellent agreement with the experimental ^{19}F and ^{129}Xe spectra, and account for the observed peaks and the second-order effects that are manifested as small asymmetries resulting from the relatively small frequency difference (36 Hz) between coupled ^{19}F nuclei A and B and their coupling constants (23 Hz) in the ABΩ and AA′ΩΩ′ subspectra. The simulations also account for the ^{19}F–^{19}F coupling observed in the ^{129}Xe NMR spectrum, and the ^{129}Xe–^{129}Xe coupling observed in the ^{19}F NMR spectrum. However, the simulations do reproduce the broadening of the ^{129}Xe satellites, caused by the chemical shieding anisotropy (CSA) at Xe, in the ^{19}F NMR spectrum. The isotopomers and their most prominent spectral features are discussed below.

The ^{19}F NMR spectrum of $O(XeF)_2$ consists of a singlet (S) flanked by an AB spin pattern. Satellite doublet subspectra, that are symmetrically disposed about the singlet, result from the ABΩ and AA′ΩΩ′ isotopomeric subspectra (Figures 3.2c and 3.2d, respectively). The singlet ($\delta(^{19}F_S)$, –90.251 ppm; Figure 1a) is assigned to the F^mXeO^mXeF isotopomers (Figure 3.2a), while the AB spin pattern arises from the $F^mXeO^{m'}XeF$ isotopomers (Figure 3.2b). Modeling of the ABΩ and AA′ΩΩ′ isotopomeric subspectra established that $\delta(^{19}F_A)$ is equal to –90.210 ppm, $\delta(^{19}F_B)$ is equal to –90.286 ppm, and that the $^4J(^{19}F_A–^{19}F_B)$ is equal to 23.3 Hz (Table 3.1). However, when these parameters were applied to model the AB isotopomeric subspectrum, the modeled results were inconsistent with the experimental ^{19}F NMR spectrum. An AB spin pattern gives rise to four transitions, with two equal-intensity inner transitions that are

Table 3.3. Experimental and Calculated NMR Chemical Shifts and Coupling Constants for $O(XeF)_2$, XeF_2, and $F(XeF)_2^+$

NMR parameter[a]	$O(XeF)_2$			XeF_2			$F(XeF)_2^+$[b]	
	exptl[c]	SVWN DZVP	PBE1PBE DZVP	exptl[c]	SVWN DZVP	PBE1PBE DZVP	exptl[c,d,e]	SVWN DZVP
$\delta(^{19}F_t)$, ppm	–90.2	–31.8	–54.1	–179.1	–117.2	–132.2	–252	–220.3
$\delta(^{129}Xe)$, ppm	–2437.5	–2534.9	–2324.7	–1783.1	–1934.9	–1720.5	–1059	–538.8
$\delta(^{17}O/^{19}F_b)$, ppm	147.4	366.9	287.6				–185	–119.7
$^1J(^{19}F_t–^{129}Xe)$, Hz	4997.8	–5609.5	–5106.6	5645.8	–6437.1	–5961.8	6740	–9267.4
$^1J(^{19}F_b–^{129}Xe)$, Hz							4865	–4867.6
$^2J(^{19}F_t–^{19}F_b)$, Hz							308	–543.1
$^2J(^{129}Xe–^{129}Xe)$, Hz	364.7	414.5	401.7				n.o.	737.7
$^3J(^{19}F–^{129}Xe)$, Hz	46.7	–2.99	–75.4				n.o.	568.2
$^4J(^{19}F–^{129}Xe)$, Hz	23.3	–28.5	–80.5				n.o.	60.0

[a] The chemical shift, δ, was calculated by taking the calculated isotropic magnetic shielding tensor of the reference compound ($\delta(^{17}O)$, H_2O; $\delta(^{19}F)$, $CFCl_3$; $\delta(^{129}Xe)$, $XeOF_4$) and subtracting the shielding tensor calculated for the species of interest. Coupling constants are taken from the values computed for the total nuclear spin-spin coupling (*J*, Hz). [b] A single-point NMR calculation was not performed for $F(XeF)_2^+$ using the PBE1PBE method, because optimization failed to give a reasonable geometry. [c] Coupling constants were measured and/or modeled using absolute values. [d] Spectra were obtained in BrF_5 solvent at –62 °C; taken from ref 136. [e] The abbreviation, n.o., denotes not observed.

more intense than the two equal-intensity outer transitions. The separation and relative intensities of the transitions are dependant on the ratio of the coupling constant (J) to the chemical shift difference ($\delta\nu_o$). The modeled and experimental spectra were made to agree by reducing the $^4J(^{19}F_A–^{19}F_B)$ coupling to a near-zero value, causing the inner and outer transitions to overlap ($J/\delta\nu_o \approx 0$), resulting in two discreet transitions that could not be resolved because of the relatively large linewidth (ca. 5 Hz). The small value for $^4J(^{19}F_A–^{19}F_B)$ in the AB spin pattern is not well understoood, but may be caused by the removal of a through-bond spin-coupling pathway when both xenon are spin inactive. The $^2J(^{129}Xe–^{129}Xe)$ coupling observed in the ^{19}F NMR spectrum is unprecedented for ^{129}Xe, but its $^{13}C–^{13}C$ counterpart has been observed previously for other AA′ΩΩ′ spin systems such as $F_2C{=}CH_2$.[137]

The singlet ($\delta(^{19}F)$, –90.251 ppm) is shifted by –0.003 ppm relative to the central transition assigned to the AA′ΩΩ′ subspectra ($\delta(^{19}F)$, –90.248 ppm). This low-frequency shift is consistent with the secondary isotope effect of xenon on fluorine, $^1\Delta^{19}F(^{132/129}Xe)$ (where ^{132}Xe is the most abundant spinless isotope of xenon), and is comparable to the value of –0.00122 ppm u^{-1} determined for XeF_2 at 20 °C.[138]

The ^{129}Xe NMR spectrum of $O(XeF)_2$ (Figure 3.1b) consists of a single ^{129}Xe resonance at –2438 ppm. The ^{129}Xe spectrum arises from the ABΩ and AA′ΩΩ′ subspectra (Figures 3.2c and 3.2d, respectively). Again, the $^4J(^{19}F–^{19}F)$ coupling observed in the ^{129}Xe NMR spectrum arises from the AA′ΩΩ′ spin system.[137]

The ^{17}O NMR spectrum of both natural abundance and ^{17}O-enriched (^{16}O, 35.4%; ^{17}O, 21.9%; ^{18}O, 42.7%) $O(XeF)_2$ showed a broad singlet at 147 ppm ($\Delta\nu_{½}$ = 1500 Hz;

Figure 3.3). Because the ^{17}O nucleus is quadrupolar ($I = {}^5/_2$), the asymmetric environment about the oxygen nucleus results in a non-zero electric field gradient, and quadrupolar relaxation of the ^{17}O nucleus, which broadens the resonance, precludes the observation of both the $^1J(^{17}O–^{129}Xe)$ and $^2J(^{17}O–^{19}F)$ couplings. Comparison of the ^{16}O and ^{17}O NMR spectra indicate that all species contain equivalent amounts of ^{17}O in the latter spectrum, as opposed to selective enrichment of $^*O(XeF)_2$ (vide supra), suggesting that further oxygen exchange occurs in CH_3CN solution, as illustrated in eq 3.18. The

$$FXe^*OXeF + [NO][AsF_6] + XeF_2 \rightleftharpoons FXe^*ONO + [F(XeF)_2][AsF_6] \quad (3.18)$$

FXe^*ONO molecule could then undergo the reactions outlined in eq 3.5, 3.6, 3.7, 3.10, and 3.11, eventually leading to the observed distribution of enriched ^{17}O and ^{18}O oxygen isotopes. It is also worth noting that the linwidths associated with the transitions in the ^{129}Xe NMR spectrum of $^{17}O(XeF)_2$ do not appear affected by the enrichment, though this may result from the broadening caused by the CSA at Xe and the low abundance of ^{17}O (21.9%). The ^{19}F NMR signals are much broader ($\Delta\nu_{1/2}$ = 85 Hz) and show no coupling to ^{17}O, which is again attributable to quadrupolar relaxation.

The calculated NMR chemical shifts and coupling constants (Tables 3.1 and 3.3) were found to be in reasonable agreement with the experimental values, and followed experimental trends when compared with the calculated XeF_2 and $F(XeF)_2^+$ benchmarks (Table 3.3). The calculated $\delta(^{19}F)$ of –54.1 ppm is to high frequency of the experimental value, but is 78.1 ppm to high frequency of that calculated for XeF_2 ($\delta(^{19}F)$, –132.2) in

good agreement with the experimental separation (88.9 ppm). The ^{129}Xe NMR shift was better reproduced (exptl, -2438; calcd, -2325 ppm), and is 604 ppm to low frequency of the value calculated for XeF_2 ($\delta(^{129}Xe)$, -1720 ppm), in reasonable agreement with the experimental separation (654 ppm). The calculated $|^1J(^{19}F-^{129}Xe)|$ value of 5107 Hz is quite close to the measured value (4998), and is paralleled by the good agreement obtained for the experimental and calculated $|^1J(^{19}F-^{129}Xe)|$ values for XeF_2 (5646 and 5962 Hz, respectively). Although the other calculated coupling constants were slightly overestimated at this level of theory (Table 3.1), the calculations support the current assignments of both the ^{19}F and ^{129}Xe NMR spectra.

3.2.4. Raman Spectroscopy

3.2.4.1. Raman Spectra of Natural Abundance, ^{17}O-, and ^{18}O-enriched $O(XeF)_2$

The low-temperature, solid-state Raman spectra of ^{17}O- and ^{18}O-enriched and natural abundance $O(XeF)_2$ were recorded. The natural abundance and ^{18}O-enriched (^{18}O, 99.99%) spectra are shown in Figure 3.4. The observed and calculated frequencies and their assignments are listed in Table 3.4 (SVWN/(SDB-)cc-pVTZ) and Table 3.5 (PBEPBE/(SDB-)cc-pVTZ). The low-frequency shifts upon ^{17}O- and ^{18}O-substitution follow similar trends, and therefore only the results for $^{16/18}O(XeF)_2$ are considered in the ensuing discussion.

The $O(XeF)_2$ molecule (C_{2v}) possesses nine fundamental vibrational modes belonging to the irreducible representations 4 A_1 + A_2 + 3 B_1 + B_2, all of which are Raman active and all but the A_2 mode are infrared active. There is overall slightly better agreement between the observed and calculated frequencies and frequency trends for

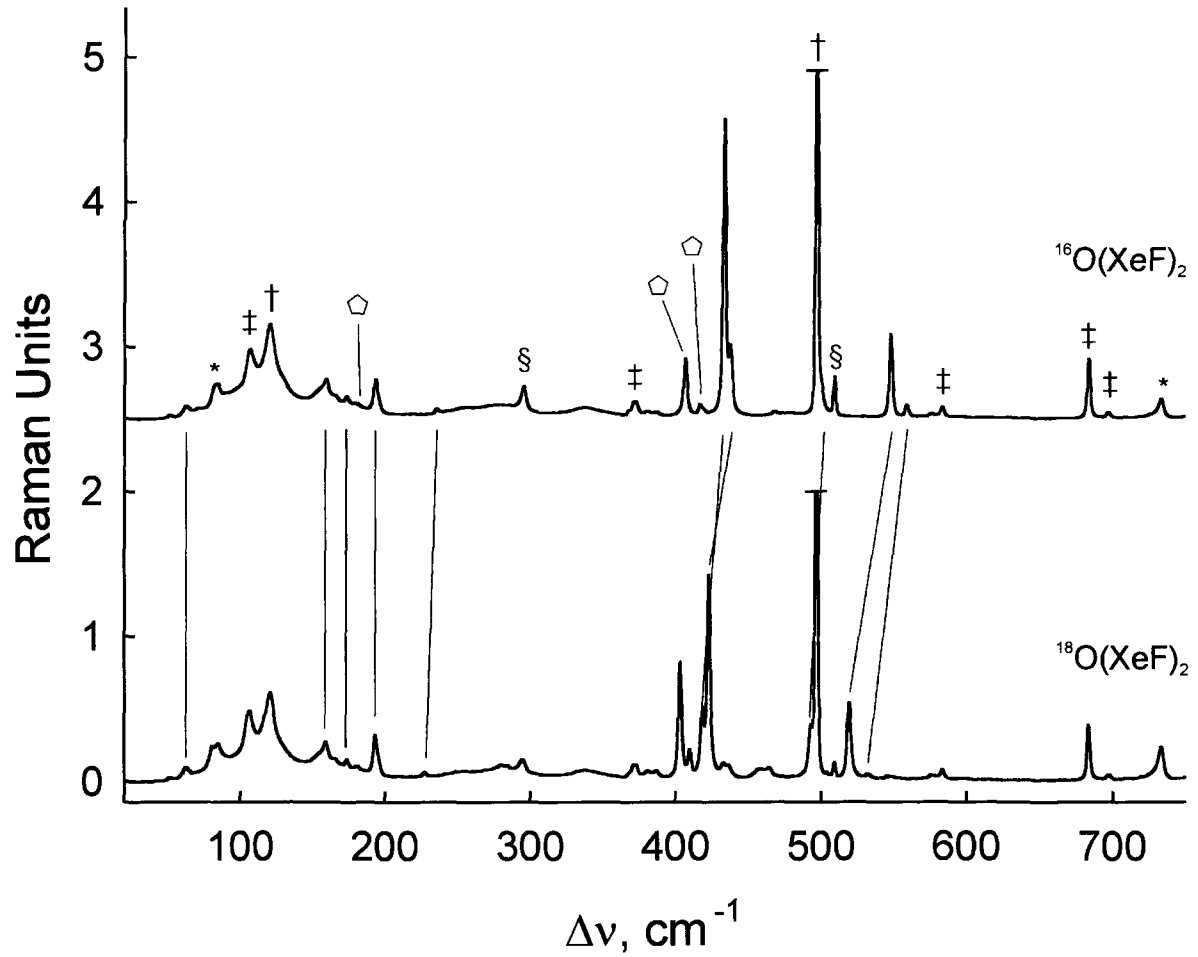

Figure 3.4. Raman spectra of $^{16}O(XeF)_2$ and $^{18}O(XeF)_2$ recorded at –160 °C using 1064-nm excitation. The symbols *, †, ‡, §, and denote bands arising from FEP, XeF_2, [NO][AsF_6], $XeF_2 \cdot N_2O_4$, and the $(XeO)_n$ cyclic polymer, respectively. Lines drawn between the $^{16}O(XeF)_2$ and $^{18}O(XeF)_2$ spectra denote Raman shifts between natural abundance and ^{18}O-enriched $O(XeF)_2$.

Table 3.4. Experimental and Calculated Frequencies for $O(XeF)_2$ (SVWN)

frequencies, cm^{-1}						
exptl[a]			calcd[b]			
^{16}O[c,d]	^{17}O[c,d]	^{18}O[c]	^{16}O	^{17}O	^{18}O	assignts (C_{2v})[e]
558.5(4)	n.o.	531.9(1)	563.6(3)	549.1(2)	535.8(1)	$\nu_7(B_2)$, $\nu_{as}(XeO)_2$
547.5(28)	532.3 sh	519.2(36)	526.9(33)	526.6(36)	525.5(38)	$\nu_1(A_1)$, $\nu_s(XeO)_2 - \nu_s(XeF)_2$
498.0 sh	n.o.	493.2(3)	491.0(13)	490.8(14)	489.9(15)	$\nu_8(B_2)$, $\nu_{as}(XeF)_2$
437.7(7) 433.1(100)	427.4(100)	422.5(100) 418.3(14)	440.7(36)	430.3(32)	420.6(29)	$\nu_2(A_1)$, $\nu_s(XeO)_2 + \nu_s(XeF)_2$
235.6(1)	228.9(5)	227.4(2)	212.4(<1)	209.2(<1)	205.9 (<1)	$\nu_6(B_1)$, δ(FXeO) o.o.p.
193.1(10)	193.0(72)	193.1(18)	171.1(4)	172.4(4)	172.4(4)	$\nu_3(A_1)$, δ(FXeO + δ(FXeO)
173.7(2)	173.7(36)	173.7(3)	147.4(1)	148.0(1)	148.0(1)	$\nu_5(A_2)$, ρ_t(FXeO)
159.3(6)	159.3(64)	159.3(11)	142.9(<1)	143.5(<1)	143.5(<1)	$\nu_9(B_2)$, δ(FXeO – δ(FXeO)
62.4(2)	62.2(18)	62.4(4)	57.3(7)	57.4(7)	57.2(7)	$\nu_4(A_1)$, δ(XeOXe)

[a] Raman frequencies and intensities for ^{16}O, ^{17}O, and ^{18}O were obtained from samples of natural abundance, ^{17}O-enriched $O(XeF)_2$ (^{16}O, 35.4%; ^{17}O, 21.9%; ^{18}O, 42.7%), and ^{18}O-enriched $O(XeF)_2$ (^{18}O, 99.99%), respectively. [b] SVWN/(SDB-)cc-pVTZ. Raman intensities (in $Å^4$ amu^{-1}) are given in parentheses. [c] Values in parentheses denote relative Raman intensities. [d] The abbreviation (sh) denotes a shoulder. [e] The abbreviations denote stretch (ν), bend (δ), and twist (ρ_t). Bond elongations and angle openings are denoted by plus (+) signs and bond contractions and angle closings are denoted by minus (–) signs.

Table 3.5. Experimental and Calculated Frequencies for $O(XeF)_2$ (PBEPBE)

frequencies, cm^{-1}						
exptl[a]			calcd[b]			
^{16}O[c,d]	^{17}O[c,d]	^{18}O[c]	^{16}O	^{17}O	^{18}O	assignments (C_{2v})[e]
558.5(4)	n.o.	531.9(1)	513.9(2)	501.6(1)	490.5(<1)	$\nu_7(B_2)$, $\nu_{as}(XeO)_2$
547.5(28)	532.3 sh	519.2(36)	489.5(39)	488.9(42)	487.6(45)	$\nu_1(A_1)$, $\nu_s(XeO)_2 - \nu_s(XeF)_2$
498.0 sh	n.o.	493.2(3)	450.3(16)	449.4(17)	447.6(17)	$\nu_8(B_2)$, $\nu_{as}(XeF)_2$
437.7(7) 433.1(100)	427.4(100)	422.5(100) 418.3(14)	410.4(41)	401.1(37)	392.2(33)	$\nu_2(A_1)$, $\nu_s(XeO)_2 + \nu_s(XeF)_2$
235.6(1)	228.9(5)	227.4(2)	197.9(<1)	194.8(<1)	192.0(<1)	$\nu_6(B_1)$, δ(FXeO) o.o.p.
193.1(10)	193.0(72)	193.1(18)	159.2(5)	160.4(5)	160.4(5)	$\nu_3(A_1)$, δ(FXeO + δ(FXeO)
173.7(2)	173.7(36)	173.7(3)	138.7(1)	139.3(1)	139.3(1)	$\nu_5(A_2)$, ρ_t(FXeO)
159.3(6)	159.3(64)	159.3(11)	134.6(<1)	135.2(<1)	135.2(<1)	$\nu_9(B_2)$, δ(FXeO – δ(FXeO)
62.4(2)	62.2(18)	62.4(4)	55.9(9)	56.0(9)	55.9(9)	$\nu_4(A_1)$, δ(XeOXe)

[a] Raman frequencies and intensities for ^{16}O, ^{17}O, and ^{18}O were obtained from samples of natural abundance, ^{17}O-enriched $O(XeF)_2$ (^{16}O, 35.4%; ^{17}O, 21.9%; ^{18}O, 42.7%), and ^{18}O-enriched $O(XeF)_2$ (^{18}O, 99.99%), respectively. [b] PBEPBE/(SDB-)cc-pVTZ. Raman intensities (in $Å^4$ amu^{-1}) are given in parentheses. [c] Values in parentheses denote relative Raman intensities. [d] The abbreviation (sh) denotes a shoulder. [e] The abbreviations denote stretch (ν), bend (δ), and twist (ρ_t). Bond elongations and angle openings are denoted by plus (+) signs and bond contractions and angle closings are denoted by minus (–) signs.

$O(XeF)_2$ for SVWN than PBEPBE methods. For this reason only the SVWN results are discussed. The highest frequency mode at 558.5 cm^{-1} is assigned to the $\nu_{as}(XeO)_2$ stretch, which displays a substantial low-frequency shift (26.6 cm^{-1}) upon substitution of ^{18}O, in good agreement with the calculated $^{16/18}O$ isotope shift (27.8 cm^{-1}). The $\nu_s(XeO)_2$ mode is coupled to $\nu_s(XeF)_2$ with the out-of-phase component, $\nu_s(XeO)_2 - \nu_s(XeF)_2$, at 547.5 cm^{-1} and in-phase component, $\nu_s(XeO)_2 + \nu_s(XeF)_2$, at 437.7 and 433.1 cm^{-1}. The totally symmetric in-phase band is, as expected, the most intense mode of the spectrum, corresponding to the observed solid-state $^{16/18}O$ isotope shifts of 14.8 and 15.2 cm^{-1}, which are smaller than the calculated gas-phase shift (20.1 cm^{-1}). The out-of-phase mode displays a large experimental $^{16/18}O$ isotopic shift (28.3 cm^{-1}) in marked contrast to the calculated value (1.4 cm^{-1}). The three coupled modes involving $\nu(XeO)_2$ appear at lower frequencies than $\nu(XeO)$ in $O{=}XeF_2$ (749.9 cm^{-1}),[66] in agreement with a formal Xe–O bond order of one (see Section 3.2.5). The $\nu_{as}(XeF)_2$ mode is not significantly coupled and appears at 498.0 cm^{-1}, displaying an $^{16/18}O$ isotopic shift of 4.8 cm^{-1} (calculated, 1.1 cm^{-1}), as expected for a mode in which the oxygen atom is not expected to have a large displacement. The remaining modes have been assigned as bending and twisting modes, and only the bend at 235.6 cm^{-1} reveals a significant isotopic shift of 8.2 cm^{-1}, compared to the expected shift of 6.5 cm^{-1}.

The ^{17}O- and ^{18}O-enrichment experiments have also provided valuable information about the reaction pathway of $[Xe_3OF_3][AsF_6]$ with NOF (see Section 3.2.1), as both enriched N^*O^+ and $XeF_2{\cdot}N_2O_3{}^{18}O$ were observed in the Raman spectra. The $\nu(NO)$ stretches for $N^{17}O^+$ and $N^{18}O^+$ occur at 2223.2 and 2196.8 cm^{-1}, respectively, and

display isotopic shifts of 30.3 and 56.7 cm^{-1} relative to $N^{16}O^+$ (calculated shifts: ^{17}O, 33.8 cm^{-1}; ^{18}O, 63.8 cm^{-1}). The frequencies for $XeF_2 \cdot N_2O_4$ and $XeF_2 \cdot N_2O_3{}^{18}O$ are given in Table 3.6 (also see Chapter 4).

3.2.4.2. Raman Spectra of Natural Abundance and ^{18}O-enriched $(XeO)_n$

Oxygen-18 experiments have also given insight into the nature of the three unassigned Raman bands at 416.5, 406.6, and 180.7 cm^{-1} that occur in the natural abundance spectrum, and that shift to lower frequencey by 7.0, 3.4, and 0.0 cm^{-1}, respectively. The absence of any higher-frequency Xe–F stretching modes, and the small number of observed modes, have led to the proposed oligomeric $(XeO)_n$ structures (eq 3.5), which could exist as either a chain or a ring. A chain structure is unlikely because it lacks any obvious termination, except with a fluorine atom, which should give rise to a mode that should be visible in the Raman spectrum, and because more peaks would be expected for a low-symmetry chain than for a highly symmetric ring. The mechanism of ring formation (eq 3.7) would involve incorporation of enriched oxygen, explaining the observed isotopic shifts, and have been reproduced with electron structure calculations. The natures of such rings are fully discussed in Section 3.2.5.3.

3.2.5. Computational Results

The electronic structure calculations of $O(NgF)_2$ (Ng = Kr, Xe) and the isoelectronic $F(NgF)_2^+$ cations (Section 3.2.5.1) were optimized and resulted in stationary points with all frequencies real. Only the SVWN/(SDB-)cc-pVTZ and PBEPBE/(SDB-)cc-pVTZ (PBEPBE values in the present discussion are given in

Table 3.6. Experimental and Calculated[a] Raman Frequencies for $XeF_2 \cdot N_2O_4$ and $XeF_2 \cdot N_2O_3{}^{18}O$

frequencies, cm^{-1}				
exptl[b]		calcd[c]		
$XeF_2 \cdot N_2O_4$	$XeF_2 \cdot N_2O_3{}^{18}O$	$XeF_2 \cdot N_2O_4$	$XeF_2 \cdot N_2O_3{}^{18}O$	assgnt (C_1)[d]
n.o.	n.o.	1870.2(1)	1863.2(2)	$\nu(NO_A) + \nu(NO_A)' - (\nu(NO_B) + \nu(NO_B)')$
1711.7(6)	1706.5	1838.9(8)	1828.2(7)	$\nu(NO_A) + \nu(NO_B)' - (\nu(NO_B) + \nu(NO_A)')$
1394.4(7)	1384.4[e]	1456.5(42)	1445.4(41)	$\nu(NO_A) + \nu(NO_A)' + \nu(NO_B) + \nu(NO_B)'$
1353.5(14)	1345.6			$2\nu_4$
n.o.	n.o.	1327.9(<1)	1313.2(1)	$\nu(NO_A) + \nu(NO_B) - (\nu(NO_A)' + \nu(NO_B)')$
817.5(16)	811.6	847.8(12)	840.9(12)	$\delta(NO_2) + \delta(NO_2)'$
n.o.	n.o.	759.4(<1)	752.8(<1)	$\delta(NO_2) - \delta(NO_2)'$
691(<1)	683.5[f]	688.0(<1)	686..4(1)	$\delta_w(NO_2) - \delta_w(NO_2)'$
n.o.	n.o.	558.1(6)	558.1(6)	$\nu(XeF) - \nu(XeF)$
509.1(100)	496.8[g]	510.3(8)	504.4(8)	$\rho_r(NO_2) - \rho_r(NO_2)'$
496.8(41)[g]	496.8[g]	503.0(19)	503.0(19)	$\nu(XeF) + \nu(XeF)$
n.o.	n.o.	443.3(2)	441.6(2)	$\delta_w(NO_2) + \delta_w(NO_2)'$
296.1(58)	295.0	312.0(21)	308.7(21)	$\nu(N–N)$
		238.3(1)	237.2(1)	$\rho_r(NO_2) + \rho_r(NO_2)'$ + small $\delta(XeF_2)$
n.o.	n.o.	222.8(<1)	220.5(<1)	$\rho_r(NO_2) + \rho_r(NO_2)'$ – small $\delta(XeF_2)$
		206.5(<1)	206.4(<1)	$\rho_t(NO_2) - \rho_t(NO_2)'$ + small $\delta(XeF_2)$
n.o.	n.o.	131.5(<1)	130.8(<1)	$\rho_t(NO_2) - \rho_t(NO_2)'$
121(70)[h]	120.5[h]	121.8(6)	121.8(6)	$\delta(XeF_2) + \rho_r(N_2O_4)$
98(10)	106.1	74.1(1)	73.1(1)	$\rho_t(NO_2) - \rho_t(NO_2)' + \rho_t(XeF_2)$
71(7)	81.0	69.0(2)	67.7(2)	$\rho_r(XeF_2) + \rho_r(N_2O_4)$
64(7)	62.2	61.1(<1)	61.0(<1)	$\rho_r(XeF_2) - \rho_r(N_2O_4)$
		38.5(<1)	38.2(1)	$\rho_t(XeF_2) + \rho_t(N_2O_4)$

[a] SVWN/(SDB-)cc-pVTZ. Raman intensities (in $Å^4$ amu^{-1}) are given in parentheses. [b] Abbreviation denotes not observed (n.o.). [c] Values are taken from Chapter 4. [d] The abbreviations denote stretch (ν), bend (δ), and twist (ρ_t). Bond elongations and angle openings are denoted by plus (+) signs and bond contractions and angle closings are denoted by minus (–) signs. [e] This band is coincident with FEP. [f] The band is coincident with the $\nu_1(A_{1g})$ band of AsF_6^-. [g] The band is coincident with the $\nu_1(\Sigma_g^+)$ band of free XeF_2. [h] The band is coincident with the $\nu_3(\Pi_u)$ band of free XeF_2.

parentheses) results are discussed, and the geometries are compared with those experimentally determined for the $[F(NgF)_2][MF_6]$ (M = As, Sb) salts[23,139] (Table 3.7). Computations performed using MP2 and hybrid DFT (B3PW91, BHandH, and BHandHLYP) methods failed to give reasonable geometries for $F(XeF)_2^+$ and/or $F(KrF)_2^+$, and for that reason have not been included in the ensuing discussion. Computations have also been performed to elucidate the energy barrier to the FXeONO rearrangement (Section 3.2.5.2) and the nature of the $(XeO)_n$ ring (Section 3.2.5.3).

3.2.5.1 $O(NgF)_2$ and $F(NgF)_2^+$ (Ng = Kr, Xe)

3.2.5.1.1. Geometries

The geometries of both $O(NgF)_2$ and $F(NgF)_2^+$ optimized to C_{2v} symmetry. The Ng–O [2.0806 (2.1219) Å, Xe; 1.9512 (2.0021) Å, Kr] and Ng–F_t [2.0414 (2.0802) Å, Xe; 1.9182 (1.9675) Å, Kr] bond lengths in $O(NgF)_2$ are indicative of more covalently bound molecules when compared with the Ng---F_b [2.1963 (2.2436), Xe; 2.0521 (2.1070), Kr] and Ng–F_t [1.9253 (1.9531) Å, Xe; 1.7854 (1.8200) Å, Kr] bond lengths calculated for the $F(NgF_2)^+$ cations (Table 3.7). The latter bond lengths are in good agreement with those determined in the X-ray crystal structures of the $[Ng_2F_3][AsF_6]$ and $[Ng_2F_3][SbF_6]$ salts and the previously calculated gas-phase structures of the free cations.[23,139] The differences in bond lengths between the neutral and cationic species are mirrored in the bond angles. The Ng–O–Ng and Ng---F_b---Ng bridge angles vary considerably among the four species, and follow the trend $O(KrF)_2$ [111.3 (111.9)°] < $O(XeF)_2$ [115.9 (116.4)°] < $F(KrF)_2^+$ [135.4 (134.3)°] < $F(XeF)_2^+$ [148.7 (146.3)°]. All angles were found to be larger than the ideal tetrahedral angle of 109.5°. The angles

Table 3.7. Experimental and Calculated Geometries for $O(NgF)_2$ and $F(NgF)_2^+$ (Ng = Kr, Xe)

	exptl[a]		calcd[a,b]			
	$F(NgF)_2^+$		$O(NgF)_2$		$F(NgF)_2^+$	
	$[F(NgF)_2][AsF_6]$[d]	$[F(NgF)_2][SbF_6]$[e]	SVWN	PBEPBE	SVWN	PBEPBE
Ng–O(F_b) (Å)[c]	2.142(7)–2.157(3)	2.141(8)–2.146(8)	2.0806	2.1219	2.1966	2.2436
	[2.049(6)–2.061(6)]	[2.027(5)–2.065(4)]	[1.9510]	[2.0021]	[2.0521]	[2.1070]
Ng–F_t (Å)[c]	1.908(6)–1.929(6)	1.918(9)–1.922(9)	2.0414	2.0802	1.9253	1.9531
	[1.780(7)–1.803(6)]	[1.787(4)–1.805(5)]	[1.9182]	[1.9675]	[1.7854]	[1.8200]
Ng–O(F_b)–Ng	148.6(4)–149.5(4)	160.3(3)	115.9	116.4	148.7	146.3
(deg)[c]	[127.5(3)]	[126.0(2)–142.5(3)]	[111.3]	[111.9]	[135.4]	[134.3]
O(F_b)–Ng–F_t	177.3(4)–177.7(3)	176.9(3)–178.6(4)	177.2	176.7	177.9	177.8
(deg)[c]	[178.2(3)–178.6(3)]	[175.1(2)–178.3(2)]	[177.3]	[177.0]	[177.3]	[177.2]

[a] Unbracketed values are for the Xe analogue and the square-bracketed values are for the Kr analogue. [b] (SDB-)cc-pVTZ basis sets. [c] The symbols F_b and F_t refer to the bridging and terminal fluorine atoms, respectively. [d] Geometric parameters were taken from ref 23 (monoclinic $[F(XeF)_2][AsF_6]$) and ref 139 ($[F(KrF)_2][AsF_6]\cdot[KrF][AsF_6]$), respectively. [e] Geometric parameters were taken from ref 23 ($F(XeF)_2][SbF_6]$) and ref 139 ($[F(KrF)_2]_2[SbF_6]_2\cdot KrF_2$ and $[F(KrF)_2][SbF_6]\cdot KrF_2$), respectively.

are larger for $F(NgF)_2^+$ than the angles for $O(NgF)_2$, since the lone pairs on the oxygen are expected to exert stronger repulsive forces on the more covalent Ng–O bonds, compressing the Ng–O–Ng angle to a greater extent than the Ng---F_b---Ng angle, which is more ionic and is expected to experience weaker repulsive forces from the two lone pair domains on fluorine.

The F_t–Ng–O bond angles [177.2° (176.7°), Xe; 177.3° (177.0°), Kr] are close to those calculated for the F_t–Ng---F_b angles of the $F(NgF)_2^+$ cations [177.9° (177.8°), Xe; 177.3° (177.2°), Kr]. The X-ray crystal structures of $[Ng_2F_3][AsF_6]$ and $[Ng_2F_3][SbF_6]$ give F_t–Ng---F_b bond angles of 176.9(3)–178.6(3)° in the case of Xe and 175.1(2)–178.6(3)° in the case of Kr, confirming the predicted angle.[23,139] The non-linearity of the angles is apparently a result of the asymmetric environment about the noble-gas atom in both $O(NgF)_2$ and $F(NgF)_2^+$; as such there is no symmetry constraint to keep the bond angle linear. Thus, the 3c-4e hypervalent bond at the noble-gas atom can build in other orbital character and deviate from linearity. With no orbital symmetry constraint, the bond angles about the noble-gas atom can adjust to maximize the interactions with oxygen in $O(NgF)_2$ and the bridging fluorine in $F(NgF)_2$, and, at the same time, minimize any repulsive interactions.

3.2.5.1.2. Natural Bonding Orbital Analyses

Natural bond orbital (NBO) analyses on the SVWN- and PBEPBE-optimized gas-phase geometries have been performed to evaluate the strength and covalency of the Ng–F_t and Ng–O(F_b) bonds (Table 3.8). Both sets of values were very similar, thus only the SVWN values will be discussed here. Electron localization function (ELF) analyses

Table 3.8. Natural Bond Orbital (NBO) Charges, Valencies, and Bond Orders[a] for $O(NgF)_2$ and $F(NgF)_2^{+}$ [b]

	$O(XeF)_2$				$F(XeF)_2^+$			
	SVWN		PBEPBE		SVWN		PBEPBE	
	Charges [Valencies]							
$O(F_b)$	–0.978	[1.545]	–0.890	[0.747]	–0.602	[0.370]	–0.581	[0.328]
Xe	1.089	[1.108]	1.028	[0.647]	1.244	[0.577]	1.205	[0.540]
F_t	–0.600	[0.659]	–0.578	[0.263]	–0.443	[0.389]	–0.514	[0.376]
	Bond Orders							
$Xe–O(F_b)$	0.374		0.372		0.184		0.163	
$Xe–F_t$	0.283		0.262		0.389		0.375	
	$O(KrF)_2$				$F(KrF)_2^+$			
	SVWN		PBEPBE		SVWN		PBEPBE	
	Charges [Valencies]							
$O(F_b)$	–0.756	[0.745]	–0.697	[0.682]	–0.492	[0.349]	–0.467	[0.316]
Kr	0.901	[0.625]	0.848	[0.567]	1.070	[0.577]	1.029	[0.516]
F_t	–0.523	[0.264]	–0.499	[0.237]	–0.324	[0.386]	–0.295	[0.360]
	Bond Orders							
$Kr–O(F_b)$	0.369		0.338		0.173		0.157	
$Kr–F_t$	0.261		0.235		0.384		0.359	

[a] (SDB-)cc-pVTZ basis sets. [b] The symbols F_b and F_t refer to the bridging and terminal fluorine atoms, respectively.

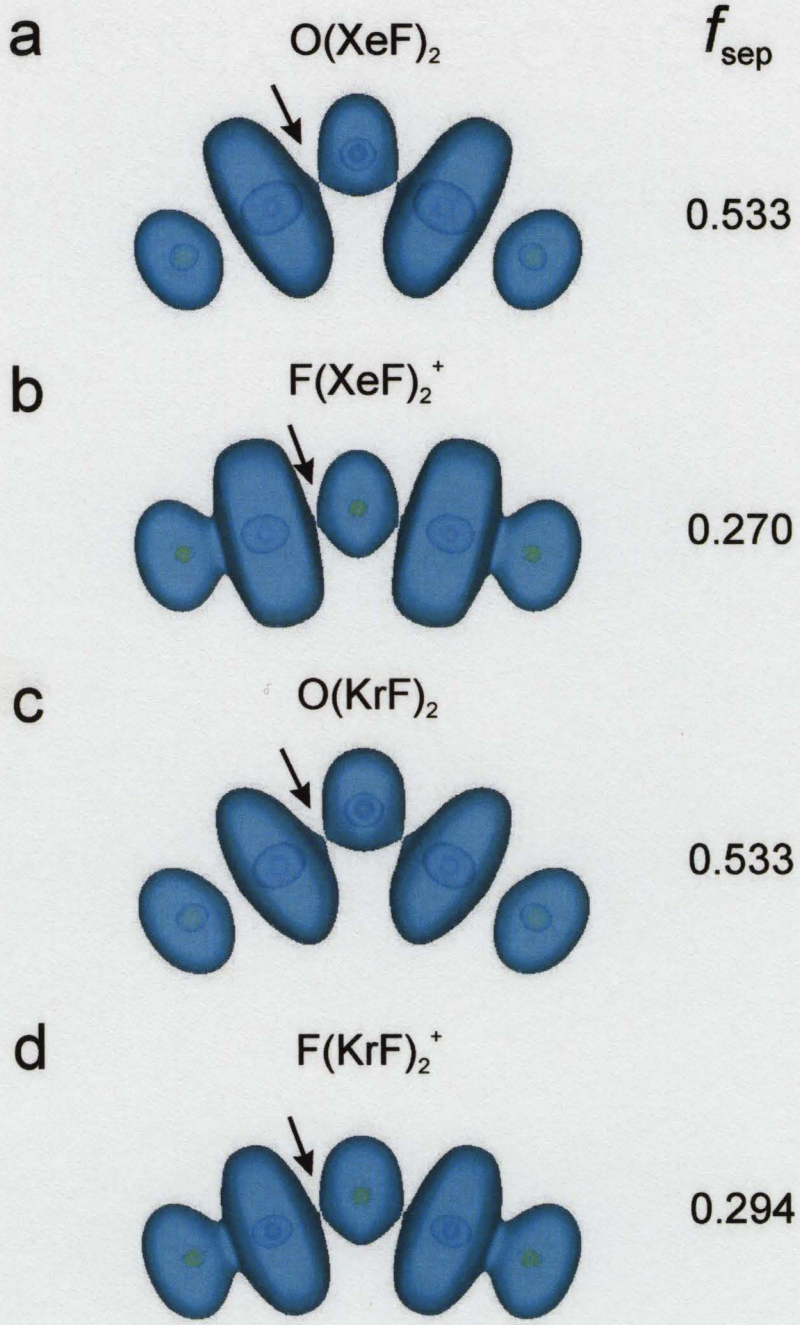

Figure 3.5. ELF isosurface plots for $O(NgF)_2$ and $F(NgF)_2^+$ (Ng = Kr, Xe) at the SVWN/(SDB-)cc-pVTZ//SVWN/(SDB-)cc-pVTZ level of theory, showing the f_{sep}-values for the $V(Ng)$ and $V(O(F))$ basins. Color scheme: blue, lone-pair (monosynaptic) basin, $V(X_i)$; green, bond (bisynaptic basin, $V(E,X_i)$; red, core basin, C(E).

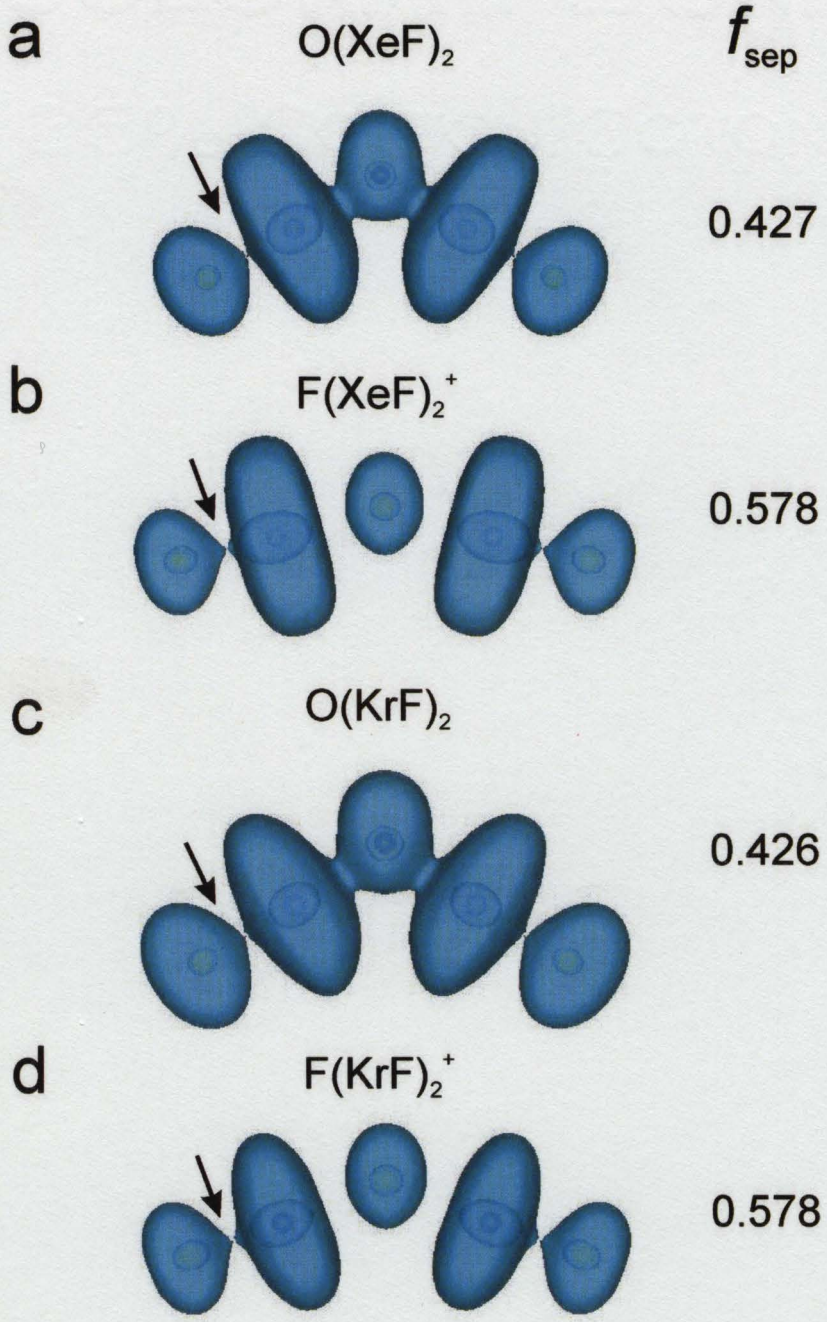

Figure 3.6. ELF isosurface plots for $O(NgF)_2$ and $F(NgF)_2^+$ (Ng = Kr, Xe) at the SVWN/(SDB-)cc-pVTZ//SVWN/(SDB-)cc-pVTZ level of theory, showing the f_{sep}-values for the $V(Ng)$ and $V(F_t)$ basins. Color scheme: blue, lone-pair (monosynaptic) basin, $V(X_i)$; green, bond (bisynaptic basin, $V(E,X_i)$; red, core basin, C(E).

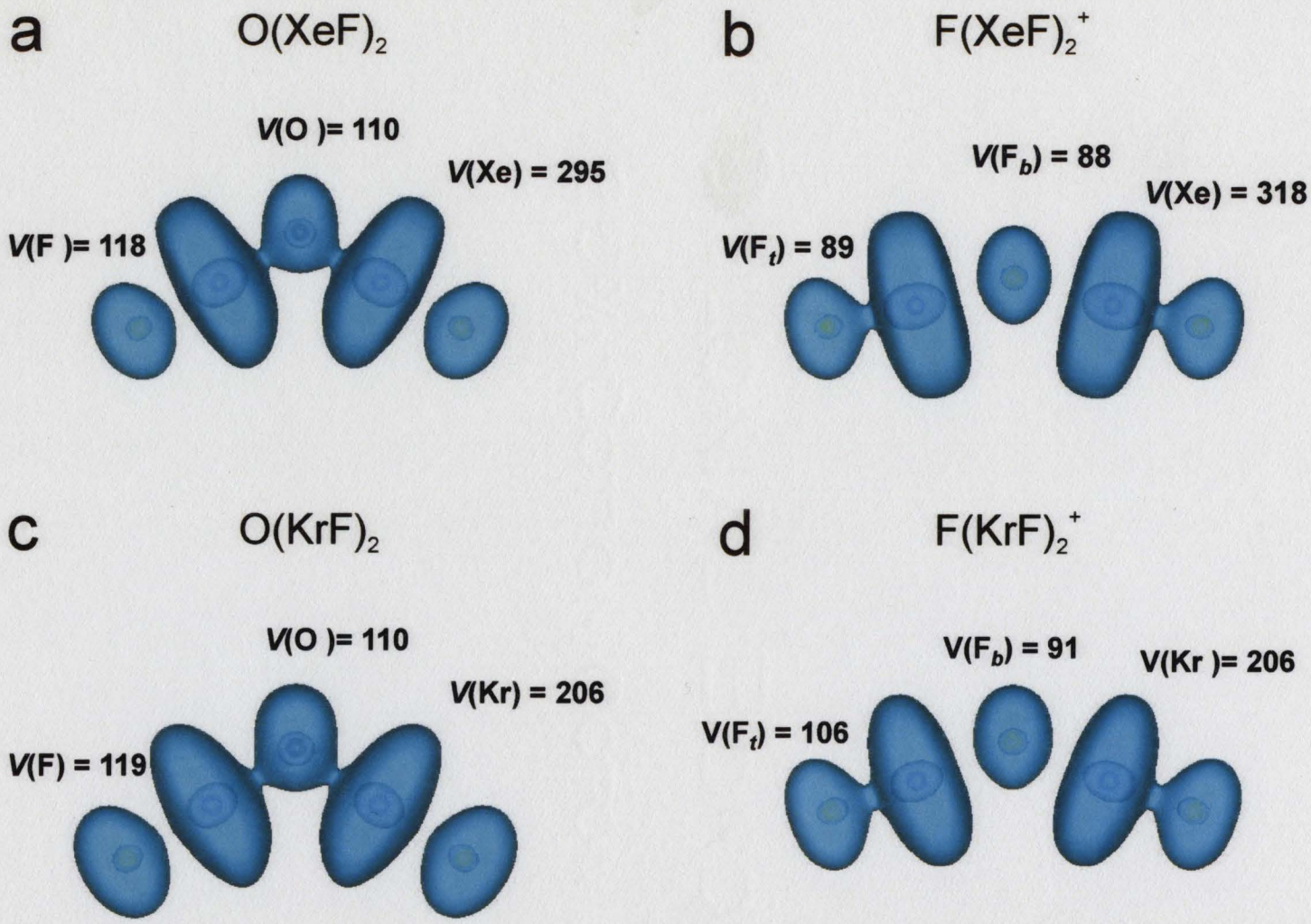

Figure 3.7. ELF isosurface plots for $O(NgF)_2$ and $F(NgF)_2^+$ (Ng = Kr, Xe) at the SVWN/(SDB-)cc-pVTZ//SVWN/(SDB-)cc-pVTZ level of theory, showing the f_{sep}-values for the V(Ng) and $V(F_t)$ basins. Color scheme: blue, lone-pair (monosynaptic) basin, $V(X_i)$; green, bond (bisynaptic) basin, $V(E,X_i)$; red, core basin, C(E).

have also been performed on the SVWN-optimized gas-phase geometries. The f_{sep}-values (i.e., the value of the isosurface at which the basins separate) are given in Figure 3.5 and 3.6, while the total noble gas lone-pair basin volumes are provided in Figure 3.7. Details of ELF analyses in relation to systems that contain xenon have been described in a previous paper, and require no further discussion.[140]

The NBO analyses give natural charges of 1.089 and 1.244 for Xe in $O(XeF)_2$ and $F(XeF)_2^+$, respectively. These charges are an approximate average of the formal charge 0, expected for a covalent model, and the formal oxidation number two expected for a purely ionic model for Xe, with the number being closer to two in the case of $F(XeF)_2^+$. These values are in accord with the natural charges for $O(F_b)$ (–0.978/–0.602) and F_t (–0.600/–0.443). In both cases, the charges are about half of their respective oxidation numbers, indicating polar covalent bonding that is consistent with 3c-4e bonding. The Xe–O/Xe–F bond order ratio (1.32) and the Xe/O/F valencies (1.108/1.545/0.659) are in agreement with this description of polar covalent bonding, whereas the Xe---F_b/Xe–F_t bond order ratio (0.47) and Xe/F_b/F_t valencies (0.577/0.370/0.389) are better described as more covalent Xe–F_t bonding with more ionic interactions between Xe and F_b. These results are further confirmed by ELF analyses (vide infra). Similar trends were observed for $O(KrF)_2$ and the $F(KrF)_2^+$ cation (Table 3.8).

The relative strengths of the Ng–$O(F_b)$ and Ng–F_t bonds have also been assessed on the basis of the f_{sep}-value at which the contours between the noble-gas atom and the $O(F_b)$ or F_t atoms separate. Separation of the F_t basin from Ng in $O(NgF)_2$ occurs at an f_{sep} value of 0.427 in the case of xenon and 0.426 in the case of krypton, whereas the

value of 0.578 is calculated for $F(NgF)_2^+$, providing evidence that the F_t–Ng bond is more covalent for the latter species. A much larger gap exists for the separation of the $O(F_b)$ basin from Ng for $O(NgF)_2$, with a value of 0.533, and $F(NgF)_2^+$, which has values of 0.294 and 0.270 for Kr and Xe, respectively. Again, the basin separation value reflects the bond orders for Ng–O and Ng---F_b and indicates that the $O(NgF)_2$ molecules are more covalently bound than the $F(NgF)_2^+$ cations. It is also interesting to note the difference between the f_{sep}-values for $F(XeF)_2^+$ (0.270) and $F(KrF)_2^+$ (0.294) also reflect the stronger covalent interaction between Kr---F_b relavtive to Xe---F_b (Table 3.7).

The noble-gas valence basin (torus) volumes given by ELF population analyses (f = 0.500) decrease in the order $F(XeF)_2^+$ (318) > $O(XeF)_2$ (295) > $F(KrF)_2^+$ (206) = $O(KrF)_2$ (206). The smaller torus volumes for the krypton atom in $O(KrF)_2$ and $F(KrF)_2^+$ can be viewed as a contraction of the Kr valence lone-pair basin by the closer proximity of the two negative electric fields of the $O(F_b)$ and F_t atoms, and the higher effective nuclear charge on Kr relative to Xe. The basin volume for xenon in $F(XeF)_2^+$ is larger than that calculated for $O(XeF)_2$, as expected, because the interaction with the oxygen atom is stronger in the latter species, causing a contraction of the toroidal surface.

3.2.5.2. The FXeONO Rearrangement

It has been proposed that the enriched N^*O^+ cation, as well as natural abundance $O(XeF)_2$, resulting from the reaction of $[Xe_3{}^*OF_3][AsF_6]$ with NOF, arises from the intramolecular rearrangement of the FXe^*ONO intermediate (Figure 3.8). The rearrangement was computationally evaluated by decreasing the distance between Xe(1)

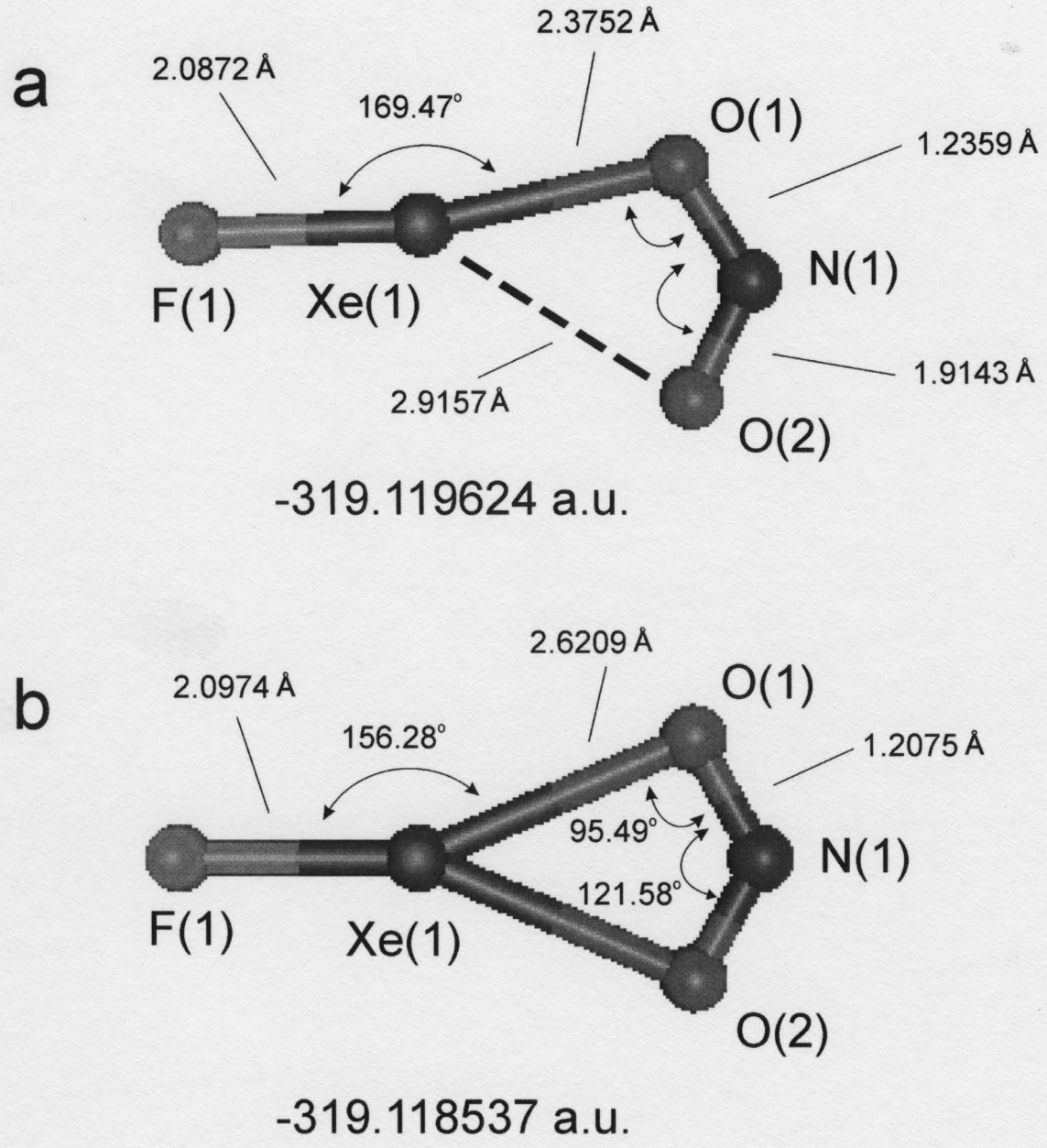

Figure 3.8. Calculated (SVWN/(SDB-)cc-pVTZ) geometries and energies for (a) the ground-state configuration of FXeONO, and (b) the transition-state configuration of FXeONO. The energy difference is 2.85 kJ mol^{-1} (Figure 3.9).

and O(2) in 0.05 Å increments, followed by a geometry optimization at that bond length, which yielded one local energy maximum transition state between the two energy minima for the optimized ground states (Figure 3.9). The ground state geometry shows an unusually long Xe(1)–O(1) bond length of 2.3752 Å, with a short Xe(1)···O(2) contact of 2.9157 Å (Xe–O van der Waals radii, 3.68 Å).[26] The long Xe(1)–O(1) bond length appears to account for the high reactivity of FXeONO and the inability to observe this intermediate as a long-lived intermediate on the NMR time scale. The transition state obtained from the scan was then optimized (one negative frequency), and the energy difference when compared with the ground state energy was found to be 2.85 kJ mol^{-1}. The low barrier to rearrangement is expected considering the relatively small difference between the Xe(1)–O(1) bond length and the Xe(1)···O(2) contact distance, and appears to be a reasonable explanation for the presence of enriched oxygen in the N^*O^+ cation proposed in eq 3.10.

3.2.5.3. The $(XeO)_n$ Cyclic Polymer

As discussed previously, the observation of three peaks in the $^{16}O(XeF)_2$ Raman spectrum at 416.5, 406.6, and 180.7 cm^{-1} is consistent with an $(XeO)_n$ oligomer of very high symmetry. A computational study of $(XeO)_n$ rings (n = 4–6) possessing D_{nh} symmetry was conducted at the SVWN5/(SDB-)cc-pVTZ level of theory (all calculations done without symmetry constraints (C_1) were very close to D_{nh} symmetry, except for n = 6, vide infra). The vibrational frequencies are summarized in Table 3.9, and the

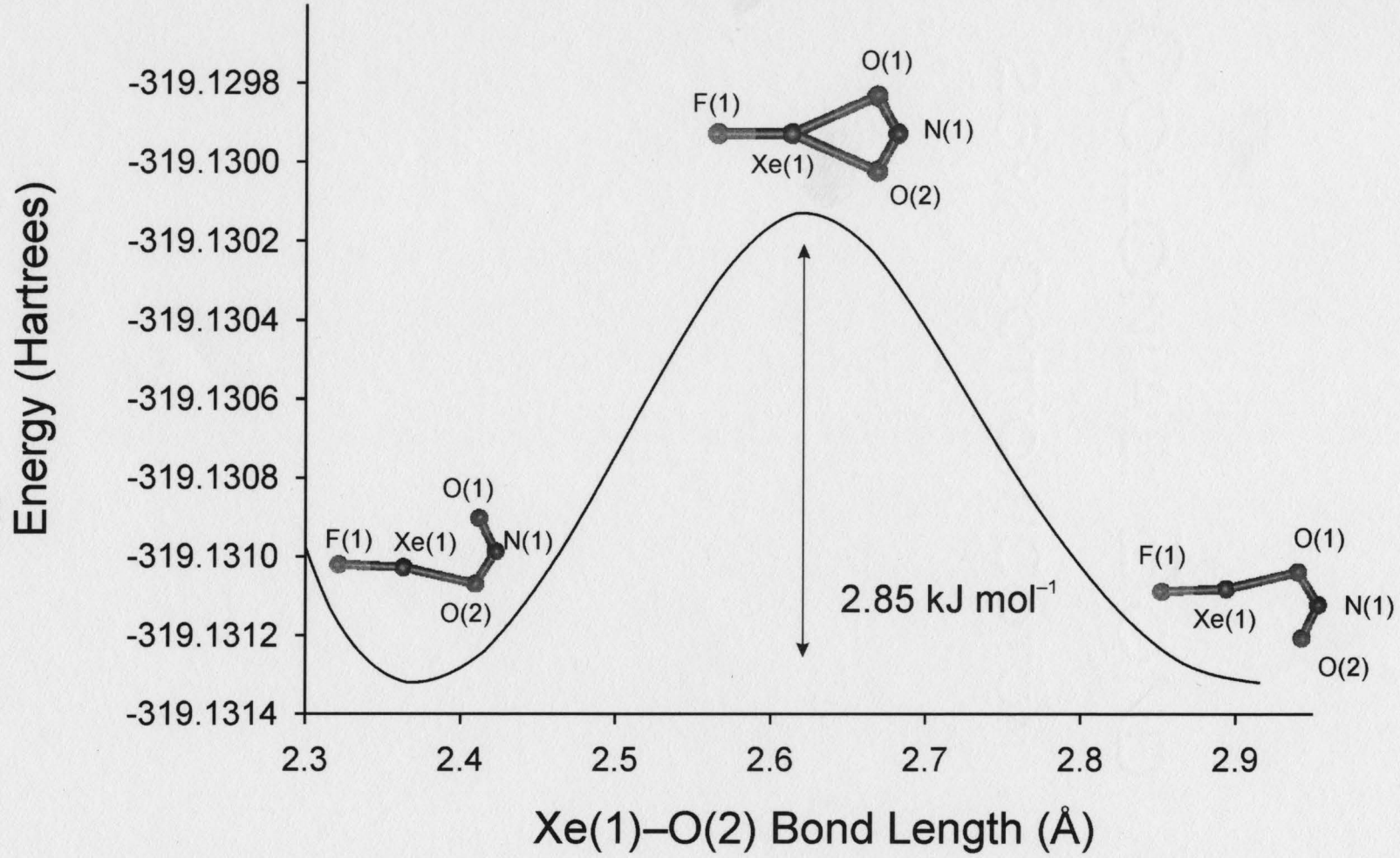

Figure 3.9. Energy surface plot for the intramolecular rearrangement of the FXeONO intermediate.

Table 3.9. Experimental and Calculated[a,b] Vibrational Frequencies and Intensities for $(XeO)_n$ (n = 4–6)

frequencies, cm^{-1}							
		calcd[d]					
exptl[c]		$(XeO)_4$ (D_{4h})		$(XeO)_5$ (D_{5h})		$(XeO)_6$ (D_{6h})	
^{16}O	^{18}O	^{16}O	^{18}O	^{16}O	^{18}O	^{16}O	^{18}O
		481.4(54)	454.8(47)	499.6(32)	473.7(28)	533.1(57)	505.7(50)
416.5(17)	409.5(15)	452.2(14)	433.0(12)	462.1(90)	437.0(78)	441.7(141)	417.9(122)
406.6(100)	403.2(100)	435.7(33)	410.8(29)	434.6(1)	414.3(<1)	406.1(2)	386.5(1)
180.7(6)	180.7(2)	186.5(2)	178.1(2)	197.2(2)	188.3(2)	197.0(3)	187.7(2)
		143.0(15)	144.3(15)	125.6(2)	125.8(2)	137.1(2)	137.7(2)
		110.7(5)	110.3(5)	115.6(22)	116.6(22)	97.5(31)	98.3(32)
		68.8(2)	69.6(2)	48.8(6)	49.1(6)	29.6(8)	29.7(8)
		482.2[372]	459.9[338]	505.7[579]	481.8[530]	524.5[980]	499.2[894]
		423.5[2]	399.4[1]	433.2[20]	409.3[16]	417.9[25]	395.1[20]
		240.4[34]	228.4[31]	232.4[45]	221.1[41]	221.7[56]	210.7[50]
		158.2[<1]	159.4[<1]	144.1[<1]	145.1[<1]	129.4[2]	130.3[2]

[a] SVWN5/(SDB-)cc-pVTZ. [b] Raman intensities are given in parentheses and infrared intensities are given in square brackets. [c] Values in parentheses denote relative Raman intensities. [d] Raman intensities (in $Å^4$ amu^{-1}) and infrared intensities (km mol^{-1}).

optimized structures are shown in Figure 3.10. Ring structures calculated with $n < 4$ failed to optimize, while rings with $n > 6$ possessing D_{nh} symmetry possessed negative frequencies (i.e. $n = 7$, three imaginary frequencies). When $n = 6$, the D_{6h} ring possesses one negative frequency, whereas the S_6 structure optimized with all frequencies real, and was slightly out of the plane, mimicking the chair conformation of cyclohexane, presumably to minimize Xe···Xe interactions (Figure 3.10).

Some interesting trends are observed upon increasing the ring size from 4 to 6. The Xe–O bond length decreased from 2.1570 Å to 2.1212 Å, while the O–Xe–O angle increased from 100° to 115.2°. Moreover, the coplanar O–Xe–O angles bend outward when $n = 4$ (170.0°), are near linear for $n = 5$ (179.3°), and bend inward when $n = 6$ (175.2°).

The frequencies calculated for the cyclic oligomers of $(XeO)_n$ ($n = 4$–6) under D_{nh} symmetries show that these species possess few Raman active modes, as expected for molecules that possess an inversion center. The low-frequency isotopic shifts that result from ^{18}O-substitution support the proposed structures, and any one of the proposed structures can reasonably be used to account for the observed Raman bands. It is expected that the highest frequency peak, calculated between 481 and 533 cm^{-1}, is obscured by either XeF_2 ($\nu_s(XeF_2)$) or by the Xe–F stretching modes of $O(XeF)_2$.

3.3. Conclusions

The missing neutral oxide fluoride of xenon(II), $O(XeF)_2$, has now been synthesized, showing marked stability at temperatures at or below –30 °C. The ^{17}O- and

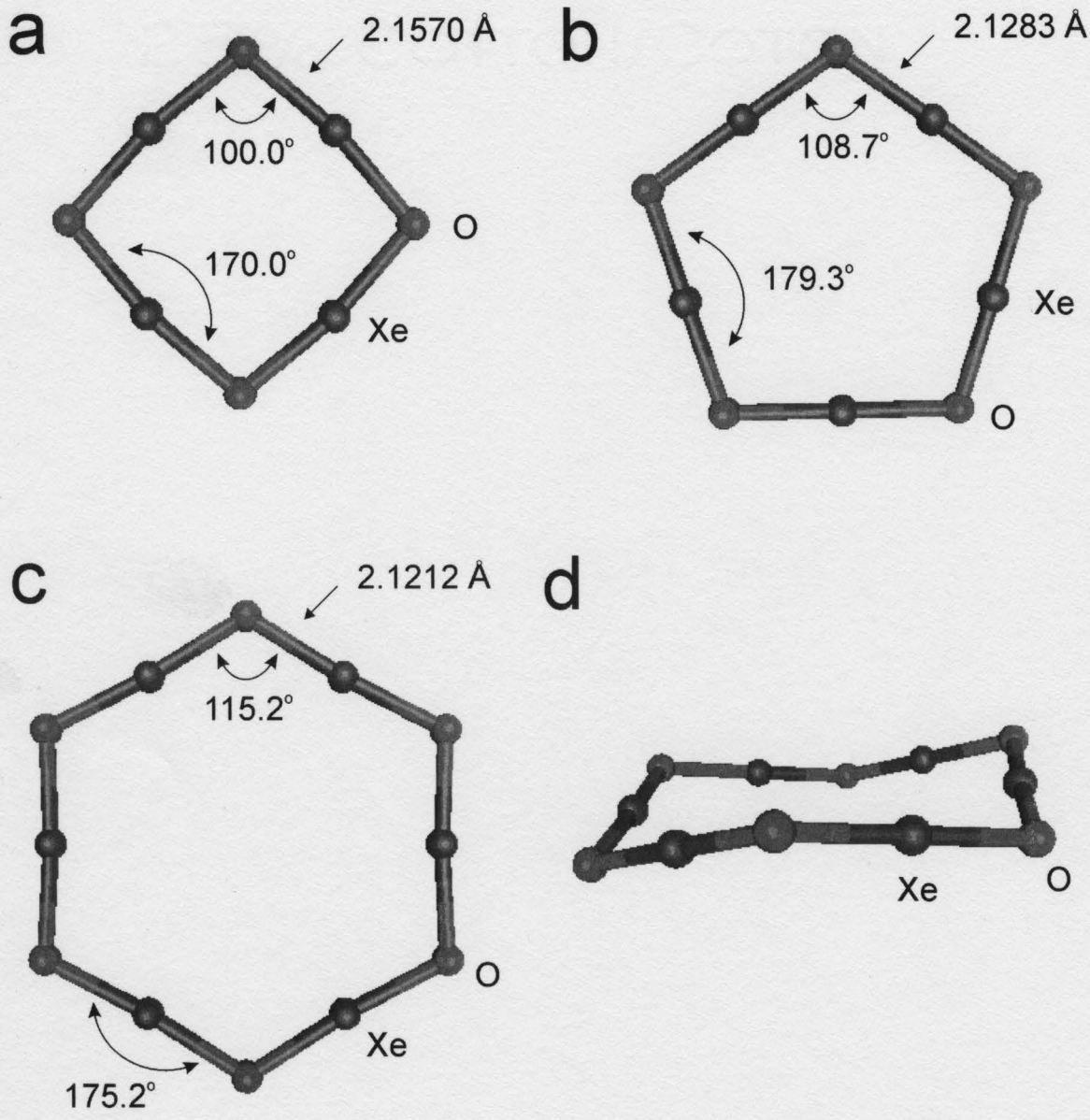

Figure 3.10. Calculated geometries for the cyclic $(XeO)_n$ (n = 4–6) oligomers: (a) $(XeO)_4$ (D_{4h}), (b) $(XeO)_5$ (D_{5h}), (c) $(XeO)_6$ (D_{6h}, one imaginary frequency), and (d) $(XeO)_6$ (C_1).

^{18}O-enrichment studies have also provided useful mechanistic data, suggesting that the formation of $O(XeF)_2$ first goes through the unstable intermediate, FXeONO, and that this intermediate can undergo facile intramolecular rearrangement, allowing for redistribution of enriched oxygen among the various oxygen-containing products. Solution state ^{19}F and ^{129}Xe NMR spectra have been successfully modeled and provide the first example of ^{129}Xe–^{129}Xe coupling. The unique coupling patterns that result from the natural abundance subspectra and the ability to simulate these spectra, as well as the broadening of the ^{19}F NMR linewidths observed with ^{17}O-substitution, provide definitive proof for FXeOXeF and its proposed structure. Solid-state characterization of $O(XeF)_2$ by Raman spectroscopy shows the expected isotopic shifts upon ^{18}O-substitution. An in-depth computational study of $O(NgF)_2$ and $F(NgF)_2^+$ (Ng = Kr, Xe) has shown that the $O(NgF)_2$ molecules are more covalently bound when compared to the isoelectronic $F(NgF)_2^+$ cations. Computational studies have also verified the facile nature of the FXeONO rearrangement, and provide a possible explanation for the unexplained bands observed in both the natural abundance and ^{18}O-enriched Raman spectra of $O(XeF)_2$, namely the $(XeO)_n$ oligomer.

CHAPTER 4

AN ISOLATED NITRATE OF XENON: SYNTHESES AND STRUCTURAL CHARACTERIZATION OF $FXeONO_2$, $XeF_2 \cdot HNO_3$, AND $XeF_2 \cdot N_2O_4$

4.1. Introduction

Two prior reports have claimed the formation of xenon(II) nitrates. The first report of xenon nitrate formation stemmed from the reactions of XeF_2 with anhydrous HNO_3 and with anhydrous HNO_3, containing 20% by weight of NO_2, at –20 °C.[99] Although formation of $FXeONO_2$ (red-brown) and $Xe(ONO_2)_2$ (blue) was proposed, no structural characterizations of either $FXeONO_2$ or $Xe(ONO_2)_2$ were provided. It is likely that the blue color attributed to $Xe(ONO_2)_2$ arose from N_2O_3.[135] In a subsequent study, $FXeONO_2$ was reported to have been generated by reaction of XeF_2 with HNO_3 in CH_2Cl_2 at –30 °C which was, in turn, reacted in situ with various alkenes to give 1,2-disubstituted fluoro-nitrato alkanes (1 = F, 2 = ONO_2).[100] No attempts were made to characterize the proposed intermediate xenon compound in solution or to isolate it for further study.

The absence of a well-characterized xenon nitrate is surprising, because the nitrate anion meets the general criteria that are normally associated with a ligand that is suitable for stabilization of Xe in its +2 oxidation state: 1) it is the conjugate base of a strong monoprotic acid, 2) the least electronegative atom (nitrogen) is in its highest oxidation state, and 3) the group electronegativity (scaled to the Pauling values, 3.95)[141] is very close to that of fluorine (3.98)[141] and greater than that established for $OTeF_5$ (3.87),[70] for

which both the $FXeOTeF_5$ and $Xe(OTeF_5)_2$ derivatives are known and have been structurally well characterized. This electronegativity trend has been confirmed by conductivity measurements, which show that the following acids can be arranged in order of increasing acidity: $HNO_3 < HOTeF_5 < HCl < HOTs < H_2SO_4 < HBr < HClO_4$.[142,143]

Recent work has shown that XeF_2 and $[H_3O][AsF_6]$ react in anhydrous HF (aHF) to form the only known oxide fluoride cation of Xe(II), $[FXeOXeFXeF][AsF_6]$.[67] This cation has shown synthetic utility in generating the first neutral oxide fluoride of Xe(II), $O(XeF)_2$.[67] The present chapter details the synthesis of $FXeONO_2$, providing a further application of the $FXeOXeFXeF^+$ cation to the syntheses of a novel xenon compound. The decomposition of $FXeONO_2$ is also described along with the attempted synthesis of $XeONO_2^+$ and the syntheses and structural characterizations of $XeF_2 \cdot HNO_3$ and $XeF_2 \cdot N_2O_4$.

4.2. Results and Discussion

4.2.1. Syntheses and Properties

4.2.1.1. Synthesis and Decomposition of $FXeONO_2$

Liquid NO_2F was allowed to react with magenta-colored $[FXeOXeFXeF][AsF_6]$ at −50 °C for ca. 5 h. Over the course of the reaction, the magenta suspension of $[FXeOXeFXeF][AsF_6]$ slowly reacted to form a solid white suspension. Isolation by removal of excess NO_2F under vacuum at −110 °C yielded white, microcrystalline $FXeONO_2$, XeF_2, and $[NO_2][AsF_6]$ according to eq 4.1 and 4.2. The proposed reaction

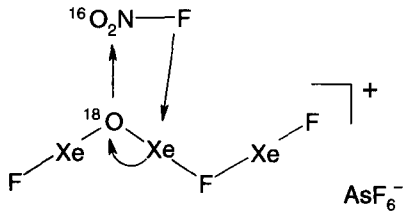

(4.1)

$$[Xe_2F_3][AsF_6] + NO_2F \longrightarrow 2\,XeF_2 + [NO_2][AsF_6] \quad (4.2)$$

pathway is supported by a double enrichment study using $^{15}NO_2F$ and $FXe^{18}OXeFXeF^+$, giving $FXe^{16}O^{15}NO_2$ and $FXe^{18}O^{14}NO_2$, respectively. Failure to observe $FXe^{16}ON^{18}O^{16}O$ indicated that no oxygen isotope scrambling between the bridging and terminal oxygen atoms had occurred, either by intermolecular exchange or by intramolecular rearrangement.

Attempts to isolate $FXeONO_2$ from the bulk mixture by dynamic vacuum sublimation at −35 °C failed, producing XeF_2, xenon gas, and N_2O_5, which is postulated to arise from the unstable intermediate, $O_2NO–ONO_2$ (eq 4.3). The latter rapidly decomposes at −78 °C (eq 4.4),[144,145] but was inferred by the observation of NO_3^- in the

$$2FXeONO_2 \longrightarrow XeF_2 + [O_2NO–ONO_2] + Xe \quad (4.3)$$

$$[O_2NO–ONO_2] \longrightarrow N_2O_5 + \tfrac{1}{2}\,O_2 \quad (4.4)$$

Raman spectrum, arising from N_2O_5, which exists as $[NO_2][NO_3]$ in the solid state.[146] Monitoring a solution of $FXeONO_2$ in SO_2ClF by ^{19}F NMR spectroscopy at −50 °C demonstrated that $FXeONO_2$ was 50% decomposed after 7 h at 0 °C, producing XeF_2 as the only fluorine-containing product. In contrast, a sample of $FXeONO_2$, left for seven

days at –78 °C, partially decomposed to give N_2O_4 and $XeF_2 \cdot N_2O_4$ according to eq 4.5–4.7.

$$FXeONO_2 \longrightarrow [FXeNO_2] + \tfrac{1}{2} O_2 \quad (4.5)$$

$$2\,[FXeNO_2] \longrightarrow XeF_2 + Xe + N_2O_4 \quad (4.6)$$

$$XeF_2 + N_2O_4 \longrightarrow XeF_2 \cdot N_2O_4 \quad (4.7)$$

It was found that $FXeONO_2$ and XeF_2 could be separated from $[NO_2][AsF_6]$ by extraction into SO_2ClF at –30 °C, followed by decanting the $FXeONO_2/XeF_2$ extract from $[NO_2][AsF_6]$ and coprecipitation of $FXeONO_2$ and XeF_2 at –78 °C (see Chapter 2).

4.2.1.2. Reactions of XeF_2 with HNO_3

Attempts were made to repeat the earlier reported syntheses of $FXeONO_2$ and $Xe(ONO_2)_2$ by reaction of XeF_2 with HNO_3.[99] In the present study, XeF_2 was allowed to react with stoichiometric amounts of anhydrous HNO_3 in SO_2ClF solution, as well as with excess, neat HNO_3. Xenon-129 NMR spectroscopy at –30 °C in SO_2ClF solution revealed that xenon gas was the major product (–5374 ppm). It is speculated that $Xe(ONO_2)_2$ is formed, but decomposes too rapidly to be observed by ^{129}Xe NMR spectroscopy (eq 4.8–4.10). Unreacted XeF_2, but no $FXeONO_2$, which is known from the

$$XeF_2 + HNO_3 \longrightarrow FXeONO_2 + HF \quad (4.8)$$

$$FXeONO_2 + HNO_3 \longrightarrow Xe(ONO_2)_2 + HF \quad (4.9)$$

$$Xe(ONO_2)_2 \longrightarrow O_2NO\text{–}ONO_2 + Xe \quad (4.10)$$

present work to be stable indefinitely in SO_2ClF at –30 °C, was detected by ^{19}F spectroscopy. Thus, it is likely that reaction 4.9, and the ensuing decomposition of $Xe(ONO_2)_2$ (eq 4.10) and N_2O_6 (eq 4.4), are rapid, precluding the isolation of the mono-substituted species under these conditions. Although $Xe(ONO_2)_2$ was not observed under these conditions, $XeF_2 \cdot HNO_3$ was isolated at low temperature from SO_2ClF solution and characterized in the solid state by Raman spectroscopy and single-crystal X-ray diffraction (see Sections 4.2.3 and 4.2.4). These results, in conjunction with the reaction of N_2O_5 with $[XeF][AsF_6]$ (vide infra), suggest that $Xe(ONO_2)_2$ is inherently unstable towards decomposition, which is supported by gas-phase thermochemical calculations (see Section 4.2.5).

4.2.1.3. Reactions of XeF_2 and $[XeF][AsF_6]$ with N_2O_5

Attempts to react XeF_2 and $[XeF][AsF_6]$ with N_2O_5 in SO_2ClF to give $FXeONO_2$ and/or $Xe(ONO_2)_2$ were unsuccessful. Both reactions were monitored by Raman spectroscopy and showed only the starting materials in the former case, beginning at –40 °C with stepwise warming to 10 °C. The reaction between $[XeF][AsF_6]$ and N_2O_5 did not occur at –78 °C. Gradual warming of the reaction mixture demonstrated that N_2O_5 only had a significant solubility in SO_2ClF above –30 °C, at which point reaction occurred. Low-temperature Raman spectroscopy showed only XeF_2, $[NO_2][AsF_6]$, and N_2O_5 as products. The reaction likely proceeds through $FXeONO_2$ to give $Xe(ONO_2)_2$ (eq 4.11 and 4.12), which decomposes at –30 °C according to eq 4.10, thus accounting for N_2O_5.

$$[XeF][AsF_6] + N_2O_5 \longrightarrow FXeONO_2 + [NO_2][AsF_6] \qquad (4.11)$$

$$FXeONO_2 + N_2O_5 \longrightarrow Xe(ONO_2)_2 + NO_2F \quad (4.12)$$

Nitryl fluoride, which was not observed in the Raman spectrum, in turn, reacts with $[XeF][AsF_6]$, accounting for its absence and the presence of XeF_2 (eq 4.13).

$$[XeF][AsF_6] + NO_2F \longrightarrow XeF_2 + [NO_2][AsF_6] \quad (4.13)$$

4.2.1.4. Reaction of XeF_2 with N_2O_4

Dissolution of XeF_2 in liquid N_2O_4 at 0 to 25 °C resulted in NOF ($\delta(^{19}F)$, 492.2 ppm at 30 °C) and a small steady-state concentration of $FXeONO_2$ which apparently arise according to eq 4.14 and 4.15, where the self-ionization of N_2O_4 has been well

$$N_2O_4 \rightleftharpoons NO^+ + NO_3^- \quad (4.14)$$

$$XeF_2 + NO^+ + NO_3^- \longrightarrow FXeONO_2 + NOF \quad (4.15)$$

established from electrical conductivity measurements ($2.36 \times 10^{-13}\ \Omega^{-1}\ cm^{-1}$ at 17 °C)[147] and by measurement of the self-ionization of N_2O_4 in sulfolane at 303 K ($K_{N_2O_4} = 7.1 \times 10^{-8}$ mol L^{-1}).[148] The small steady-state concentration of the NO_3^- anion in equilibrium (eq 4.14) and the instability of $FXeONO_2$ (eq 4.3–4.6) at room temperature (vide supra), account for the low product concentrations in solution (see Section 4.2.2).

Dissolution of XeF_2 in liquid N_2O_4 resulted in the observation of an $XeF_2 \cdot N_2O_4$ adduct by Raman spectroscopy of the frozen mixture (–160 °C, see Section 4.2.4) and it

was found that $XeF_2 \cdot N_2O_4$ crystallizes from solutions of XeF_2 in N_2O_4 at –3 °C (see Section 4.2.3).

4.2.1.5. Reaction of $FXeONO_2$ with AsF_5

In an attempt to form a salt of the $XeONO_2^+$ cation, a mixture of $FXeONO_2$ and XeF_2 was allowed to react with excess liquid AsF_5 at –78 °C. The reaction was monitored by low-temperature Raman spectroscopy over a period of 24 h and showed that AsF_5 had partially reacted with XeF_2 to yield $[XeF][AsF_6]$, while $FXeONO_2$ remained unreacted. Warming the reaction mixture to –50 °C for 12 h with periodic monitoring by Raman spectroscopy at –160 °C showed $[XeF][AsF_6]$ and $[NO_2][AsF_6]$ were the only products. The findings are consistent with the formation of an unstable $XeONO_2^+$ salt (eq 4.16) that rapidly decomposes according to eq 4.17. The instability of $XeONO_2^+$ is supported by

$$FXeONO_2 + AsF_5 \longrightarrow [XeONO_2][AsF_6] \quad (4.16)$$

$$[XeONO_2][AsF_6] \longrightarrow [NO_2][AsF_6] + Xe + \tfrac{1}{2}O_2 \quad (4.17)$$

gas-phase thermochemical calculations (see Section 4.2.5).

4.2.2. Solution Characterization of $FXeONO_2$ by ^{14}N, ^{19}F, and ^{129}Xe NMR Spectroscopy

The ^{19}F and ^{129}Xe NMR spectra of $FXeONO_2$ and XeF_2 mixtures were recorded in SO_2ClF solution at –70 °C and in CH_3CN solution at –50 °C, while the ^{14}N NMR spectrum was recorded in SO_2ClF solution at –50 °C. The ^{19}F and ^{129}Xe NMR spectra of

XeF_2, $FXeONO_2$, and NOF were determined in N_2O_4 solution at 30 °C (see Reactions of XeF_2 with N_2O_4). The NMR parameters for the three solvent systems are provided in Table 4.1.

The ^{19}F NMR spectrum of $FXeO^{15}NO_2$ (98+ % enrichment) in SO_2ClF consisted of a singlet ($\delta(^{19}F)$, −135.1 ppm) with accompanying ^{129}Xe (I = ½, 26.44 %) satellites ($^1J(^{19}F–^{129}Xe)$, 5424 Hz). No three-bond coupling to ^{15}N (I = ½, 98+ %) was observed, presumably because $^3J(^{15}N–^{19}F)$ is smaller than the width of the ^{19}F resonance ($\Delta\nu_{½}$ = 13 Hz at 11.7440 T, $\Delta\nu_{½}$ = 6 Hz at 7.0463 T).

The ^{129}Xe NMR spectrum of $FXeO^{15}NO_2$ (11.744 T) in SO_2ClF solvent consisted of a doublet at −1973 ppm in the xenon(II) region of the spectrum. The $^2J(^{15}N–^{129}Xe)$ coupling was not observed, resulting from the broad line width of the ^{129}Xe resonance ($\Delta\nu_{½}$ = 60 Hz). In an attempt to reduce the line broadening that results from the chemical shielding anisotropy, the sample was recorded at a lower field strength (7.0463 T). However, the line width ($\Delta\nu_{½}$ = 50 Hz) was not sufficiently reduced to observe the $^2J(^{15}N–^{129}Xe)$ coupling.

Both the ^{19}F and ^{129}Xe NMR chemical shifts are consistent with trends previously observed for FXe–R species (R = $OSeF_5$, $OTeF_5$, OSO_2F, $OS(O)(F)OMoOF_4$, $OS(O)(F)OWOF_4$, $OWOF_5(WOF_4)$, $OWOF_5(WOF_4)_2$),[149] which demonstrates that an increase in the electronegativity of the oxygen-bonded ligand causes a shift to high frequency for the ^{19}F resonance and a shift to high frequency for the ^{129}Xe resonance. These measurements suggest that the ONO_2 group is slightly more electronegative than $OTeF_5$ (SO_2ClF, –50 °C; $\delta(^{19}F)$, –151 ppm, $\delta(^{129}Xe)$, –2051 ppm). Furthermore, it is

Table 4.1. NMR Parameters of $FXeONO_2$ and Related Species[a]

	solvent	$\delta(^{19}F)$, ppm	$\delta(^{129}Xe)$, ppm	$\delta(^{14}N)$, ppm	$^1J(^{19}F-^{129}Xe)$, Hz	temp, °C
$FXeONO_2$	SO_2ClF	–130.1	–1973		5498	–70
	SO_2ClF			–65.8[b]		–50
	CH_3CN	–135.1	–1874		5463	–40
	N_2O_4[c]	–130.1	–1989		5408	30
XeF_2	SO_2ClF	–183.1	–1712		5621	–70
	CH_3CN	–179.1	–1783		5649	–40
	N_2O_4[c]	–179.2	–1840		5625	30
NOF	N_2O_4[c]	492.2				30

[a] Unless otherwise noted, the reaction products result from eq 4.1. [b] An attempt was made to acquire at ^{15}N NMR spectrum on ^{15}N-enriched (98+ %) $FXeONO_2$ (SO_2ClF solvent, –70 °C). [c] Equations 4.14 and 4.15.

anticipated that the higher effective group electronegativity of ONO_2 should result in a more ionic Xe–F bond relative to that of $OTeF_5$, which is suggested by the smaller $^1J(^{19}F–^{129}Xe)$ coupling constant for $FXeONO_2$ (5424 Hz) when compared with that of $FXeOTeF_5$ (5729 Hz).

The ^{14}N NMR spectrum in SO_2ClF solvent consisted of a singlet at –65.8 ppm ($\Delta\nu_{1/2}$ = 50 Hz). The resonance was quadrupole broadened to an extent that $^3J(^{14}N–^{19}F)$ and $^2J(^{14}N–^{129}Xe)$ could not be observed. A ^{15}N NMR study on a ^{15}N-enriched sample of $FXeONO_2$ in the same spectral region indicated that the relaxation time of ^{15}N was sufficiently long to preclude its observation, even at delay times of 180 s. The relaxation time is presumably long because the ^{15}N is surrounded by spinless oxygen nuclei, which does not afford a significant dipolar intramolecular spin-lattice relaxation pathway.

4.2.3. X-ray Crystallography

Details of the data collection parameters and other crystallographic information for $FXeONO_2$, $XeF_2{\cdot}HNO_3$, and $XeF_2{\cdot}N_2O_4$ are given in Table 4.2. The experimental and calculated bond lengths and angles are summarized in Table 4.3.

4.2.3.1. $FXeONO_2$

The $FXeONO_2$ molecules, which possess C_s site symmetry, are well isolated, discrete molecular units as inferred from the shortest contacts (Figure 4.1). Many of the Xe···O/F contacts (3.322(4) – 3.570(5) Å) are near or at the limit of the van der Waals radii for the xenon and fluorine atoms (3.63 Å)[26] and xenon and oxygen atoms (3.68 Å),[26]

Table 4.2. Crystallographic Data for $FXeONO_2$, $XeF_2 \cdot HNO_3$, and $XeF_2 \cdot N_2O_4$

chem formula	NO_3FXe	$N_2O_4F_2Xe$	HNO_3F_2Xe
space group	$P2_1/c$	$P\bar{1}$	$Pnma$
a (Å)	4.6663(4)	4.5822(3)	17.3543(7)
b (Å)	8.7995(7)	5.0597(3)	5.6539(2)
c (Å)	9.4153(8)	6.2761(5)	4.7658(2)
α (deg)	90	79.170(7)	90
β (deg)	90.325(5)	88.454(5)	90
γ (deg)	90	81.083(5)	90
V (Å^3)	386.60(6)	141.19(2)	467.62(5)
molecules/unit cell	4	1	4
mol wt (g mol^{-1})	212.30	261.30	232.30
calcd density (g cm^{-3})	3.648	3.073	3.300
T (°C)	−173	−173	−160
μ (mm^{-1})	8.80	6.10	7.32
R_1 [a]	0.0417	0.0385	0.0140
wR_2 [b]	0.0807	0.0742	0.0317

[a] R_1 is defined as $\Sigma||F_o| - |F_c||/\Sigma|F_o|$ for $I > 2\sigma(I)$. [b] wR_2 is defined as $[\Sigma[w(F_o^2 - F_c^2)^2]/\Sigma w(F_o^2)^2]^{1/2}$ for $I > 2\sigma(I)$.

Table 4.3. Experimental and Calculated[a] Geometric Parameters for $FXeONO_2$, $XeF_2 \cdot HNO_3$, and $XeF_2 \cdot N_2O_4$

		$FXeONO_2$			
		bond lengths (Å)			
Xe(1)–F(1)	1.992(4)	[2.018]	N(1)–O(2)	1.199(6)	[1.197]
Xe(1)–O(1)	2.126(4)	[2.144]	N(1)–O(3)	1.224(6)	[1.206]
O(1)–N(1)	1.365(7)	[1.382]			
		bond angles (deg)			
F(1)–Xe(1)–O(1)	177.6(2)	[176.0]	O(1)–N(1)–O(3)	118.4(5)	[117.9]
Xe(1)–O(1)–N(1)	114.7(3)	[113.8]	O(2)–N(1)–O(3)	127.1(5)	[129.8]
O(1)–N(1)–O(2)	114.5(4)	[112.3]			
		contacts (Å)			
Xe(1)···F(1A)	3.420(4)		Xe(1)···F(1B)	3.299(4)	
Xe(1)···O(1A)	3.322(4)		Xe(1)···O(2B)	3.545(4)	
Xe(1)···O(2A)	3.478(4)		Xe(1)···O(3B)	3.570(5)	
Xe(1)···O(3A)	3.390(4)		Xe(1)···O(3C)	3.518(4)	
N(1)···F(1A)	2.780(6)		O(1)···F(1A)	2.935(5)	
O(2)···N(1A)	2.923(6)		Xe(1)···O(3C)	2.965(7)	[2.933]
		$XeF_2 \cdot HNO_3$			
		bond lengths (Å)			
Xe(1)–F(1)	1.9737(8)	[1.983]	N(1)–O(2)	1.368(2)	[1.360]
Xe(1)–F(2)	2.0506(8)	[2.064]	N(1)–O(3)	1.216(2)	[1.220]
O(1)–N(1)	1.206(2)	[1.193]	O(2)–H(1)	0.83(2)	[1.046]
		bond angles (deg)			
F(1)–Xe(1)–F(2)	178.98(3)	[180.0]	O(2)–N(1)–O(3)	117.2(1)	[120.7]
O(1)–N(1)–O(2)	114.6(1)	[116.3]	N(1)–O(2)–H(1)	106(2)	[104.1]
O(1)–N(1)–O(3)	128.2(1)	[128.1]			
		contacts (Å)			
H(1)···F(2)	1.86(2)	[1.520]	Xe(1)···F(1B)	3.3050(4)	
Xe(1)···O(3)	3.317(1)	[3.034]	Xe(1)···F(1C)	3.3050(4)	
Xe(1)···F(1A)	3.4897(9)		Xe(1)···O(1B)	3.4156(6)	
Xe(1)···O(1A)	3.4156(6)		Xe(1)···O(1C)	3.456(1)	
Xe(1)···F(2A)	3.4859(8)		Xe(1)···O(2B)	3.5284(6)	
Xe(1)···O(2A)	3.5284(6)		O(2)···F(2)	2.690(1)	[2.566]

Table 4.3. (continued...)

		$XeF_2 \cdot N_2O_4$[b]			
		bond lengths (Å)			
Xe(1)–F(1)	1.985(3)	[1.996, 2.030] (2.014, 2.012)	N(1)–O(2)	1.182(6)	[1.181] (1.198)
N(1)–O(1)	1.194(6)	[1.188] (1.198)	N(1)–N(1A)	1.738(8)	[1.759] (1.766)
		bond angles (deg)			
F(1)–Xe(1)–F(1A)	180.0	[178.9] (179.1)	O(1)–N(1)–O(2)	134.5(5)	[135.0] (134.0, 135.4)
O(1)–N(1)–N(1A)	112.5(4)	[112.5] (113.4, 112.4)	O(2)–N(1)–N(1A)	113.0(4)	[112.5] (112.6, 112.2)
		contacts (Å)			
Xe(1)···F(1B)	3.370(3)		Xe(1)···F(1C)	3.370(3)	
Xe(1)···O(1B)	3.516(4)	[3.262]	Xe(1)···O(1C)	3.440(4)	[3.332]
Xe(1)···O(1D)	3.440(4)	[3.332]	Xe(1)···O(1E)	3.516(4)	[3.262]
Xe(1)···O(2)	3.490(4)		Xe(1)···O(2B)	3.435(4)	[3.262]
Xe(1)···O(2C)	3.490(4)		Xe(1)···O(2D)	3.435(4)	[3.262]
Xe(1)···O(2E)	4.180(4)	[3.314]	Xe(1)···O(2F)	4.180(4)	[3.314]
F(1)···N(1B)	2.720(4)	[2.564]	F(1)···N(1C)	2.834(5)	[2.564]

[a] SVWN/(SDB-)cc-pVTZ. Calculated values are given in square brackets or in parentheses. [b] Calculated geometric parameters for N_2O_4 coordinated to XeF_2 through two oxygens bound to two different nitrogen atoms (square brackets) and two oxygens bound to the same nitrogen atom (parentheses).

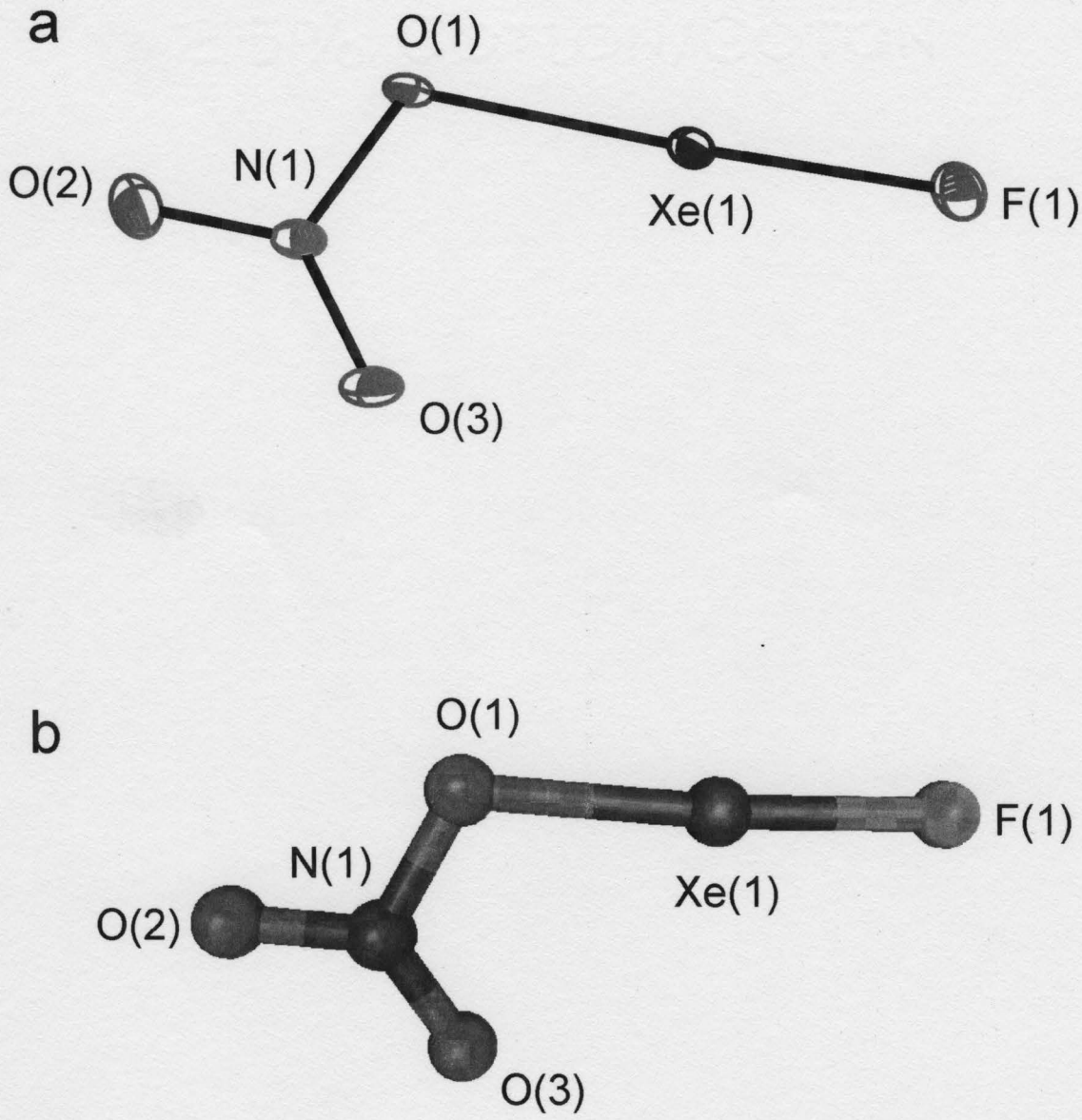

Figure 4.1. (a) X-ray crystal structure of $FXeONO_2$; thermal ellipsoids are shown at the 50% probability level. (b) Calculated geometry of $FXeONO_2$ (SVWN/(SDB-)cc-pVTZ). Experimental and calculated geometrical parameters are provided in Table 4.3.

and avoid the torus of electron lone pair density about xenon, which is further verified by the good agreement between the experimental and calculated geometric parameters (see Section 4.2.5).

The Xe–O bond length of 2.126(4) Å is indicative of a polar-covalent bond (see Section 4.2.5), and is comparable to that found for the neutral $FXeOSO_2F$ (2.155(8) Å)[27] and $Xe(OTeF_5)_2$ (2.119(11) Å)[75] molecules. Correspondingly, the Xe–F bond length (1.992(4) Å) and O–Xe–F angle (177.6(2)°) are comparable to those determined for $FXeOSO_2F$ (1.940(8) Å and 177.4(3)°, respectively).[27] The Xe–O–N angle (114.7(3)°) was found to be larger than those determined for $ClONO_2$ (112.49(4)°)[150] and $BrONO_2$ (113.8(4)°)[151] in the solid state, which is commensurate with the lower bond density (i.e. bond order) of the order Xe–O < Br–O < Cl–O (see Table 4.4). The geometric parameters for the ONO_2 moiety determined for $FXeONO_2$ and $XONO_2$ (X = Cl, Br) differ in that the $N–O_{cis}$ bond length is shorter than $N–O_{trans}$ for the halogen nitrates, and longer for the xenon nitrate, which agrees with the bond orders determined at the PBE1/aug-cc-pVTZ(-PP) level of theory.

4.2.3.2. $XeF_2 \cdot HNO_3$

The structure of the $XeF_2 \cdot HNO_3$ adduct (Figure 4.2) is one of only two examples of hydrogen-bonded adducts of XeF_2, the other being $[H_3O][AsF_6] \cdot 2XeF_2$.[67] All the atoms are coplanar by symmetry, allowing the molecules to pack in sheets of XeF_2 and HNO_3 molecules (Figure 4.3). This self assembly results from short H···F (1.86(2) Å)

Table 4.4. Geometric Parameters and NBO Analyses for $FXeONO_2$, $BrONO_2$, and $ClONO_2$ at the PBE1/aug-cc-pVTZ(-PP) and MP2/aug-cc-pVTZ(-PP) Levels of Theory

	$FXeONO_2$		$BrONO_2$[a]		$ClONO_2$[b]	
			bond lengths (Å)			
	exptl	calcd [c]	exptl	calcd [c]	exptl	calcd [c]
R–O	2.126(4)	2.1319 (2.0999)	1.860(5)	1.8171 (1.8069)	1.6834(6)	1.6684 (1.6761)
O_R–N	1.365(7)	1.3705 (1.4036)	1.414(7)	1.4437 (1.5218)	1.4694(7)	1.4747 (1.5687)
N–O_{cis}	1.224(6)	1.2042 (1.2138)	1.192(8)	1.1847 (1.1912)	1.1872(7)	1.1797 (1.1862)
N–O_{trans}	1.199(6)	1.1931 (1.2065)	1.213(8)	1.1862 (1.1946)	1.2030(7)	1.1824 (1.1900)
R···O_{cis}	2.965(7)	2.9759 (2.9446)	N/A[d]	2.8302 (2.8123)	N/A[d]	2.7241 (2.7284)
			bond angles (°)			
R–O_R –N	114.7(3)	115.46 (114.18)	113.8(4)	114.84 (112.22)	112.49(4)	113.34 (110.65)
O–N–O_{cis}	118.4(5)	117.82 (117.43)	120.0(5)	114.84 (116.96)	118.36(5)	117.50 (116.10)
O–N–O_{trans}	114.5(4)	113.21 (112.68)	110.1(5)	109.60 (108.47)	109.37(5)	108.97 (107.81)
O–N–O	127.1(5)	129.00 (129.89)	130.0(6)	132.30 (134.57)	132.27(5)	133.53 (136.09)
			tortional angles (°)			
R–O–N–O	0.00	0.02 (0.04)	N/A[d]	0.01 (0.08)	N/A[d]	0.00_4 (0.04)
			natural charges			
	PBE1	MP2	PBE1	MP2	PBE1	MP2
R	1.162	1.157	0.365	0.337	0.283	0.256
O_R	–0.573	–0.586	–0.474	–0.509	–0.419	–0.465
N	0.723	0.657	0.727	0.662	0.726	0.659
O_{cis}	–0.397	–0.345	–0.318	–0.245	–0.298	–0.221
O_{trans}	–0.325	–0.285	–0.301	–0.245	–0.292	–0.229
			natural bond orders			
R–O	0.269	0.339	0.553	0.575	0.654	0.628
O_R–N	0.836	0.793	0.708	0.606	0.658	0.545
N–O_{cis}	1.215	1.216	1.265	1.267	1.278	1.277
N–O_{trans}	1.228	1.214	1.248	1.243	1.260	1.256
R···O_{cis}	0.021	0.027	0.020	0.035	0.004	0.034

[a] Taken from ref 151. [b] Taken from ref 150. [c] MP2 values given in parentheses. [d] The symbol N/A denotes not available.

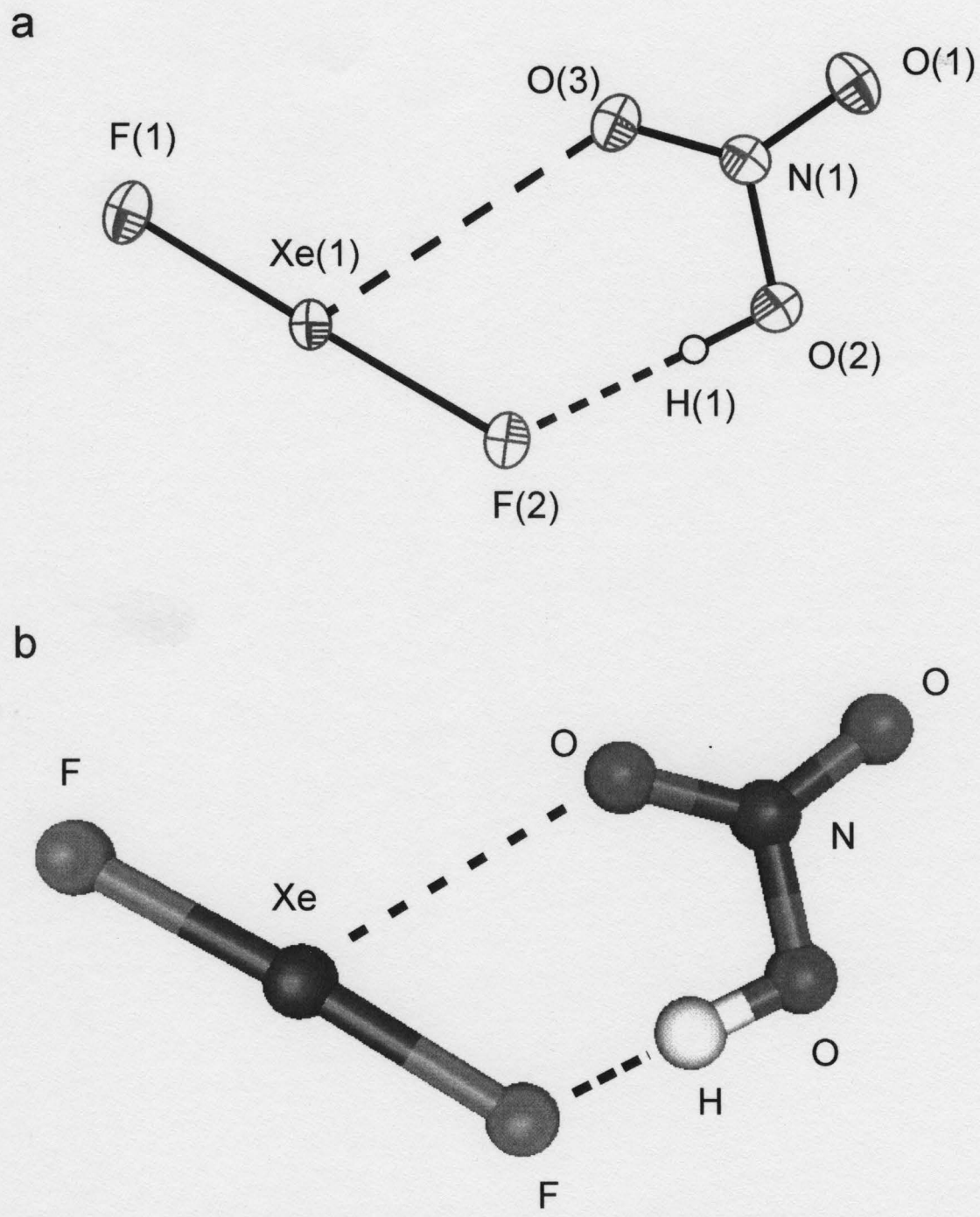

Figure 4.2. (a) The X-ray crystal structure of $XeF_2 \cdot HNO_3$ showing the H···F and Xe···O contacts; thermal ellipsoids are shown at the 70% probability level. (b) The calculated geometry of $XeF_2 \cdot HNO_3$ (SVWN/(SDB-)cc-pVTZ). Experimental and calculated geometric parameters are provided in Table 4.3.

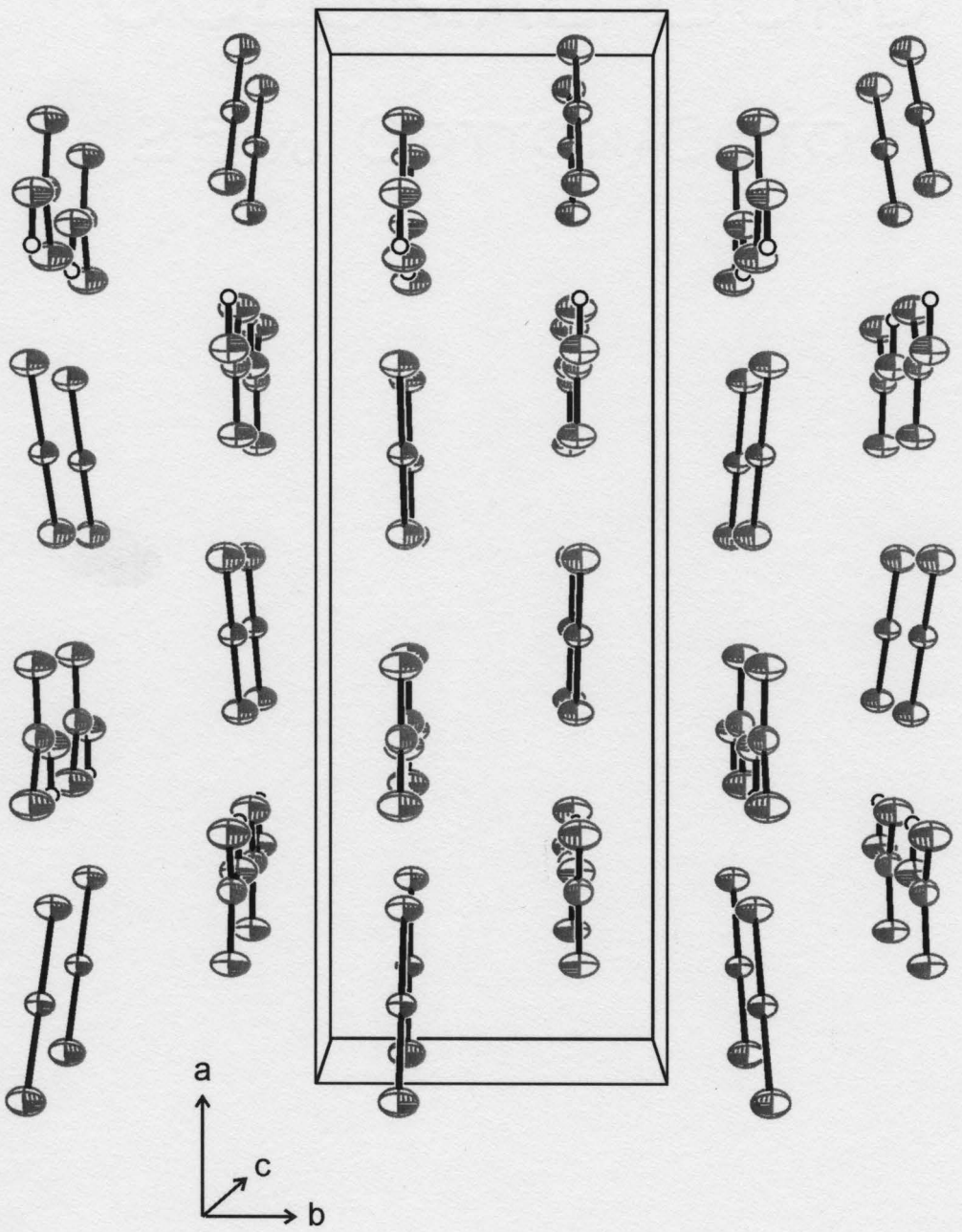

Figure 4.3. Packing diagram of $XeF_2 \cdot HNO_3$ viewed along the *c*-axis with thermal ellipsoids shown at the 70% probability level.

contacts and weak Xe···O (3.317(1) Å) contacts, which are well within the sums of the van der Waals radii (2.67 and 3.68 Å, respectively).[26]

The strong hydrogen bond was found to distort the local symmetry of the XeF_2 molecule from $D_{\infty h}$ to $C_{\infty v}$ symmetry. The Xe–F bond length distortions (terminal, 1.9737(8) Å; bridge, 2.0506(8) Å) are similar to the distortions found in compounds where XeF_2 is coordinated to a metal ion, $[M^{n+}(XeF_2)_p](AF_6)_n$ (M = Li, Ag, Mg, Ca, Sr, Ba, Pb, Zn, Cu, Cd, La, Nd; A = P, As, Sb).[152] For example, in $[Mg(XeF_2)_2](AsF_6)_2$, the Xe–F bridge and terminal distances are 2.051(4) Å and 1.913(5) Å.[50] The geometric parameters obtained for HNO_3 (N–O_H, 1.368(2) Å; N–O_{cis}, 1.216(2) Å; N–O_{trans}, 1.206(2) Å; O_{cis}–N–O_{trans}, 128.2(1)°) are much better resolved when compared with the previous structure obtained for the pure acid (N–O_H, 1.41(2) Å; N–O_{cis} = N–O_{trans}, 1.22(2) Å; O_{cis}–N–O_{trans}, 130(5)°),[153] though they do not differ significantly to within ±3σ.

4.2.3.3. $XeF_2 \cdot N_2O_4$

The XeF_2 moiety of the $XeF_2 \cdot N_2O_4$ adduct (Figure 4.4) is constrained by crystal symmetry to $D_{\infty h}$ symmetry, and possesses an Xe–F bond length of 1.985(3) Å, which does not differ significantly from the bond length determined for pure XeF_2 at –173 °C (1.999(4) Å).[154] Although the N_2O_4 molecules were found to have a local C_{2v} symmetry (N–O, 1.194(6) and 1.182(6) Å; N–N, 1.738(8) Å; O–N–O, 134.5(5)°), the N–O bond

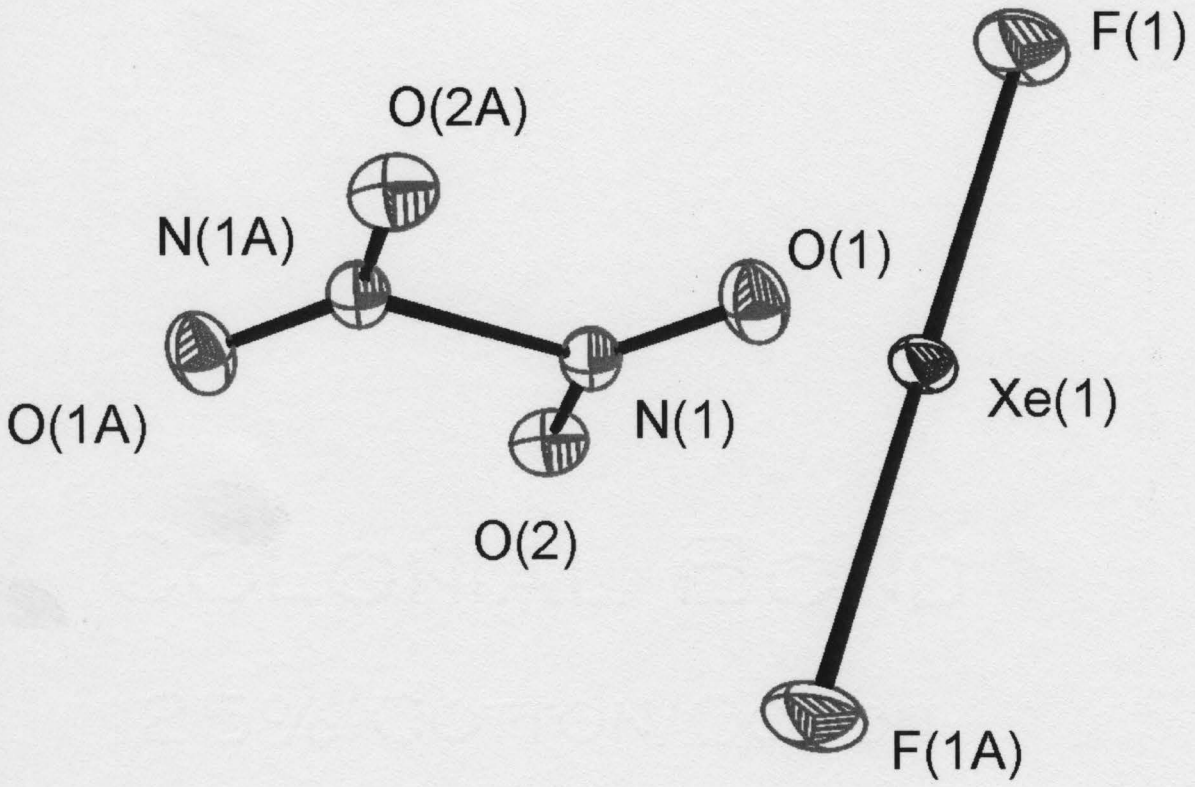

Figure 4.4. X-ray crystal structure of the $XeF_2 \cdot N_2O_4$ adduct; thermal ellipsoids are shown at the 50% probability level. Experimental and calculated geometric parameters are provided in Table 4.3.

lengths do not differ from each other by more than ±3σ, and thus may be regarded as having D_{2h} symmetry. The argument for D_{2h} symmetry (and thus a very weakly coordinated N_2O_4) is supported by the lack of band splittings in the Raman spectrum (see Section 4.2.4). The N_2O_4 geometric parameters do not differ significantly from those determined for the pure compound at 100 K (N–O, 1.1855(9) Å; N–N, 1.7560(14) Å; O–N–O, 134.46(12)°).[155]

Oxygen coordination at Xe comprises three coordination modalities; a bidentate interaction with two oxygens bound to different nitrogen atoms (3.435(4) Å and 3.516(4) Å), a bidentate interaction with two oxygens bound to the same nitrogen (3.440(4) Å and 4.180(4) Å), and an interaction with a single oxygen atom (3.490(4) Å) (Figure 4.5). While most of these long contacts differ significantly from the two calculated bidentate interactions in the gas phase, the bidentate interaction with each oxygen bound to different nitrogen atoms was found to be 22.3 kJ mol^{-1} more stable, in accord with the experimental findings. There are also two long contacts from xenon to two other fluorine atoms from different XeF_2 units (3.370(3) Å) that fall within the sum of the van der Waals radii. The absence of a significant distortion in the XeF_2 molecule is likely a result of the symmetric arrangement of long contacts around the xenon atom. Two long F···N contacts were also observed (2.720(4) and 2.834(5) Å) that are likely the result of electrostatic attractions (van der Waals radii, 3.02 Å).[26]

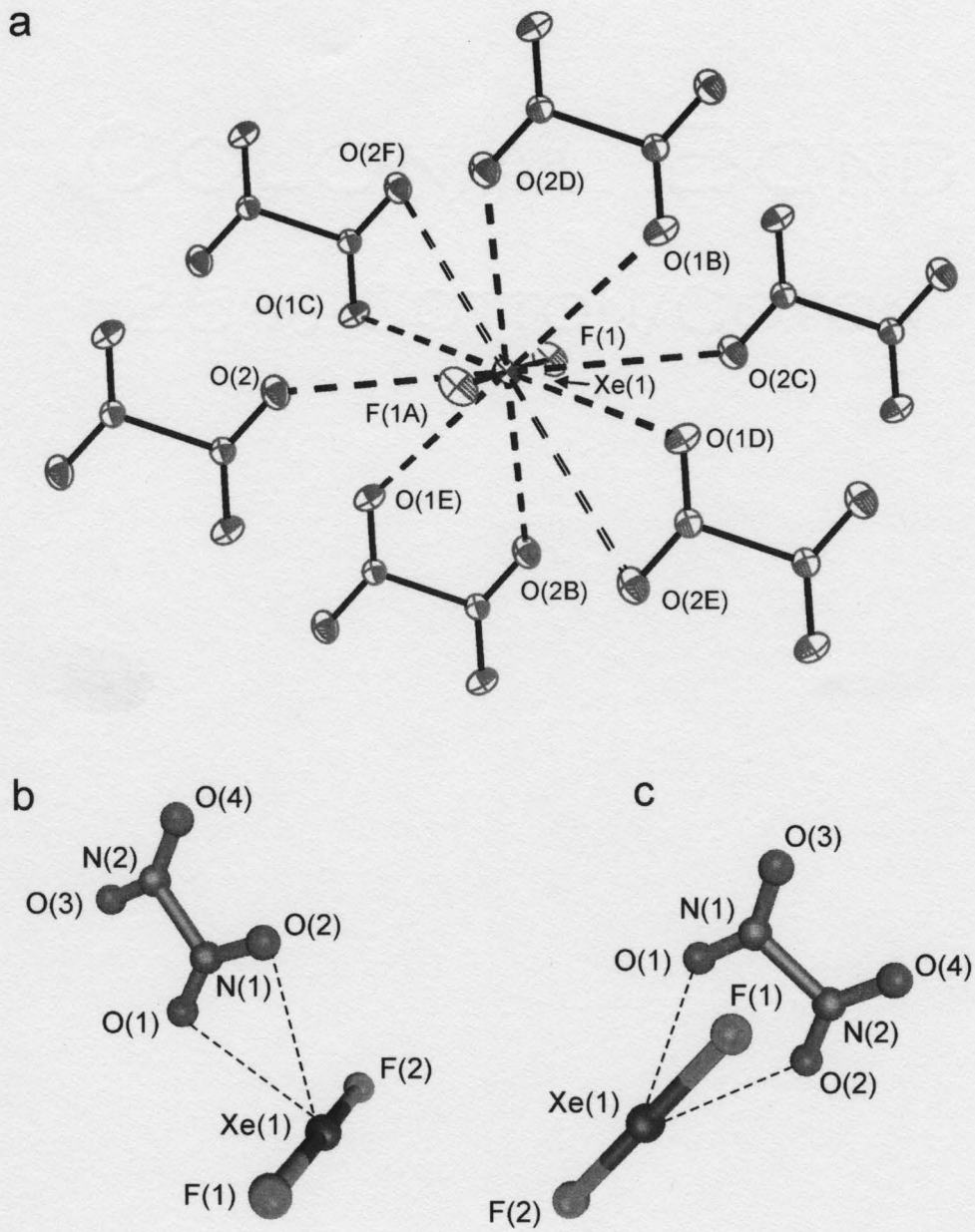

Figure 4.5. (a) Crystal structure of $XeF_2 \cdot N_2O_4$ showing the three coordination modalities that occur between the xenon atom and N_2O_4. The calculated geometry of N_2O_4 coordinated to the xenon atom of XeF_2 through two oxygens bound to (b) the same nitrogen atom and (c) two different nitrogen atoms.

4.2.4. Raman Spectroscopy

The low-temperature, solid-state Raman spectra of $FXeONO_2$, $XeF_2 \cdot HNO_3$, and $XeF_2 \cdot N_2O_4$ are shown in Figures 4.6 and 4.7, respectively. The experimental and calculated frequencies and their assignments are listed in Tables 4.5–4.7.

The spectral assignments for $FXe^{16/18}ONO_2$ and $FXeO^{14/15}NO_2$ were made by comparison with the calculated frequencies and Raman intensities (Table 4.5) of the energy-minimized geometries (Figure 4.1b). The assignments have also been compared with those of $FXeOSO_2F$,[28] which have been improved upon in this work with the aid of electronic structure calculations (Table 4.8). The assignments for the $XeF_2 \cdot HNO_3$ and $XeF_2 \cdot N_2O_4$ adducts were made by comparison with the calculated frequencies and Raman intensities (Tables 4.6 and 4.7) of the energy-minimized geometries (Figures 4.2 and 4.5) and, in the case of the XeF_2, HNO_3, and N_2O_4 modes, by comparison with those of free XeF_2, HNO_3 (Table 4.9), and N_2O_4 (Table 4.10) and other XeF_2 adducts such as $[Mg(XeF_2)_2](AsF_6)_2$.[50]

4.2.4.1. $FXeONO_2$

The $FXeONO_2$ molecule (C_s) possesses 12 fundamental vibrational modes belonging to the irreducible representations 9A′ + 3A″, all of which are Raman and infrared active. The four $FXeONO_2$ molecules have C_1 site symmetry in the crystallographic unit cell. The factor-group analysis for $FXeONO_2$ in the solid state (Table 4.11) predicts that each gas-phase Raman- and infrared-active mode of $FXeONO_2$

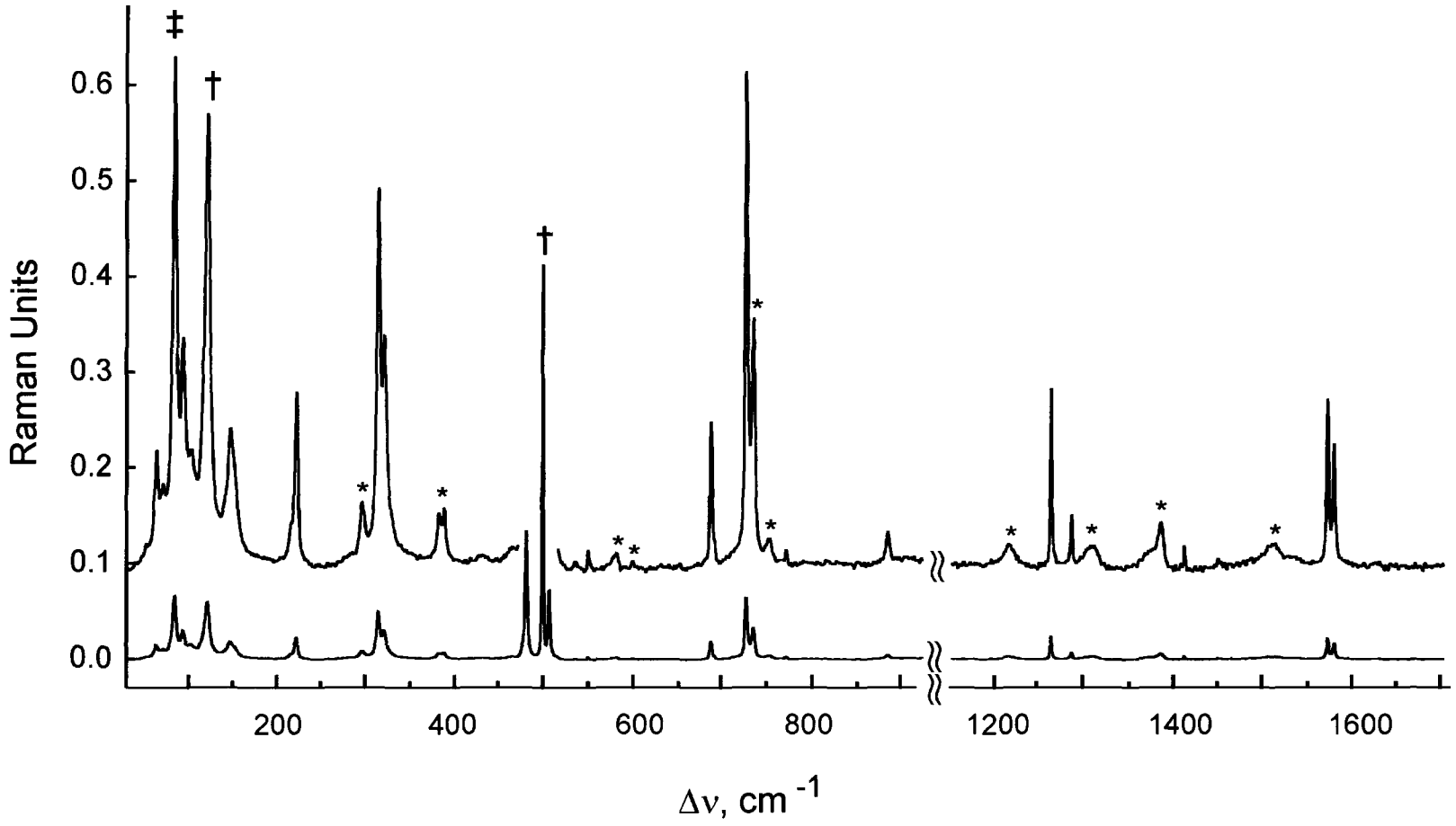

Figure 4.6. Raman spectrum of $FXeONO_2$ recorded at –160 °C using 1064-nm excitation. Symbols denote XeF_2 (†), FEP sample tube lines (*), and laser artifact (‡).

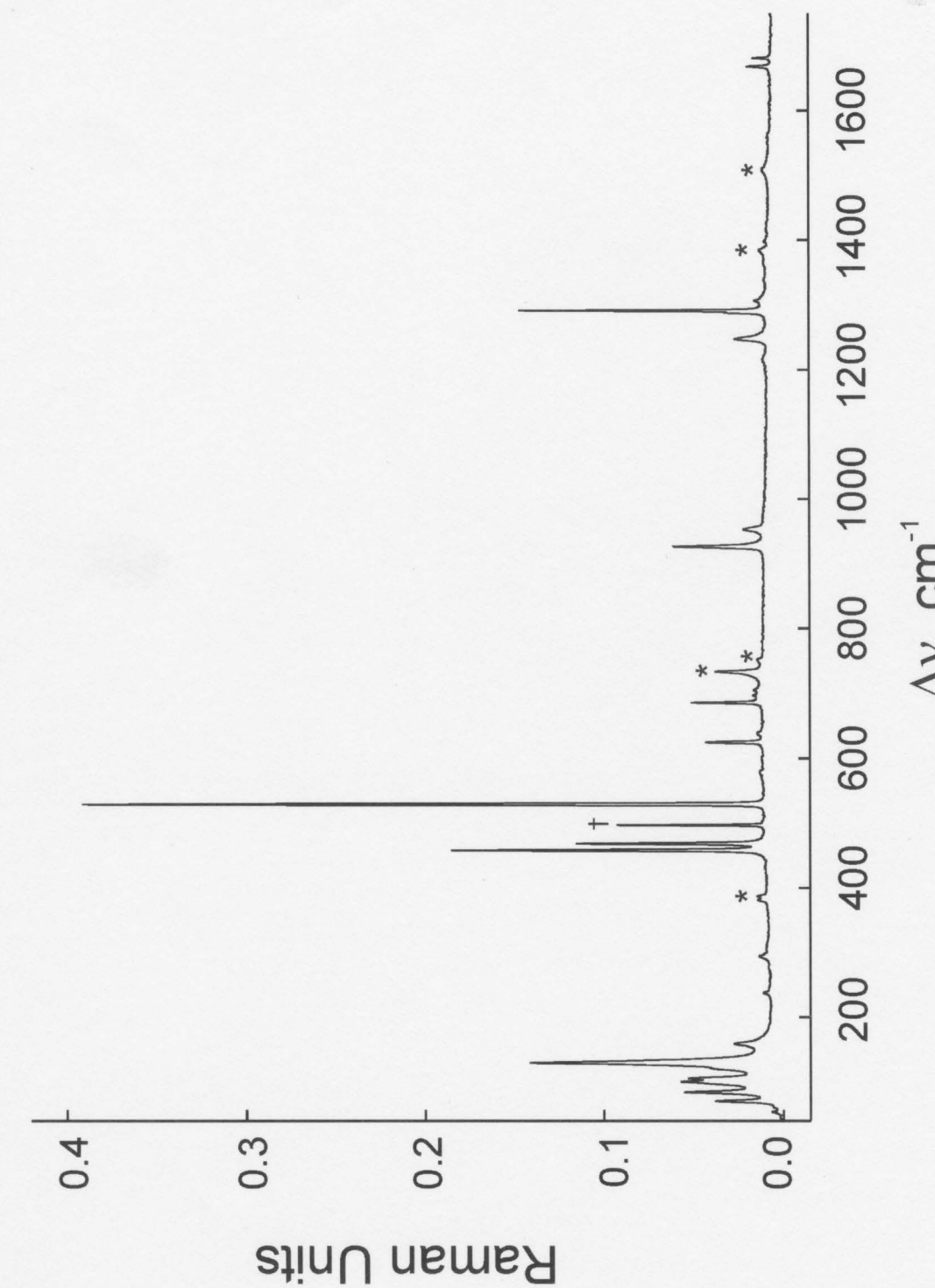
a
Raman Units
0.0
0.1
0.2
0.3
0.4
200
400
600
800
1000
1200
1400
1600
Δν, cm-1
*
†

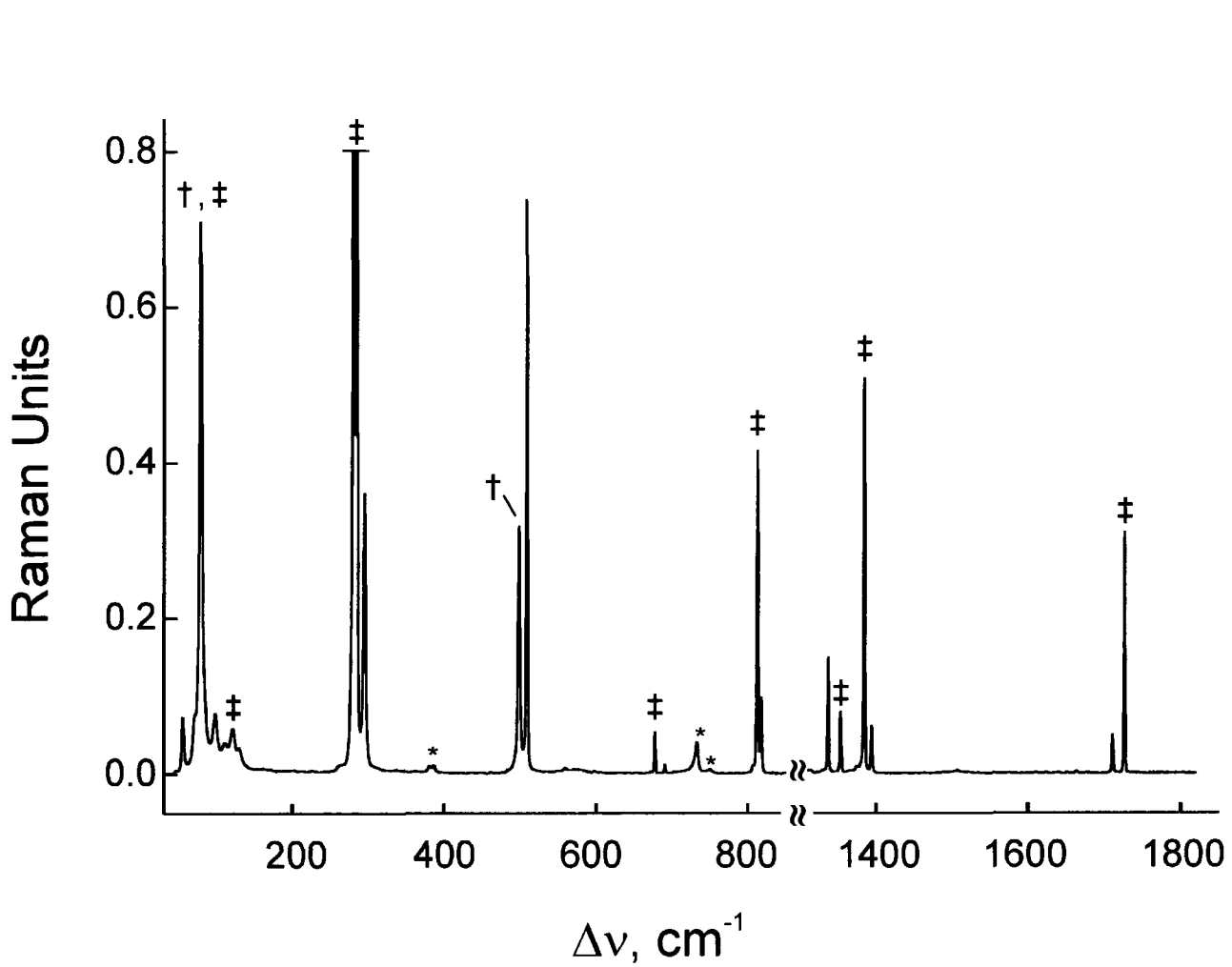

Figure 4.7. Raman spectra of the XeF_2 adducts: (a) The spectrum of solid $XeF_2 \cdot HNO_3$. (b) The spectrum of solid $XeF_2 \cdot N_2O_4$ under frozen N_2O_4 solution. The symbols denote XeF_2 (†), FEP (*), and N_2O_4 (‡) (Table 4.10).

Table 4.5. Experimental and Calculated[a] Raman Frequencies for $FXe^{16}O^{14}NO_2$, $FXe^{18}O^{14}NO_2$, and $FXe^{16}O^{15}NO_2$

frequencies, cm^{-1}						
$FXe^{16}O^{14}NO_2$		$FXe^{18}O^{14}NO_2$		$FXe^{16}O^{15}NO_2$		
exptl[b]	calcd	exptl[b]	calcd	exptl[b]	calcd	assignt (C_s)[c]
1578.8(12) 1571.7(16)	1717.7(92)	1569.8 sh 1562.5(5)	1717.6(92)	1543.2(<0.1) 1536.6(2)	1678.8(88)	$\nu_1(A')$, $\nu(NO-NO)$
1448.3(<1)		n.o.		n.o.		$2\nu_4$
1410.3(2)		1407.3(4)		n.o.		$\nu_4+\nu_5$
1285.5(5) 1262.1(17)	1322.4(28)	1278.4(<0.1) 1242.5(2)	1322.1(29)	1264.3(<0.1) 1246.7(8)	1307.7(27)	$\nu_2(A')$, $\nu(NO+NO)$
882.9(3)	873.1(10)	873.8(2)	866.7(8)	n.o.	860.2(10)	$\nu_3(A')$, $\nu(O_{Xe}-N)+\delta(NO_2)$
769.4(2)	781.7(<1)	n.o.	779.7(<1)	n.o.	761.4(<1)	$\nu_{10}(A'')$, $\rho_w(NO_3)$
725.5(49)	712.0(9)	719.5 sh 717.8(5)	689.4(7)	723.2(8)	710.5(9)	$\nu_4(A')$, $\delta(O_{Xe}-N-O)+\rho_r(NO_2)$
685.4(15)	654.9(42)	677.4(5) 663.7(3)	630.5(36)	690.3(100)[d] 683.5(61)	654.7(42)	$\nu_5(A')$, $\nu(O_{Xe}-N)-\delta(NO_2)$
503.8(54) 478.1(100)	517.7(36)	503.8(40) 477.7(100)	518.3(36)	503.6(14) 478.4(73)	518.4(36)	$\nu_6(A')$, $\nu(Xe-F)$
428.0 br		n.o.		n.o.		$2\nu_{11}$
318.9(23) 312.7(37)	320.7(26)	314.1 sh 307.9(24)	315.2(26)	317.9(4) 310.9(14)	320.1(25)	$\nu_7(A')$, $\nu(Xe-O)+\rho_r(NO_3)$
220.6(15)	203.5(<1)	219.3(14)	198.7(<1)	220.3(10)	203.9(<1)	$\nu_{11}(A'')$, $\rho_w(F-Xe-O)$
146.9(14)	192.0(9)	146.0(12)	191.7(9)	146.4(8)	192.0(9)	$\nu_8(A')$, $\delta(F-Xe-O)+\rho_r(NO_3)$
102.2(11) 93.6(16)	115.3(3)	92.1(8)	115.2(3)	n.o.	115.3(3)	$\nu_9(A')$, $\delta(F-Xe-O)-\rho_r(NO_3)$
64.3(11)	79.1(<1)	n.o.	78.7(<1)	n.o.	79.2(<1)	$\nu_{12}(A'')$, ρ_t about Xe–O bond

[a] SVWN/(SDB-)cc-pVTZ. Raman intensities (in $Å^4$ amu^{-1}) are given in parentheses. [b] Abbreviations denote shoulder (sh), broad (br), and not observed (n.o.). [c] The abbreviations denote stretch (ν), bend (δ), twist (ρ_t), wag (ρ_w), and rock (ρ_r). Bond elongations and angle openings are denoted by plus (+) signs and bond contractions and angle closings are denoted by minus (–) signs. [d] The band is coincident with the $\nu_1(A_{1g})$ band of AsF_6^-.

Table 4.6. Experimental and Calculated[a] Raman Frequencies for $XeF_2 \cdot HNO_3$

frequencies, cm^{-1}				
HNO_3		$XeF_2 \cdot HNO_3$		
exptl[b]	exptl[c,d]	exptl[d]	calcd	assgnt (C_s)[e]
	3097(<1)			
3490	2966(3)	3080 br	3036(186)	A′, ν(O–H)
	2899(<1)			
1697	1663(4)	1681(4), 1668(4)	1749(2)	A′, $\nu_{as}(NO_2)$ + δ(N–O–H)
	1549(2)			
	1424(8)	1301(4)		
1343	1366(9)	1291(35)	1414(6)	A′, δ(N–O–H)
	1338(9)	1289 sh		
1311	1247(100)	1247(6)	1334(68)	A′, $\nu_s(NO_2)$ – δ(N–O–H)
902	971(4), 953(58)	953(4)	961(5)	A′, ν(N–O_H) + δ(NO_2)
767	779(<1)	926(14)	847(<1)	A″, ρ_w(N–O–H)
	705(18)	706(<1)	799(<1)	A″, $\rho_w(NO_3)$
660	697(21)	698(<1), 686(11)	692(3)	A′, ν(N–O_H) – δ(NO_2)
597	638(13), 623(6)	638(1), 624(10)	640(6)	A′, δ(O–N–O_H) + $\rho_r(NO_2)$
		529(100)	559(20)	A′, ν(Xe–F_t) – small ν(Xe–F_H)
		496(24)[f]		
479	461 br			
		468(29), 458(47)	474(33)	A′, ν(Xe–F_H) + small ν(Xe–F_t)
		294(2)	284(1)	A′, δ(XeF_2)i.p. + $\rho_r(HNO_3)$
	167(18)	238(1)	192(<1)	A″, δ(XeF_2)o.o.p. + ρ_w(N–O–H)
	159(24)	159(5)	176(1)	A′, δ(XeF_2)i.p. – $\rho_r(HNO_3)$
	135 sh, 123(11)	130(32)	120(3)	strongly coupled deformations
	100(55)	106(11)	80(2)	
	90 sh	101(12)	77(1)	
	85 sh	70(2), 54(1)	29(<1)	

[a] SVWN/(SDB-)cc-pVTZ. Raman intensities (in $Å^4$ amu^{-1}) are given in parentheses. [b] Infrared spectrum of monomeric HNO_3 in a N_2 matrix, taken from ref 156. [c] Raman spectrum of solid HNO_3 recorded at –160 °C. [d] Abbreviations denote shoulder (sh) and broad (br). [e] The abbreviations denote stretch (ν), bend (δ), wag (ρ_w), rock (ρ_r), in-plane (i.p.), and out-of-plane (o.o.p). Bond elongations and angle openings are denoted by plus (+) signs and bond contractions and angle closings are denoted by minus (–) signs. The symbols F_H and F_t are used to differentiate the fluorine atom that is hydrogen bonded to HNO_3 and the terminal fluorine atom, respectively. [f] The band is coincident with the $\nu_1(\Sigma_g^+)$ band of free XeF_2.

Table 4.7. Experimental and Calculated[a] Raman Frequencies for $XeF_2 \cdot N_2O_4$

frequencies, cm^{-1}				
N_2O_4	$XeF_2 \cdot N_2O_4$			
exptl[b,c]	exptl[c]	calcd[d]	calcd[e]	assgnt (C_1)[f]
	n.o.	1870(1)	1780(2)	$\nu(NO_A) + \nu(NO_A') - (\nu(NO_B) + \nu(NO_B'))$
1726(21)	1711(6)	1839(8)	1736(9)	$\nu(NO_A) + \nu(NO_B') - (\nu(NO_B) + \nu(NO_A'))$
1385(36) 1375 sh	1394(7)	1456(42)	1403(14)	$\nu(NO_A) + \nu(NO_A') + \nu(NO_B) + \nu(NO_B')$
1337(10)	1354(14)			$2\nu_4$
	n.o.	1328(<1)	1273(<1)	$\nu(NO_A) + \nu(NO_B) - (\nu(NO_A') + \nu(NO_B'))$
812(30)	817(16)	848(12)	847(17)	$\delta(NO_2) + \delta(NO_2')$
	n.o.	759(<1)	764(2)	$\delta(NO_2) - \delta(NO_2')$
678(4)	691(<1)	688(<1)	711(<1)	$\rho_w(NO_2) - \rho_w(NO_2')$
	n.o.	557(6)	555(<1)	$\nu(XeF) - \nu(XeF)$
499(22)	509(100)	510(8)	508(26)	$\rho_r(NO_2) - \rho_r(NO_2')$
	497(41)[g]	503(19)	504(8)	$\nu(XeF) + \nu(XeF)$
	n.o.	443(2)	472(<1)	$\rho_w(NO_2) + \rho_w(NO_2')$
285(100) 281(63)	296(58)	312(21)	302(64)	$\nu(N–N)$
		238(1)	254(<1)	$\rho_r(NO_2) + \rho_r(NO_2')$ + small $\delta(XeF_2)$
	n.o.	223(<1)	201(<1)	$\rho_r(NO_2) + \rho_r(NO_2') -$ small $\delta(XeF_2)$
		206(<1)	200(<1)	$\rho_t(NO_2) - \rho_t(NO_2')$ + small $\delta(XeF_2)$
	n.o.	131(<1)	153(<1)	$\rho_t(NO_2) - \rho_t(NO_2')$
	121(70)[h]	121(6)	100(6)	$\delta(XeF_2) + \rho_r(N_2O_4)$
121(3)	98(10)	74(1)	86(<1)	$\rho_t(NO_2) - \rho_t(NO_2') + \rho_t(XeF_2)$
79(50)	71(7)	70(2)	61(<1)	$\rho_r(XeF_2) + \rho_r(N_2O_4)$
56(5)	64(7)	61(<1)	34(4)	$\rho_r(XeF_2) - \rho_r(N_2O_4)$
		38(<1)	–22(1)	$\rho_t(XeF_2) + \rho_t(N_2O_4)$

[a] SVWN/(SDB-)cc-pVTZ. Raman intensities (in $Å^4$ amu^{-1}) are given in parentheses. [b] Raman spectrum of solid N_2O_4 recorded at –160 °C. [c] Abbreviations denote shoulder (sh) and not observed (n.o.). [d] Values are taken from the computed structure c in Figure 4.5. [e] Values are taken from the computed structure b in Figure 4.5. [f] The abbreviations denote stretch (ν), bend (δ), wag (ρ_w), and rock (ρ_r). Bond elongations and angle openings are denoted by plus (+) signs and bond contractions and angle closings are denoted by minus (–) signs. [g] The mode is coincident with $\nu_1(\Sigma_g^+)$ of free XeF_2. [h] The mode is coincident with $\nu_3(\Pi_u)$ of free XeF_2.

Table 4.8. Experimental[a] and Calculated[b] Vibrational Frequencies for $FXeOSO_2F$

frequencies, cm^{-1}			
exptl (IR)	exptl (R)	calcd [c]	assignt (C_1)
1393(s)	1390(w)	1428(83)[155]	ν(S=O) – ν(S=O)
1210(vs)	1197(w)	1204(71)[182]	ν(S=O) + ν(S=O)
970(vs)	970(w)	881(49)[347]	ν(S–O)
798(s)	800(w)	779(6)[144]	ν(SF)
614(m)	616(mw)		
597(w)	584(mw)	587(15)[103]	ν(XeO) – ν(XeF)
540(s)	536(m)	543(16)[3]	ν(XeF) + δ(O–S=O)
	530(m)	520(59)[167]	ν(XeF) + δ(O=S=O)
518(vs)	521(m)	504(5)[17]	umbrella (SO_3)
	433(s)	411(15)[3]	δ(F–S=O) + ρ_t(O–S=O)
	395(mw)	366(2)[1]	ρ_t(F–S=O) + ρ_t(O–S=O)
	253(s) 243(m)	256(16)[17]	δ(O=S–O) + ν(XeO)
		171(3)[7]	δ(FXeO), i.p.
		165(1)[6]	δ(FXeO), o.o.p.
		94(3)[2]	δ(XeOS), i.p.
		43(<1)[1]	$\rho_r(SO_3F)$

[a] Taken from ref 28. [b] SVWN/cc-pVTZ. [c] Raman (in $Å^4$ amu^{-1}) and infrared intensities are given in parentheses and square brackets, respectively. [d] The abbreviations denote stretch (ν), bend (δ), rock (ρ_r), twist (ρ_t), in-plane (i.p.), and out-of-plane (o.o.p). Bond elongations and angle openings are denoted by plus (+) signs and bond contractions and angle closings are denoted by minus (–) signs.

Table 4.9. Experimental and Calculated[a] Raman Frequencies for HNO_3

frequencies, cm^{-1}				
IR[b]	Raman[c]	Raman[d]		
exptl	exptl	exptl[e]	calcd	assignt (C_s)[f]
		3097(<1)		
3490	3386(6)	2966(3)	3611(48)	$\nu_1(A')$, ν(OH)
		2899(<1)		
1697	1680(8)	1663(4)	1795(2)	$\nu_2(A')$, ν(NO) – ν(NO) + δ(NOH)
	1538(4)	1549(2)		$2\nu_8$
		1424(8)		
1343	1394(4)	1366(9)	1359(10)	$\nu_3(A')$, ν(NO) + ν(NO) + δ(NOH)
		1338(9)		
1311	1301(20)	1247(100)	1266(4)	$\nu_4(A')$, δ(NOH)
902	926(15)	971(4)	902(9)	$\nu_5(A')$, $\nu(NO_H)$ + δ(ONO)
		953(58)		
767		779(<1)	788(<1)	$\nu_8(A'')$, $\rho_w(NO_3)$
	675(10)	705(18)	654(7)	$\nu_6(A')$, $\nu(NO_H)$ – δ(ONO)
		697(21)		
660	607(8)	638(13)	577(2)	$\nu_7(A')$, $\delta(ONO_H)$
		623(6)		
597	480(1)	461 br	517(2)	$\nu_9(A'')$, ρ_w(NOH)
		167(18)		
		159(24)		
479		135 sh		lattice modes
		123(11)		
		100(55)		
		90 sh		
		85 sh		

[a] SVWN/cc-pVTZ. Raman intensities (in $Å^4$ amu^{-1}) are given in parentheses. [b] Infrared spectrum recorded on monomeric HNO_3 in a N_2 matrix, taken from ref 156. [c] Raman spectrum recorded on liquid HNO_3 at room temperature, taken from ref 157. [d] Recorded on the solid at −160 °C. [e] Abbreviations denote shoulder (sh) and broad (br). [f] The abbreviations denote stretch (ν), bend (δ), and wag (ρ_w). Bond elongations and angle openings are denoted by plus (+) signs and bond contractions and angle closings are denoted by minus (−) signs.

Table 4.10. Experimental and Calculated[a] Raman Frequencies for N_2O_4

frequencies, cm^{-1}				
exptl[b]	exptl[c]	exptl[d,e]	calcd	assignt (D_{2h})[f]
1780 1759 1750	n.o.	n.o.		($\nu_6 + \nu_{10}$)
1737	n.o.	n.o.	1875[580]	$\nu_9(B_{2u})$, $\nu_{as}(NO_2) + \nu_{as}(NO_2')$
n.o.	1727	1726(21)	1842(10)	$\nu_5(B_{3g})$, $\nu_{as}(NO_2) - \nu_{as}(NO_2')$
n.o.	1384 1377	1385(36) 1375 sh	1459(15)	$\nu_1(A_g)$, $\nu_s(NO_2) + \nu_s(NO_2')$
n.o.	1336 1330 sh	1337(10)		$2\nu_4$
1257 1240	n.o.	n.o.	1328[385]	$\nu_{10}(B_{1u})$, $\nu_s(NO_2) - \nu_s(NO_2')$
n.o.	811 804 sh	812(30)	848(14)	$\nu_2(A_g)$, $\delta(NO_2) + \delta(NO_2')$
761 742	n.o.	n.o.	757[219]	$\nu_8(B_{1u})$, $\delta(NO_2) - \delta(NO_2')$
n.o.	677	678(4)	693(<1)	$\nu_4(B_{2g})$, $\rho_w(NO_2) - \rho_w(NO_2')$
n.o.	496	499(22)	502(9)	$\nu_6(B_{3g})$, $\rho_r(NO_2) - \rho_r(NO_2')$
439	n.o.	n.o.	426[14]	$\nu_{12}(B_{3u})$, $\rho_w(NO_2) + \rho_w(NO_2')$
n.o.	283 279	285(100) 281(63)	307(27)	$\nu_3(A_g)$, ν(N–N)
265	n.o.	n.o.	218[<1]	$\nu_{11}(B_{2u})$, $\rho_r(NO_2) + \rho_r(NO_2')$
113	n.o.	n.o.	98[0]	$\nu_7(A_g)$, $\rho_t(NO_2) + \rho_t(NO_2')$
n.o.	180	n.o.		($\nu_{T1} + \nu_{T2}$)
n.o.	119	121(3)		
71	76	79(50)		lattice modes
n.o.	52	56(5)		

[a] SVWN/cc-pVTZ. Raman intensities (in $Å^4$ amu^{-1}) are given in parentheses. [b] Infrared spectrum recorded at –253.15 °C, taken from ref 158. [c] Raman spectrum recorded at –253.15 °C, taken from ref 158. [d] Raman spectrum recorded at –160 °C (this work). [e] Abbreviations denote shoulder (sh) and not observed (n.o.). [f] The abbreviations denote stretch (ν), bend (δ), wag (ρ_w), twist (ρ_t), and rock (ρ_r). Bond elongations and angle openings are denoted by plus (+) signs and bond contractions and angle closings are denoted by minus (–) signs.

Table 4.11. Factor-Group Analysis for $FXeONO_2$

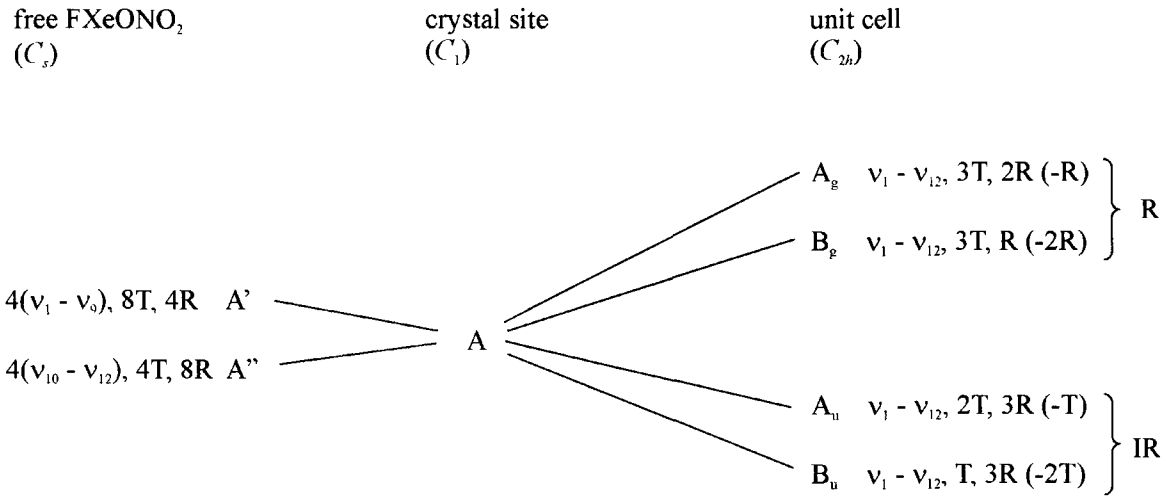

Table 4.12. Factor-Group Analysis for $XeF_2 \cdot HNO_3$

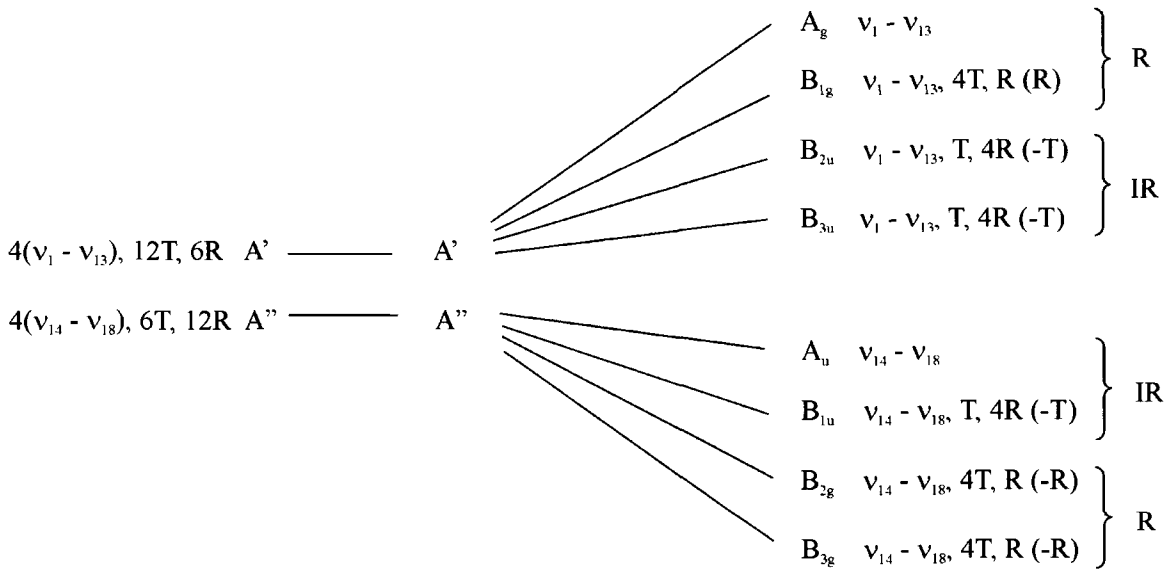

is split, as a result of vibrational mode coupling within the centrosymmetric unit cell (C_{2h} crystal symmetry), into a maximum of two Raman-active (A_g and B_g) and infrared-active (A_u and B_u) components. Two components were resolved for every stretching mode except $\nu(O_{Xe}–N) + \rho_r(NO_2)$.

Vibrational frequencies calculated at the SVWN level of theory reproduced all experimental frequency trends for $FXe^{16}O^{14}NO_2$, $FXe^{18}O^{14}NO_2$, and $FXe^{16}O^{15}NO_2$, although the $\nu(NO - NO)$ and $\nu(NO + NO)$ frequencies were predicted to be ca. 140 and 40 cm^{-1} higher, respectively. The isotopic shift trends were also accurately reproduced (Table 4.5).

The highest frequency modes at 1571.7, 1578.8 cm^{-1} and 1262.1, 1285.5 cm^{-1} are assigned to the $\nu(NO - NO)$ and $\nu(NO + NO)$ stretches, respectively, and display substantial low-frequency shifts (35.1, 35.6 and 15.4, 21.2 cm^{-1}, respectively) upon substitution of ^{15}N which are in good agreement with the calculated shifts (38.9 and 14.7 cm^{-1}). The $\delta(O_{Xe}–N–O) + \rho_r(NO_2)$ (725.5 cm^{-1}) and $\nu(O_{Xe}–N) - \delta(NO_2)$ (685.4 cm^{-1}) modes are most sensitive to ^{18}O substitution, and their bands are each split into two components in the $FXe^{18}ONO_2$ spectrum (719.5, 717.8 and 677.4, 663.8 cm^{-1}, respectively). The latter mode is in accord with that observed for $FXeOSO_2F$, $\nu(Xe–O) – \nu(Xe–F)$, which occurs at 584 cm^{-1}. The bands display isotopic shifts of 6.0, 7.7 and 8.0, 21.7 cm^{-1}, respectively, which differ from the calculated isotopic shifts (22.6 and 24.4 cm^{-1}). The $\nu(Xe–F)$ stretching mode occurs at 478.1, 503.8 cm^{-1} and was readily assigned because it is the most intense band in the spectrum and because the band was insensitive to both ^{15}N and ^{18}O substitution. Although a pure $\nu(Xe–F)$ stretch is not

observed for $FXeOSO_2F$, both the ν(Xe–F) + δ(O–S=O) and ν(Xe–F) + δ(O=S=O) modes observed at 536 and 531 cm^{-1}, respectively, are in accord with this assignment. Bands below 300 cm^{-1} were readily assigned with the aid of the computed vibrational frequencies and showed no or very small isotopic dependencies, as expected for low-frequency bending and rocking modes.

4.2.4.2. $XeF_2 \cdot HNO_3$

The vibrational modes of $XeF_2 \cdot HNO_3$ were assigned under C_s symmetry. A total of 18 fundamental vibrations are expected, all of which are Raman and infrared active. Many of the vibrations assigned to HNO_3 in $XeF_2 \cdot HNO_3$ are very close to those of monomeric, martix-isolated HNO_3 recorded at the same temperature[31] and those observed for liquid HNO_3 in previous study[157] (Table 4.6 and 4.9), with a few notable exceptions. There is overall good agreement between the observed and calculated frequencies (Table 4.6). The four $XeF_2 \cdot HNO_3$ molecular units occupy C_s sites in the crystallographic unit cell. The factor-group analysis for the adduct within its crystal lattice is provided in Table 4.12 and predicts that each gas-phase Raman- and infrared-active band of $XeF_2 \cdot HNO_3$ is split, as a result of vibrational-mode coupling within the crystallographic unit cell (D_{2h} crystal symmetry), into a maximum of four Raman-active (A_g, B_{1g}, B_{2g}, and B_{3g}) and four infrared-active (A_u, B_u, B_{2u}, and B_{3u}) components. Experimentally, however, three components are observed for the δ(N–O–H) band, while four other bands are split into two components (Table 4.6).

Adduct formation resulting from hydrogen bonding to one fluorine atom causes the $\nu_1(\Sigma_+)$ stretching band of free XeF_2 to split into $\nu(Xe–F_t)$ (529 cm^{-1}) and $\nu(Xe–F_H)$ (458, 468 cm^{-1}) components, because symmetry lowering destroys the inversion center at xenon. The magnitude of the splitting is similar to those observed in $[Mg(XeF_2)_2](AsF_6)_2$,[50] where the terminal and bridging Xe–F stretching modes were found to be 578 and 412 cm^{-1}, respectively.

The δ(N–O–H) frequency (1289, 1291, 1301 cm^{-1}) is, on average, 85 cm^{-1} lower than that observed for solid HNO_3 (1338, 1366, 1424 cm^{-1}) and 42–54 cm^{-1} lower than that observed for matrix-isolated HNO_3. Similarly, the ρ_w(N–O–H) frequency (926 cm^{-1}) is 147 cm^{-1} higher than that observed for solid HNO_3 (779 cm^{-1}) and 159 cm^{-1} higher than that observed for matrix-isolated HNO_3 (767 cm^{-1}). Both shifts are attributed to the hydrogen bonding interaction (see Section 4.2.3), which would lower the frequency for the bend occurring in the molecular plane, while increasing the frequency for the out-of-plane vibration. Similarly, the coupled $\delta(XeF_2)$o.o.p. + ρ_w(N–O–H) frequency observed at 238 cm^{-1} is 71 cm^{-1} higher than that observed for the ρ_w(N–O–H) in HNO_3 (167 cm^{-1}).

4.2.4.3. $XeF_2 \cdot N_2O_4$

The vibrational modes of $XeF_2 \cdot N_2O_4$ were assigned under C_1 symmetry. A total of 21 fundamental vibrations are expected, all of which are Raman and infrared active. There is overall good agreement between the observed and calculated frequencies (Table 4.7).

Unlike $XeF_2 \cdot HNO_3$, the XeF_2 portion of the Raman spectrum of $XeF_2 \cdot N_2O_4$ is not indicative of a strong molecular adduct (Table 4.7, also see Section 4.2.5). Only one $\nu(XeF_2)$ stretch is observed, which is only 13 cm^{-1} higher than $\nu_1(\Sigma_+)$ of free XeF_2 (498 cm^{-1}), indicating the interactions with N_2O_4 are weak and that $D_{\infty h}$ symmetry and the inversion center of XeF_2 are retained at the local symmetry level. Moreover, none of the modes assigned to the N_2O_4 molecule of the adduct are shifted significantly from that of free N_2O_4 [158] (Tables 4.7 and 4.10). The weak interaction between XeF_2 and N_2O_4 is confirmed by the absence of bands in the Raman spectrum of $XeF_2 \cdot N_2O_4$ that can be assigned to the formally Raman-inactive *ungerade* modes of free N_2O_4, indicating that N_2O_4 retains its D_{2h} symmetry and center of symmetry and in the solid state. In accord with the calculated C_1 symmetry of the adduct, the modes that are formally inactive under $D_{\infty h}$ (XeF_2) and D_{2h} (N_2O_4) have been calculated to possess weak Raman intensities (Table 4.7), but could not be observed in the experimental spectrum.

4.2.5. Computational Results

The electronic structures of $FXeONO_2$, $XeF_2 \cdot HNO_3$, and $XeF_2 \cdot N_2O_4$ were optimized at both the SVWN/(SDB-)cc-pVTZ and MP2/(SDB-)cc-pVTZ levels of theory and resulted in stationary points with all frequencies real (Table 4.5), except in the case of the bidentate interaction of two oxygen atoms bound to the same nitrogen atom of N_2O_4 in $XeF_2 \cdot N_2O_4$, where an imaginary frequency (–22 cm^{-1}, SVWN) was obtained.

4.2.5.1. Geometries

The MP2 (Table 4.13) and SVWN (Table 4.3) results were found to be similar for all calculated species; only the SVWN results are discussed because they provide the best agreement with the experimental vibrational frequencies (see Section 4.2.4), except in the case of $Xe(ONO_2)_2$, for which no structural data is available, where the results of both methods are discussed.

(i) $FXeONO_2$. The $FXeONO_2$ geometry optimized to C_s symmetry at both the SVWN and MP2 levels of theory (Figure 4.1). There is excellent agreement between the calculated (2.144 Å) and experimental (2.126(4) Å) Xe–O bond lengths, as well as for the Xe–F bond length (2.018 and 1.992(4) Å, respectively). The calculations also accurately reproduce the slight difference between the terminal N–O bonds, which were 1.197 Å for the N–O bond trans to xenon and 1.206 Å for the N–O bond cis to xenon (experimental, 1.199(6) and 1.224(6) Å, respectively). Similarly, all of the calculated angles were in good agreement with experimental values.

(ii) $Xe(ONO_2)_2$. Although $Xe(ONO_2)_2$ could not be synthesized in the present work, the structure was optimized at C_1 symmetry (Figure 4.8 and Table 4.14). The calculated (SVWN and MP2) geometric parameters for the mono- and bis-nitrate species are very similar, with the Xe–O bond length being slightly longer for $Xe(ONO_2)_2$ (2.178 Å) than for $FXeONO_2$ (2.144 Å). Both the cis- (C_s) and trans- (C_{2v}) isomers of $Xe(ONO_2)_2$ were

Table 4.13. Experimental and Calculated[a] Geometric Parameters for $FXeONO_2$, $XeF_2 \cdot HNO_3$, and $XeF_2 \cdot N_2O_4$

		$FXeONO_2$			
		bond lengths (Å)			
Xe(1)–F(1)	1.992(4)	[2.013]	N(1)–O(2)	1.199(6)	[1.205]
Xe(1)–O(1)	2.126(4)	[2.110]	N(1)–O(3)	1.224(6)	[1.213]
O(1)–N(1)	1.365(7)	[1.406]			
		bond angles (deg)			
F(1)–Xe(1)–O(1)	177.6(2)	[175.3]	O(1)–N(1)–O(3)	118.4(5)	[117.7]
Xe(1)–O(1)–N(1)	114.7(3)	[114.3]	O(2)–N(1)–O(3)	127.1(5)	[129.9]
O(1)–N(1)–O(2)	114.5(4)	[112.4]			
		contacts (Å)			
Xe(1)···F(1A)	3.420(4)		Xe(1)···F(1B)	3.299(4)	
Xe(1)···O(1A)	3.322(4)		Xe(1)···O(2B)	3.545(4)	
Xe(1)···O(2A)	3.478(4)		Xe(1)···O(3B)	3.570(5)	
Xe(1)···O(3A)	3.390(4)		Xe(1)···O(3C)	3.518(4)	
N(1)···F(1A)	2.780(6)		O(1)···F(1A)	2.935(5)	
O(2)···N(1A)	2.923(6)				
		$XeF_2 \cdot HNO_3$			
		bond lengths (Å)			
Xe(1)–F(1)	1.9737(8)	[1.976]	N(1)–O(2)	1.368(2)	[1.376]
Xe(1)–F(2)	2.0506(8)	[2.036]	N(1)–O(3)	1.216(2)	[1.220]
O(1)–N(1)	1.206(2)	[1.204]	O(2)–H(1)	0.83(2)	[0.986]
		bond angles (deg)			
F(1)–Xe(1)–F(2)	178.98(3)	[178.7]	O(2)–N(1)–O(3)	117.2(1)	[116.4]
O(1)–N(1)–O(2)	114.6(1)	[114.8]	N(1)–O(2)–H(1)	106(2)	[103.4]
O(1)–N(1)–O(3)	128.2(1)	[128.8]			
		contacts (Å)			
H(1)···F(2)	1.86(2)	[1.689]	Xe(1)···F(1B)	3.3050(4)	
Xe(1)···O(3)	3.317(1)	[3.304]	Xe(1)···F(1C)	3.3050(4)	
Xe(1)···F(1A)	3.4897(9)		Xe(1)···O(1B)	3.4156(6)	
Xe(1)···O(1A)	3.4156(6)		Xe(1)···O(1C)	3.456(1)	
Xe(1)···F(2A)	3.4859(8)		Xe(1)···O(2B)	3.5284(6)	
Xe(1)···O(2A)	3.5284(6)		O(2)···F(2)	2.690(1)	[2.674]

Table 4.13. (continued...)

		$XeF_2 \cdot N_2O_4$[b]			
		bond lengths (Å)			
Xe(1)–F(1)	1.985(3)	[1.989, 2.012]	N(1)–O(2)	1.182(6)	[1.196]
N(1)–O(1)	1.194(6)	[1.199]	N(1)–N(1A)	1.738(8)	[1.795]
		bond angles (deg)			
F(1)–Xe(1)–F(1A)	180.0	[179.5]	O(1)–N(1)–O(2)	134.5(5)	[135.0]
O(1)–N(1)–N(1A)	112.5(4)	[112.6]	O(2)–N(1)–N(1A)	113.0(4)	[112.4]
		contacts (Å)			
Xe(1)···F(1B)	3.370(3)		Xe(1)···F(1C)	3.370(3)	
Xe(1)···O(1B)	3.516(4)	[3.500]	Xe(1)···O(1C)	3.440(4)	
Xe(1)···O(1D)	3.440(4)		Xe(1)···O(1E)	3.516(4)	
Xe(1)···O(2)	3.490(4)		Xe(1)···O(2B)	3.435(4)	
Xe(1)···O(2C)	3.490(4)		Xe(1)···O(2D)	3.435(4)	
Xe(1)···O(2E)	4.180(4)		Xe(1)···O(2F)	4.180(4)	
F(1)···N(1B)	2.720(4)	[2.746]	F(1)···N(1C)	2.834(5)	

[a] MP2/(SDB-)cc-pVTZ. Calculated values are given in square brackets.
[b] Calculated geometric parameters for N_2O_4 coordinated to XeF_2 through two oxygens bound to two different nitrogen atoms.

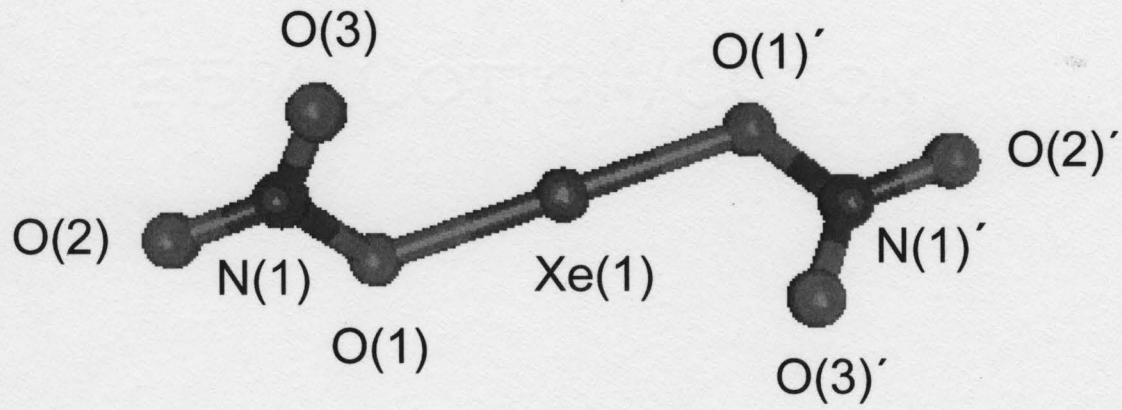

Figure 4.8. Calculated geometry for $Xe(ONO_2)_2$ (MP2/(SDB-)cc-pVTZ).

Table 4.14. Experimental and Calculated[a] Geometric Parameters for $Xe(ONO_2)_2$

	$Xe(ONO_2)_2$	
	bond lengths (Å)[b]	
	SVWN	MP2
Xe(1)–O(1)	2.178	2.144
O(1)–N(1)	1.377	1.407
N(1)–O(2)	1.198	1.205
N(1)–O(3)	1.206	1.213
	bond angles (deg)[b]	
	SVWN	MP2
O(1)′–Xe(1)–O(1)	175.5	174.1
Xe(1)–O(1)–N(1)	113.4	113.8
O(1)–N(1)–O(2)	112.1	112.3
O(1)–N(1)–O(3)	118.2	117.8
	dihedral angles (deg)	
	SVWN	MP2
N(1)–O(1)---O(1)′–N(1)′	107.6	100.6

[a] (SDB-)cc-pVTZ. [b] The bond lengths and angles follow the labeling scheme given in Figure 4.8.

utilized as starting geometries, but both geometries optimized to the lower energy C_1 geometry, with an N–O---O–N dihedral angle of 107.6° (MP2, 100.6°).

(iii) $XeF_2 \cdot HNO_3$. The experimental Xe–F_t and Xe–F_H bond lengths, 1.983 Å and 2.064 Å, respectively, as well as the remaining bond lengths and angles, were accurately reproduced by electronic structure calculations. The difference between the experimental and calculated Xe(1)···O(3) contact distance (3.317(1) and 3.034 Å, respectively) is attributed to weak contacts from neighboring XeF_2 and HNO_3 molecules within the crystal lattice, which are not taken into account by the calculations and seem to weaken these contacts. The O–H (1.046 Å) and H···F (1.520 Å) distances were found to differ significantly from the experimentally determined values of 0.83(2) and 1.86(2) Å, and are attributed to the uncertainty in the location of the hydrogen atom in the experimental electron density map (see Section 4.2.3). Although the experimental and calculated O–H and H···F distances differ significantly, the calculated O(2)···F(2) contact distance (2.566 Å) is very close to the experimental distance (2.690(1) Å).

(iv) $XeF_2 \cdot N_2O_4$. Unlike the symmetric arrangement of N_2O_4 molecules depicted in Figure 4.5a, both calculated adducts (Figures 4.5b and 4.5c) are asymmetric and do not accurately reproduce the bond lengths, angles, and contact distances of the experimental structure in all cases. However, both calculated structures show that the two bidentate interactions observed in the crystal structure correspond to a local minimum (Figure 4.5c) or close to a local minimum (Figure 4.5b). The vibrational frequencies of both calculated

structures were helpful in assigning the Raman spectrum (see Section 4.2.4). An attempt was made to calculate the structure depicted in Figure 4.5a from the crystal structure coordinates, but failed to optimize using either HF or DFT methods.

4.2.5.2. Natural Bond Orbital (NBO) Analyses

The NBO analyses were carried out for the MP2- and SVWN-optimized gas-phase geometries of $FXeONO_2$, $XeF_2{\cdot}HNO_3$, and $XeF_2{\cdot}N_2O_4$. The NBO results are given in Table 4.15. The MP2 and SVWN results are similar; only the MP2 results will be discussed here.

(i) $FXeONO_2$ and $Xe(ONO_2)_2$. As with the geometric parameters, the charges, valencies and bond orders were found to be very similar for $FXeONO_2$ and $Xe(ONO_2)_2$. The charge on Xe is higher for $FXeONO_2$ (1.13) than for $Xe(ONO_2)_2$ (1.04), indicative of the greater electron withdrawing ability of the fluorine when compared with that of the nitrate ligand.

(ii) $XeF_2{\cdot}HNO_3$ and $XeF_2{\cdot}N_2O_4$. The charges and valencies calculated for HNO_3 and N_2O_4 in their XeF_2 adducts are similar to those calculated for free HNO_3 and N_2O_4. In the case of $XeF_2{\cdot}HNO_3$, the H···F bond order (0.04) is approximately four times greater than the Xe···O bond order (0.01), with their small values being consistent with the weak interactions observed in the crystal structure. No significant bond orders (i.e. < 0.01)

Table 4.15. Natural Bond Orbital (NBO) Charges, Valencies and Bond Orders[a] for $FXeONO_2$, $Xe(ONO_2)_2$, $XeF_2 \cdot HNO_3$, and $XeF_2 \cdot N_2O_4$

	$FXeONO_2$				$Xe(ONO_2)_2$			
	charges		valencies		charges		valencies	
atom	MP2	SVWN	MP2	SVWN	MP2	SVWN	MP2	SVWN
Xe(1)	1.126	1.086	0.632	0.641	1.042	0.986	0.636	0.658
F(1)	–0.586	–0.566	0.280	0.281				
O(1)	–0.588	–0.539	0.938	0.962	–0.570	–0.519	0.912	0.943
N(1)	0.695	0.676	3.135	3.222	0.692	0.675	3.132	3.227
O(2)	–0.291	–0.288	1.052	1.082	–0.289	–0.283	1.059	1.076
O(3)	–0.355	–0.369	1.061	1.087	–0.355	–0.367	1.061	1.095

	bond orders			
bond	MP2	SVWN	MP2	SVWN
Xe(1)–O(1)	0.340	0.318	0.300	0.284
Xe(1)–F(1)	0.278	0.280		
O(1)–N(1)	0.740	0.785	0.742	0.796
N(1)–O(2)	1.202	1.220	1.200	1.215
N(1)–O(3)	1.194	1.212	1.194	1.212

	$XeF_2 \cdot HNO_3$				HNO_3			
	charges		valencies		charges		valencies	
atom	MP2	SVWN	MP2	SVWN	MP2	SVWN	MP2	SVWN
Xe(1)	1.218	1.187	0.639	0.728				
F(1)	–0.623	–0.592	0.325	0.374				
F(2)	–0.561	–0.541	0.339	0.384				
O(1)	–0.307	–0.305	1.044	1.085	–0.296	–0.300	1.050	1.075
O(2)	–0.524	–0.495	1.211	1.250	–0.534	–0.520	1.218	1.251
O(3)	–0.402	–0.429	1.057	1.081	–0.348	–0.352	1.064	1.080
N(1)	0.710	0.688	3.144	3.236	0.706	0.687	3.132	3.185
H(1)	0.488	0.487	0.654	0.727	0.472	0.486	0.655	0.695

	bond orders			
bond	MP2	SVWN	MP2	SVWN
Xe(1)–F(1)	0.338	0.373		
Xe(1)–F(2)	0.284	0.289		
N(1)–O(1)	1.200	1.235	1.193	1.224
N(1)–O(2)	0.765	0.813	0.715	0.741
N(1)–O(3)	1.170	1.171	1.211	1.209
O(2)–H(1)	0.591	0.591	0.643	0.657
H(1)···F(1)	0.046	0.106		
Xe(1)···O(3)	0.013	0.053		

Table 4.15. (continued...)

	$XeF_2 \cdot N_2O_4$[b]				N_2O_4			
	charges		valencies		charges		valencies	
atom	MP2	SVWN	MP2	SVWN	MP2	SVWN	MP2	SVWN
Xe(1)	1.197	1.174	0.696	0.763				
F(1)	–0.610	–0.594	0.351	0.368				
F(2)	–0.580	–0.561	0.345	0.363				
N(1)	0.485	0.507	2.683	2.791	0.471	0.491	2.660	2.751
N(2)	0.485	0.507	2.683	2.791				
O(1)	–0.262	–0.282	1.112	1.148	–0.235	–0.246	1.100	1.123
O(2)	–0.262	–0.282	1.112	1.148				
O(3)	–0.227	–0.234	1.105	1.134				
O(4)	–0.227	–0 234	1.105	1.134				

	bond orders			
bond	MP2	SVWN	MP2	SVWN
Xe(1)–F(1)	0.324	0.326		
Xe(1)–F(2)	0.350	0.362		
N(1)–O(1)	1.209	1.230	1.210	1.236
N(2)–O(2)	1.209	1.230		
N(1)–O(3)	1.217	1.248		
N(2)–O(4)	1.217	1.248		
N(1)–N(2)	0.357	0.402	0.348	0.392

[a] Both MP2 and SVWN calculations were performed using the (SDB-)cc-pVTZ basis sets. [b] The numbering scheme is taken from Figure 4.5c.

were calculated for the O···Xe interactions in $XeF_2 \cdot N_2O_4$, which agrees well with the crystallographic data (see Section 4.2.3).

4.2.5.3. Thermochemistry

The decomposition of $FXeONO_2$, and failures to observe $Xe(ONO_2)_2$ and the $XeONO_2^+$ cation, prompted an examination of the thermochemistry for these systems. The enthalpies (ΔH°) and free energies (ΔG°) of decomposition for $FXeONO_2$, $Xe(ONO_2)_2$, and $XeONO_2^+$ were obtained at the MP2/(SDB-)cc-pVTZ level of theory, and are summarized in Scheme 4.1. The decomposition pathway for $FXeONO_2$ that leads

	ΔH°	$\Delta H_{195.15}$	ΔG°	$\Delta G_{195.15}$
$2FXeONO_2 \longrightarrow XeF_2 + N_2O_6 + Xe$	–137.1	–162.8	–163.2	–179.5
$N_2O_6 \longrightarrow N_2O_5 + \frac{1}{2}O_2$	–24.0	–24.0	–50.8	–41.5
$2FXeONO_2 \longrightarrow XeF_2 + N_2O_5 + Xe + \frac{1}{2}O_2$	–161.1	–186.8	–214.0	–221.0
$FXeONO_2 \longrightarrow FXeNO_2 + \frac{1}{2}O_2$	44.5	41.2	16.3	23.4
$2FXeNO_2 \longrightarrow XeF_2 + Xe + N_2O_4$	–275.6	–284.1	–292.6	–293.5
$Xe(ONO_2)_2 \longrightarrow Xe + N_2O_6$	–160.5	–160.6	–187.9	–178.4
$Xe(ONO_2)_2 \longrightarrow Xe + N_2O_5 + \frac{1}{2}O_2$	–184.5	–184.6	–238.7	–219.9
$FXeONO_2 + AsF_5 \longrightarrow XeONO_2^+ + AsF_6^-$	379.3	366.5	386.3	371.2
$XeONO_2^+ \longrightarrow Xe + \frac{1}{2}O_2 + NO_2^+$	–175.5	–175.8	–222.3	–206.1

Scheme 4.1. Gas-phase values of ΔH° and ΔG° (298.15 K) and ΔH and ΔG (195.15 K) for the decomposition reactions of $FXeONO_2$, $Xe(ONO_2)_2$, and the $XeONO_2^+$ cation (MP2/cc-pVTZ).

to XeF_2, N_2O_6, and Xe (eq 4.3 and 4.4) was found to be spontaneous under both standard conditions and at –78 °C, with a ΔG^o value of –81.6 kJ mol^{-1} ($\Delta G_{195.15}$, –89.8 kJ mol^{-1}, for one mole of $FXeONO_2$), with a release of –25.4 kJ mol^{-1} ($\Delta G_{195.15}$, –20.8 kJ mol^{-1}) for the further decomposition of a half a mole of N_2O_6 to N_2O_5 and O_2 (overall ΔG^o, –107.0 kJ mol^{-1}; overall $\Delta G_{195.15}$, –110.6 kJ mol^{-1}, for one mole of $FXeONO_2$). The remaining pathway (eq 4.5 and 4.6) involves the non-spontaneous generation $FXeNO_2$ (ΔG^o, 16.3 kJ mol^{-1}; $\Delta G_{195.15}$, 23.4 kJ mol^{-1}), which is compensated for by the spontaneous decomposition of $FXeNO_2$ to XeF_2, Xe, and N_2O_4 (ΔG^o, –146.3 kJ mol^{-1} of $FXeNO_2$; $\Delta G_{195.15}$, –146.8 kJ mol^{-1} of $FXeNO_2$).

Failure to observe $Xe(ONO_2)_2$ can be accounted for by the large negative ΔG^o that corresponds to the spontaneous decomposition to N_2O_6 and Xe (eq 4.10; ΔG^o, –187.9 kJ mol^{-1}; $\Delta G_{195.15}$, –178.4 kJ mol^{-1}). The proposed N_2O_6 intermediate appears reasonable based on previous work involving N_2O_6,[144,145] and by analogy with the decomposition of $Xe(OSO_2F)_2$ to Xe and $S_2O_6F_2$.[28] Failure to observe the $XeONO_2^+$ cation can similarly be explained by the large negative ΔG^o for the spontaneous decomposition of the cation in the gas phase to Xe, O_2, and the NO_2^+ cation (eq 4.17; ΔG^o, –222.3 kJ mol^{-1}; $\Delta G_{195.15}$, –206.1 kJ mol^{-1}).

4.3. Conclusions

The synthesis and structural characterization of $FXeONO_2$ confirms the ability of the nitrate ligand to stabilize the +2 oxidation state of xenon. Attempts to repeat previous

work in which $FXeONO_2$ and $Xe(ONO_2)_2$ were reported to have been synthesized by reactions of HNO_3 with XeF_2 failed. In addition, attempts to react XeF_2 and $[XeF][AsF_6]$ with N_2O_5 also proved unfruitful. The present synthesis of $FXeONO_2$ from $[FXeOXeFXeF][AsF_6]$ and NO_2F is the only synthetic route to $FXeONO_2$ that is presently known. Raman and NMR spectroscopic studies, as well as an X-ray crystallographic study, demonstrate that $FXeONO_2$, like other compounds containing oxygen-bonded ligands, is strongly covalently bound to xenon, and was confirmed by gas-phase quantum mechanical calculations.

The X-ray crystallographic study and Raman spectroscopic study of the $XeF_2 \cdot HNO_3$ adduct provides the first example of a H-bonded adduct of XeF_2, while the study of the $XeF_2 \cdot N_2O_4$ adduct shows that N_2O_4 can interact, in a bidentate fashion, with the xenon center through two oxygens bound to two different nitrogen atoms, or through two oxygens bound to the same nitrogen atom. Computational studies have accurately reproduced the geometric parameters and vibrational frequencies of $FXeONO_2$, $XeF_2 \cdot HNO_3$, and $XeF_2 \cdot N_2O_4$, as well as those of the unknown $Xe(ONO_2)_2$ molecule. The calculated ΔH° and ΔG° values show that decompositions of $FXeONO_2$, $Xe(ONO_2)_2$, and the $XeONO_2^+$ cation are spontaneous for all reaction channels considered and support the experimental observations.

CHAPTER 5

SYNTHESIS, STRUCTURAL CHARACTERIZATION, AND COMPUTATIONAL STUDY OF THE STRONG OXIDANT SALT, $[XeOTeF_5][Sb(OTeF_5)_6]\cdot SO_2ClF$

5.1. Introduction

The relevant introductory material for this Chapter can be found in Sections 1.4 and 1.5. This work details the synthesis and structural characterization of the synthetically useful low-temperature oxidant, $[XeOTeF_5][Sb(OTeF_5)_6]\cdot SO_2ClF$, and provides an example of a noble-gas salt in which the noble-gas cation is not coordinated to its counter ion. Electronic structure calculations have been employed to assess bonding in the title compound, evaluate its oxidant properties, and to compare the relative Lewis acid strengths of the XeF^+ and $XeOTeF_5^+$ cations and the relative Lewis basicities of SO_2ClF and the MF_6^- (M = As, Sb) anions towards both cations.

5.2. Results and Discussion

5.2.1. Synthesis of $[XeOTeF_5][Sb(OTeF_5)_6]\cdot SO_2ClF$

The ability of $Xe(OTeF_5)_2$ to introduce two $OTeF_5$ groups oxidatively has been previously exploited in the syntheses of $[NR_4][Sb(OTeF_5)_6]$ salts (R = CH_3 or CH_3CH_2) from $[NR_4][Sb(OTeF_5)_4]$.[35] In the present work, a similar tack has been taken to produce a fully substituted $OTeF_5$ noble-gas salt, $[XeOTeF_5][Sb(OTeF_5)_6]$. The stoichiometric reaction of $Xe(OTeF_5)_2$ and $Sb(OTeF_5)_3$ (<1% molar excess of $Xe(OTeF_5)_2$) in SO_2ClF solvent at –20 °C (eq 5.1) yields bright yellow to yellow-orange solutions. Unlike its

$$2\ Xe(OTeF_5)_2 + Sb(OTeF_5)_3 \longrightarrow [XeOTeF_5][Sb(OTeF_5)_6] + Xe \qquad (5.1)$$

fluorine analogue, $[XeF][SbF_6]$, which is insoluble in SO_2ClF at room temperature, the solubility of $[XeOTeF_5][Sb(OTeF_5)_6]$ in SO_2ClF at –78 °C is high, exceeding 2 M. The solid salt was isolated as the pale yellow solvate, $[XeOTeF_5][Sb(OTeF_5)_6]\cdot SO_2ClF$, after pumping for several hours at –78 to 0 °C and is stable to pumping at 0 °C for at least 4–5 h. The solid decomposes above 10 °C after 4–6 h, in marked contrast with $[XeOTeF_5][AsF_6]$[71,72,75] and $[XeF][SbF_6]$,[10] which are stable at room temperature. Solutions of $[XeOTeF_5][Sb(OTeF_5)_6]$ in SO_2ClF show significant decomposition after 30 min to 1 h at –10 °C.

5.2.2. Solution Characterization of $[XeOTeF_5][Sb(OTeF_5)_6]$ by ^{17}O, ^{19}F, ^{125}Te, and ^{129}Xe NMR Spectroscopy

The ^{19}F, ^{121}Sb, ^{125}Te, and ^{129}Xe NMR spectra of $[XeOTeF_5][Sb(OTeF_5)_6]$ have been recorded at –50 °C in SO_2ClF; the corresponding chemical shifts and coupling constants are provided in Table 5.1. The ^{17}O NMR spectrum was recorded for an enriched $[^{17,18}O]$-$[XeOTeF_5][Sb(OTeF_5)_6]$ sample at –15 °C, which was prepared according to eq 5.1 by reaction of natural abundance $Sb(OTeF_5)_3$ with a stoichiometric amount of enriched $[^{17,18}O]$-$Xe(OTeF_5)_2$ (^{16}O, 35.4%; ^{17}O, 21.9%; ^{18}O, 42.7%).

The ^{19}F NMR spectrum of $[XeOTeF_5][Sb(OTeF_5)_6]$ (Figure 5.1) consists of an AX_4 pattern, assigned to the $XeOTeF_5^+$ cation, which is well-resolved at 11.744 T with

Table 5.1. The ^{19}F, ^{125}Te, ^{129}Xe, ^{17}O, and ^{121}Sb NMR Parameters for $[XeOTeF_5][Sb(OTeF_5)_6]$[a]

	chem shift (δ), ppm					coupling constant, Hz		
Species	^{19}F[b]	^{125}Te	^{129}Xe	^{17}O[c]	^{121}Sb	$^2J(^{19}F_A-^{19}F_X)$[b]	$^1J(^{19}F-^{125}Te)$[b]	$^1J(^{19}F-^{123}Te)$
$XeOTeF_5^+$	–51.7 (F_A) –40.3 (F_X)	579.9	–1459.5	133		175	3776 (F_A) 3810 (F_X)	
$Sb(OTeF_5)_6^-$	–42.4 ($F_A \approx F_B$)	548.4		107	–13		3553	2950

[a] All NMR spectra were recorded in SO_2ClF solvent at –50 °C except the ^{17}O spectrum, which was recorded at –15 °C. [b] The subscripts A and B/X, denote axial and equatorial fluorine atoms, respectively. [c] The ^{17}O NMR parameters for solvent SO_2ClF at natural abundance were also determined in the present study: doublet at $\delta(^{17}O)$, 227.0 ppm; $^2J(^{17}O-^{19}F)$, 27.9 Hz.

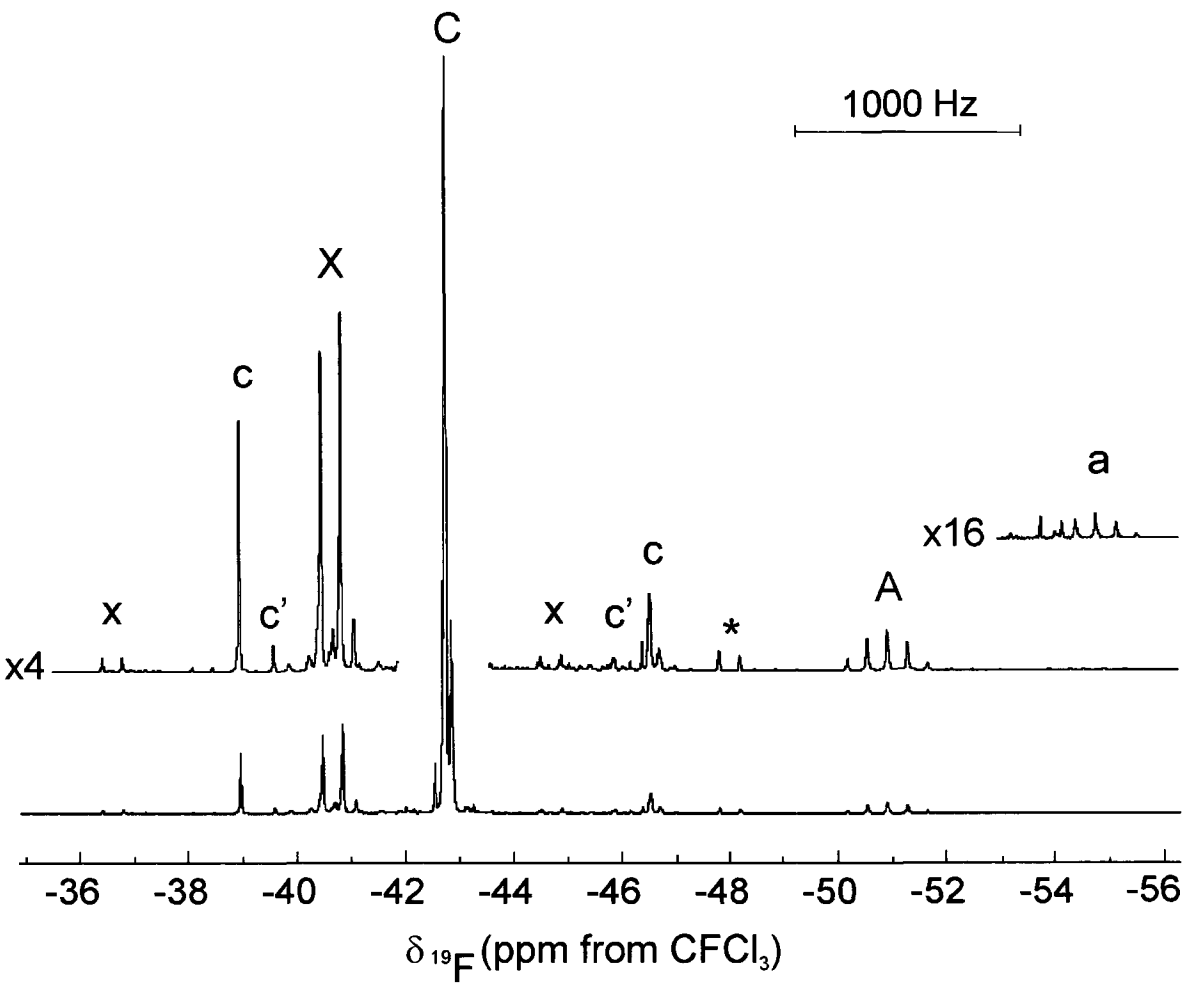

Figure 5.1. The ^{19}F NMR spectrum (470.571 MHz) of $[XeOTeF_5][Sb(OTeF_5)_6]\cdot SO_2ClF$ in SO_2ClF solvent at –80 °C, where the labels A and X denote the AX_4 spectrum of $XeOTeF_5^+$ and C denotes the A and B_4 parts of the severe AB_4 spectrum of $Sb(OTeF_5)_6^-$. Peaks denoted by a, x and c are ^{125}Te satellites that arise from $^1J(^{19}F–^{125}Te)$ and peaks denoted by c′ are ^{123}Te satellites that arise from $^1J(^{19}F–^{123}Te)$.

accompanying ^{123}Te (I = ½, 0.87%) and ^{125}Te (I = ½, 6.99%) satellites, and a second very severe AB_4 pattern, with ^{123}Te and ^{125}Te satellites, that is assigned to the $Sb(OTeF_5)_6^-$ anion. The AB_4 pattern of $Sb(OTeF_5)_6^-$ is severely higher order, even at a field strength of 11.744 T, as a result of the near equivalence of the equatorial and axial fluorine environments, appearing as a single, intense broad line and three weaker lines, which are similar in appearance to those previously reported for the anion at the same field strength.[35] Consequently, it is neither possible to provide a value for $^2J(^{19}F_A–^{19}F_B)$ nor to differentiate the chemical shifts of F_A and F_B, however, these parameters have been estimated in a previous publication.[15] The ^{19}F resonances of the anion are accompanied by ^{123}Te and ^{125}Te satellites having asymmetric line shapes that arise from the higher order AB_4 portion of the $AB_4\Omega$ (Ω = ^{123}Te or ^{125}Te) spin systems.[35]

The ^{125}Te NMR spectrum of $XeOTeF_5^+$ consisted of a well-resolved binomial doublet of quintets ($\delta(^{125}Te)$, 579.9 ppm) arising from $^1J(^{125}Te–^{19}F_A)$ (3776 Hz) and $^1J(^{125}Te–^{19}F_X)$ (3810 Hz). The doublet of quintets of the $Sb(OTeF_5)_6^-$ anion was more shielded (548.4 ppm) and was broadened, appearing as a sextet ($^1J(^{125}Te–^{19}F_{A,B})$, 3550 Hz). The line broadening is a consequence of quadrupolar relaxation by the antimony nuclides (^{121}Sb, I = $^5/_2$, 57.25%; ^{123}Sb, I = $^7/_2$, 42.75%) that results in near-complete collapse of the $^2J(^{125}Te–^{121,123}Sb)$ couplings.

The ^{129}Xe NMR spectrum consisted of a singlet at –1489.0 ppm ($\Delta\nu_{1/2}$ = 388 Hz) in the xenon(II) region of the spectrum. In contrast with the previously reported low-field (2.1139 T) NMR study of this cation in SbF_5 solvent at 25 °C ($\delta(^{129}Xe)$, –1472 ppm; $^3J(^{129}Xe–^{19}F_X)$, 18.5 Hz),[76] the $^3J(^{129}Xe–^{19}F_X)$ coupling was not resolved, which is likely

a consequence of the increased relaxation rate and line width that attends the higher field strength used to record the spectrum in the present study. The increased relaxation rate likely arises from shielding anisotropy, which is expected to be large in xenon(II) species,[159] and is proportional to the square of the applied field.[160]

The ^{121}Sb NMR spectrum consisted of a broad singlet at –13 ppm ($\Delta\nu_{1/2}$ = 1240 Hz), which is in good agreement with the previously reported chemical shift of the $Sb(OTeF_5)_6^-$ anion in CH_3CN solvent.[35] The large linewidth and inability to observe the $^2J(^{125}Te–^{121}Sb)$ coupling reported for this anion in CH_3CN is most likely a result of the higher viscosity of SO_2ClF and lower temperature used to record the spectrum, leading to a longer rotational correlation time and shorter relaxation time.[161]

The ^{17}O spectrum of $[^{17,18}O]$-$[XeOTeF_5][Sb(OTeF_5)_6]$ gave two broad, partially overlapping singlets. The most intense spectral feature was at 133.3 ppm ($\Delta\nu_{1/2}$ = 1350 Hz), which is assigned to the $Sb(OTeF_5)_6^-$ anion. The weaker resonance at 107.0 ppm ($\Delta\nu_{1/2}$ = 980 Hz) is assigned to the $XeOTeF_5^+$ cation. This resonance is shifted to low frequency with respect to those of $Xe(OTeF_5)_2$ (152.1 ppm) and $FXeOTeF_5$ (128.8 ppm) recorded in SO_2ClF solvent at –16 °C.[77] The low-frequency shift (shielding) upon $XeOTeF_5^+$ cation formation with respect to the parent molecules is analogous to that observed for XeF^+ and XeF_2.[14]

Although SO_2ClF is a very weak Lewis base and has been extensively used as a solvent medium for strong Lewis acid fluoride ion acceptors, ^{19}F NMR studies of MF_5 (M = As,[162] Sb[163]) in SO_2ClF and in SO_2F_2 have shown that, unlike SO_2F_2, SO_2ClF is sufficiently basic to form weak donor-acceptor adducts with strong Lewis acid

pentafluorides at low temperatures. Although Raman spectroscopy and single-crystal X-ray crystallography of the $[XeOTeF_5][Sb(OTeF_5)_6]\cdot SO_2ClF$ have shown that SO_2ClF solvent is coordinated through an oxygen atom to the xenon atom of the $XeOTeF_5^+$ cation (see Sections 5.2.3 and 5.2.4), the ^{19}F NMR spectrum provides no direct evidence for SO_2ClF. This is attributed to the lability of the Xe···O donor-acceptor bond in solution that results in rapid chemical exchange between the bulk SO_2ClF solvent molecules and coordinated SO_2ClF at temperatures as low as –80 °C.

5.2.3. X-ray Crystal Structure of $[XeOTeF_5][Sb(OTeF_5)_6]\cdot SO_2ClF$

A summary of the refinement results and other crystallographic information is provided in Table 5.2. Important bond lengths and bond angles are listed in Table 5.3 along with the calculated values. The structure consists of well-separated $XeOTeF_5^+$ cations and $Sb(OTeF_5)_6^-$ anions in which each $XeOTeF_5^+$ cation is oxygen-coordinated to an SO_2ClF molecule (Figure 5.2).

The structural parameters for the $Sb(OTeF_5)_6^-$ anion are in good agreement with those previously reported[35,79,80,164] and those calculated in this work (see Section 5.2.5 and Table 5.4) and therefore require no further comment.

The $XeOChF_5^+$ (Ch = Se, Te) cations have been characterized in the $[XeOChF_5][AsF_6]$ salts, where all bond lengths and bond angles of the $XeOChF_5^+$ cations were influenced by four-fold orientational disorders.[75] The $XeOChF_5^+$ cations were, however, shown to be strongly ion paired with their AsF_6^- anions by means of fluorine bridges between the cations and the anions, a structural feature that is also encountered in XeF^+ salts.[12,25,75,78] In contrast, the $XeOTeF_5^+$ cation in the current structure is neither

Table 5.2. Crystallographic Data for $[XeOTeF_5][Sb(OTeF_5)_6]\cdot SO_2ClF$

$[XeOTeF_5][Sb(OTeF_5)_6]\cdot SO_2ClF$	
chem formula	$O_9F_{36}SClSbTe_7Xe$
space group	$P\bar{1}$
a (Å)	9.7665(5)
b (Å)	9.9799(4)
c (Å)	18.5088(7)
α (deg)	89.293(2)
β (deg)	82.726(2)
γ (deg)	87.433(3)
V (Å^3)	1787.67(13)
molecules/unit cell	2
mol wt (g mol^{-1})	2041.76
calcd density (g cm^{-3})	3.793
T (°C)	–173
μ (mm^{-1})	7.656
R_1 [a]	0.0451
wR_2 [b]	0.0930

[a] R_1 is defined as $\Sigma||F_o|-|F_c||/\Sigma|F_o|$ for $I > 2\sigma(I)$. [b] wR_2 is defined as $[\Sigma[w(F_o^2 - F_c^2)^2]/\Sigma w(F_o^2)^2]^{1/2}$ for $I > 2\sigma(I)$.

Table 5.3. Experimental and Calculated[a] Geometrical Parameters for the $XeOTeF_5^+ \cdot SO_2ClF$ Adduct-Cation

bond lengths (Å)	exptl	calcd (C_1)	bond angles (deg)	exptl	calcd (C_1)
Xe(1)–O(7)	1.969(4)	1.998	Xe(1)–O(7)–Te(7)	120.8(2)	117.4
Te(7)–O(7)	1.938(5)	1.958	O(7)–Te(7)–F(33)	177.2(2)	179.7
Te(7)–F(33)	1.810(4)	1.826	O(7)–Te(7)–F(31)	86.6(2)	87.4
			O(7)–Te(7)–F(32)	91.4(2)	88.9
			O(7)–Te(7)–F(34)	89.5(2)	88.8
			O(7)–Te(7)–F(35)	88.6(2)	87.4
Te(7)–F(31)	1.813(4)	1.834	F(33)–Te(7)–F(31)	90.6(2)	92.3
Te(1)–F(32)	1.831(4)	1.854	F(33)–Te(7)–F(32)	91.3(2)	91.3
Te(7)–F(34)	1.829(4)	1.855	F(33)–Te(7)–F(34)	90.9(2)	91.3
Te(7)–F(35)	1.817(4)	1.834	F(33)–Te(7)–F(35)	91.0(2)	92.4
			F(31)–Te(7)–F(32)	177.8(2)	176.1
			F(31)–Te(1)–F(34)	90.1(2)	90.7
			F(31)–Te(7)–F(35)	90.3(2)	90.6
			F(32)–Te(7)–F(34)	89.0(2)	87.7
			F(32)–Te(7)–F(35)	90.6(2)	90.8
			F(34)–Te(7)–F(35)	178.1(2)	176.0
Xe(1)···O(8)	2.479(4)	2.388	O(7)–Xe(1)···O(8)	174.2(2)	175.2
S(1)–O(9)	1.437(5)	1.423	O(9)–S(1)–O(8)	115.7(2)	119.5
S(1)–O(8)	1.429(5)	1.476	O(9)–S(1)–F(36)	109.6(3)	109.8
S(1)–F(36)	1.474(5)	1.549	O(9)–S(1)–Cl(1)	108.2(4)	114.1
S(1)–Cl(1)	1.932(2)	1.958	O(8)–S(1)–F(36)	110.6(3)	104.5
			O(8)–S(1)–Cl(1)	108.4(2)	106.8
			Cl(1)–S(1)–F(36)	103.6(2)	100.0
			Xe(1)···O(8)–S(1)	139.6(3)	122.5

[a] SVWN/(SDB-)cc-pVTZ.

Table 5.4. Experimental and Calculated Geometrical Parameters for the $Sb(OTeF_5)_6^-$ Anion

				HF(S_6)	HF(S_6)	SVWN(S_6)
	bond lengths (Å)					
Sb(1)–O(1)	1.954(4)	Sb(2)–O(4)	1.966(4)			
Sb(1)–O(2)	1.965(4)	Sb(2)–O(5)	1.961(4)	1.880	1.943	1.976
Sb(1)–O(3)	1.940(4)	Sb(2)–O(6)	1.952(4)			
Te(1)–O(1)	1.846(4)	Te(4)–O(4)	1.847(4)			
Te(2)–O(2)	1.841(4)	Te(5)–O(5)	1.832(4)	1.801	1.829	1.866
Te(3)–O(3)	1.852(4)	Te(6)–O(6)	1.843(4)			
Te(1)–F_{ax}	1.834(4)	Te(4)–F_{ax}	1.845(4)			
Te(1)–F_{eq}	1.815(4)–1.837(4)	Te(4)–F_{eq}	1.817(4)–1.842(4)			
Te(2)–F_{ax}	1.830(4)	Te(5)–F_{ax}	1.847(4)	1.863	1.817	1.855
Te(2)–F_{eq}	1.827(4)–1.835(4)	Te(5)–F_{eq}	1.823(4)–1.833(4)	1.856–1.858	1.814–1.815	1.851–1.855
Te(3)–F_{ax}	1.825(4)	Te(6)–F_{ax}	1.825(4)			
Te(3)–F_{eq}	1.825(4)–1.836(4)	Te(6)–F_{eq}	1.825(4)–1.831(4)			
	bond angles (deg)					
Sb(1)–O(1)–Te(1)	139.7(2)	Sb(2)–O(4)–Te(4)	136.3(2)			
Sb(1)–O(2)–Te(2)	137.8(2)	Sb(2)–O(5)–Te(5)	140.9(2)	145.7	139.0	131.7
Sb(1)–O(3)–Te(3)	139.3(2)	Sb(2)–O(6)–Te(6)	137.6(3)			
O(1)–Te(1)–F_{ax}	176.7(2)	O(4)–Te(4)–F_{ax}	178.2(2)			
O(1)–Te(1)–F_{eq}	87.3(2)–95.2(2)	O(4)–Te(4)–F_{eq}	90.4(2)–95.6(2)			
O(2)–Te(2)–F_{ax}	177.4(2)	O(5)–Te(5)–F_{ax}	175.7(2)	178.7–179.5	179.6–180.0	176.7
O(2)–Te(2)–F_{eq}	89.5(2)–94.9(2)	O(5)–Te(5)–F_{eq}	90.0(2)–96.1(2)	91.3–93.7	90.4–94.4	89.2–95.1
O(3)–Te(3)–F_{ax}	179.0(2)	O(6)–Te(6)–F_{ax}	177.8(2)			
O(3)–Te(3)–F_{eq}	91.3(2)–93.8(2)	O(6)–Te(6)–F_{eq}	89.4(2)–94.6(2)			
F_{ax}–Te(1)–F_{eq}	87.3(2)–88.3(2)	F_{ax}–Te(4)–F_{eq}	86.0(2)–88.0(2)			
F_{ax}–Te(2)–F_{eq}	87.4(2)–88.0(2)	F_{ax}–Te(5)–F_{eq}	86.0(2)–87.8(2)	87.3–87.6	87.2–87.7	87.4–87.9
F_{ax}–Te(3)–F_{eq}	86.1(2)–88.4(2)	F_{ax}–Te(6)–F_{eq}	87.7(2)–88.4(2)			
F_{eq}–Te(1)–F_{eq}	175.6(2)–176.0(2)	F_{eq}–Te(4)–F_{eq}	173.5(2)–174.0(2)			
	87.3(2)–90.6(2)		89.0(2)–90.7(2)			
F_{eq}–Te(2)–F_{eq}	175.0(2)–175.5(2)	F_{eq}–Te(5)–F_{eq}	173.8(2)–173.9(2)			175.0–175.6
	89.4(2)–90.8(2)		89.0(2)–90.9(2)	89.0–91.6	89.7–90.2	89.4–90.3
F_{eq}–Te(3)–F_{eq}	174.9(2)–179.0(2)	F_{eq}–Te(6)–F_{eq}	176.0(2)–176.1(2)			
	88.9(2)–90.5(2)		89.6(2)–90.2(2)			

Table 5.4. (continued…)

[a] The symbols F_{eq} and F_{ax} denote equatorial and axial fluorine atoms, respectively. [b] Stuttgart. [c] (SDB-)cc-pVTZ.

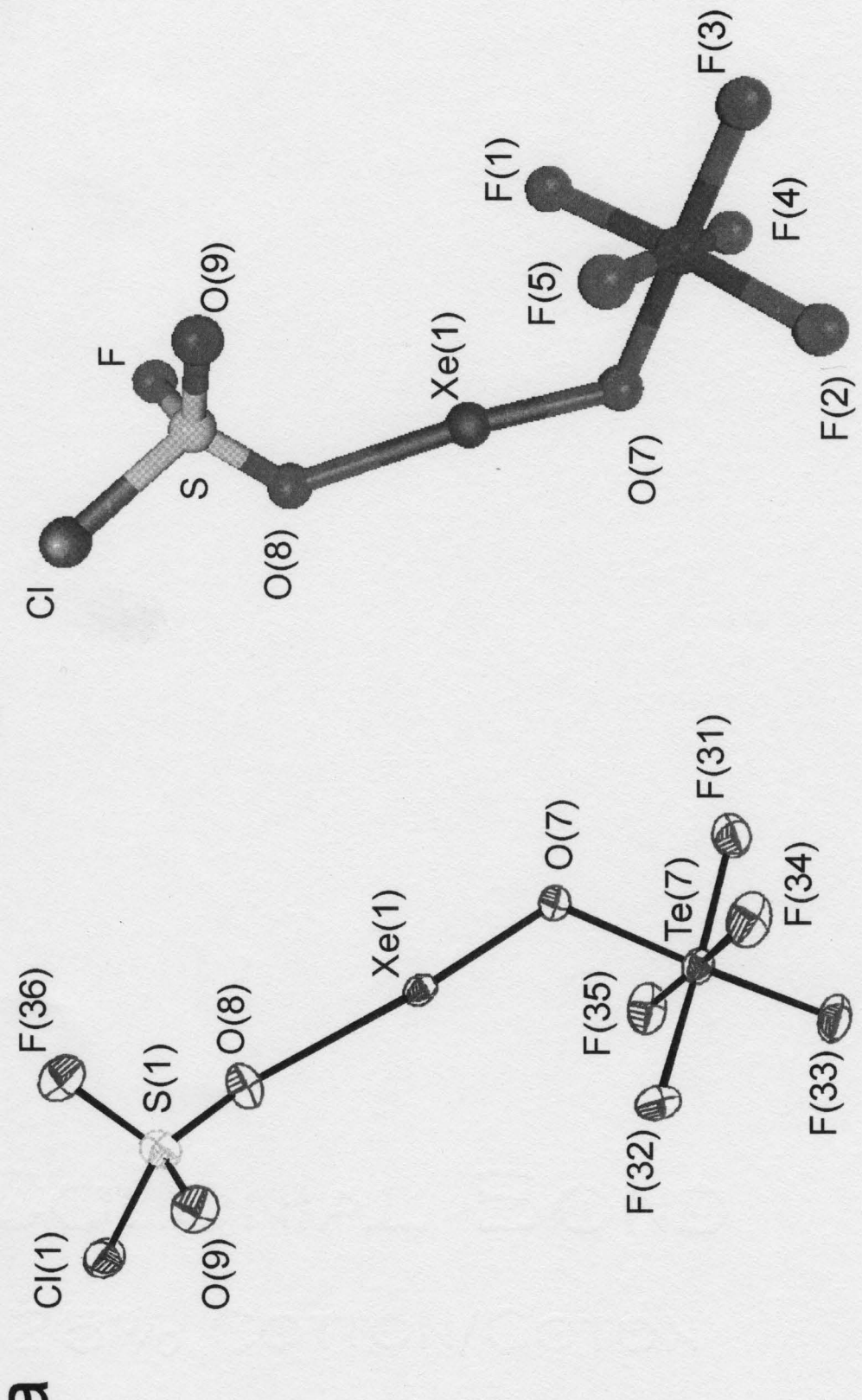
a
Cl(1)
O(9)
F(36)
S(1)
O(8)
Xe(1)
O(7)
Te(7)
F(31)
F(34)
F(35)
F(32)
F(33)
Cl
F
S
O(9)
O(8)
Xe(1)
O(7)
F(1)
F(5)
F(3)
F(4)
F(2)

Figure 5.2. X-ray crystal structure of (a) $XeOTeF_5^+ \cdot SO_2ClF$ and (b) $Sb(OTeF_5)_6^-$ in $[XeOTeF_5][Sb(OTeF_5)_6] \cdot SO_2ClF$; thermal ellipsoids are shown at the 50% probability level. Calculated geometries of the $XeOTeF_5^+ \cdot SO_2ClF$ adduct-cation and $Sb(OTeF_5)_6^-$ anion appear on the right-hand side.

coordinated to the anion nor disordered. Rather, the xenon atom of $XeOTeF_5^+$ is coordinated through an oxygen atom of the weak Lewis base solvent molecule, SO_2ClF, forming the adduct-cation, $XeOTeF_5^+ \cdot SO_2ClF$. The difference in solid state coordination behavior is attributed to the weakly coordinating nature of the $Sb(OTeF_5)_6^-$ anion relative to those of the AsF_6^-, SbF_6^-, $Sb_2F_{11}^-$ and related anions derived from strong Lewis acid pentafluorides (see Section 1.4; also see Section 5.2.5). The crystal structure of $[C(OTeF_5)_3][Sb(OTeF_5)_6] \cdot 3SO_2ClF$ has been reported, in which two of the three SO_2ClF solvent molecules in the formula unit are oxygen-coordinated to the carbon atom along the pseudo three-fold axis of the $C(OTeF_5)_3^+$ cation (see Chapter 6).[80] The only other published example of a crystal structure in which SO_2ClF forms an oxygen-coordinated adduct with a Lewis acid center is $Fe(OTeF_5)_3 \cdot 3SO_2ClF$.[165]

Any comparison of the geometric parameters determined for the present structure with those of $[XeOTeF_5][AsF_6]$ are compromised by disorder in the latter structure.[75] The absence of disorder in the present structure, however, allows valid comparisons to be made with the geometric parameters of $Xe(OTeF_5)_2$.[75] As anticipated, and by analogy with XeF^+ salt formation from XeF_2,[12] the Xe–O(7) distance (1.969(4) Å) is shorter than in neutral $Xe(OTeF_5)_2$ (2.119(11) Å) and is consistent with the calculated increases in bond orders for Xe–F and Xe–O (also see Section 5.2.5). The Te–O(7) bond distance (1.938(5) Å) in $XeOTeF_5^+$ is significantly longer than in $Xe(OTeF_5)_2$ (1.843(11) Å), which is consistent with the increased bond order and decreased bond length of the Xe–O(7) bond trans to it. The Te–F bond distances of the $XeOTeF_5^+$ cation (Table 5.3) are similar to those found in other $OTeF_5$ compounds.[35,79,80,164]

When compared with free SO_2ClF,[166] the S–Cl and S–F bond lengths of the adducted SO_2ClF molecule in the salt are shorter, whereas the lengths of both the coordinated and non-coordinated S–O bonds in the adduct-cation have increased and are equal within $\pm 3\sigma$. The S–O bond lengthenings and S–F and S–Cl bond contractions are corroborated by lower SO_2 and higher S–F/S–Cl vibrational stretching frequencies (Section 5.2.4).

Although the Xe···O(8) distance points to a significant covalent interaction between the xenon and oxygen atoms based on a comparison of the sum of the xenon and oxygen van der Waals radii (vide supra), the S–O bond lengths of coordinated SO_2ClF are only marginally longer than those of free SO_2ClF (vide infra). The latter observation is consistent with a very weak Xe···O donor-acceptor bond, but is at apparent odds with the short Xe···O(8) distance (2.471(5) Å). Comparison of the Xe···O(8) distance with the sums of the van der Waals radii of xenon and oxygen may not be valid because the distribution of the three equatorial valence electron lone pair domains of xenon that are associated with the AX_2E_3 VSEPR arrangement of the near-linear O(8)···Xe–O(7) moiety is not spherical, but toroidal in shape, allowing the incoming electron lone pair of the oxygen donor atom to approach more closely (see Section 5.2.5). Similar contacts have been noted in the structures of $[C(OTeF_5)_3][Sb(OTeF_5)_6]\cdot 3SO_2ClF$ (see Chapter 6) and $Fe(OTeF_5)_3\cdot 3SO_2ClF$,[165] where two and three SO_2ClF molecules, respectively, coordinate to the central atom. The S–O bonds of the coordinated SO_2ClF molecules are also equal, within $\pm 3\sigma$, to those of uncoordinated SO_2ClF, with the exception of one coordinated S–O bond in $Fe(OTeF_5)_3\cdot 3SO_2ClF$ that is elongated.

A number of weak inorganic oxygen bases such as COF_2,[167,168] SOF_2,[167] SO_2F_2,[167] SO_2,[167] $PO_2F_2^-$ [169] and POF_3[167] have been studied by vibrational spectroscopy and shown to form oxygen coordinated adducts with AsF_5 and SbF_5. The only other example of a weak inorganic oxygen base coordinated to a strong Lewis acid and that has been structurally characterized by X-ray crystallography is $SbF_5 \cdot SO_2$. In this instance, the terminal S–O bond (1.402(4) Å) is contracted and that of the coordinated oxygen is elongated (1.469(4) Å) relative to the S–O bond lengths of free SO_2 (1.434(1) Å).[170]

The Xe–O(7)–Te angle (120.8(2)°) is comparable to that reported previously for $Xe(OTeF_5)_2$ (122.3(5)°). The Xe···O(8) donor-acceptor bond distance (2.471(5) Å) is longer than the Xe–O(7) bond, but is significantly shorter than the sum of the xenon and oxygen van der Waals radii (3.68 Å)[26] and has been reproduced by electronic structure calculations (see Section 5.2.5). The O(7)–Xe···O(8) angle (174.2(2)°) deviates slightly from the anticipated linear AX_2E_3 VSEPR arrangement characteristic of Xe(II) compounds, and is similar to the O–Xe---F bridge angle observed in $[XeOTeF_5][AsF_6]$ (174(1) °).[75] The O(7)–Xe···O(8) and Xe–O(7)–Te angles are reproduced by the gas-phase, energy-minimized structure, but the experimental Xe···O(8)–S angle is larger than the calculated value (Table 5.3). The difference is likely a consequence of crystal packing, anion-cation interactions, and the weak covalent nature of the Xe···O(8) donor-acceptor bond. The angle deformation may, in part, stem from four interionic contacts that occur around xenon (range, 3.065(4) to 3.231(4) Å) which are shorter than the sum of xenon and fluorine van der Waals radii (3.63 Å).[26]

5.2.4. Raman Spectroscopy

5.2.4.1. $XeOTeF_5^+ \cdot SO_2ClF$

A series of low-temperature Raman spectra were recorded for several SO_2ClF:$[XeOTeF_5][Sb(OTeF_5)_6] \cdot SO_2ClF$ ratios at –160 °C (Table 5.5), and permitted assignments to be made of modes arising from coordinated and uncoordinated SO_2ClF based on changes in their relative intensities. The relative ratios of free SO_2ClF and coordinated SO_2ClF were determined by integration of the in-phase SO_2 stretching bands of coordinated and uncoordinated SO_2ClF in their Raman spectra. Changes in SO_2ClF composition did not result in significant relative intensity or frequency changes for the vibrational modes of either $XeOTeF_5^+$ or $Sb(OTeF_5)_6^-$. The final spectrum corresponding to $[XeOTeF_5][Sb(OTeF_5)_6] \cdot SO_2ClF$ is shown in Figure 5.3 and the frequencies of the vibrational bands, their intensities, and their origins are provided in Table 5.6.

The Raman assignments for the adduct-cation, $XeOTeF_5^+ \cdot SO_2ClF$, were made by comparison with the calculated frequencies, and were also guided by previous vibrational assignments for SO_2ClF[171] and $XeOTeF_5^+$,[71,72,75] and by more recent detailed assignments (Tables 5.7 and 5.8, respectively). Calculations of the vibrational frequencies were carried out using HF and DFT methods and using Stuttgart and (SDB-)cc-pVTZ basis sets, but only the DFT results are reported in Tables 5.6, 5.9, and 5.10. The experimental and calculated frequencies for SO_2ClF, $XeOTeF_5^+$, and $XeOTeF_5^+ \cdot SO_2ClF$ and the assignments for $XeOTeF_5^+ \cdot SO_2ClF$ are also provided in Table 5.6. Although the present assignments for SO_2ClF are in agreement with those previously reported for the neat liquid,[171] they are now more precisely described. The present assignments for

Table 5.5. Experimental[a] Raman Frequencies for $[XeOTeF_5][Sb(OTeF_5)_6]$ in SO_2ClF

composition[b]				
I[e]	II[d]	III	assgnt[c]	
1444(14), br	1444(5)			uncoordinated free SO_2ClF
1432(8)	1432(6)			
1226(34)	1226(17)			
1218(72)	1218(27)			
1214(79)				
839(17)	839(5)		A+u	
821(18)	821(7)		A+u	
629(34)	630(14)			
625(34)				
503(35)	504(11)			
478(37)	478(18)		C+u	
430(156)	430(22)			
423, sh	423(9)			
	313, sh			
309(62)	309(24)		A+u or C+u	
	298(15)		C+u	
296(45)	295(15)		C+u	
	1424(4)	1423(6)		coordinated SO_2ClF
	1415(6)	1415(14)		
	1178(4)	1177(10)		
1166(20)	1166(26)	1168(27)		
		1155(8)		
		1147(5)		
		860(4)		
		830(5)		
	510(6)	506(5)		
486, sh	486(10)	486(13)		
		476(15)		
	440, sh	442(14)		
436, sh	437(39)	436(8)	A+c	
	254(8)	254(20)		

Table 5.5. (continued...)

745(11)	745(11)	745, sh	C+A	$XeOTeF_5^+$
741(10)	741(13)	741(19)	C+A	
733(72)	734(49)	734(46)	C+A	
713(18)	716, sh	716(35)	C	
	712(23)	712(31)		
667(40)	667(45)	669(48)	C+A	
662(100)	662(100)	663(100)	C+A	
494(13)	494(15)	493(12)	C	
478(37)	478(18)	478, sh	C+u or C	
	319(11)	322(11)	C+A	
309(62)	309(24)	310(21)	A+u or C+u or u	
296(45)	298(15)			
	295(15)	294(14)	C+u or u	
249(14)	249(15)		C	
	187(4)		C	
173(11)	173(22)	172(24)	C	
	122(9)	121(10)	C+A	
839(17)	839(5)	841(3)	A+n or A	$Sb(OTeF_5)_6^-$
821(18)	821(7)	823(5)	A+n or A	
753, sh	753, sh	753(14)		
750(15)	750(17)	748(19)		
745(11)	745(11)	745, sh	C+A	
741(10)	741(13)	741(19)	C+A	
733(72)	734(49)	734(46)	C+A	
721(20)	722(17)	724(20)	A	
		709(27)	A	
704(76)	704(74)	703(52)	A	
		697(17)	A	
693(11)	693(15)	693(20)	A	
688(12)	688(13)	686(12)	A	
685(10)				
667(40)	667(45)	669(48)	C+A	
662(100)	662(100)	663(100)	C+A	
655(21)	655(19)	653, sh	A	
650(23)	650(20)			
646(25)	645(20)	644(22)	A	
436, sh	437(39)	436(8)	A+c	
415(24)	414(24)	411(27)		
370(9)	369(9)	369(10)	A	
367(8)				
	345, sh	344(10)	A	
337(11)	336(14)	338(16)	A	
332(14)	331(15)	332(16)	A	
	328(13)		C+A	
324(11)	326(12)	326, sh	C+A	
	319(11)	322(11)	C+A	
309(62)[d,e]	309(24)[d,e]	310(21)	C+A or C+u	
	303(19)	304(17)	A	
244(3)	244(10)	242(13)	A	
240(11)	240(13)			
	230(5)	229(6)	A	
147(11)	147(12)	145(10)	A	
139(9)	139(10)	140(14)	A	
134(7)	136(8)	134(9)	A	
		131(7)		
	122(9)	121(10)	C+A	
	117(9)		A	
112(8), br	113(9)	111(11), br	A	

Table 5.5. (continued...)

[a] Values in parentheses represent experimental relative Raman intensities. [b] Roman numerals refer to SO_2ClF:$[XeOTeF_5][Sb(OTeF_5)_6]\cdot SO_2ClF$ composition of 7.95:1.00 (I), 1.09:1.00 (II) and no excess SO_2ClF (III). [c] Bands were also observed at 1263(4) and 1407(11) cm^{-1} which are tentatively assigned to 2ν(630) of uncoordinated SO_2ClF and 2ν(704) of $Sb(OTeF_5)_6^-$. [d] A band was also observed at 1407(14) which is tentatively assigned to 2ν(704) of $Sb(OTeF_5)_6^-$. [e] The labels denote spectral line coincidences corresponding to the cation (C), the anion (A), coordinated SO_2ClF (c) and uncoordinated SO_2ClF (u).

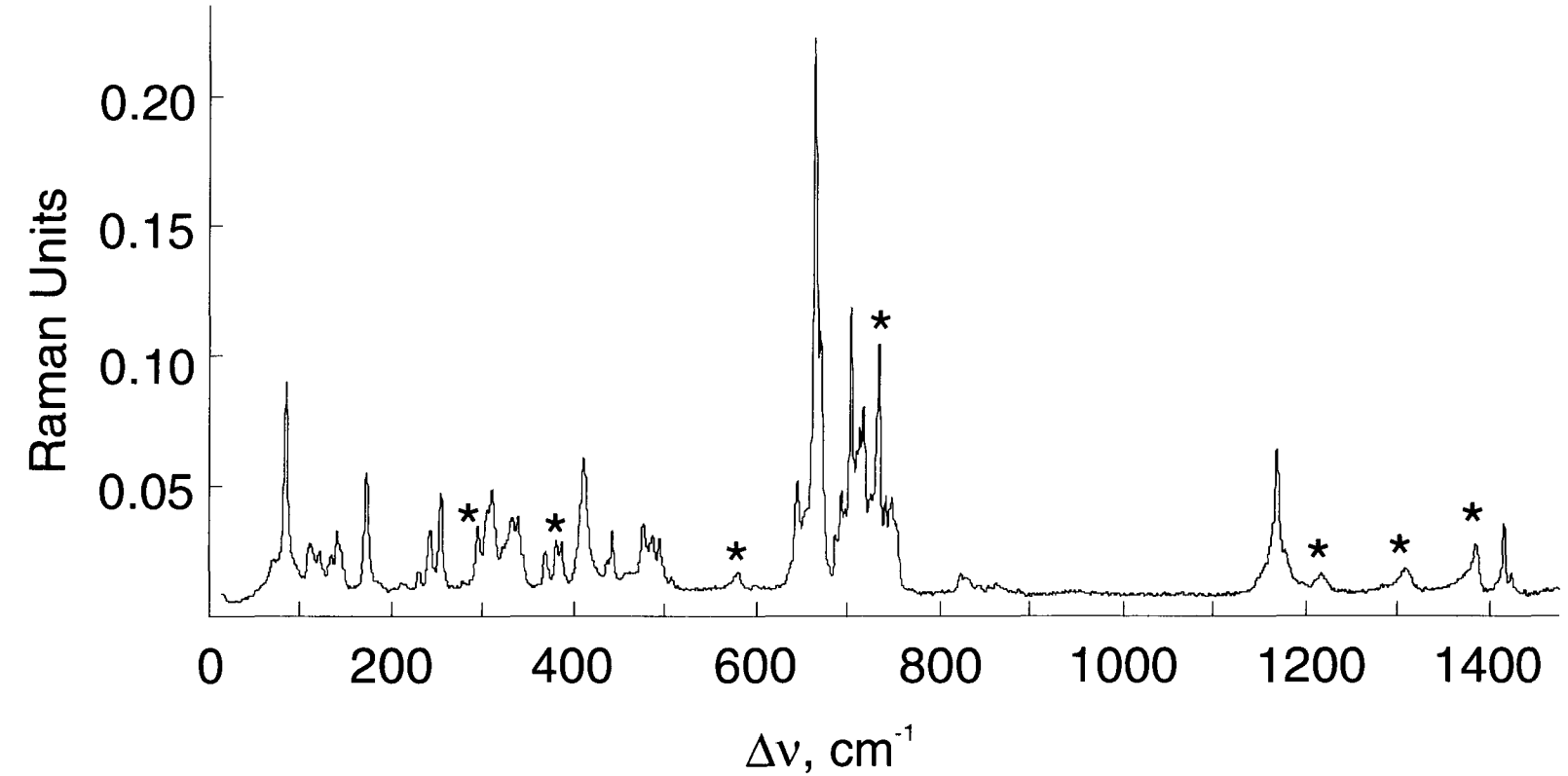

Figure 5.3. Raman spectrum of $[XeOTeF_5][Sb(OTeF_5)_6]\cdot SO_2ClF$ recorded at –160 °C using 1064-nm excitation; asterisks (*) denote FEP sample tube lines.

Table 5.6. Experimental and Calculated Vibrational Frequencies for SO_2ClF, $XeOTeF_5^+$, and $XeOTeF_5^+ \cdot SO_2ClF$

SO_2ClF			$XeOTeF_5^+$		$XeOTeF_5^+ \cdot SO_2ClF$		
calcd[a]	liquid[b]	solid[c]	calcd[a]	$Sb_2F_{11}^-$ salt[d]	calcd[a]	exptl[e]	assgnts (C_1)[f]
1453(183)	1450(5)	1441(6) 1437(4) 1431(18)			1389(172)	1423(6) 1415(14)	$\nu(SO_2)$ o o p
1214(141)	1217(51)	1215(18) 1208(28) 1205(31)			1100(734)	1177(10) 1168(27) 1155(8) 1147(5)	$\nu(SO_2)$ i.p
799(183)	820(10)	826(8) 819(30)			856(158)	860(4) 830(5)	ν(SF) + some $\nu(SO_2)$ i.p.
			746(83)	748(2)	735(75)	745, sh[g]	ν(TeF3–TeO7) + ν(TeF1–TeF2) + ν(TeF4–TeF5)
			740(82)	741(14)	730(180)	741(19)[g]	ν(TeF3–TeO7) + ν(TeF1–TeF2) + ν(TeF4–TeF5)
			739(89)		732(97)	734(49)[g]	ν(TeF1–TeF2) + ν(TeF5–TeF4)
			675(20)	714(23)	676(176)	716,sh 712(23)	ν(TeO7–XeO7) + $\nu(TeF_5)$
			659(5)	671(64)	650(8)	669(48)	ν(TeF1+TeF2) – ν(TeF4+TeF5)
			655(12)	661(31)	645(99)	663(100)	ν(XeO7–TeO7) + $\nu(TeF_{4e})$
597(199)	624(33)	612(61)			630(203)		ν(SCl) + $\delta(SFO_2)$
				487(41)	510(39)	506(5)	ν(XeO7+TeO7) – ν(XeO8) + δ(SO8FCl)
465(12)	502(7)	508(29)	478(30)	474, sh	483(13)	493(12)	ν(XeO7+TeO7) + ν(XeO8) – δ(SO8FCl) + some $\delta(SO_2)$
440(13)	476(6)	481(24)			453(14)	486(13) 478, sh 476(15)	$\rho_r(SO_2)$ + δ(OSF) + ν(XeO8)
393(<1)	425(100) 418(45)	431(100) 426(46)			414(6)	442(14)[h] 436(8)	ν(SCl) – $\delta(SFO_2)$
			305(90)	320(4) 311(10)	316(44)	322(11) 310(21)	ν(XeO8) – TeF_{4e} umbrella + some (δ(F4TeF1) – δ(F5TeF2)) + δ(SFCl) ± $\rho_t(SO_2)$ ± ρ_t(SFCl)
			293(22)	293(9)	304(93)	298(15)	ν(XeO8) + TeF_{4e} umbrella – some (δ(F4TeF1) – δ(F5TeF2)) + δ(SFCl) ± $\rho_t(SO_2)$ ± ρ_t(SFCl)
			290(35)		296(31) 296(31)	295(15)	δ(TeO7F3F4F5) umbrella + ρ_r(F2TeF1) δ(TeO7F3F2F1) umbrella + ρ_r(F4TeF5)
			290(7)	252(28)	286(1)	249(15)	δ(F4TeF2) + δ(F1TeF5)

Table 5.6. (continued...)

279(<1)	306(16)	313(25) 310(13)			275(<1)		δ(FSCl) ± $\rho_t(SO_2)$ ± ρ_t(SFCl) + some torsions
266(<1)	294(13)	295(11)	254(3)		272(3)	254(20)	(δ(F3TeF1) + δ(F3TeF5)) + (δ(O7TeF2) + δ(O7TeF4))
			234(2)	210(3)	234(9)		(δ(F3TeF2) + δ(F3TeF5)) – (δ(F3TeF4) + δ(F3TeF1))
			186(<1)	173(31)	193(<1)	187(4)	ρ_t(TeF1F3F4) + ρ_t(TeF5F2O7)
			157(1)		172(35)	173(22)	δ(FSCl) + ρ_w(FSCl) + ν(XeO8) + δ(XeO7Te) + δ(F4TeF1) i.p. + ρ_w(F2TeF5) + (δ(XeO7Te) i.p. + δ(O7TeF3) i.p.)
			138(<1)	125(4)	160(<1)	121(10)	δ(F3TeO7) + ρ_t(F4TeF1) + ρ_t(F2TeF5)
					132(4)		$\rho_r(SO_2)$ + ρ_w(SFCl) + ρ_r(TeF5F4F3) + ρ_w(F1TeF2) in the TeF_{4e} plane + ν(XeO8)
			88(1)		109(<1)		Strongly coupled deformation and torsion modes involving both $XeOTeF_5^+$ and SO_2ClF + lattice modes
					101(5)		
					59(1)		
			31(1)		49(<1)		
					20(0)		
					17(0)		
					–5(<1)		

[a] SVWN/(SDB-)cc-pVTZ; infrared intensities, in km mol^{-1}, are given in parentheses. [b] Values for liquid SO_2ClF (22 °C) [c] Values for solid SO_2ClF (–163 °C). [d] Values taken from ref 76. [e] Frequencies are from column III in Table 5.5. [f] The labelling scheme corresponds to that in Figure 5.2a (calculated, right hand side). Elongation of a bond(s) and angle opening(s) are denoted by plus (+) signs and bond contraction(s) and angle closing(s) are denoted by negative (–) signs. The abbreviations denote stretch (ν), bending (δ), twisting (ρ_t), wagging (ρ_w), rocking (ρ_r), in-plane bending (i.p.) and out-of-plane bending (o.o.p.) modes. The in-plane and out-of-plane motions of SO_2ClF are relative to the S,O(8),O(9)-plane in Figure 5.2a while the in-plane motions of the $XeOTeF_5^+$ group are relative to the Xe,O(7),Te,F(3)-plane in Figure 5.2a. [g] Both $XeOTeF_5^+$ and $Sb(OTeF_5)_6^-$ have a band that is coincident at this frequency. [h] The ν(SCl) mode of the $XeOTeF_5^+ \cdot SO_2ClF$ adduct-cation displays a $^{35}Cl/^{37}Cl$ isotope splitting (6.2 cm^{-1}), in close agreement with the previously published value of 7 cm^{-1} (ref 80) and the values obtained in the present study (liquid SO_2ClF, 7.0 cm^{-1}; solid at –143/–163 °C, 6.8/6.7 cm^{-1}).

Table 5.7. Experimental and Calculated Geometrical Parameters, Vibrational Frequencies (cm^{-1}) and Calculated Infrared Intensities for SO_2ClF

	exptl[a]	Stutt.			cc-pVTZ	
		HF(C_1)	HF(C_s)	SVWN(C_s)	HF(C_s)	SVWN(C_s)
bond lengths (Å)						
S–Cl	1.9638(8)	1.986	1.986	2.042	1.983	2.015
S–F	1.5383(13)	1.540	1.540	1.609	1.514	1.575
S–O	1.4083(10)	1.400, 1.401	1.401	1.450	1.392	1.428
bond angles (deg)						
Cl–S–F	98.70(6)	97.6	97.6	96.7	98.1	97.2
Cl–S–O	109.60(8)	109.3, 109.3	109.3	109.2	109.0	109.0
F–S–O	106.83(10)	106.9, 107.0	106.9	106.7	107.3	107.0
O–S–O	122.55(11)	123.6	123.5	124.7	123.1	124.3

exptl[b]	Stutt.[c]			cc-pVTZ[c]		assgnt (C_s)[d]
	HF(C_1)	HF(C_s)	SVWN(C_s)	HF(C_s)	SVWN(C_s)	
1450(5)	1551	1550	1391(170)	1600	1453(183)	ν(A"), $\nu_{as}(SO_2)$
1217(51)	1312	1312	1160(132)	1360	1214(141)	ν(A'), $\nu_s(SO_2)$
820(10)	916	917	766(178)	962	799(183)	ν(A'), ν(SF)
624(33)	696	697	576(178)	711	597(199)	ν(A'), ν(SCl) + $\delta(SO_2F)$
502(7)	540	541	439(10)	564	465(12)	ν(A'), $\delta(SO_2)$ + ν(SF) + $\rho_w(SO_2)$
476(6)	501	501	410(11)	529	440(13)	ν(A"), $\rho_r(SO_2)$ + δ(OSF)
425(100)	460	460	378(<1)	469	393(<1)	ν(A'), ν(SCl) – $\delta(SO_2F)$
418(45)						
306(16)	322	322	264(<1)	331	279(<1)	ν(A"), $\rho_t(SO_2)$ + ρ_t(FSCl)
294(13)	312	312	251(<1)	322	266(<1)	ν(A'), δ(FSCl) + $\rho_w(SO_2)$

Table 5.7. (continued...)

[a] Averaged bond lengths and bond angles are from ref 166. [b] Values are for liquid SO_2ClF (22 °C); values in parentheses are Raman intensities. [c] Values in parentheses are calculated infrared intensities in km mol^{-1}. [d] See Figure 5.2a for the atom numbering scheme. Elongation of a bond(s) and angle opening(s) are denoted by plus (+) signs and bond contraction(s) and angle closing(s) are denoted by negative (–) signs. The abbreviations denote stretch (ν), bending (δ), twisting (ρ_t), and wagging (ρ_w) modes.

Table 5.8. Calculated Geometrical Parameters and Experimental and Calculated Vibrational Frequencies and Calculated Infrared Intensities for the $XeOTeF_5^+$ Cation

	DZVP2[a]	Stutt.		(SDB-)cc-pVTZ	
	SVWN (C_1)	HF(C_1)	SVWN(C_1)	HF(C_1)	SVWN(C_1)
		bond lengths (Å)[b]			
Xe–O	1.893	1.911	1.967	1.899	1.830
Te–O	1.969	1.973	2.045	1.949	1.957
Te–F_a	1.776	1.786	1.843	1.763	1.818
Te–F_e	1.788	1.797	1.876	1.770	1.830
	1.801	1.811	1.857	1.785	1.848
	1.810	1.811	1.857	1.785	1.848
	1.788	1.797	1.876	1.770	1.830
		bond angles (deg)[b]			
Xe–O–Te	119.6	123.3	115.7	125.8	117.5
O–Te–F_a	178.4	180.1	179.5	179.8	179.1
O–Te–F_e	86.6	86.3	85.3	86.3	85.1
		87.3	87.3	87.6	87.8
		87.3	87.3	87.6	87.8
		86.3	85.3	86.4	85.1
F_a–Te–F_e	93.4	93.7	94.2	93.5	94.1
		92.7	93.2	92.6	93.1
		92.7	93.2	92.6	93.1
		93.7	94.2	93.5	94.1
F_e–Te–F_e	173.1	178.5	178.3	178.8	178.5
	89.8	90.3	90.6	90.3	90.6
		90.8	90.5	90.6	90.3
		87.9	87.3	88.2	87.7
		90.3	90.6	90.2	90.6
		178.4	178.3	178.7	178.5

Table 5.8. (continued...)

exptl[c]	Stutt.		cc-pVTZ		assgnt (C_1)[d]
	HF(C_1)	SVWN(Cs)	HF(C_1)	SVWN(C_1)	
748(2)	874	711(69)	872	746(83)	ν(TeF3–TeO7) + ν(TeF1–TeF2) + ν(TeF4–TeF5)
741(14)	871	706(75)	869	740(82)	ν(TeF3) + ν(TeF1–TeF2) + ν(TeF4–TeF5)
714(14)	855	705(790	863	739(89)	ν(TeF1–TeF2) + ν(TeF5–TeF4)
671(64)	813	646(26)	835	675(20)	ν(TeO7–XeO7) + some ν(TeF_5)
661(31)	769	636(7)	780	659(5)	ν(TeF1+TeF2) – ν(TeF4+TeF5)
	758	632(7)	760	655(12)	ν(XeO7–TeO7) + ν(TeF_{4e})
487(41) 474, sh	498	470(28)	491	478(30)	ν(XeO7+TeO7)
320(4)	343	282(83)	366	305(90)	δ(F4TeF1) – TeF_{4e} umbrella
311(10)	339	269(15)	363	293(22)	δ(F1TeF3) + δ(F4TeF3)
293(9)	334	264(12)	362	290(35)	(δ(F3TeF5) + δ(F3TeF1) + δ(O7TeF3)) – δ(F4TeF2)
	332	263(32)	359	290(7)	(δ(F3TeF2) + δ(F3TeF5)) + δ(F1TeF4)
252(28)	313	233(3)	333	254(3)	(δ(F3TeF1) + δ(F3TeF5)) + (δ(O7TeF2) + δ(O7TeF4))
210(3)	270	213(3)	290	234(2)	(δ(F3TeF2) + δ(F3TeF5)) – (δ(F3TeF4) + δ(F3TeF1))
173(31)	213	168(<1)	232	186(<1)	ρ_t(TeF1F3F4) + ρ_t(TeF5F2O7)
	184	147(2)	203	157(1)	δ(F4TeF1) i.p. + ρ_w(F2TeF5) + (δ(XeO7Te) i.p. + δ(O7TeF3) i.p.)
125(4)	178	119(<1)	187	138(<1)	δ(F3TeO7) + ρ_r(F4TeF1) + ρ_t(F2TeF5)
	101	85(1)	101	88(1)	(ρ_w(F4TeF1) – ρ_w(F5TeF2)) + (δ(XeO7Te) i.p. – δ(O7TeF3) i.p.)
	39	32(<1)	38	31(1)	O7TeF3 o.o.p. torsion + TeF_{4e} torsion

[a] From ref 75. [b] See Figure 5.2a for the atom numbering scheme. [c] From ref 76. [d] The abbreviations denote stretch (ν), bending (δ), twisting (ρ_t), wagging (ρ_w), and rocking (ρ_r), in-plane bending (i.p.) and out-of-plane bending (o.o.p.) modes. The in-plane and out-of-plane motions are relative to the Xe,O(7),Te,F(3)-plane in Figure 5.2a. Elongation of a bond(s) and angle opening(s) are denoted by plus(+) signs and bond contraction(s) and angle closing(s) are denoted by negative (–) signs.

Table 5.9. Experimental and Calculated Geometrical Parameters for the $XeOTeF_5^+ \cdot SO_2ClF$ Adduct-Cation

	exptl	Stutt.		(SDB-)cc-pVTZ	
		HF(C_1)	SVWN(C_1)	HF(C_1)	SVWN(C_1)
		bond lengths (Å)			
Xe(1)–O(1)	1.965(4)	1.912	2.015	1.899	1.998
Te(1)–O(1)	1.937(5)	1.935	1.986	1.915	1.958
Te(1)–F(3)	1.813(4)	1.790	1.851	1.767	1.826
Te(1)–F(1)	1.812(4)	1.799	1.860	1.773	1.834
Te(1)–F(2)	1.831(4)	1.815	1.883	1.788	1.854
Te(1)–F(4)	1.823(4)	1.814	1.883	1.788	1.855
Te(1)–F(5)	1.812(4)	1.815	1.860	1.773	1.834
Xe(1)–O(3)	2.471(5)	2.568	2.385	2.588	2.388
S(1)–O(2)	1.435(5)	1.396	1.443	1.386	1.423
S(1)–O(3)	1.431(5)	1.430	1.502	1.419	1.476
S(1)–F(6)	1.476(5)	1.523	1.581	1.499	1.549
S(1)–Cl(1)	1.931(2)	1.955	1.984	1.952	1.958
		bond angles (deg)			
Xe(1)–O(1)–Te(1)	121.0(2)	124.4	115.4	127.3	117.4
O(1)–Te(1)–F(3)	177.4(2)	180.3	180.0	180.0	179.7
O(1)–Te(1)–F(1)	86.8(2)	87.7	88.0	87.5	87.4
O(1)–Te(1)–F(2)	91.3(2)	88.1	88.6	88.3	88.9
O(1)–Te(1)–F(4)	89.7(2)	88.1	88.6	88.3	88.8
O(1)–Te(1)–F(5)	88.4(2)	87.7	88.0	87.5	87.4
F(3)–Te(1)–F(1)	90.6(2)	92.6	92.3	92.5	92.3
F(3)–Te(1)–F(2)	91.3(2)	91.6	91.2	91.7	91.3
F(3)–Te(1)–F(4)	90.6(2)	91.6	91.2	91.7	91.3
F(3)–Te(1)–F(5)	91.3(2)	92.6	92.3	92.5	92.4
F(1)–Te(1)–F(2)	177.8(2)	178.5	178.2	178.8	176.1
F(1)–Te(1)–F(4)	90.2(2)	90.4	90.9	90.3	90.7
F(1)–Te(1)–F(5)	90.4(2)	90.9	90.9	90.7	90.6
F(2)–Te(1)–F(4)	88.7(2)	88.0	87.2	88.4	87.7
F(2)–Te(1)–F(5)	90.7(2)	90.4	90.9	90.3	90.8
F(4)–Te(1)–F(5)	178.0(2)	178.5	178.2	178.8	176.0
O(1)–Xe(1)–O(3)	174.2(2)	178.5	173.3	175.2	175.2
O(2)–S(1)–O(3)	115.7(2)	120.0	119.6	119.9	119.5
O(2)–S(1)–F(6)	109.4(3)	109.0	109.7	109.3	109.8
O(2)–S(1)–Cl(1)	108.4(4)	112.2	114.6	111.7	114.1
O(3)–S(1)–F(6)	110.4(3)	105.1	104.2	105.5	104.5
O(3)–S(1)–Cl(1)	108.6(2)	108.7	106.8	108.4	106.8
Cl(1)–S(1)–F(6)	103.6(2)	99.7	99.6	100.0	100.0
Xe(1)–O(3)–S(1)	140.0(3)	138.6	118.4	148.3	122.5

Table 5.10. Vibrational Frequencies (cm^{-1}) and Calculated Infrared Intensities for the $XeOTeF_5^+ \cdot SO_2ClF$ Adduct-Cation

exptl	Stutt.		(SDB-)cc-pVTZ	
	HF(C_1)	SVWN(Cs)	HF(C_1)	SVWN(Cs)
1415(14), 1423(6)	1503(328)	1331(116)	1555(367)	1388(172)
1168(27), 1177(10)	1261(638)	1045(660)	1313(636)	1101(734)
830(5), 860(4)	961(198)	821(145)	1006(204)	856(158)
745, sh	867(103)	699(68)	884(286)	735(75)
734(49)	863(133)	697(86)	863(186)	732(97)
741(19)	861(421)	693(128)	861(130)	730(180)
712(23), 716, sh	831(23)	640(199)	844(42)	676(176)
669(48)	765(17)	625(10)	776(12)	650(8)
663(100)	751(4)	618(135)	754(3)	645(99)
	718(203)	612(117)	731(244)	630(203)
506(5)	548(37)	503(23)	565(40)	510(39)
493(12)	533(45)	468(34)	540(9)	483(13)
476(15), 486(13)	513(5)	425(12)	520(37)	453(14)
436(8), 442(14)	474(17)	393(8)	484(9)	414(6)
310(21), 322(11)	352(155)	300(13)	374(188)	316(44)
298(15)	340(69)	283(106)	367(77)	304(93)
295(15)	340(40)	272(17)	364(41)	296(31)
	333(12)	270(35)	357(5)	296(31)
249(15)	333(44)	262(2)	345(5)	286(1)
	327(1)	259(1)	342(15)	275(<1)
254(20)	318(1)	252(2)	328(1)	272(3)
	271(9)	214(8)	291(4)	234(9)
187(4)	218(0)	175(<1)	238(0)	193(<1)
173(22)	193(<1)	166(31)	213(<1)	172(35)
121(10)	186(21)	141(<1)	195(13)	160(<1)
	114(6)	124(2)	117(8)	132(4)
	104(12)	105(4)	93(3)	109(<1)
	90(6)	98(<1)	81(11)	101(5)
	52(3)	77(3)	59(7)	59(1)
	37(<1)	36(<1)	37(0)	49(<1)
	22(1)	24(<1)	19(<1)	20(0)
	17(0)	17(<1)	16(0)	17(0)
	2(1)	2(<1)	3(<1)	–5(<1)

$XeOTeF_5^+$ reproduce the previously published assignments for this cation.[75] The $XeOTeF_5^+$ cation is expected to be more weakly coordinated in the $Sb_2F_{11}^-$ salt than in $[XeOTeF_5][AsF_6]$ and thus represents a better approximation of a weakly coordinated $XeOTeF_5^+$ cation. For this reason, the vibrational frequencies of $XeOTeF_5^+$ in $[XeOTeF_5][Sb(OTeF_5)_6]\cdot SO_2ClF$ are compared with, and found to be most similar to, those of $[XeOTeF_5][Sb_2F_{11}]$[76] (Table 5.6).

The Raman spectrum of a sample containing a 7.95:1.00 molar ratio of SO_2ClF:$[XeOTeF_5][Sb(OTeF_5)_6]\cdot SO_2ClF$ showed several frequencies assigned to uncoordinated SO_2ClF that were slightly shifted with respect to those of pure solid SO_2ClF and liquid SO_2ClF (Tables 5.6 and 5.7). Three bands at 436, 486, and 1166 cm^{-1} were also observed which are assigned to coordinated SO_2ClF (vide infra). At a 1.09:1.00 molar ratio, the bands associated with uncoordinated SO_2ClF greatly diminished in intensity, while the three bands assigned to coordinated SO_2ClF gained in intensity and several new, but weaker, bands appeared that are also assigned to coordinated SO_2ClF. Finally, in a Raman spectrum of a sample containing no free SO_2ClF, the bands attributed to uncoordinated SO_2ClF are absent and the spectrum of coordinated SO_2ClF is better resolved (Table 5.9). The calculated vibrational frequencies show that the formation of the adduct-cation is accompanied by low-frequency shifts of the strongly coupled in-phase and out-of-phase SO_2 stretching modes, while the S–F and S–Cl stretches are shifted to higher frequency relative to those of free SO_2ClF. Unlike free SO_2ClF, the S–F stretching mode is weakly coupled to the in-phase SO_2 stretching mode. The SO_2ClF stretching modes show no significant coupling with the cation stretching modes. The

TeF_5 group and out-of-phase XeOTe stretching frequencies between 645 and 735 cm^{-1} are little affected by complexation with SO_2ClF, thus their mode descriptions are the same as in uncomplexed $XeOTeF_5^+$. The in-phase XeO(7)Te and bridging XeO(8) stretching modes are strongly coupled and their in-phase and out-of-phase components, in turn, couple with the SO(8)FCl umbrella bend. Aside from four modes that are pure $XeOTeF_5^+$ (286, 296, 296 cm^{-1}) and SO_2ClF (275 cm^{-1}) modes, all modes below 316 cm^{-1} are strongly coupled deformation and torsion modes involving both $XeOTeF_5^+$ and SO_2ClF (Table 5.6).

There is good agreement between observed and calculated frequencies in Table 5.6, moreover, the observed frequency shifts arising from complexation are also reproduced. The in-phase SO_2 and out-of-phase SO_2 stretching modes exhibit the anticipated low-frequency shift upon complexation, while the ν(SF) and ν(SCl) modes shift to higher frequency relative to those of free SO_2ClF. The low-frequency shifts of the strongly coupled SO_2 stretching modes and the high frequency shifts of the sulfur-halogen stretching modes are consistent with the increased S–O bond lengths and the shorter S–F and S–Cl bond lengths observed in the crystal structure. While the S–O bond order is expected to decrease for the S–O bond of the coordinated oxygen atom, the terminal S–O bond order is expected to increase, but to a lesser extent. This is supported by the NBO analyses and is accompanied by increased S–F and S–Cl bond orders. The frequency shifts and calculated bond orders are also consistent with increased negative charge on the coordinated oxygen atom and a smaller decrease in negative charge on the terminal oxygen atom (see Section 5.2.5).

Although the S–O bond length differences in $SbF_5 \cdot SO_2$ are clearly distinguishable and the terminal S–O bond is significantly shorter than the coordinated S–O bond, the strongly coupled in-phase and out-of-phase SO_2 stretching modes of this adduct are also shifted to lower frequencies when compared with those of free SO_2. Other examples of main-group oxide fluorides that function as Lewis bases (e.g., COF_2,[167,168] SOF_2,[167] SO_2F_2,[167] SO_2,[167] $PO_2F_2^-$ [169] and POF_3[167]) that form oxygen-coordinated adducts with AsF_5 and/or SbF_5 show analogous decreases in ν(CO), ν(SO), ν(SO_2), and ν(PO_2) and increases in ν(CF), ν(SF), and ν(PF) when compared with the corresponding frequencies of the free donor species.

The experimental difference between the in-phase and out-of-phase SO_2 stretching frequencies (Δ) of SO_2ClF increases from 218 cm^{-1} (solid mixtures), 226 cm^{-1} (pure solid, –163 °C), and 233 cm^{-1} (pure liquid, 22 °C) in uncoordinated SO_2ClF to 246 cm^{-1} in coordinated SO_2ClF. The increase in Δ is consistent with the difference in the S–O bond orders that results from complexation, and is reflected in the S–O bond orders of the bridging Xe–O–S moiety (1.14) and that of the terminal S–O bond (1.29) (see Section 5.2.5). Similar increases in Δ have been observed for the $F_5M\cdots OSO$ (M = Sb, As) adducts (185 cm^{-1} in free SO_2; 225 (Sb) and 206 (As) cm^{-1} in the adduct) and for $F_5As\cdots OPF_2O\cdots AsF_5^-$ (165 cm^{-1} in $PO_2F_2^-$; 197 cm^{-1} in the complex anion).

5.2.4.2. $Sb(OTeF_5)_6^-$

The prior vibrational assignments for $Sb(OTeF_5)_6^-$,[35,172] have been improved upon and are presented in Table 5.11.

Table 5.11. Experimental and Calculated[a] Vibrational Frequencies for the $Sb(OTeF_5)_6^-$ Anion

HF/Stutt[b,e]	SVWN/ (SDB-)cc-pVTZ[b]	exptl[d]	assgnt (S_6)[c]
970(5)	889(13)	841(3)	A_g, $\nu(SbO_6 - 6TeO)$
860(3)	801(13)	823(5)	E_g, $\nu[SbO_4 - (4TeO)] - \nu[SbO'_2 - (2Te'O')_{trans}]$
751(1)	720(3)	753(14)	
		748(19)	A_g, $\nu[6(TeF_{2e\ cis} - TeF_{2e\ cis})]$
		745, sh	
747(2)	717(3)	724(20)	E_g, $\nu[4(TeF_{2e\ cis} - TeF_{2e\ cis}) + 2(Te'F_{2e\ trans} - Te'F_{2e\ trans})]$
735(3)	706(14)	709(27)	A_g, $\nu[4(TeF_{2e\ cis} - TeF_{2e\ cis}) - 2(Te'F_{2e\ cis} - Te'F_{2e\ cis})]$
		703(52)	
732(<1)	700(<1)	697(17)	E_g, $\nu[4(TeF_{e\ trans} - TeF_{e\ trans}) + 2(Te'F_{2e\ cis} - Te'F_{2e\ cis})]$
		693(20)	
707(92)	678(87)	669(48)	A_g, $\nu[6(TeF_5)]$
		663(100)	
701(2)	675(13)	686(12)	E_g, $\nu[4(TeF_5)_{trans} - 2(TeF_5)_{trans}]$
662(19)	643(95)		A_g, $\nu[6(TeF_{4e} - TeF_a)]$
656(2)	639(6)	653, sh	E_g, $\nu[4(TeF_{4e} - TeF_a) + 2((Te'F_{2e\ cis} - Te'F_{2e\ cis}) - Te'F_a)]$
652(<1)	635(<1)	644(22)	A_g, $\nu[6(TeF_{2e\ trans} - TeF_{2e\ trans})]$
651(7)	632(3)		E_g, $\nu[4(TeF_{2e\ trans} - TeF_{2e\ trans}) + 2(Te'F_{4e} - Te'F_a)] + \nu[SbO'_2 - (2Te'O')_{trans}]$
475(2)	475(2)		E_g, $\nu[SbO_4 + (4TeO)] - \nu[SbO'_2 + (2Te'O')_{trans}]$
430(22)	431(56)	411(27)	A_g, $\nu(SbO_6 + 6TeO)$
377(3)	349(5)	369(10)	A_g, $\delta[6(SbOTe)] - \delta[6TeF_{4e}$ umbrella$]$
346(<1)	329(<1)	344(10)	A_g, $\delta[6(SbOTe)] + \delta[6TeF_{4e}$ umbrella$]$
327(2)	316(1)	338(16)	strongly coupled deformation and torsion modes involving both $OTeF_5$ and SbOTe moieties
327(3)	312(5)	332(16)	
325(1)	310(3)	326, sh	
319(<1)	306(1)	322(11)	
319(<1)	306(<1)		
305(1)	292(3)		
297(1)	280(1)	304(17)	
295(1)	279(1)		
234(1)	231(3)		
232(1)	226(1)		
221(1)	214(1)	242(13)	
207(<1)	202(<1)	229(6)	
206(<1)	198(<1)		
203(1)	199(0)		
132(1)	134(3)	145(10)	
		140(14)	
124(<1)	125(<1)	134(9)	
		131(7)	
110(<1)	106(<1)	121(10)	
104(<1)	101(<1)	111(11), br	
79(<1)	88(1)		
68(<1)	85(<1)		
42(<1)	53(<1)		
35(<1)	45(<1)		
28(<1)	38(<1)		
24(<1)	33(<1)		

Table 5.11. (continued ...)

[a] Only Raman-active modes are reported. [b] Calculated Raman intensities, in $Å^4$ amu^{-1}, are given in parentheses. [c] Frequencies calculated at the HF level have been scaled by multiplying by 0.90. [d] Relative Raman intensities are given in parentheses. [e] Elongation of a bond(s) and angle opening(s) are denoted by plus (+) signs and bond contraction(s) and angle closing(s) are denoted by negative (–) signs. The abbreviations denote stretch (ν) and bending (δ) modes. The prime symbols (′) differentiate Te or O atoms belonging to two $OTeF_5$ groups that are trans to one another from atoms belonging to remaining four groups which are also mutually trans to one another.

5.2.5. Computational Results

5.2.5.1. Geometry of $XeOTeF_5^+ \cdot SO_2ClF$

The electronic structure of the $XeOTeF_5^+ \cdot SO_2ClF$ adduct has been calculated starting from C_1 symmetry using Hartree-Fock (HF) and pure density functional theory (DFT) methods and Stuttgart and (SDB-)cc-pVTZ basis sets, yielding an optimized geometry having C_1 symmetry. Although both types of calculations resulted in stationary points with all frequencies real for SO_2ClF and $XeOTeF_5^+$, the energy minimizations of the $XeOTeF_5^+ \cdot SO_2ClF$ adduct cation gave rise to a local minimum at the HF level, but gave one imaginary frequency at the DFT level (Table 5.6). Overall, the DFT method gave better agreement between the experimental and calculated geometries and vibrational frequencies. For this reason, only the DFT results are discussed; the other calculated values can be found in Tables 5.9 and 5.10. The $XeOTeF_5^+$ cation[75,80] and SO_2ClF[80] have been the subject of previous theoretical calculations. They were, however, recalculated in the present study at the same level of theory as $XeOTeF_5^+ \cdot SO_2ClF$ in order to study the changes in geometric parameters and vibrational frequencies that occur upon coordination. The present optimized geometric parameters for SO_2ClF (C_s) and $XeOTeF_5^+$ (C_1) are listed in Tables 5.7 and 5.8, respectively.

Overall, there is very good agreement between the calculated and the observed geometries, in particular for the Xe–O–Te and O–Xe···O angles. The largest deviation is for the O–S–O···Xe dihedral angle (calc, -13.2°; obs, $24.9(6)^{\circ}$), which is expected because it can be more easily deformed by crystal packing. At the HF level, the O–Xe···O bond angle is almost linear and the Xe–O bond is shorter than the Te–O bond.

The HF method has previously been shown to incorrectly predict linear geometries for the $Xe_2F_3^+$ [23] and $Kr_2F_3^+$ [139] cations. Although there is no crystal structure containing a well-isolated $XeOTeF_5^+$ cation, the calculated geometry of $XeOTeF_5^+ \cdot SO_2ClF$ shows several significant changes when compared with the calculated geometry of the $XeOTeF_5^+$ cation. As expected, the Xe–O bond length increases upon coordination; the F_a–Te–F_e angles are smaller, moving the equatorial fluorine atoms away from the oxygen atom, while the Te–O and Te–F bond lengths and the Xe–O–Te angle remain essentially unchanged. As observed experimentally, the calculated S–F and S–Cl bond lengths are found to be shorter than in free SO_2ClF, while the coordinated S–O(8) bond is found to be elongated and the terminal S–O(9) bond length is comparable to that in uncomplexed SO_2ClF. The calculated geometrical changes are also in accord with changes observed in the structures of the $SbF_5 \cdot SO_2$ adduct[173] and $Fe(OTeF_5)_3 \cdot 3SO_2ClF$.[165] The increase in Cl–S–F bond angle and corresponding decrease in O–S–O bond angle relative to the experimental values of uncomplexed SO_2ClF are reproduced at both levels of theory.

5.2.5.2. Bonding in $XeOTeF_5^+ \cdot SO_2ClF$ and Related Systems

Natural Bond Orbital (NBO, Table 5.12) and Electron Localization Function (ELF) analyses have been performed for XeF_2, free XeF^+, the $XeOTeF_5^+ \cdot SO_2ClF$ adduct-cation, and for the $[XeF][SbF_6]$, $[XeF][AsF_6]$, $[XeOTeF_5][SbF_6]$, and $[XeOTeF_5][AsF_6]$ ion pairs to (1) determine the relative strengths of the Xe---F and Xe···O donor-acceptor interactions and to (2) correlate the valence electron lone-pair basin distribution with the strength of the donor-acceptor interaction. The total xenon lone pair basin volumes and

Table 5.12. Calculated[a] Natural Atomic Charges, Mayer Bond Orders, and Mayer Natural Atomic Orbital Valencies for SO_2ClF, $XeOTeF_5^+$ and $XeOTeF_5^+ \cdot SO_2ClF$

		$XeOTeF_5^+ \cdot SO_2ClF$	$XeOTeF_5^+$	SO_2ClF
charge	Xe(1)	1.16	1.18	
	O(7)	–0.95	–0.87	
	Te(1)	3.52	3.51	
	F(33)	–0.56	–0.55	
	F(31)	–0.56	–0.55	
	F(32)	–0.60	–0.59	
	F(34)	–0.60	–0.59	
	F(35)	–0.56	–0.55	
	S(1)	2.18		2.18
	O(8)	–0.87		–0.78
	O(9)	–0.74		–0.78
	Cl(1)	–0.003		–0.17
	F(36)	–0.39		–0.44
valency	Xe(1)	0.68	0.58	
	O(7)	0.97	0.99	
	Te(1)	3.22	3.20	
	F(33)	0.52	0.53	
	F(31)	0.50	0.51	
	F(32)	0.48	0.49	
	F(34)	0.48	0.49	
	F(35)	0.50	0.51	
	S(1)	3.63		3.60
	O(8)	1.06		1.02
	O(9)	1.06		1.02
	Cl(1)	0.64		0.56
	F(36)	0.55		0.52
bond order	Xe(1)–O(7)	0.47	0.54	
	Te(1)–O(7)	0.55	0.49	
	Te(1)–F(33)	0.55	0.56	
	Te(1)–F(31)	0.54	0.54	
	Te(1)–F(32)	0.51	0.52	
	Te(1)–F(34)	0.51	0.52	
	Te(1)–F(35)	0.54	0.54	
	Xe(1)···O(8)	0.16		
	S(1)–O(8)	1.03		1.15
	S(1)–O(9)	1.18		1.15
	S(1)–Cl(1)	0.76		0.67
	S(1)–F(36)	0.66		0.62

[a] SVWN/(SDB-)cc-pVTZ.

separation values (f_{sep}) are given in Figures 5.4, 5.5, and 5.6. Further details associated with the NBO analyses are provided in Tables 5.9 and 5.13.

Gas-phase complexation energies were calculated at the SVWN/(SDB-)cc-pVTZ level of theory and were exothermic for $[XeF][AsF_6]/[XeF][SbF_6]$ (–624.3/–610.0 kJ mol^{-1}), $[XeOTeF_5][AsF_6]/[XeOTeF_5][SbF_6]$ (–557.7/–543.9 kJ mol^{-1}), and $XeOTeF_5^+ \cdot SO_2ClF$ (–116.3 kJ mol^{-1}), showing that the ion-pairing energies are greater for XeF^+ than for $XeOTeF_5^+$ for both AsF_6^- and SbF_6^-, and that the donor-acceptor interaction between $XeOTeF_5^+$ and SO_2ClF is only ca. 20% that of the fluorine-bridge bond energy in the AsF_6^- and SbF_6^- salts and ca. 50% of the complexation energy for $XeF^+ \cdot H_2O$ (–216.3 kJ mol^{-1}). At the opposite end of the scale, the complexation energy for XeF^+ and naked F^- ion (–1086.9 kJ mol^{-1}), leading to XeF_2 formation, is nearly double that of the aforementioned ion pairing energies.

Gas-phase thermodynamic donor-acceptor bond strengths are corroborated by the higher bond orders for Xe---F(7) in $[XeF][AsF_6]/[XeF][SbF_6]$ (0.216/0.199) than for Xe---F(6) in $[XeOTeF_5][AsF_6]/[XeOTeF_5][SbF_6]$ (0.197/0.192), and by the lower natural charges on xenon in $[XeOTeF_5][AsF_6]/[XeOTeF_5][SbF_6]$ (1.194/1.195) when compared with those for xenon in $[XeF][AsF_6]/[XeF][SbF_6]$ (1.222/1.232). Each fluorine, (F(6) and F(7)), that has a long contact to the xenon atom of the ion-pair, is assigned four valence electron pairs by their NBO analyses. The longer M---F(6) and M---F(7) bridge bond lengths and their lower bond orders indicate considerably weaker, less covalent bonding when compared with the terminal M–F bond strengths of the anions. The calculated

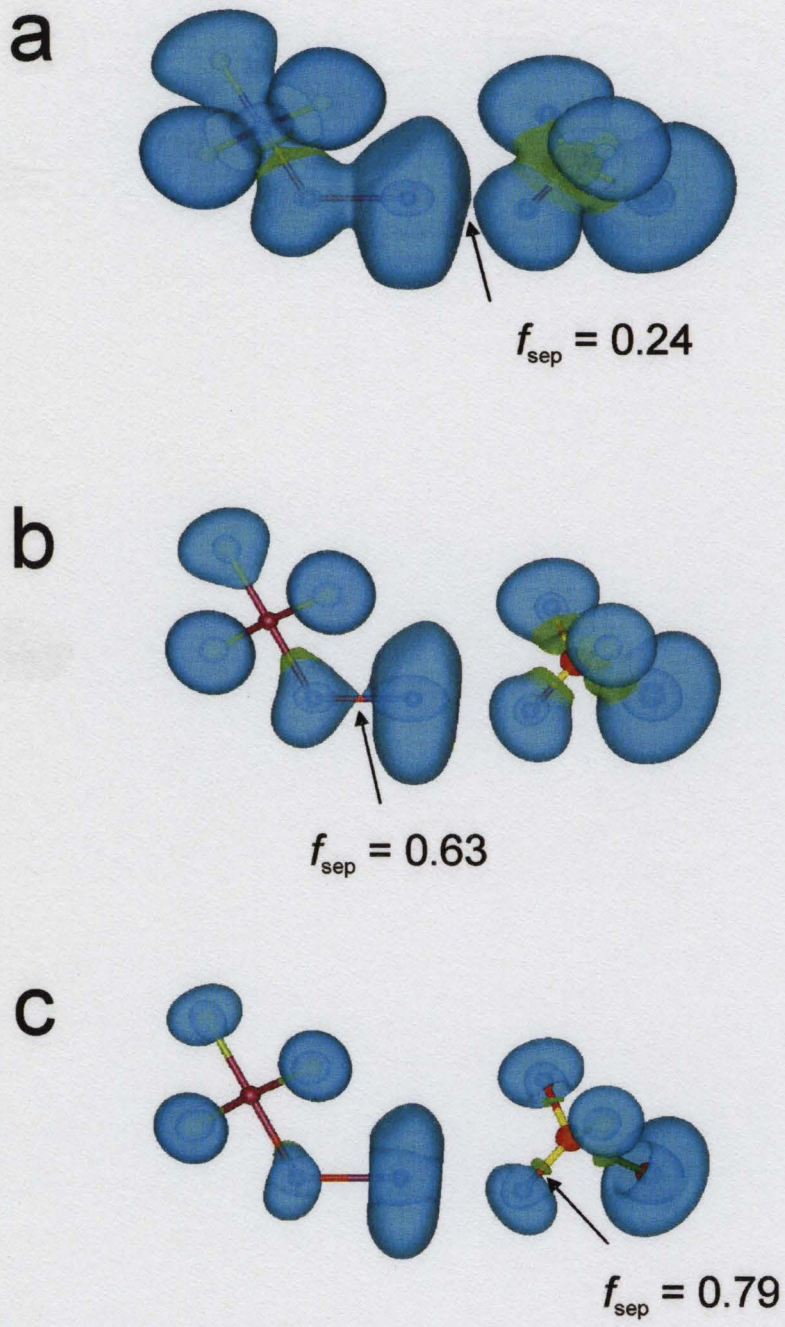

Figure 5.4. ELF isosurface plots at contour levels for $XeOTeF_5^+ \cdot SO_2ClF$ corresponding to the indicated basin separation values, f_{sep}, (a) 0.24, (b) 0.63, and (c) 0.79 at the SVWN/(SDB-)cc-pVTZ//SVWN/(SDB-)cc-pVTZ level of theory. Color scheme: blue, lone pair (monosynaptic) basin, $V(X_i)$; green, bond (bisynaptic) basin, $V(E,X_i)$; red, core basin, C(E).

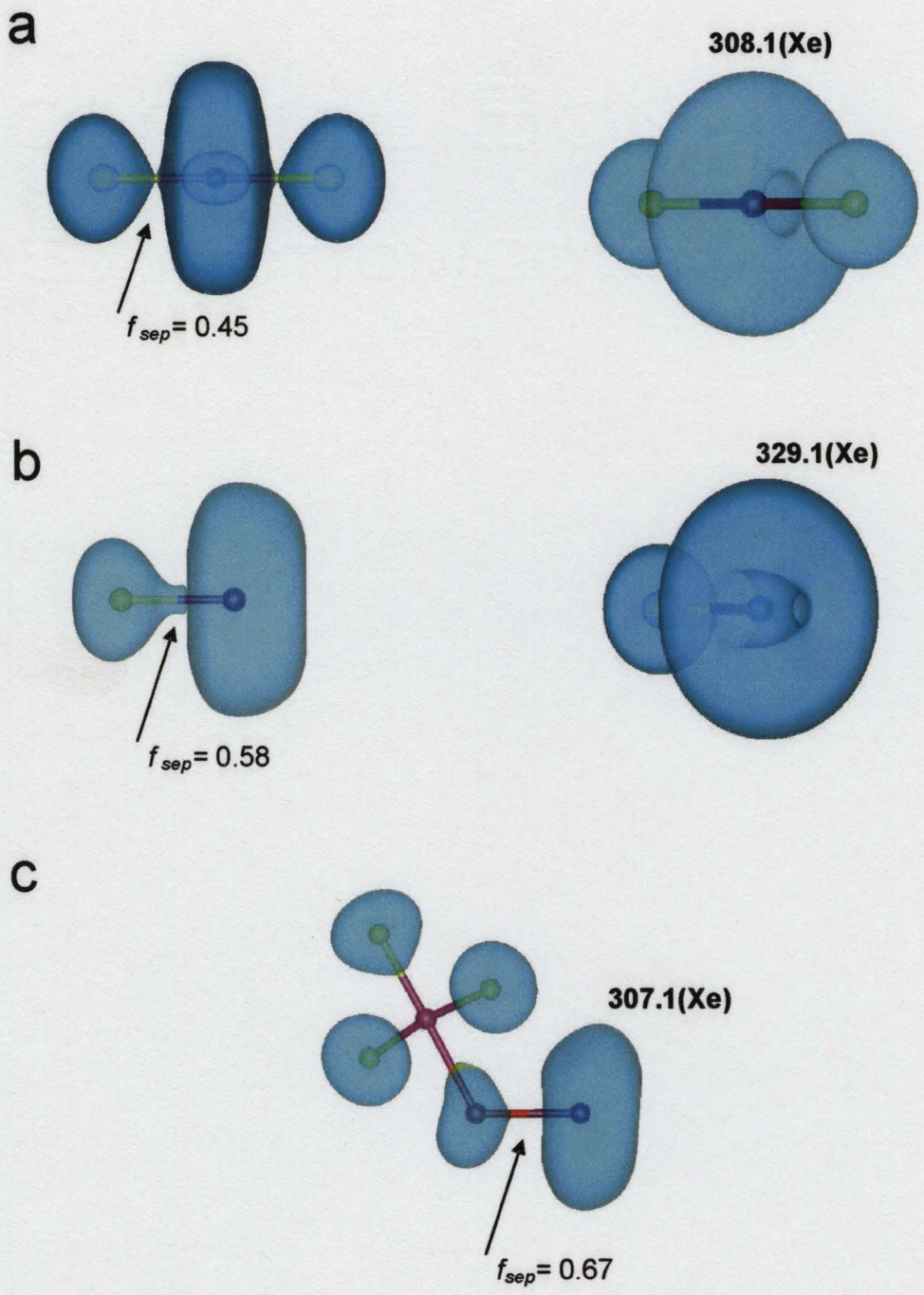

Figure 5.5. ELF isosurface plots at the SVWN/(SDB-)cc-pVTZ//SVWN/(SDB-)cc-pVTZ level of theory for (a) XeF_2, f_{sep} = 0.45 contour level, (b) XeF^+, f_{sep} = 0.58 contour level, and (c) $XeOTeF_5^+$, f_{sep} = 0.70 contour level. The tilted, right-hand side views in (a) and (b) are plotted at the 0.70 contour level. See Figure 5.4 for color scheme.

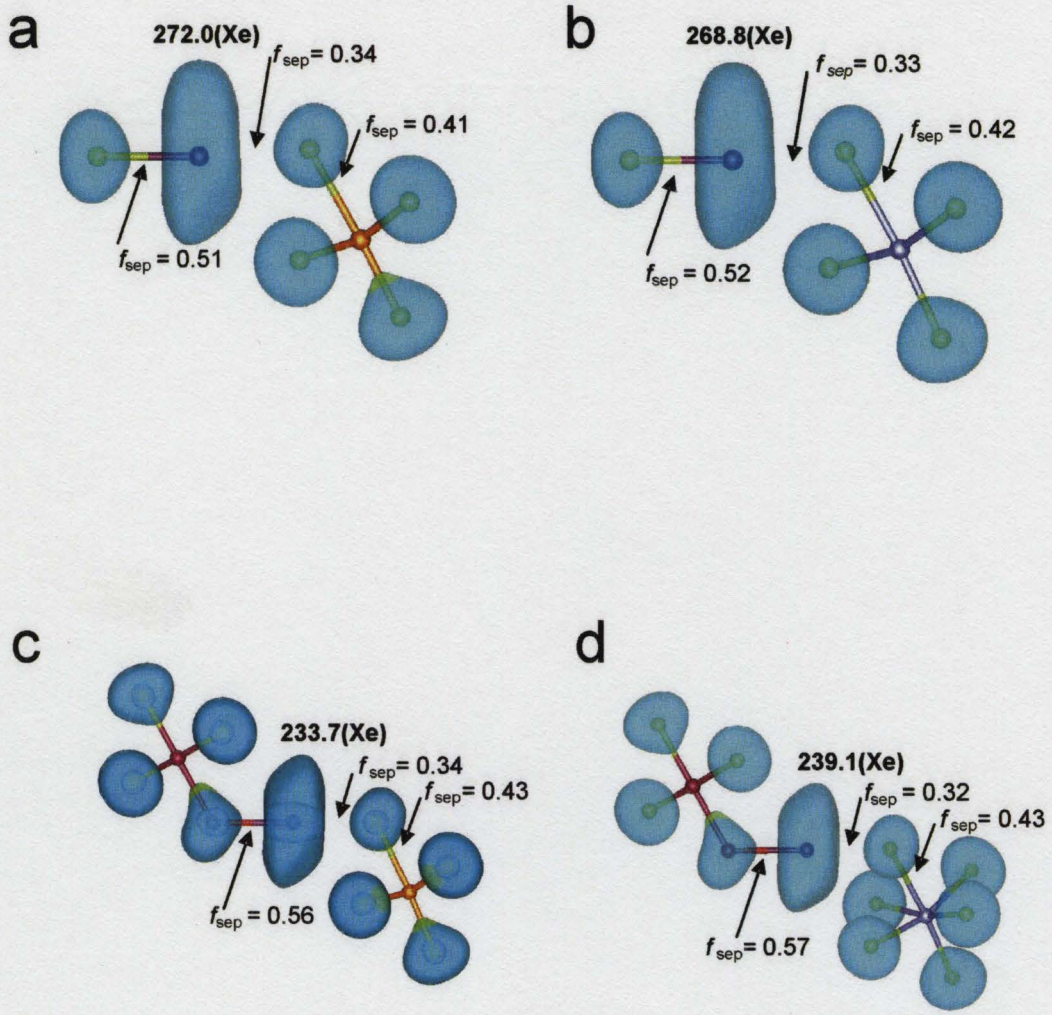

Figure 5.6. ELF isosurface plots at the 0.70 contour level for (a) [XeF][AsF_6], (b) [XeF][SbF_6], (c) [$XeOTeF_5$][AsF_6], and (d) [$XeOTeF_5$][SbF_6] at the SVWN/(SDB-)cc-pVTZ//SVWN/(SDB-)cc-pVTZ level of theory. Basin separation values and xenon torus volumes are indicated. See Figure 5.4 for color scheme.

Table 5.13. Calculated[a] Bond Lengths (Å), Natural Atomic Charges, Mayer Bond Orders, and Mayer Natural Atomic Orbital Valencies for $[XeF][SbF_6]$, $[XeOTeF_5][MF_6]$ (M = As, Sb), XeF^+ and XeF_2

$[XeF][MF_6]$ (C_1)			$[XeOTeF_5][MF_6]$ (C_1)		
	M = As	M = Sb		M = As	M = Sb
	charge			charge	
Xe(1)	1.222	1.232	Xe(1)	1.194	1.195
F(1)	–0.511	–0.505	O(1)	–1.016	–1.005
			Te(1)	3.515	3.513
			F(3)	–0.584	–0.591
			F(1)	–0.588	–0.587
			F(2)	–0.609	–0.604
			F(4)	–0.587	–0.585
			F(5)	–0.611	–0.608
M(1)	2.837	3.111	M(1)	2.840	3.107
F(2)	–0.585	–0.637	F(6)	–0.563	–0.596
F(3)	–0.613	–0.665	F(7)	–0.589	–0.638
F(4)	–0.588	–0.640	F(8)	–0.616	–0.665
F(5)	–0.613	–0.665	F(9)	–0.586	–0.636
F(6)	–0.585	–0.637	F(10)	–0.615	–0.664
F(7)	–0.565	–0.595	F(11)	–0.586	–0.636
	valency			valency	
Xe(1)	0.614	0.600	Xe(1)	0.693	0.681
F(1)	0.352	0.353	O(1)	0.973	0.960
			Te(1)	3.241	3.255
			F(3)	0.498	0.501
			F(1)	0.488	0.492
			F(2)	0.474	0.483
			F(4)	0.488	0.494
			F(5)	0.474	0.481
M(1)	3.282	2.767	M(1)	3.273	2.783
F(2)	0.556	0.485	F(6)	0.473	0.471
F(3)	0.534	0.466	F(7)	0.576	0.498
F(4)	0.581	0.494	F(8)	0.527	0.469
F(5)	0.534	0.466	F(9)	0.553	0.488
F(6)	0.556	0.485	F(10)	0.527	0.469
F(7)	0.486	0.467	F(11)	0.553	0.487

Table 5.13. (continued...)

bond length [bond order]			bond length [bond order]		
Xe(1)–F(1)	1.963 [0.352]	1.958 [0.352]	Xe(1)–O(1)	2.055 [0.409]	2.048 [0.402]
			Te(1)–O(1)	1.908 [0.616]	1.911 [0.610]
			Te(1)–F(3)	1.838 [0.536]	1.838 [0.537]
			Te(1)–F(1)	1.843 [0.525]	1.843 [0.529]
			Te(1)–F(2)	1.858 [0.508]	1.857 [0.516]
			Te(1)–F(4)	1.843 [0.525]	1.842 [0.530]
			Te(1)–F(5)	1.858 [0.508]	1.858 [0.513]
Xe(1)---F(7)	2.133 [0.216]	2.149 [0.199]	Xe(1)---F(6)	2.150 [0.197]	2.168 [0.192]
M(1)–F(7)	2.014 [0.298]	2.131 [0.278]	M(1)–F(6)	1.999 [0.304]	2.120 [0.288]
M(1)–F(2)	1.697 [0.603]	1.879 [0.504]	M(1)–F(7)	1.683 [0.618]	1.872 [0.514]
M(1)–F(3)	1.723 [0.569]	1.905 [0.474]	M(1)–F(8)	1.726 [0.564]	1.907 [0.474]
M(1)–F(4)	1.682 [0.621]	1.872 [0.511]	M(1)–F(9)	1.697 [0.601]	1.879 [0.506]
M(1)–F(5)	1.723 [0.569]	1.905 [0.474]	M(1)–F(10)	1.724 [0.564]	1.907 [0.475]
M(1)–F(6)	1.697 [0.603]	1.879 [0.504]	M(1)–F(11)	1.697 [0.601]	1.879 [0.506]

Table 5.13. (continued...)

XeF^+ ($C_{\infty v}$)		XeF_2 ($D_{\infty h}$)	
charge		charge	
Xe(1)	1.327	Xe(1)	1.161
F(1)	–0.327	F(1)	–0.580
		F(2)	–0.580
valency		valency	
Xe(1)	0.454	Xe(1)	0.626
F(1)	0.454	F(1)	0.314
		F(2)	0.314
bond length [bond order]		bond length [bond order]	
Xe(1)–F(1)	1.878 [0.454]	Xe(1)–F(1)	2.010 [0.313]
		Xe(1)–F(2)	2.010 [0.313]

[a] SVWN/(SDB-)cc-pVTZ.

terminal M–F bond lengths in the ion-pairs are shorter and their bond orders are slightly higher and more covalent for AsF_6^- than for SbF_6^-. The interaction between F_5TeOXe^+ and SO_2ClF is shown to be considerably weaker and more ionic, having a Xe···O(3) bond order of only 0.164 and a larger charge difference on the donor and acceptor atoms (Xe, 1.159; O(3), –0.868).

When ELF isosurface contours are drawn at progressively increasing function values (f), the basins separate at f_{sep} and the lobes thus formed contain more localized electron density with increasing f-value (Figure 5.4). In the case of the lone pair (monosynaptic) basins, a noteworthy feature is the toroidal valence electron pair density on xenon and the more exposed core charge at the "openings" of the torus. The torus results from the combination of the three non-bonding ELF basins corresponding to the three electron lone pair domains of XeF_2 in its AX_2E_3 VSEPR arrangement of bond pair domains (X) and valence electron lone pair domains (E). Thus, the individual valence lone pairs are not individually localized. The three-dimensional xenon valence isosurface is similar in appearance to that of isovalent ClF_2^-.[174] All xenon(II) species considered in the present study exhibit toroidal xenon valence electron pair basins with XeF_2 providing the most symmetric example (Figure 5.5). For the AXE_3 VSEPR arrangement of XeF^+, the xenon valence lone pair density also forms a torus, however, it is asymmetric and the opening opposite the Xe–F bond exposing the core basin density is more closed. Thus, the donor atoms of the $XeOTeF_5^+ \cdot SO_2ClF$ adduct-cation and ion pairs presently under discussion can be viewed as approaching the xenon atoms of the parent XeF^+ and $XeOTeF_5^+$ cations at the centers of their respective tori where the positive charges of the

xenon core basins are more exposed. A likely consequence of the toroidal xenon valence electron distributions is that the xenon van der Waals radii of xenon(II) species are significantly diminished along their xenon-ligand atom bond axes (see Section 5.2.3).

The relative strengths of the donor-acceptor interactions between the xenon(II) Lewis acidic cations and the weakly fluorobasic MF_6^- (M = As, Sb) anions and SO_2ClF have been assessed on the basis of ELF separation function (f_{sep}) values; that is to say, the *f*-function value at which the contour between the acceptor atom (xenon) and the donor atom (oxygen or fluorine) separate. Separation of the basin on the xenon atom of F_5TeOXe^+ and the oxygen atom of SO_2ClF occurs at an f_{sep} value of 0.24 and is consistent with weak, highly polar bonding and the long Xe···O(3) bond (2.388 Å). The separations of the corresponding basins for XeF^+ and AsF_6^-/SbF_6^- occur at higher f_{sep} values (0.35/0.33) with no assigned bond basins, indicative of more polar-covalent bonding and in accord with long Xe---F(7) bridge bonds (2.133/2.149 Å). The separations of F_5TeOXe^+ and AsF_6^-/SbF_6^- occur at f_{sep} values (0.34/0.32) similar to those of $[XeF][AsF_6/SbF_6]$ and have Xe---F bridge bond lengths (2.150/2.168 Å) that are also similar to those of XeF^+ salts.

The xenon valence basin (torus) volumes, given by ELF population analyses, decrease in the order XeF^+ (329.1) > XeF_2 (308.1) > $[XeF][AsF_6/SbF_6]$ (272.0/268.8). For XeF^+ and XeF_2, the smaller volume of XeF_2 can be viewed as a contraction of the XeF^+ valence lone pair basin volume by the negative electric field of a second fluoride ion. While one may have anticipated the xenon lone pair basin volume of $[XeF][AsF_6/SbF_6]$ to be intermediate with respect to those of XeF^+ and XeF_2, it is further

contracted by interaction with a fluorine atom of the anion cis to the Xe---F–As/Sb bridge (Figure 5.6a). Analogous behavior is exhibited by $XeOTeF_5^+$ (307.1) and $[XeOTeF_5][AsF_6/SbF_6]$ (241.4/239.1) and, moreover, the contraction is even more pronounced and may be a consequence of the higher natural charge on oxygen (O, –0.870; F, –0.327). The F-on-Te···Xe interaction deforms the xenon lone pair basin in the manner shown in Figures 5.6c and 5.6d. For the least strongly bound case, $[XeOTeF_5][SO_2ClF]$, the xenon torus volume (263.6) is less contracted with respect to that of $[XeOTeF_5][AsF_6]$, and is indicative of a weaker donor-acceptor interaction with SO_2ClF than with AsF_6^-/SbF_6^-. In all cases, the xenon lone pair volumes are sensitive to nearest neighbor interactions, and correlate with the strength of the donor-acceptor interaction as assessed on the basis of their f_{sep} values.

5.3. Conclusions

The present study provides a reliable synthesis of the strong oxidant noble-gas salt, $[XeOTeF_5][Sb(OTeF_5)_6]\cdot SO_2ClF$, which is of proven and potential synthetic utility. The structural characterization of $[XeOTeF_5][Sb(OTeF_5)_6]\cdot SO_2ClF$ in solution and in the solid state has provided insight into its low-temperature oxidant properties which are primarily consequences of the weakly coordinating nature of the $Sb(OTeF_5)_6^-$ anion, the weak Xe···O donor-acceptor bond between $XeOTeF_5^+$ and SO_2ClF, and the high solubility of the salt in SO_2ClF at low temperatures. The study has afforded a rare example of the weak Lewis base, SO_2ClF, coordinated to a Lewis acid center, $XeOTeF_5^+$. As well as reproducing the geometric parameters and vibrational frequencies of the $XeOTeF_5^+\cdot SO_2ClF$ adduct-cation, quantum mechanical calculations have provided

consistent trends for the relative strengths of the Xe···O donor-acceptor bond in $XeOTeF_5^+ \cdot SO_2ClF$ and related ion-pair bonds in $[XeL][MF_6]$ (L = F, $OTeF_5$; M = As, Sb) based on their gas-phase complexation energies, and NBO and ELF analyses. These weak interactions are highly polar in nature, with $XeOTeF_5^+ \cdot SO_2ClF$ providing the weakest donor-acceptor interaction within the series that was examined. The use of ELF separation contours has provided a semi-quantitative approach to assessing the relative strengths of the donor-acceptor interactions in these species, and may be generally applicable. The ELF calculations also show that the three valence electron lone pairs on xenon(II) are in fact not localized in three discreet pairs, but rather combine to form a torus around the xenon atom; even when the coordination about the xenon atom is highly asymmetric, this toroidal electron pair density distribution survives, albeit distorted.

CHAPTER 6

THE SYNTHESES OF CARBOCATIONS BY USE OF THE NOBLE-GAS OXIDANT, $[XeOTeF_5][Sb(OTeF_5)_6]$; THE SYNTHESES AND CHARACTERIZATION OF THE CX_3^+ (X = Cl, Br, $OTeF_5$) AND $CBr(OTeF_5)_2^+$ CATIONS AND THEORETICAL STUDIES OF CX_3^+ AND BX_3 (X = F, Cl, Br, I, $OTeF_5$)

6.1. Introduction

Trihalomethyl cations, CX_3^+ (X = Cl, Br, I), have been the subject of considerable interest. The CCl_3^+ and CBr_3^+ cations have been postulated as superelectrophilic intermediates that catalyze efficient cracking, isomerization and oligimerization of alkanes and cycloalkanes, as well as facilitating the syntheses of carbocations by means of hydride abstraction by the CCl_3^+ cation.[175] The CCl_3^+ cation, the first perhalomethyl cation to have been reported, was observed in the gas phase by mass spectrometry[176] and by ion cyclotron resonance (ICR) mass spectrometry.[177] The CCl_3^+ cation has also been isolated in the solid state by ultraviolet or microwave irradiation of $CHCl_3$ and trapping of the free ion in an argon matrix at 14 K,[178,179] and by codeposition of CCl_4 and SbF_5 on a CsI window at 77 K followed by warming to 150 K to produce $[CCl_3][Sb_2F_{10}Cl]$ in an SbF_5 matrix.[180] In all three cases, CCl_3^+ was characterized by infrared spectroscopy. The CBr_3^+ and CI_3^+ cations have been more recently observed in the gas phase by ICR mass spectrometry.[181] The CF_3^+ cation has been observed by mass spectrometry[176] and ICR mass spectrometry,[177] and was first produced in the condensed state by photodecomposition of CF_3X (X = Cl, Br, I, H) in argon matrices.[182] The CF_3^+ cation has also been obtained by decomposition of an Ar/F_3CNNCF_3 mixture at 14 K codeposited

with microwave-excited neon atoms,[183] and by codeposition of a Ne/CF_4 mixture at 5 K with excited neon atoms produced in a microwave discharge.[184] Matrix-isolated CF_3^+, derived in the aforementioned manners, was characterized by infrared spectroscopy, and the vibrational assignments for CF_3^+ have been confirmed by ab initio calculations.[185] The first syntheses of long-lived perhalomethyl cations in solution were achieved by the reactions of CX_4 (X = Cl, Br, I) with SbF_5 in SO_2ClF solvent at –78 °C to give $[CX_3][Sb_nF_{5n}X]$ (X = Cl, Br, I).[186,187] All three cations were characterized by ^{13}C NMR spectroscopy. The CCl_3^+ cation was also generated by reaction of $CCl_3C(O)Cl$, CCl_3SO_2Cl, and $CCl_3C(O)F$ with SbF_5 in SO_2ClF at –78 °C.[186,187] Similar attempts to prepare CF_3^+ by reaction of SbF_5 with CF_4, $CF_3C(O)F$ and CF_3SO_2Cl in SO_2ClF at –78 °C were unsuccessful and, in the cases of $CF_3C(O)F$ and CF_3SO_2Cl, yielded CF_4.[186,187] The CI_3^+ cation has been recently synthesized as the $[CI_3][Al(OC(CF_3)_3)_4]$ salt by the abstraction of iodide as AgI from CI_4 in CH_2Cl_2 solution by use of $[Ag][Al(OC(CF_3)_3)_4]$ as the Ag^+ ion source, and characterized by X-ray crystallography.[101]

The series of peralkoxymethyl cations, $C(OR)_3^+$, has been extensively studied and characterized in solution, and were first generated by alkylation of a carbonic ester[188] or by Meerwein's method,[189,190] which involves alkoxy group abstraction from an ortho ester by BF_3. Peralkoxymethyl cations, generated in acid solutions from ortho esters or ketals, have been characterized by ultraviolet and infrared spectroscopy and by ^1H and ^{13}C NMR spectroscopy.[191] The trihydroxymethyl cation, $C(OH)_3^+$, was first generated by dissolution of M_2CO_3 (M = Na, K), $BaCO_3$, or $NaHCO_3$ in FSO_3H–SbF_5–SO_2 superacid solutions at –78 °C and studied by ^1H and ^{13}C NMR spectroscopy.[192] Prior to the present

work, the $C(OH)_3^+$ cation was the only $C(OX)_3^+$ cation to have been isolated and studied in the solid state. The low-temperature crystal structure of $[C(OH)_3][AsF_6]$ and infrared and Raman spectra of $[C(OH)_3][MF_6]$ (M = As, Sb) were obtained by the HF solvolysis of $O{=}C(OSiMe_3)_2$ in the superacidic media HF/MF_5.[193] The salts were found to decompose to CO_2 and $[H_3O][MF_6]$ above –16 °C (M = As) and –4 °C (M = Sb).

While there have been a considerable number of structures determined for non-halogen/oxygen substituted carbocations,[194] relatively few crystal structures have been determined for halogen- and oxygen-substituted carbocations. These include $[F_2C{-}S{-}CF{-}S]^+$,[195] $[(CH_3)_2CF]^+$,[196] $[(m\text{-}CF_3C_6H_4)(C_6H_5)CF]^+$,[196] $[CH_3OCHF]^+$,[197] $[(o\text{-}ClC_6H_4)(C_6H_5)CCl]^+$,[198] $[ClCO]^+$,[199] $[Cl_2C{=}NH_2]^+$,[200] $[ClBrC{=}NH_2]^+$,[201] $[CH_3OCHCl]^+$,[197] $[C(OH)_2CH_3]^+$,[202,203] $[HC(OH)_2]^+$,[204] $[(C_6H_5)C(-OCH_2CH_2O-)]^+$,[205] and $[(CH_3)C(-OC(CH_3)_2C(CH_3)_2O-)]^+$.[206] Until the present work, the CI_3^+ and $C(OH)_3^+$ cations were the only perhalogen- and peroxygen-substituted cations to have been characterized by single crystal X-ray diffraction.[101,193]

Given the relative paucity of solid state structural data for trihalomethyl cations, electronic structure calculations have been heavily relied upon for metric data and have been used to account for the bonding and chemical properties of these cations. The relative stabilities of the trihalomethyl cations have been assessed in terms of relative degrees of σ and p(π) donation from the halogen atom to the carbon center.[101,187,196,199,207-210] The σ effect, from the perspective of the halogen atoms of CX_3^+, has been found to be strongly withdrawing in the case of fluorine and weakly donating in the cases of chlorine, bromine and iodine (I > Br > Cl). Conversely, p(π) back-donation is weak for fluorine

and stronger for the heavier halogens (I > Br > Cl). Other properties have been computed for the CX_3^+ series, including ^{13}C chemical shifts,[211] fluoride ion affinities (as measures of Lewis acidities),[101,210] vibrational frequencies,[185] and atomic charges.[101,187,196,199,207-210]

While prior syntheses of long-lived perhalomethyl cations have been achieved by halide abstraction by use of either a strong Lewis acid (in superacidic or SO_2ClF solvent media) or Ag^+ (vide supra), no routes to such carbocations through oxidative removal of a halogen bound to carbon are presently known. Among the objectives of this chapter are to provide structural and spectroscopic data for the perhalomethyl cations and related $OTeF_5$-substituted cations that, thus far, have been lacking for these systems. The present chapter details an oxidative route to carbocations using the strongly oxidizing salt, $[XeOTeF_5][Sb(OTeF_5)_6]$ (see Chapter 5), and represents an interesting new application of noble-gas compounds to chemical syntheses (see Chapter 1).[81,87,89] The present solution, solid state, and computational studies compliment previous solution ^{13}C NMR studies of the CCl_3^+, CBr_3^+, and CI_3^+ [101,186,187] cations and the X-ray structure of the CI_3^+ cation.[101]

6.2. Results and Discussion

6.2.1. Syntheses of $[CCl_3][Sb(OTeF_5)_6]$, $[CBr_n(OTeF_5)_{3-n}][Sb(OTeF_5)_6]$ (n = 0, 1, 3), $[Br(OTeF_5)_2][Sb(OTeF_5)_6]$, and $C(OTeF_5)_4$ and Solution Characterization by ^{19}F and ^{13}C NMR Spectroscopy

The products of the reactions described below were initially characterized in SO_2ClF solution by ^{13}C and ^{19}F NMR spectroscopy, and their NMR parameters are provided in Table 6.1.

Table 6.1. The ^{13}C and ^{19}F NMR Parameters[a] for $C(OTeF_5)_4$ and $CBr_n(OTeF_5)_{3-n}^+$ (n = 0–3), and Products Resulting from the Reaction of $[XeOTeF_5][Sb(OTeF_5)_6]$ with CCl_4 and CBr_4

	chem shift (δ), ppm [b]			coupling constant, Hz [b]						100 (total satellite intens /central peak intens) [c]
Species	^{13}C	$^{19}F_B$	$^{19}F_A$	$^2J(^{13}C–^{125}Te)$	$^2J(^{19}F_A–^{19}F_B)$	$^1J(^{19}F_B–^{125}Te)$	$^1J(^{19}F_A–^{125}Te)$	$^1J(^{19}F_B–^{123}Te)$	$^1J(^{19}F_A–^{123}Te)$	^{125}Te
CCl_3^+ [d]	237.1									
CBr_3^+ [d]	209.7									
$CBr_2(OTeF_5)^+$ [d]	201.1[e]	–19.9	–61.3		156	4099				
$CBr(OTeF_5)_2^+$ [d]	187 6	–24.4	–59 3		162	4029	(4075)	3343		
$C(OTeF_5)_3^+$ [d]	168.8	–31.6	–57.6	69	164	4025	4012	3337		12 ± 1 (12 7)
$C(OTeF_5)_4$	115.8	–41.5	–49.9	64	180	3758	3653	3120	3029	16.9 ± 0.1 (16.8)
$Br(OTeF_5)_2^+$ [d]		–24 4	–58 2		164	4013	(4047)	3324	(3350)	
$BrOTeF_5$ [f]		–53.8	–47.0		180	3786	3419	3140		
$ClOTeF_5$		–54 0	–49.2		178	3852	3474			
$Sb(OTeF_5)_6^-$ [d]		–42.6				3563				

[a] Nuclear magnetic resonance spectra were obtained for SO_2ClF solutions at –80 °C ($\delta(^{19}F)$, 98.3 ppm; primary and secondary isotope shifts: $^2\Delta^{19}F(^{16/18}O)$, 0.043 ppm, $^1\Delta^{19}F(^{32/34}S)$, 0.061 ppm and $^2\Delta^{19}F(^{35/37}Cl)$, 0.008 ppm. [b] The symbols, F_B and F_A, denote equatorial and axial fluorine atoms, respectively. [c] Ratios calculated from natural isotopic abundances are given in parentheses. [d] The $Sb(OTeF_5)_6^-$ anion parameters apply to all carbocation salts and to the $Br(OTeF_5)_2^+$ salt of $Sb(OTeF_5)_6^-$; also see ref 35. [e] Predicted from pairwise additivity parameters as described in Section 6.2.5. [f] See ref 212 and 164.

The synthesis and X-ray crystal structure of $[XeOTeF_5][Sb(OTeF_5)_6]\cdot SO_2ClF$ has been described in Chapter 5.[140] Unlike its fluorine analogue, $[XeF][SbF_6]$, which is insoluble in SO_2ClF at room temperature, the solubility of $[XeOTeF_5][Sb(OTeF_5)_6]$ in SO_2ClF exceeds 2M at –78 °C, forming an intense yellow solution. The salt rapidly oxidizes equimolar amounts of CCl_4 at –78 °C to yield clear, colorless solutions of $[CCl_3][Sb(OTeF_5)_6]$ according to eq 6.1. Removal of SO_2ClF and other volatile

$$[XeOTeF_5][Sb(OTeF_5)_6] + CCl_4 \longrightarrow [CCl_3][Sb(OTeF_5)_6] + ClOTeF_5 + Xe \quad (6.1)$$

components under vacuum between –78 and 0 °C gave colorless, crystalline $[CCl_3][Sb(OTeF_5)_6]$ (see Section 6.2.2), which was found to be stable indefinitely at room temperature.

The ^{13}C NMR spectrum (SO_2ClF solvent, –80 °C) of the products resulting from eq 6.1 give rise to a sharp singlet (237.1 ppm) assigned to $[CCl_3][Sb(OTeF_5)_6]$, which is in agreement with the previously reported value (236.3 ppm).[186] The ^{13}C chemical shift of CCl_3^+ is significantly deshielded relative to CCl_4 [$\delta(^{13}C)$, 96.4 ppm; SO_2ClF, –80 °C], which is consistent with carbocation formation (see Section 6.2.5). The ^{19}F NMR spectrum shows the severe AB_4 pattern that typifies the $Sb(OTeF_5)_6^-$ anion[35] and a well-resolved AB_4 pattern for $ClOTeF_5$ (Table 6.1).[213]

The reaction of equimolar amounts of CBr_4 with $[XeOTeF_5][Sb(OTeF_5)_6]$ in SO_2ClF is initially rapid at –78 °C, giving a deep red-brown solution which lightens to red-orange over a period of several hours at ca. –50 °C. The color change corresponds to

the further reaction of the CBr_3^+ cation with $BrOTeF_5$ to produce Br_2 and the mixed carbocations, $CBr_2(OTeF_5)^+$, $CBr(OTeF_5)_2^+$, and, ultimately, $C(OTeF_5)_3^+$ according to eq 6.2–6.5, with the overall reaction being represented by eq 6.6. Removal of SO_2ClF and

$$3[XeOTeF_5][Sb(OTeF_5)_6] + 3CBr_4 \longrightarrow 3[CBr_3][Sb(OTeF_5)_6] + 3BrOTeF_5 + 3Xe \quad (6.2)$$

$$[CBr_3][Sb(OTeF_5)_6] + BrOTeF_5 \longrightarrow [CBr_2(OTeF_5)][Sb(OTeF_5)_6] + Br_2 \quad (6.3)$$

$$[CBr_2(OTeF_5)][Sb(OTeF_5)_6] + BrOTeF_5 \longrightarrow [CBr(OTeF_5)_2][Sb(OTeF_5)_6] + Br_2 \quad (6.4)$$

$$[CBr\,(OTeF_5)_2][Sb(OTeF_5)_6] + BrOTeF_5 \longrightarrow [C(OTeF_5)_3][Sb(OTeF_5)_6] + Br_2 \quad (6.5)$$

$$3[XeOTeF_5][Sb(OTeF_5)_6] + 3CBr_4 \longrightarrow 2[CBr_3][Sb(OTeF_5)_6] + [C(OTeF_5)_3][Sb(OTeF_5)_6] + 3Br_2 + 3Xe \quad (6.6)$$

other volatile components under vacuum between –78 and 0 °C resulted in a pale yellow-orange solid that was stable indefinitely at room temperature. The $[CBr_3][Sb(OTeF_5)_6]$ and $[C(OTeF_5)_3][Sb(OTeF_5)_6]$ salts have been characterized by single-crystal X-ray diffraction and Br_2 was identified by determination of the unit cell parameters from a single crystal at –173 °C (see Chapter 2).

The ^{13}C NMR spectrum of $[CBr_3][Sb(OTeF_5)_6]$ in SO_2ClF at –80 °C gave rise to a singlet (209.7 ppm), in good agreement with the previously reported value (207 ppm).[186]

As in the case of CCl_3^+, the ^{13}C resonance of CBr_3^+ is significantly deshielded with respect to that of its parent molecule, CBr_4 ($\delta(^{13}C)$, –29.7 ppm; SO_2ClF, –80 °C), which is characteristic of carbocation formation (see Section 6.2.5). The ^{19}F NMR spectrum shows a severe AB_4 pattern corresponding to the $Sb(OTeF_5)_6^-$ anion (Table 6.1), similar to that obtained for $[CCl_3][Sb(OTeF_5)_6]$. The ^{19}F NMR spectrum of a sample of pure $BrOTeF_5$ dissolved in SO_2ClF at –80 °C (Table 6.1) was also obtained and demonstrated that $BrOTeF_5$, as proposed in eq 6.2, was not present in detectable quantities. The absence of $BrOTeF_5$ is consistent with the formation of mixed Br/$OTeF_5$-substituted methyl cations and the oxidation of $BrOTeF_5$ by $[XeOTeF_5][Sb(OTeF_5)_6]$ to give the new $Br(OTeF_5)_2^+$ cation (eq 6.7). The formation of $Br(OTeF_5)_2^+$ was confirmed by reaction of $BrOTeF_5$

$$[XeOTeF_5][Sb(OTeF_5)_6] + BrOTeF_5 \longrightarrow [Br(OTeF_5)_2][Sb(OTeF_5)_6] + Xe \quad (6.7)$$

with $[XeOTeF_5][Sb(OTeF_5)_6]$ in SO_2ClF at –78 °C in a separate experiment.

The formation of the $CBr_n(OTeF_5)_{3-n}^+$ (n = 1–3) cations and their NMR assignments were confirmed by addition of $BrOTeF_5$ at –20 °C to the reaction products of eq 6.6, in a 3:1 molar ratio relative to the initial amounts of $[XeOTeF_5][Sb(OTeF_5)_6]$ and CBr_4. This resulted in increased amounts of the $OTeF_5$-containing carbocations and Br_2 as outlined in eq 6.3–6.5 (Table 6.1). The ^{13}C NMR spectrum indicated that a small quantity of $[CBr_3][Sb(OTeF_5)_6]$ remained unreacted (7% based on integration of all ^{13}C resonances), with $[C(OTeF_5)_3][Sb(OTeF_5)_6]$ as the major product (70%; $\delta(^{13}C)$, 168.8 ppm). Of the mixed $OTeF_5$-substituted bromocations, $CBr_n(OTeF_5)_{3-n}^+$ (n = 1, 2), only

the $CBr(OTeF_5)_2^+$ cation was detected by ^{13}C NMR spectroscopy (10%; $\delta(^{13}C)$, 187.6 ppm), while the ^{13}C chemical shift of the $CBr_2(OTeF_5)^+$ cation was predicted by use of pairwise additivity parameters ($\delta(^{13}C)$, 201.1 ppm; see Section 6.2.5). A singlet was also observed (13%; $\delta(^{13}C)$, 124.7 ppm) that is tentatively assigned to $O{=}C(OTeF_5)_2$ based on the similarity of its ^{13}C chemical shift to that of $O{=}CF_2$ (134.2 ppm),[214] and may arise from the formal loss of the TeF_5^+ cation from $C(OTeF_5)_3^+$ according to eq 6.8. Alternatively, $O{=}C(OTeF_5)_2$ may prove to be unstable, decomposing to CO_2 ($\delta(^{13}C)$, 124.2 ppm)[215] and $O(TeF_5)_2$ ($\delta(^{19}F_B)$, –41.4 ppm; F_A was not observed because of overlap with F_A of $C(OTeF_5)_3^+$; $^2J(^{19}F_B{-}^{19}F_A)$, 164 Hz) according to eq 6.9. The TeF_5^+ cation

$$[C(OTeF_5)_3][Sb(OTeF_5)_6] \longrightarrow O{=}C(OTeF_5)_2 + [TeF_5][\,Sb(OTeF_5)_6] \quad (6.8)$$

$$O{=}C(OTeF_5)_2 \longrightarrow CO_2 + O(TeF_5)_2 \quad (6.9)$$

presumably is not observed because of its high electrophilicity, which leads to $OTeF_5^-$ abstraction from $Sb(OTeF_5)_6^-$, forming $O(TeF_5)_2$ according to eq 6.10 and/or F^- abstractions to form TeF_6 [$\delta(^{19}F)$, –52.6 ppm; $^1J(^{19}F{-}^{125}Te)$, 3747 Hz; $^1J(^{19}F{-}^{123}Te)$, 3095 Hz] according to eq 6.11. The proposed species, $Sb(OTeF_5)_5$, which is known to be unstable,[110,216] and $F_4TeOSb(OTeF_5)_5$, have not been investigated further in this study.

$$[TeF_5][Sb(OTeF_5)_6] \longrightarrow O(TeF_5)_2 + Sb(OTeF_5)_5 \quad (6.10)$$

$$[TeF_5][Sb(OTeF_5)_6] \longrightarrow TeF_6 + F_4TeOSb(OTeF_5)_5 \quad (6.11)$$

The formation of the $C(OTeF_5)_3^+$ cation was confirmed by the presence of a satellite doublet in the ^{13}C NMR spectrum ($^2J(^{13}C–^{125}Te)$, 69 Hz). The similar gyromagnetic ratios of ^{123}Te and ^{125}Te and the low natural abundance of ^{123}Te (0.87%) relative to ^{125}Te (6.99%) precluded the observation of separate ^{123}Te satellites because of overlap with the more intense ^{125}Te satellites ($\nu_{1/2} \approx 5$ Hz), however, using $^nJ_{AB} = (\gamma_A {}^nJ_{A'B}/\gamma_{A'})$, the calculated value for $^2J(^{13}C–^{123}Te)$ is 57 Hz. By combining the intensities expected for coupling to ^{123}Te and ^{125}Te (7.86 %), the observed satellite peak/central peak integrated intensity ratios 0.111 : 1.000 : 0.123 in the ^{13}C NMR spectrum was shown to be consistent with the calculated satellite peak/central peak intensity ratios 0.0001 : 0.0054 : 0.1268 : 1.0000 : 0.1268 : 0.0054 : 0.0001 expected for a series of overlapping subspectra that arise from coupling to three chemically equivalent tellurium atoms.[161] Tellurium satellites were not observed for the $CBr(OTeF_5)_2^+$ cation owing to the low concentration of this species (10%).

In order to compare the NMR parameters of $C(OTeF_5)_3^+$ with those of the unknown neutral parent, $C(OTeF_5)_4$, CBr_4 was allowed to react with a stoichiometric amount of $BrOTeF_5$ at –78 °C according to eq 6.12. Details of the synthesis and

$$CBr_4 + 4\ BrOTeF_5 \longrightarrow C(OTeF_5)_4 + 4\ Br_2 \qquad (6.12)$$

structural characterization of $C(OTeF_5)_4$ are provided in Chapter 8. As expected, the ^{13}C chemical shift of $C(OTeF_5)_4$ (115.8 ppm) is significantly shielded with respect to that of the $C(OTeF_5)_3^+$ cation.

6.2.2. X-ray Crystal Structures of $[CCl_3][Sb(OTeF_5)_6]$, $[CBr_3][Sb(OTeF_5)_6]\cdot SO_2ClF$, and $[C(OTeF_5)_3][Sb(OTeF_5)_6]\cdot 3SO_2ClF$

Details of data collection parameters and other crystallographic information are provided in Table 6.2. Bond lengths and bond angles for the CCl_3^+, CBr_3^+, and $C(OTeF_5)_3^+$ cations are listed in Table 6.3. Closest secondary contacts between the carbon and halogen atoms of the cations and the fluorine atoms of the anion or oxygen atoms of the SO_2ClF solvent molecules are also given in Table 6.3 together with important bond lengths and bond angles for the $Sb(OTeF_5)_6^-$ anions and SO_2ClF solvent molecules. A complete list of bond lengths and bond angles for the $Sb(OTeF_5)_6^-$ anions and SO_2ClF solvent molecules is also provided (Table 6.3).

The present work reports the first crystal structures of the CCl_3^+, CBr_3^+, and $C(OTeF_5)_3^+$ cations. The $Sb(OTeF_5)_6^-$ anion, which has been described previously,[35,79] is comprised of a central antimony atom coordinated to six oxygen atoms and each of the six tellurium atoms is octahedrally coordinated to one oxygen and five fluorine atoms so that the anion structure can be described as an octahedron of octahedra. Bond angles and bond lengths of the $Sb(OTeF_5)_6^-$ anions reported in the present study are in good agreement with those reported in the crystal structures of, for example, $[SbBr_4][Sb(OTeF_5)_6]$,[79] $[SbCl_4][Sb(OTeF_5)_6]$,[79] $[N(CH_3)_4][Sb(OTeF_5)_6]$[35] and$[N(CH_2CH_3)_4][Sb(OTeF_5)_6]$,[35] and therefore require no further comment. The SO_2ClF solvent molecules present in the structures of $[CBr_3][Sb(OTeF_5)_6]\cdot SO_2ClF$ and $[C(OTeF_5)_3][Sb(OTeF_5)_6]\cdot 3SO_2ClF$ have the expected pseudo-tetrahedral geometry, with the S–O, S–Cl and S–F bond lengths in agreement with those obtained from the X-ray

Table 6.2. Crystallographic Data for $[CCl_3][Sb(OTeF_5)_6]$, $[CBr_3][Sb(OTeF_5)_6]\cdot SO_2ClF$, and $[C(OTeF_5)_3][Sb(OTeF_5)_6]\cdot 3SO_2ClF$

	CCl_3^+	$C(OTeF_5)_3^+$	CBr_3^+
chem formula	$CCl_3F_{30}O_6SbTe_6$	$CCl_3F_{48}O_{15}S_3SbTe_9$	$CClBr_3F_{31}O_8SSbTe_6$
space group	$P\bar{1}$	$P\bar{1}$	$P2_1/n$
a (Å)	8.706(2)	10.082(4)	18.617(6)
b (Å)	9.181(2)	10.950(4)	9.935(3)
c (Å)	9.862(2)	24.572(10)	19.129(7)
α (deg)	104.111(5)	83.482(8)	90
β (deg)	103.507(5)	81.679(7)	90.781(7)
γ (deg)	98.851(5)	70.019(7)	90
V (Å^3)	724.5(5)	2517(3)	3538(4)
molecules/unit cell	1	2	4
mol wt (g mol^{-1})	1671.71	2636.769	1923.6
calcd density (g cm^{-3})	3.832	3.480	3.611
T (°C)	–173	–173	–173
μ (cm^{-1})	73.7	61.7	93.5
R_1 [a]	0.0355	0.0668	0.0621
wR_2 [b]	0.0736	0.1259	0.1211

[a] R_1 is defined as $\Sigma||F_o|-|F_c||/\Sigma|F_o|$ for $I > 2\sigma(I)$. [b] wR_2 is defined as $[\Sigma[w(F_o^2 - F_c^2)^2]/\Sigma w(F_o^2)^2]^{1/2}$ for $I > 2\sigma(I)$.

Table 6.3. Experimental Geometries in $[CCl_3][Sb(OTeF_5)_6]$, $[CBr_3][Sb(OTeF_5)_6]\cdot SO_2ClF$, and $[C(OTeF_5)_3][Sb(OTeF_5)_6]\cdot 3SO_2ClF$

CCl_3^+

bond lengths (Å)		bond angles (deg)	
C(1)–Cl(1)	1.672(11)	Cl(1)–C(1)–Cl(2)	118.4(8)
C(1)–Cl(2)	1.598(12)	Cl(1)–C(1)–Cl(3)	118.7(7)
C(1)–Cl(3)	1.592(13)	Cl(2) –C(1)–Cl(3)	123.3(8)
C(1)···F(14A)	2.962(9) [3°][a]		
C(1)···F(14)	3.464(9) [4°][a]		
C(1)···F(8A)	3.574(11) [13°][a]		
C(1)···F(2A)	3.574(11) [37°][a]		

CBr_3^+

bond lengths (Å)		bond angles (deg)	
C(1)–Br(1)	1.851(16)	Br(1)–C(1)–Br(2)	119.1(9)
C(1)–Br(2)	1.787(16)	Br(1)–C(1)–Br(3)	117.9(9)
C(1)–Br(3)	1.783(16)	Br(2)–C(1)–Br(3)	122.9(9)
C(1)···F(44A)	3.39(2) [8°][a]		
C(1)···F(24A)	3.09(2) [8°][a]		

$C(OTeF_5)_3^+$

bond lengths (Å)					
C(1)–O(1)	1.313(16)	C(1)–O(2)	1.279(13)	C(1)–O(3)	1.258(15)
Te(1)–O(1)	1.988(7)	Te(2)–O(2)	1.974(8)	Te(3)–O(3)	1.977(9)
Te(1)–F(1)	1.816(6)	Te(2)–F(6)	1.798(8)	Te(3)–F(11)	1.819(8)
Te(1)–F(2)	1.816(8)	Te(2)–F(7)	1.812(8)	Te(3)–F(12)	1.795(8)
Te(1)–F(3)	1.801(8)	Te(2)–F(8)	1.810(7)	Te(3)–F(13)	1.820(6)
Te(1)–F(4)	1.813(8)	Te(2)–F(9)	1.816(9)	Te(3)–F(14)	1.799(6)
Te(1)–F(5)	1.814(8)	Te(2)–F(10)	1.808(8)	Te(3)–F(15)	1.809(8)
C(1)···O(11)	2.690(17) [1°][a]	C(1)···O(15A)	2.738(18) [3°][a]		

Table 6.3. (continued...)

bond angles (deg)					
O(1)–C(1)–O(2)	119(1)	O(1)–C(1)–O(3)	119.8(9)	O(2)–C(1)–O(3)	121(1)
C(1)–O(1)–Te(1)	125.5(7)	C(1)–O(2)–Te(2)	132.7(9)	C(1)–O(3)–Te(3)	131.2(8)
O(1)–Te(1)–F(1)	176.8(4)	O(2)–Te(2)–F(6)	176.2(4)	O(3)–Te(3)–F(11)	174.6(3)
O(1)–Te(1)–F(2)	91.2(3)	O(2)–Te(2)–F(7)	90.1(4)	O(3)–Te(3)–F(12)	85.4(4)
O(1)–Te(1)–F(3)	84.2(3)	O(2)–Te(2)–F(8)	89.9(4)	O(3)–Te(3)–F(13)	91.8(4)
O(1)–Te(1)–F(4)	89.2(3)	O(2)–Te(2)-F(9)	84.5(4)	O(3)–Te(3)–F(14)	82.5(3)
O(1)–Te(1)–F(5)	86.0(3)	O(2)–Te(2)–F(10)	85.3(4)	O(3)–Te(3)–F(15)	89.1(4)
F(1)–Te(1)–F(2)	91.4(3)	F(6)–Te(2)–F(7)	92.6(4)	F(11)–Te(3)–F(12)	93.0(4)
F(1)–Te(1)–F(3)	93.9(3)	F(6)–Te(2)–F(8)	92.8(4)	F(11)–Te(3)–F(13)	93.3(3)
F(1)–Te(1)–F(4)	92.8(3)	F(6)-Te(2)–F(9)	92.8(4)	F(11)–Te(3)–F(14)	92.5(4)
F(1)–Te(1)–F(5)	91.4(3)	F(6)–Te(2)–F(10)	92.0(4)	F(11)–Te(3)–F(15)	92.7(4)
F(2)–Te(1)–F(3)	88.7(4)	F(7)–Te(2)–F(8)	89.7(4)	F(12)–Te(3)–F(13)	90.0(3)
F(2)–Te(1)–F(4)	89.7(4)	F(7)–Te(2)–F(9)	90.2(4)	F(12)–Te(3)–F(14)	90.9(3)
F(2)–Te(1)–F(5)	177.1(3)	F(7)–Te(2)–F(10)	175.4(4)	F(12)–Te(3)–F(15)	174.3(4)
F(3)–Te(1)–F(4)	173.2(3)	F(8)–Te(2)–F(9)	174.4(4)	F(13)–Te(3)–F(14)	174.1(4)
F(3)–Te(1)–F(5)	90.7(4)	F(8)–Te(2)–F(10)	90.0(4)	F(13)–Te(3)–F(15)	89.2(3)
F(4)–Te(1)–F(5)	90.6(4)	F(9)–Te(2)–F(10)	89.6(4)	F(14)–Te(3)–F(15)	89.6(3)

$Sb(OTeF_5)_6^-$	CCl_3^+ salt	CBr_3^+ salt	$C(OTeF_5)_3^+$ salt
	bond lengths (Å)		
Sb–O	1.951(3) – 1.955(3)	1.936(10) – 1.981(10)	1.934(9) – 1.957(9)
Te–O	1.844(4) – 1.854(3)	1.819(10) – 1.868(10)	1.832(9) – 1.858(9)
$Te–F_{ax}$	1.834(3) – 1.839(3)	1.833(9) – 1.852(9)	1.819(8) – 1.836(6)
$Te–F_{eq}$	1.819(3) – 1.841(3)	1.807(10) – 1.849(9)	1.809(7) – 1.840(6)
	bond angles (deg)		
Sb–O–Te	137.9(2) – 138.2(2)	138.0(6) – 140.7(6)	137.2(4) – 139.3(4)

Table 6.3. (continued...)

SO_2ClF	CBr_3^+ salt	$C(OTeF_5)_3^+$ salt
	bond lengths (Å)	
S–O	1.404(13) – 1.417(12)	1.384(11) – 1.407(9)
S–F	1.533(10)	1.519(7) – 1.520(10)
S–Cl	1.942(7)	1.918(6) – 1.951(6)
	bond angles (deg)	
O–S–O	120.9(9)	120.1(7) – 122.3(8)
O–S–Cl	109.9(6) – 110.0(6)	108.2(5) – 111.7(6)
O–S–F	107.0(8) – 108.7(7)	106.7(8) – 109.4(6)
F–S–Cl	97.8(5)	94.6(5) – 99.7(4)

[a] Values in square brackets represent the angle between the pseudo-C_3-axis passing through carbon and the C···F/C···O trajectories.

crystal structure of SO_2ClF[166] and require no further comment (Table 6.3). There are no notable differences between the metric parameters of the two coordinated and one uncoordinated SO_2ClF molecule in the $[C(OTeF_5)_3][Sb(OTeF_5)_6]\cdot 3SO_2ClF$ structure.

6.2.2.1. $[CCl_3][Sb(OTeF_5)_6]$ and $[CBr_3][Sb(OTeF_5)_6]\cdot SO_2ClF$

The trigonal planar CCl_3^+ cation in $[CCl_3][Sb(OTeF_5)_6]$ is positionally two-fold disordered about the crystallographic inversion center (Figure 6.1). In contrast, the CBr_3^+ cation in $[CBr_3][Sb(OTeF_5)_6]\cdot SO_2ClF$ is not disordered (Figure 6.2). In both cases, the three halogen atoms are crystallographically independent and carbocation planarity is not imposed by symmetry. Both cations are planar, with X–C–X bond angle sums of 360(1)° (CCl_3^+) and 360(1)° (CBr_3^+). The C–Br bond lengths and Br–C–Br angles of CBr_3^+ are all equal within ±3σ, giving the expected D_{3h} symmetry. As a consequence of the disorder, the CCl_3^+ cation gives a slightly wider range of bond lengths and angles, but displays essentially D_{3h} symmetry in its crystal structure. The C–Cl and C–Br bond lengths are found to be shorter than in CCl_4 (1.751(13) Å),[217] $CFCl_3$ (1.75(1) Å)[218] and CBr_4 (1.91(4) Å)[219] by ca. 0.15 Å, 0.13 Å, and 0.10 Å, respectively, as expected for cations (see Section 6.2.4). In the case of the previously reported structures of chloro- and bromo-substituted carbocations, the C–Cl or C–Br bond lengths are marginally longer than in CCl_3^+ and CBr_3^+, i.e. $[(o\text{-}ClC_6H_4)(C_6H_5)CCl][SbF_6]$[198] (C–Cl, 1.668(8) Å), $[Cl_2C{=}NH_2][SbCl_6]$[200] (C–Cl, 1.663(6)-1.680(6) Å), $[CH_3OCHCl][SbF_6]$[197] (C–Cl, 1.650(9) Å) and $[ClBrC{=}NH_2][SbCl_6]$[201] (C–Cl, 1.69(1); C–Br, 1.843(9) Å). In the CCl_3^+ and CBr_3^+ salts, the shortest cation-anion C···F contacts are 2.962(9) Å and 3.09(2) Å, respectively, (cf.

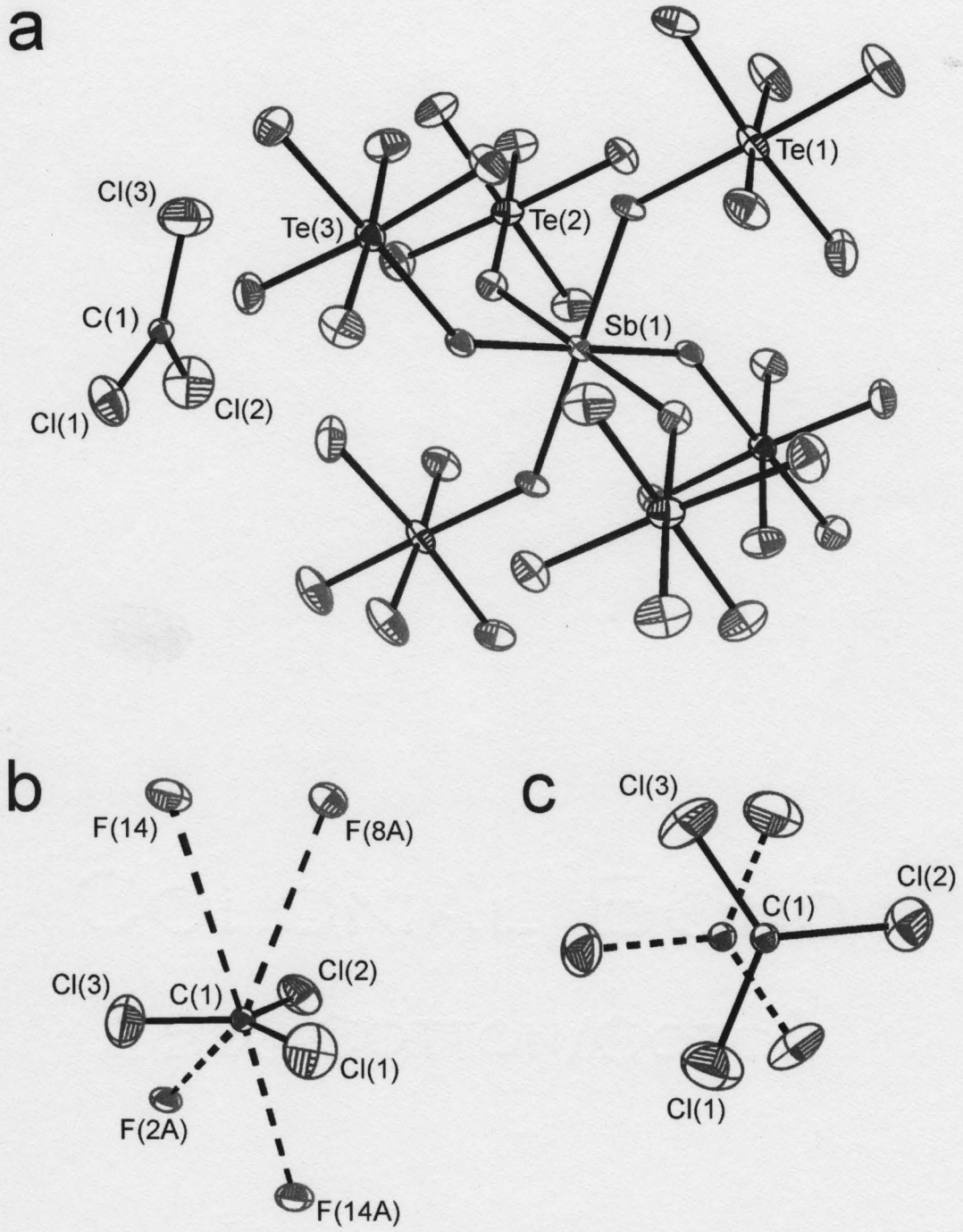

Figure 6.1. (a) Crystal structure of $[CCl_3][Sb(OTeF_5)_6]$; thermal ellipsoids are shown at the 50% probability level. (b) A view of the CCl_3^+ cation showing the shortest contacts between carbon and the fluorine atoms of the $Sb(OTeF_5)_6^-$ anion. (c) A view of the CCl_3^+ cation showing the two-fold positional disorder around the crystallographic inversion center.

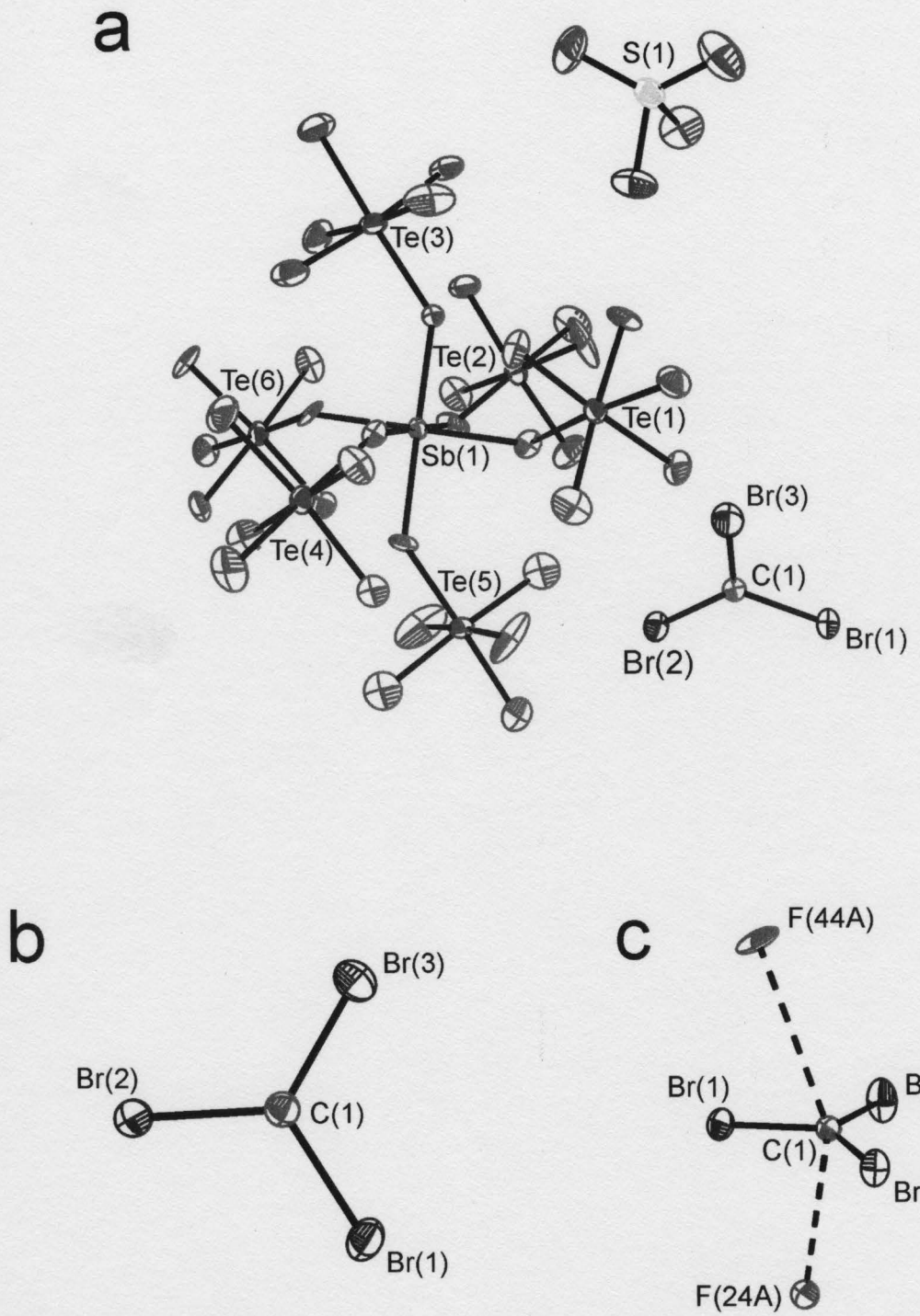

Figure 6.2. (a) Crystal structure of $[CBr_3][Sb(OTeF_5)_6]\cdot SO_2ClF$; thermal ellipsoids are shown at the 50% probability level. (b) A view of the CBr_3^+ cation showing the shortest contacts between carbon and the fluorine atoms of the $Sb(OTeF_5)_6^-$ anion.

the sum of the carbon and fluorine van der Waals radii, 3.10,[220] 3.30[26] Å). These contacts approach the carbon at angles of 3° (CCl_3^+) and 8° (CBr_3^+) with respect to the C_3-axis. As well, longer C···F contacts (CCl_3^+, 3.464(9), 3.574(11) and 3.574(11) Å; CBr_3^+, 3.39(2) Å) approach above and below the CX_3-plane at angles of 4, 13 and 37° (CCl_3^+) and 8° (CBr_3^+), respectively. The bond length and bond angle trends are consistent with the previously noted trend of decreasing contact angle with decreasing contact distance in a number of carbocation structures.[194] The present structures indicate that the $Sb(OTeF_5)_6^-$ anions are very weakly coordinated to the carbon centers. The occurrence of cation-anion contacts is a common feature, and the present C···F contact distances are comparable to those observed in $[CI_3][Al(OC(CF_3)_3)_4]$[101] (the shortest is 3.26 Å) and in $[(m\text{-}CF_3C_6H_4)(C_6H_5)CF][As_2F_{11}]$ (3.01(2) and 3.07(2) Å).[196] The chlorine and bromine atoms also interact with the fluorine atoms of the anion and, in the case of the CBr_3^+ salt, with the oxygen atoms of SO_2ClF (Cl···F: 2.833(5)–3.022(5) Å; Br···F: 2.977(9)–3.301(11) Å; Br···O: 2.778(13), 2.839(12) Å). These interactions are shorter than or are at the limit of the sum of the halogen-fluorine(oxygen) van der Waals radii (Cl···F, 3.15,[220] 3.22[26] Å; Br···O, 3.35,[220] 3.37[26] Å; Br···F, 3.30,[220] 3.32[26] Å) and are apparently a consequence of the positive charges on the halogen atoms (see Section 6.2.4). The Br···O contacts, which occur with the oxygen atoms of two SO_2ClF solvent molecules, are shorter than the secondary C···F cation-anion contacts in the CCl_3^+ and CBr_3^+ salts and are likely responsible for the absence of disorder in the CBr_3^+ structure.

6.2.2.2. $[C(OTeF_5)_3][Sb(OTeF_5)_6]\cdot 3SO_2ClF$

The crystal structure of $[C(OTeF_5)_3][Sb(OTeF_5)_6]\cdot 3SO_2ClF$ consists of $Sb(OTeF_5)_6^-$ anions that are well separated from the cations and the solvent molecules, while two of the three SO_2ClF solvent molecules are oxygen coordinated to the carbon atom of the cation (Figure 6.3).

The $C(OTeF_5)_3^+$ cation is isoelectronic and isostructural with the known $B(OTeF_5)_3$ molecule.[221] To the best of the author's knowledge, the $C(OTeF_5)_3^+$ cation is only the second example of a trioxygen-substituted carbocation to have been isolated and characterized in the solid state by X-ray crystallography, the first being the AsF_6^- salt of the trigonal planar acidium ion of carbonic acid, $C(OH)_3^+$.[193] The O–C–O angles of the $C(OTeF_5)_3^+$ cation are equal, within $\pm 3\sigma$, to the ideal 120° angle expected for a trigonal planar arrangement. Unlike $B(OTeF_5)_3$ and $C(OH)_3^+$, which have BO_3 and CO_3 arrangements that are planar by symmetry (C_{3h} point symmetry), the planarity of the CO_3 moiety of $C(OTeF_5)_3^+$ is not forced by symmetry, and the three $OTeF_5$ groups bonded to the central carbon atom are crystallographically independent. Despite the low local crystallographic symmetry of $C(OTeF_5)_3^+$ (C_1), the conformational geometry of the cation is very close to the optimized C_{3h} gas-phase geometry of this cation and the known solid state[221] and calculated gas-phase (see Section 6.2.4) geometries of $B(OTeF_5)_3$. The tellurium and axial fluorine atoms are slightly out of plane and lie to one side of the CO_3 plane by 0.087 and 0.149 Å, respectively. The C–O bond lengths are similar to those in $C(OH)_3^+$ (1.231(4) Å),[193] $CH_3C(OH)_2^+$ (1.265(6), 1.272(6) Å;[202] 1.261(7), 1.273(7) Å[203]), and $HC(OH)_2^+$ (1.239(6), 1.255(5) Å).[204] As expected for a positively charged

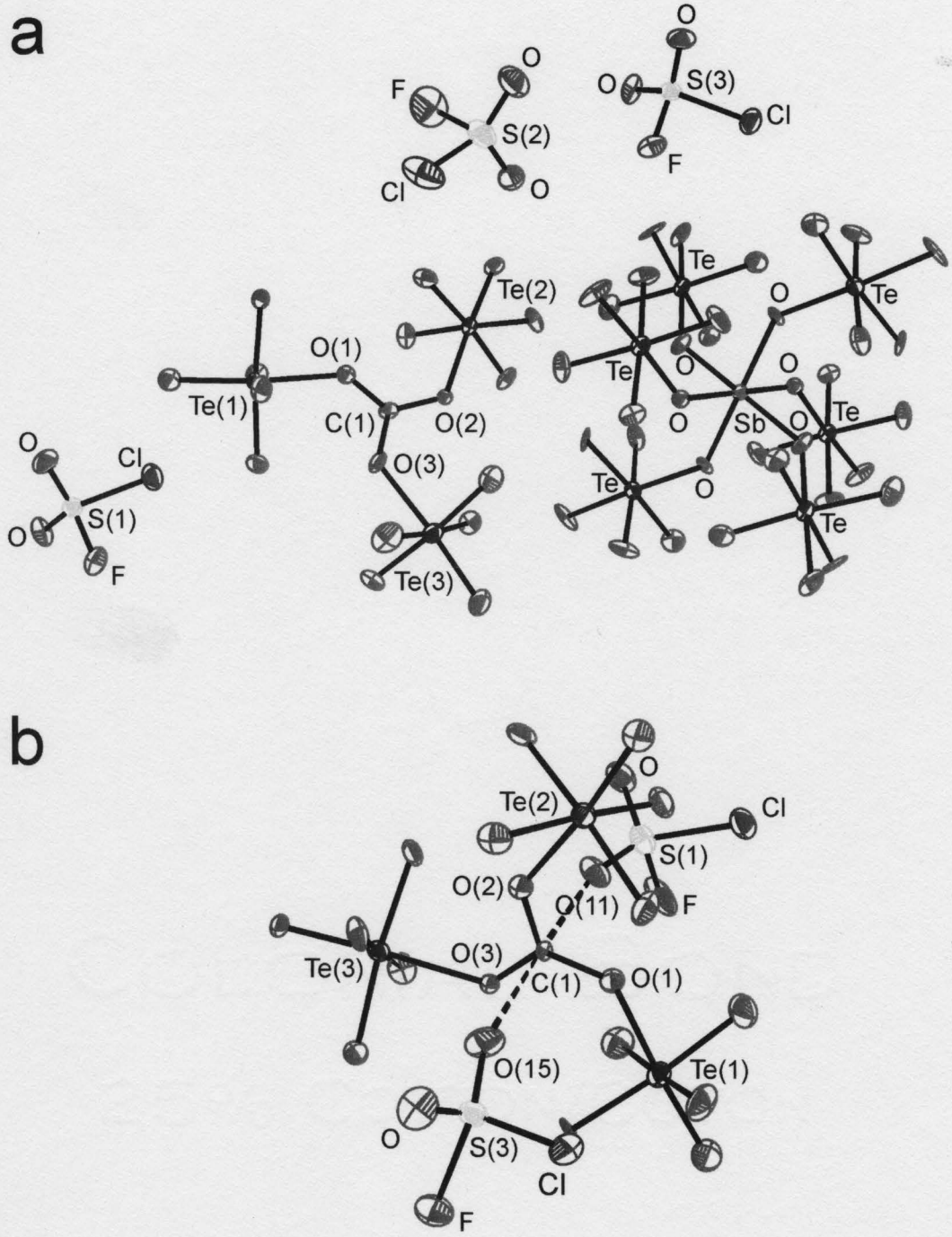

Figure 6.3. (a) Crystal structure of $[C(OTeF_5)_3][Sb(OTeF_5)_6]\cdot 3SO_2ClF$; thermal ellipsoids are shown at the 50% probability level. (b) A view of the $C(OTeF_5)_3^+$ cation showing the contacts between the carbon atom and an oxygen atom from each of two SO_2ClF molecules in the crystal lattice.

isoelectronic species, the C–O bond lengths are shorter than the B–O bond lengths of $B(OTeF_5)_3$ (1.358(6) Å)[221] and the C–O–Te bond angles, which range from 125.7(7) to 132.4(9)°, are similar to those in $B(OTeF_5)_3$ (132.3(4)°).[221] The bond lengths and bond angles in the $OTeF_5$ groups are in good agreement with those observed for the $OTeF_5$ groups of the $Sb(OTeF_5)_6^-$ anion and other $OTeF_5$ derivatives[35,79] and require no further comment.

The $C(OTeF_5)_3^+$ cation has two short C···O contacts (2.690(17) and 2.738(18) Å) with two SO_2ClF solvent molecules (Figure 6.3, Table 6.3), which are both nearly perpendicular to the trigonal CO_3 plane, approaching the carbon atoms at angles of 1 and 3° with respect to the pseudo three-fold symmetry axis of the cation. The contact distances are significantly shorter than the sum of carbon and oxygen van der Waals radii (3.15,[220] 3.20[26] Å) and the C···F contacts in $[CCl_3][Sb(OTeF_5)_6]$ and $[CBr_3][Sb(OTeF_5)_6]\cdot SO_2ClF$; but are similar to the C···F contacts observed in $[(CH_3)_2CF][AsF_6]$ (2.66(1), 2.78(1) Å) and in [*m*-$CF_3C_6H_4$)(C_6H_5)CF][AsF_6] (2.78(1), 2.79(1) Å). These interactions with the weak Lewis base, SO_2ClF,[222-224] reflect the high positive charge borne by the carbon atom and its substantial Lewis acidity (see Section 6.2.4).

6.2.3. Raman Spectroscopy

6.2.3.1. CCl_3^+ and CBr_3^+

The vibrational modes of the CCl_3^+ and CBr_3^+ cations were assigned under D_{3h} symmetry and belong to the irreducible representation $\Gamma = A_1' + A_2'' + 2E'$. A total of

four fundamental vibrations are expected, $\nu_1(A_1')$, $\nu_2(A_2'')$, $\nu_3(E')$, and $\nu_4(E')$, of which $\nu_1(A_1')$, $\nu_3(E')$ and $\nu_4(E')$ are Raman active and $\nu_2(A_2'')$, $\nu_3(E')$, and $\nu_4(E')$ are infrared active. The Raman assignments for the CCl_3^+ and CBr_3^+ cations were made by comparison with the calculated frequencies and Raman intensities (Table 6.4), which were carried out at the MP2/6-31G(2d) and MP2/cc-pVTZ levels of theory. As a benchmark, the vibrational frequencies of CCl_4 and CBr_4 were also calculated at the same levels of theory (Table 6.5).

The low-temperature solid-state Raman spectra resulting from the reactions of CCl_4 and CBr_4 with $[Xe(OTeF_5)][Sb(OTeF_5)_6]$ displayed large numbers of bands that could be assigned to the $Sb(OTeF_5)_6^-$ anion, unreacted $XeOTeF_5^+$, and CBr_4 when an excess of CBr_4 was used (Table 6.6). In the case of CBr_4, new bands were also observed in the C–O stretching region, which are discussed in the following section. Although the presence of Br_2 could not be ascertained because the expected bands at 296.5 and 302.5 cm^{-1} for solid Br_2 (–150 °C) overlapped with bands associated with $Sb(OTeF_5)_6^-$ or unreacted $XeOTeF_5^+$, the presence of Br_2 was confirmed by a unit cell determination at –173 °C (see Chapter 2). The frequency assignments for the $Sb(OTeF_5)_6^-$ anion and unreacted $XeOTeF_5^+$ cation were made by comparison with those of $[N(CH_3)_4][Sb(OTeF_5)_6]$[35] and $[SbX_4][Sb(OTeF_5)_6]$[79] (X = Cl, Br) and $[XeOTeF_5][AsF_6]$[75] and $[XeOTeF_5][Sb(OTeF_5)_6]$,[140] respectively, and require no further comment.

In the CCl_4 system, two new bands were observed at 327 and 554 cm^{-1} which were assigned to $\nu_1(A_1')$ and $\nu_4(E')$ of CCl_3^+, respectively, in excellent agreement with the calculated frequencies and Raman intensities (Table 6.4). The high-resolution Raman

Table 6.4. Experimental and Calculated (MP2) Frequencies (cm^{-1}), Raman Intensities[a] and Assignments[b] for CX_3^+ and BX_3 (X = F, Cl, Br, I)

	CF_3^+			BF_3		
assgnts	exptl[c]	6-31G(2d)	cc-pVTZ	exptl[d]	6-31G(2d)	cc-pVTZ
$\nu_1(A_1')$, ν_s(C–F)		1048(7)	1072(7)	888 0	883(4)	895(4)
$\nu_2(A_2'')$, π(C–F_3)	798 1	843(0)	825(0)	691 5	723(0)	698(0)
$\nu_3(E')$, ν_{as}(C–F)	1662.4	1692(<1)	1717(<0)	1453 5	1475(<1)	1484(<1)
$\nu_4(E')$, δ(F–C–F)		595(1)	601(1)	480.4	491(<1)	481(<1)
	CCl_3^+			BCl_3		
assgnts	exptl	6-31G(2d)	cc-pVTZ	exptl[e]	6-31G(2d)	cc-pVTZ
$\nu_1(A_1')$, ν_s(C–Cl)	554(28)[f]	559(18)	568(17)	467 3	477(9)	483(8)
$\nu_2(A_2'')$, π(C–Cl_3)		538(0)	541(0)	447 3[i]	465(0)	465(0)
$\nu_3(E')$, ν_{as}(C–Cl)	1035,[g]1037[h]	1072(<1)	1086(<1)	931	970(<1)	984(<1)
$\nu_4(E')$, δ(Cl–C–Cl)	326 9(9)	318(4)	317(4)	254.5	257(3)	259(2)
	CBr_3^+			BBr_3		
assgnts	exptl	6-31G(2d)	cc-pVTZ	exptl[j]	6-31G(2d)	cc-pVTZ
$\nu_1(A_1')$, ν_s(C–Br)	321 4(27)	341(13)	340(13)	279 6	292(7)	292(6)
$\nu_2(A_2'')$, π(C–Br_3)		461(0)	454(0)	377 3[i]	414(0)	401(0)
$\nu_3(E')$, ν_{as}(C–Br)		932(3)	931(2)	794.4	849(<1)	853(<1)
$\nu_4(E')$, δ(Br–C–Br)	183 5(15) 187 0(12) }	193(3)	186(3)	153 4	155(1)	157(2)
	CI_3^+			BI_3		
assgnts	exptl[k]	(SDB-)cc-pVTZ		exptl[j]	(SDB-)cc-pVTZ	
$\nu_1(A_1')$, ν_s(C–I)		240(14)		194.5	203(6)	
$\nu_2(A_2'')$, π(C–I_3)	339, w	384(0)		307.9[i]	336(0)	
$\nu_3(E')$, ν_{as}(C–I)	739, vs	807(14)		681	741(<1)	
$\nu_4(E')$, δ(I–C–I)		127(3)		105.3	106(2)	

[a] Values in parentheses represent experimental relative Raman intensities (see Table 6.6) or calculated Raman intensities (in $Å^4$ amu^{-1}). [b] Frequencies have been calculated and assigned for D_{3h} symmetry. [c] From ref 184. [d] From ref 225. [e] From ref 226. [f] The ν_1 band is split as a result of the mass effect of the ^{35}Cl and ^{37}Cl isotopes: 554.1(100) ($C^{35}Cl_3$), 549.1(96) ($C^{35}Cl_2{}^{37}Cl$), 544.1(32) ($C^{35}Cl^{37}Cl_2$) and 538.8(3) ($C^{37}Cl_3$) cm^{-1}; the most intense band has been scaled to 100 (see Figure 6.4). [g] From ref 180. [h] From ref 178 and ref 179. [i] Observed as $2\nu_2(A_2'')$. [j] From ref 227. [k] From ref 101.

Table 6.5. Experimental and Calculated Frequencies (cm^{-1}) and Intensities for CX_4 (T_d) [a]

CF_4

		6-31G(2d)		cc-pVTZ	
assgnt	exptl[b]	HF	MP2	HF	MP2
$\nu_1(A_1)$, ν_s	908.4	995(5)	904(6)	1012(4)	925(5)
$\nu_2(E)$, δ_s	434.5	476(<1)	435(<1)	480(<1)	440(<1)
$\nu_3(T_2)$, ν_{as}	1283.0	1435(1)	1295(<1)	1448(1)	1312(<1)
$\nu_4(T_2)$, δ_{as}	631.2	684(1)	626(1)	694(1)	640(1)

CCl_4

		6-31G(2d)		cc-pVTZ	
assgnt	exptl[c]	HF	MP2	HF	MP2
$\nu_1(A_1)$, ν_s	459(100)[d]	494(18)	463(15)	496(17)	471
$\nu_2(E)$, δ_s	220(58)	238(2)	222(3)	237(3)	221
$\nu_3(T_2)$, ν_{as}	794(20), 761(16)	891(9)	796(3)	889(8)	810
$\nu_4(T_2)$, δ_{as}	317(68)	340(3)	321(3)	340(4)	321

CBr_4

		6-31G(2d)		cc-pVTZ	
assgnt	exptl[c]	HF	MP2	HF	MP2
$\nu_1(A_1)$, ν_s	269(100)	302(16)	285	292(16)	282
$\nu_2(E)$, δ_s	128(33)	145(2)	135	138(2)	129
$\nu_3(T_2)$, ν_{as}	673(15), 664(15), 658(10)	789(13)	713	770(17)	708
$\nu_4(T_2)$, δ_{as}	182(41), 184(47)	208(2)	196	201(3)	190

CI_4

		(SDB-)cc-pVTZ	
assgnt	exptl[e]	HF	MP2
$\nu_1(A_1)$, ν_s	178(10)	201(16)	195
$\nu_2(E)$, δ_s	90(4)	94(2)	87
$\nu_3(T_2)$, ν_{as}	555, vs[f]	672(27)	618
$\nu_4(T_2)$, δ_{as}	123(5)	137(3)	129

[a] Values in parentheses represent observed or calculated Raman intensities. [b] From ref 228. [c] This work, pure solid compound (–120 °C). [d] The ν_1 band is split as a result of the mass effect of the ^{35}Cl and ^{37}Cl isotopes: 462(95) ($C^{35}Cl_3$), 459(100) ($C^{35}Cl_2{}^{37}Cl$), 456(51) ($C^{35}Cl^{37}Cl_2$) and 453(19) ($C^{37}Cl_3$) cm^{-1}. [e] From ref 229. [f] This band was only observed in the infrared spectrum; vs denotes very strong.

Table 6.6. Raman Frequencies and Assignments for $[CCl_3][Sb(OTeF_5)_6]$ and $[CBr_3][Sb(OTeF_5)_6]\cdot nSO_2ClF$ and Related Species

frequencies (cm^{-1})			assgnts				
CCl_3^+ [a,b]	CBr_3^+ [c,d,e]	CBr_3^+ [d,e,f]	CX_3^+	CBr_4	$OTeF_5$ [g]	non-coordinated SO_2ClF	coordinated SO_2ClF [h]
554(19) 549(19) 544(6) 539(<1)	321(33)	321(33)	$\nu_1(A_1')$				
327(9)	188(48) 184(54)	187(15) 184(18)	$\nu_4(E')$				
	673(24) 668, sh 653, sh			$\nu_3(T_2)$			
		654(28)					
	188(48) 184(54)	187(15) 184(18)		$\nu_4(T_2)$			
	269(93)			$\nu_1(A_1)$			
	128(36)			$\nu_2(E)$			
	1454(2) 1449(3) 1095(2), br				$\nu(CO)$[i]		
	1444(4) 1433(14) 1427, sh	1433(18)				$\nu_{asym}(SO_2)$	
	1224(32) 1219(26)	1224(42) 1218(39)				$\nu_{sym}(SO_2)$	
	847(5) 839(6)					$\nu(SF)$	

Table 6.6. (continued...)

CCl_3^{+} [a,b]	CBr_3^{+} [c,d,e]	CBr_3^{+} [d,e,f]	CX_3^{+}	CBr_4	$OTeF_5$ [g]	non-coordinated SO_2ClF	coordinated SO_2ClF [h]
	1415(4) 1407(4)	1415(11)					$\nu_{asym}(SO_2)$
	1166(8)	1168(14)					$\nu_{sym}(SO_2)$
	819, sh						ν(SF)
822(5)	827(7), br	830(10),br			[j]		
751(3)	749(11)						
	745(11)	745(21)			ν_8(E), $\nu_{as}(TeF_4)$		
724(17)	721(21)						
	717(21)	716(32)					
712(7)	714(22)				$\nu_1(A_1)$, ν(TeF)		
702(100)	703(67)	703(60)			+		
690(8)	693(24)	693(25)			ν_s(TeO + XeO)[k]		
	690, sh						
686(2)	682(9)	685(18)					
	677(9)	679(19)					
665(8)	668, sh	669(55)			$\nu_2(A_1)$, $\nu_s(TeF_4)$		
659(40)	663(100)	663(100)					
653(19)	653, sh	654(28)					
641(10)	648(24)	648(26),br			$\nu_5(B_1)$, $\nu_{as}(TeF_4)$		
	633(14)	635(18),br					
519(<1)		515(6)			[j]		
505(<1)	503(13)	503(21)			[j]		
	494(7)	495(10)					
	485, sh						
	480(16)	480(21)			ν_s(TeO + XeO)[k]		
	476, sh						
464(2)	460(5), br						

Table 6.6. (continued...)

CCl_3^+ [a,b]	CBr_3^+ [c,d,e]	CBr_3^+ [d,e,f]	CX_3^+	CBr_4	$OTeF_5$ [g]	non-coordinated SO_2ClF	coordinated SO_2ClF [h]
451(1)							
	438(25)[m]	440(14)[m]					
	435(27)[m]						
	432(26)[m]	430(54),br[m]			$\nu_3(A_1)$, ν(TeO) also coupled with ν_s(Sb-O)[l]		
	428(29)[m]						
	420(13)						
414(23)	413, sh						
395(5)	408(29)	409(31),br					
369(7)	367(11)	367(15)					
342(5)	341, sh	340(19)			$\nu_9(E)$, $\delta(FTeF_4)$		
339(14)	333(20)	332(23)					
320(7)					$\nu_{10}(E)$, $\nu(OTeF_5)$		
310(19)	309(26)	309(44)			$\nu_4(A_1)$, $\delta_s(FTeF_4)$		
306(16)	305, sh [n]	298(50) [n]			$\nu_7(B_2)$, $\delta_{sciss}(TeF_4)$		
	257(7)	258(13)					
	253(9)	254(13)			$\nu_{11}(E)$, $\delta_{as}(TeF_4)$		
246(9)	249(9)						
243(6)	240(16)	240(18)					
231(4)	231, sh						
	228(6)	230(10)			δ(TeOSb)[l]		
	215(4)	215(8)					
	173(9)	173(14)			δ(FTeO)[k]		
	167, sh						
148(14)	145, sh	146(16)					
	141(19)	141(19)			τ(TeOSb)[l]		
137(10)	134(12)	136(14)					
123(7)	128(36)				δ(XeOTe)[k]		
118(3)	120(12)	121(15)			lattice modes		
100(1)	111(13)	110(14)					

Table 6.6. (continued...)

[a] The Raman spectrum of the solid obtained from the reaction of excess CCl_4 with $[XeOTeF_5][Sb(OTeF_5)_6]$ in SO_2ClF at –78 °C (eq 6.1). [b] Experimental Raman intensities are given in parentheses. [c] The Raman spectrum of the solid obtained from the reaction of excess CBr_4 with $[XeOTeF_5][Sb(OTeF_5)_6]$ in SO_2ClF at –78 °C (eq 6.2–6.7). [d] Infrared intensities, in km mol^{-1}, are given in square brackets. [e] The symbol, sh, denotes a shoulder and br denotes a broad line. [f] The Raman spectrum of the solid obtained from the reaction of excess $[XeOTeF_5][Sb(OTeF_5)_6]$ with CBr_4 in SO_2ClF at –78 °C (eq 6.2–6.7). [g] The $OTeF_5$ group assignments for $OTeF_5$ derivatives resulting from the reactions of CBr_4 with $[XeOTeF_5][Sb(OTeF_5)_6]$ are tentative due to overlap of their Raman bands. The vibrational modes of the $OTeF_5$ groups are assigned under C_{4v} symmetry (ref 79). [h] Free SO_2ClF was observed, along with coordinated SO_2ClF, in sample mixtures that were incompletely pumped at –78 °C. [i] These modes are most likely assigned to the $CBr_{3-n}(OTeF_5)_n^+$ cations (n = 1–3). [j] Unassigned modes. [k] These modes are most likely assigned to the $XeOTeF_5^+$ cation (ref 75). [l] These modes are most likely assigned to the $Sb(OTeF_5)_6^-$ anion. [m] These bands may overlap with ν_5(S–Cl) of SO_2ClF. [n] These bands may overlap with Br_2 which occurs at 296.5 and 302.5 cm^{-1}.

spectrum of $[CCl_3][Sb(OTeF_5)_6]$ reveals that the $\nu_1(A_1')$ band is split into four components that arise from the isotopomers $C^{35}Cl_3^+$, $C^{35}Cl_2{}^{37}Cl^+$, $C^{35}Cl^{37}Cl_2^+$, and $C^{37}Cl_3^+$ (Figure 6.4). The intensities of the isotopomer bands are in excellent agreement with the intensities calculated from the chlorine natural isotopic abundances. The experimental $^{35}Cl/^{37}Cl$ isotopic shifts are 5.0–5.3 cm^{-1} and are in good agreement with the calculated values and are larger than the experimental isotopic shifts of BCl_3 (3.9–4.5 cm^{-1})[230] and CCl_4 (3.2–3.6 cm^{-1}).[231] The formally Raman-active $\nu_3(E')$ band was not observed, in accord with the low Raman intensity calculated for this band at all levels of theory used in this study (Table 6.4).

The low-temperature Raman spectrum resulting from the reaction of CBr_4 with a stoichiometric excess of $[Xe(OTeF_5)][Sb(OTeF_5)_6]$ revealed new bands at 183.5, 187.0 and 321.4 cm^{-1}. The band at 321.4 cm^{-1} is assigned to $\nu_1(A_1')$ of CBr_3^+ by comparison with the calculated value, 340 cm^{-1} (MP2/cc-pVTZ). The intense bands at 183.5 and 187.0 cm^{-1} are assigned to $\nu_4(E')$ of CBr_3^+. The splitting can most likely be accounted for on the basis of simple site symmetry lowering of this doubly degenerate mode to produce two Raman-active components. The assignment is supported by the calculated frequency of 186 cm^{-1} (MP2/cc-pVTZ). As in the case of CCl_3^+, the formally Raman-active $\nu_3(E')$ band of CBr_3^+ was not observed. Unlike CCl_3^+, where $\nu_3(E')$ is predicted to be consistently weaker in intensity than $\nu_4(E')$, the relative Raman intensities of $\nu_3(E')$ and $\nu_4(E')$ of CBr_3^+, which are also predicted to be weak, are found to vary with the level of theory used (Table 6.4), and are therefore difficult to compare with the experimental

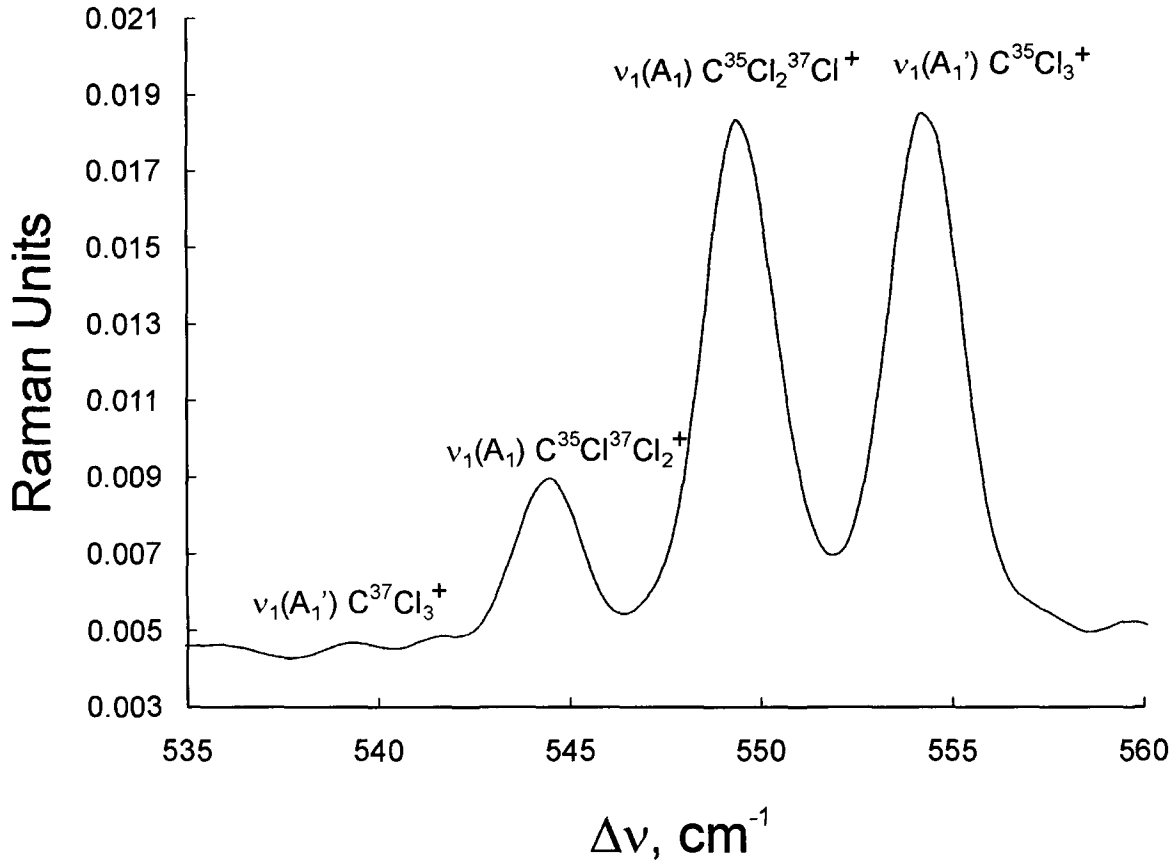

Figure 6.4. An expanded view of the symmetric $\nu_1(A_1')$ stretching band of CCl_3 in the Raman spectrum of $[CCl_3][Sb(OTeF_5)_6]$ showing the natural abundance chlorine isotope shifts.

Raman intensities. The experimental vibrational frequencies of the CX_3^+ cations are in general found to be comparable to or lower in frequency than the calculated values, a better fit being obtained for the MP2 frequencies (Table 6.4). As expected from the observed and calculated C–X and B–X bond lengths, all frequencies are higher for the CX_3^+ cations than for their BX_3 analogues. The calculated values are also in very good agreement with experimental infrared data obtained for CI_3^+ [101] and the matrix-isolated CF_3^+ [184] and CCl_3^+ [179] cations.

6.2.3.2. $C(OTeF_5)_3^+$ and $B(OTeF_5)_3$

Although $B(OTeF_5)_3$ has been known for some time and limited infrared data have been previously reported,[109] the Raman spectrum is now reported for the first time (Table 6.7). The vibrational modes of $B(OTeF_5)_3$ were assigned under C_{3h} symmetry and belong to the irreducible representation Γ = 11 A′ + 9A″ + 12 E′ + 8E″. A total of 40 fundamental bands are expected, of which the 31 A′, E′ and E″ modes are Raman active and the 23 A″ and E′ modes are infrared active. The vibrational frequencies for $C(OTeF_5)_3^+$ and $B(OTeF_5)_3$ were calculated at the HF/(SDB-)cc-pVTZ level of theory. The assignments for $B(OTeF_5)_3$ were made by comparison with the calculated frequencies and infrared and Raman intensities, which are in agreement with the experimental values (Table 6.7).

The low-temperature spectra resulting from the reaction of CBr_4 with a two-fold molar excess of $[Xe(OTeF_5)][Sb(OTeF_5)_6]$ revealed new bands in the C–O stretching region at 1168, 1218, 1224, 1407, 1415, 1427, 1433, 1444, 1449 and 1454 cm^{-1} (Table

Table 6.7. Calculated[a] Vibrational Frequencies (cm^{-1}) and Infrared and Raman Intensities for $C(OTeF_5)_3^+$ and $B(OTeF_5)_3$ and Observed Vibrational Frequencies and Infrared and Raman Intensities for $B(OTeF_5)_3$

$C(OTeF_5)_3^+$	$B(OTeF_5)_3$			
calcd[b,c,d] (C_{3h})	calcd[b,c,d] (C_{3h})	exptl Raman	exptl infrared[e]	assgnt (C_{3h})
1502 (0.2) [1266.5]	1297 (0.1) [1095.2]		1330, s	E′
1165 (0.7) [i.a.]	1066 (3.5) [i.a.]	1050(6)		A′
798 (i.a.) [316.7]	758 (i.a.) [484.5]			A″
785 (0.1) [101.4]	754 (0.3) [272.7]		740, vs	E′
780 (0.1) [179.2]	770 (0.6) [92.4]	755(5)		E′
779 (0.2) [i.a.]	751 (0.2) [i.a.]			E″
777 (i.a.) [133.6]	658 (i.a.) [2.7]			A″
777 (1.3) [i.a.]	749 (1.5) [i.a.]	732(5)		A′
764 (11.6) [i.a.]	731 (21.1) [i.a.]	716(96)		A′
755 (2.0) [112.9]	716 (1.4) [78.8]		725, vs	E′
712 (32.9) [i.a.]	683 (17.3) [i.a.]	673(100)		A′
708 (0.3) [0.8]	674 (1.2) [7.2]	702(16)	705, s	E′
682 (2.8) [i.a.]	660 (2.7) [i.a.]	660(18)		E″
680 (i.a.) [1.0]	626 (i.a.) [73.6]		615, m	A″
448 (7.5) [i.a.]	474 (10.2) [i.a.]	500(44)		A′
388 (0.1) [98.4]	430 (0.0) [125.3]		430, s	E′
346 (0.1) [i.a.]	355 (0.1) [i.a.]	338(7)		A′
331 (0.0) [i.a.]	342 (0.0) [i.a.]	332(3)		E″
328 (i.a.) [191.3]	337 (i.a.) [189.9]			A″
325 (2.3) [i.a.]	328 (0.0) [i.a.]			A′
325 (0.5) [5.1]	332 (0.7) [46.7]	325(15)		E’
321 (0.6) [92.2]	327 (0.1) [236.3]			E′
317 (0.0) [i.a.]	315 (2.0) [i.a.]	318(17)		A′

Table 6.7. (continued...)

311 (1.0) [i.a.]	327 (1.3) [i.a.]	311(18)	E″
308 (0.0) [293.9]	314 (0.3) [0.2]		E′
303 (i.a.) [0.0]	319 (i.a.) [3.9]		A″
260 (0.1) [i.a.]	256 (0.3) [i.a.]	254(3)	A′
254 (0.7) [0.3]	247 (0.5) [11.7]	246(7)	E′
216 (0.2) [i.a.]	216 (0.0) [i.a.]		E″
207 (i.a.) [0.0]	214 (i.a.) [0.1]		A″
198 (0.0) [i.a.]	210 (0.0) [i.a.]		E″
198 (i.a.) [0.0]	206 (i.a.) [0.6]		A″
140 (0.3) [i.a.]	143 (0.2) [i.a.]	140(3)	A′
129 (0.1) [0.4]	129 (0.1) [1.1]		E’
88 (0.1) [i.a.]	77 (0.0) [i.a.]	71(5)	A′
77 (0.1) [i.a.]	63 (0.1) [i.a.]	56(3)	E″
35 (0.0) [0.3]	29 (0.0) [0.1]		E′
28 (i.a.) [0.2]	24 (i.a.) [0.1]		A″
20 (i.a.) [0.3]	15 (i.a.) [0.0]		A″
20 (0.0) [i.a.]	16 (0.2) [i.a.]		E″
		159(2)	
		98(2), 91(3)	lattice modes
		84(5)	

[a] HF/(SDB-)cc-pVTZ; calculated frequencies have been scaled by multiplying the calculated frequencies by 0.890. [b] Raman intensities, in $Å^4$ amu^{-1}, are given in parentheses. [c] Infrared intensities, in km mol^{-1}, are given in square brackets. [d] The abbreviation, i.a., denotes an inactive mode. [e] Experimental values are from ref 231 (KBr, –195 °C). The abbreviations denote very strong (vs), strong (s) and medium (m) infrared intensities.

6.6). Although some of these bands fall in the range of the calculated $\nu_{sym}(CO)$ and $\nu_{asym}(CO)$ frequencies for $C(OTeF_5)_3^+$, 1309 and 1688 cm^{-1} (HF/(SDB-)cc-pVTZ), they could not be definitively assigned to the $C(OTeF_5)_3^+$ cation, but could also be associated with the mixed Br/$OTeF_5$-substituted cations, $CBr(OTeF_5)_2^+$ and $CBr_2(OTeF_5)^+$, formed in eq 6.3 and 6.4.

6.2.4. Computational Results for CX_3^+ and BX_3 (X = F, Cl, Br, I, $OTeF_5$)

Quantum mechanical ab initio calculations have been previously reported for the isoelectronic CX_3^+ [101,180,186,207,210,211,232-239] and BX_3, [101,207,210,240-245] (X = F, Cl, Br, I) series and related isovalent species such as AH_2X^+, YH_2X (X = F, Cl, Br, I; A = C, Si, Ge, Sn, Pb; Y = B, Al, Ga, In, Tl).[207] While results are abundant for species where X = F[101,210,232,234-237,240-245] or Cl,[101,210,211,232,238-247] they are relatively sparse for X = Br[101,186,210,211,232] or I.[101,186,210,211]

The series of trihalomethyl carbocations, CX_3^+, and boron trihalides, BX_3, (X = F, Cl, Br, I) have been reinvestigated, and the calculations have been extended to the related $OTeF_5$ derivatives using all-electron correlation consistent (cc-pVTZ) basis sets for all atoms other than tellurium and iodine, for which semirelativistic large core pseudopotential (SDB-cc-pVTZ) basis sets were used. The geometric parameters and vibrational frequencies (see Section 6.2.3) were calculated and a natural bond orbital (NBO) analysis was carried out using HF and MP2 methods. Energies for the MP2-optimized structures were calculated using the CCSD(T) method. Calculations for the $OTeF_5$ derivatives were only carried out at the HF/(SDB-)cc-pVTZ basis set. The

methods were benchmarked by calculating the vibrational frequencies (Table 6.5), geometries (Table 6.8) and chemical shifts of CX_4 (see Section 6.2.5) for which there are well-established experimental values.

6.2.4.1. Geometries.

Geometry optimization using D_{3h} (CX_3^+ and BX_3), and C_{3h} ($C(OTeF_5)_3^+$, $B(OTeF_5)_3$) as the initial symmetries resulted in stationary points with all frequencies real. All optimized metric parameters for CX_3^+ and BX_3 are listed in Tables 6.9 and 6.10, respectively.

The HF and MP2 calculations give similar results for CCl_3^+, CBr_3^+, CI_3^+, and the isoelectronic BX_3 molecules, while for CF_3^+ and BF_3 the MP2 calculations predict slightly longer bond lengths. The calculated bond lengths of CCl_3^+, CBr_3^+, and CI_3^+ are in good agreement with those obtained from their X-ray crystal structures. The calculated bond lengths for all BX_3 systems are in good agreement with experiment and the bond length trends, C–X < B–X, are reproduced over this series for X = Cl, Br, I.

The fully optimized (HF/(SDB-)cc-pVTZ) geometries of $C(OTeF_5)_3^+$ and $B(OTeF_5)_3$ possess C_{3h} symmetry (Figure 6.5), with trigonal planar environments around the central carbon and boron atoms. The calculated distances are in reasonable agreement with the experimental ones, although they are all slightly shorter. The calculated C–O–Te, B–O–Te, and $OTeF_5$ group angles are in good agreement with the observed angles. Overall, the calculated geometries are in very good agreement with the experimental geometries of the $C(OTeF_5)_3^+$ cation and $B(OTeF_5)_3$, indicating that the two C···O

Table 6.8. Experimental and Calculated Geometrical Parameters and NBO Study (MP2) for CX_4 (T_d)

CF_4							CCl_4						
		6-31G(2d)		cc-pVTZ					6-31G(2d)		cc-pVTZ		
	exptl	HF	MP2	HF	MP2	CCSD(T)		exptl	HF	MP2	HF	MP2	CCSD(T)
C–F	1 315(3)[d]	1.296	1.323	1.296	1.319	1 319	C–Cl	1.77(6)[a] 1.751(13)[c]	1.768	1.781	1 764	1.768	1.777
F–C–F	109.6(3)[d]						Cl–C–Cl						
F···F	2.148(4)[d]	2 117	2.161	2 116	2 154	2.154	Cl···Cl	2.89(12)[a] 2.859(6)[c]	2 888	2 908	2.881	2.887	2.902

CBr_4							CI_4				
		6-31G(2d)		cc-pVTZ					(SDB-)cc-pVTZ		
	exptl	HF	MP2	HF	MP2	CCSD(T)		exptl[e]	HF	MP2	CCSD(T)
C–Br	1.91(4)[b]	1 923	1.931	1.934	1.928	1 940	C–I	2 155(1)	2.131	2 127	2.137
Br–C–Br							I–C–I	109.5(1)			
Br···Br	3.12(7)[b]	3.140	3.154	3 158	3.148	3.168	I···I	3 518(1)	3 480	3 473	3.489

CF_4		6-31G(2d)	cc-pVTZ
charge	C	1 37	1.25
	F	–0 34	–0.31
valency	C	3.30	2 82
	F	0.75	0.61
bond order	C–F	0.82	0.70
	F···F	–0 02	–0 03

CCl_4		6-31G(2d)	cc-pVTZ
charge	C	–0.29	–0.19
	Cl	0.07	0.05
valency	C	3.36	3.56
	Cl	0.71	0.76
bond order	C–Cl	0.84	0.89
	Cl···Cl	–0 04	–0.04

CBr_4		6-31G(2d)	cc-pVTZ
charge	C	–0 63	–0.55
	Br	0 16	0 14
valency	C	3.13	3.34
	Br	0.68	0.71
bond order	C–Br	0.78	0 83
	Br···Br	–0 03	–0.04

CI_4		(SDB-)cc-pVTZ
charge	C	–1.19
	I	0 30
valency	C	3.16
	I	0 69
bond order	C–I	0.79
	I···I	–0.03

[a] Neutron diffraction from ref 248. [b] X-ray diffraction from ref 219 (Phase I). [c] X-ray diffraction from ref 217. [d] From ref 218. [e] From ref 249.

Table 6.9. Experimental and Calculated Geometries for CX_3^+ and BX_3

	CF_3^+					
		6-31G(2d)		cc-pVTZ		
		HF	MP2	HF	MP2	CCSD(T)
C–F(Å)		1.209	1.236	1.208	1.233	1.233
F–C–F(deg)		120				
F···F(Å)		2 095	2 141	2 093	2 135	2 136

	BF_3					
		6-31G(2d)		cc-pVTZ		
	exptl[a]	HF	MP2	HF	MP2	CCSD(T)
B–F(Å)	1.30(2)	1 294	1.315	1.295	1.315	1.313
F–B–F(deg)		120				
F···F(Å)	2 26(3)	2 241	2.277	2 243	2 277	2.274

	CCl_3^+					
		6-31G(2d)		cc-pVTZ		
	exptl[b]	HF	MP2	HF	MP2	CCSD(T)
C–Cl(Å)	1.62(1)	1.645	1.654	1.641	1.645	1.655
Cl–C–Cl(deg)	119.9(7)	120				
Cl···Cl(Å)	2.805(5)	2.848	2.865	2.842	2.849	2 866

	BCl_3					
		6-31G(2d)		cc-pVTZ		
	exptl[c]	HF	MP2	HF	MP2	CCSD(T)
B–Cl(Å)	1.75(2)	1.750	1.750	1.747	1 740	1.747
Cl–B–Cl(deg)		120				
Cl···Cl(Å)	2 99(3)[a]	3 031	3.031	3.025	3.015	3 026

	CBr_3^+					
		6-31G(2d)		cc-pVTZ		
	exptl[b]	HF	MP2	HF	MP2	CCSD(T)
C–Br(Å)	1.81(2)	1 800	1.803	1 808	1.801	1.816
Br–C–Br(deg)	120.0(9)	120				
Br···Br(Å)	3.129(3)	3.117	3.123	3.132	3.120	3.145

	BBr_3					
		6-31G(2d)		cc-pVTZ		
	exptl	HF	MP2	HF	MP2	CCSD(T)
B–Br(Å)	1 893(5)[d]	1.896	1.888	1.910	1.891	1.901
Br–B–Br(deg)		120				
Br···Br(Å)	3.25(3)[a]	3.284	3.270	3.308	3.275	3.293

	CI_3^+			
		(SDB-)cc-pVTZ		
	exptl[e]	HF	MP2	CCSD(T)
C–I(Å)	2.013(9)	2.001	1.990	2.007
I–C–I(deg)	120.0(5)			
I···I(Å)	3.486(8)	3.466	3.447	3.477

	BI_3			
		(SDB-)cc-pVTZ		
	exptl	HF	MP2	CCSD(T)
B–I(Å)	2.112(8)[f]	2.117	2.092	2 105
I–B–I(deg)	120 0(9)	120		
I···I(Å)	3 659[f]	3.667	3.624	3.646

[a] From ref 247. [b] Average values, present work. [c] From ref 250. [d] From ref 251. [e] From ref 101. [f] From ref 252, the I···I contact distance was calculated from the published coordinates.

Table 6.10. Calculated[a] and Experimental Geometries for $C(OTeF_5)_3^+$ and $B(OTeF_5)_3$

$C(OTeF_5)_3^+$ (C_{3h})			$B(OTeF_5)_3$ (C_{3h})		
	exptl[b]	calcd		exptl[c]	calcd
		bond lengths (Å)[d]			
C(1)–O(1)	1.28(3)	1.256	B(1)–O(1)	1.358(6)	1.354
Te(1)–O(1)	1.98(1)	1.945	Te(1)–O(1)	1.874(6)	1.833
Te(1)–F(1)	1.81(1)	1.765	Te(1)–F(1)	1.822(6)	1.785
Te(1)–F(2)	1.81(2)	1.778	Te(1)–F(2)	1.809(4)	1.790
Te(1)–F(3)	1.81(2)	1.771	Te(1)–F(3)	1.818(4)	1.785
		bond angles (deg)[d]			
C(1)–O(1)–Te(1)	129.8(1)	135.27	B(1)–O(1)–Te(1)	132.3(4)	137.32
O(1)–Te(1)–F(1)	175.9(6)	180.00	O(1)–Te(1)–F(1)	178.0(3)	180.00
O(1)–Te(1)–F(2)	90.2(9)	88.43	O(1)–Te(1)–F(2)	92.6(2)	91.88
O(1)–Te(1)–F(3)	84.7(9)	85.50	O(1)–Te(1)–F(3)		89.56
F(1)–Te(1)–F(2)	92.6(9)	92.75	F(1)–Te(1)–F(2)	88.8(2)	89.12
F(1)–Te(1)–F(3)	92.6(9)	93.32	F(1)–Te(1)–F(3)	89.0(2)	89.44
F(2)–Te(1)–F(3)	89.9(9)	89.76	F(2)–Te(1)–F(3)	90.2(2)	89.87
F(2)–Te(1)–F(4)	90.0(9)	89.68	F(2)–Te(1)–F(4)	91.2(2)	90.12
F(2)–Te(1)–F(5)	174.8(9)	173.92	F(2)–Te(1)–F(5)		178.56

[a] HF/(SDB-)cc-pVTZ. [b] Experimental values are averaged values. [c] From ref 221. [d] The atom numbering scheme corresponds to that of the equivalently labelled $OTeF_5$ group of the $C(OTeF_5)_3^+$ cation in Figure 6.3, where F(1) is the axial fluorine and F(2–5) are the equatorial fluorines. In the calculated structure, the F(2)/F(4) and the F(3)/F(5) pairs are related by symmetry.

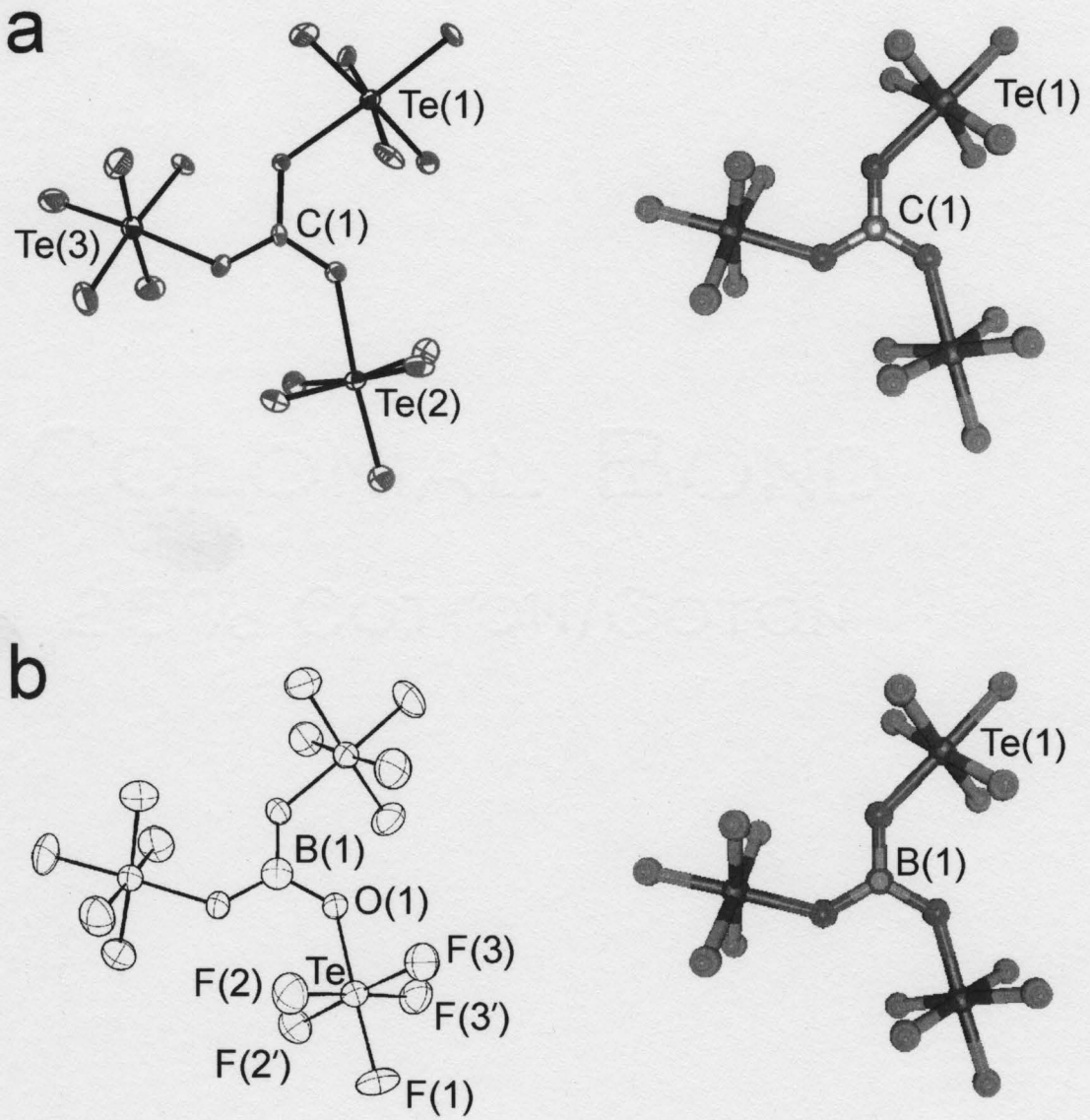

Figure 6.5. Experimental (left) and calculated (right) geometries for (a) the $C(OTeF_5)_3^+$ cation and (b) the $B(OTeF_5)_3$ molecule (experimental structure from ref 221).

contacts with two SO_2ClF solvent molecules in the crystal lattice of $[C(OTeF_5)_3][Sb(OTeF_5)_6]\cdot 3SO_2ClF$ do not have a significant effect on the structure of the cation in the solid state (see Section 6.2.2). Moreover, the slight distortions of the F–Te–F bond angles from 90° in $C(OTeF_5)_3^+$ and the near-regular pseudo-octahedral $OTeF_5$ groups observed for $B(OTeF_5)_3$ are also reproduced by the calculations.

6.2.4.2. Natural Bond Orbital (NBO) Analyses

Natural atomic charges, Mayer natural atomic orbital valencies, and natural atomic orbital bond orders between atoms in CX_3^+, CX_4 and BX_3, calculated at the MP2 level of theory, are given in Table 6.11 and those calculated for $C(OTeF_5)_3^+$ and $B(OTeF_5)_3$, at the HF level of theory, are given in Table 6.12.

(i) B–X/C–X σ- and π-Donations and Natural Atomic Charges. Following previous approaches, bonding at the central carbon and boron atoms was divided into σ- and π-donation, and the values obtained agreed well with the previous values and associated interpretations (see Tables 6.11 and 6.12).[199,207]

The NBO analyses for CX_3^+ and BX_3 (X = F or $OTeF_5$) were carried out at the same level of theory (HF/(SDB-)cc-pVTZ; see Table 6.12), so that both the carbocations and neutral boron analogues could be compared. The π-donations from the carbon bonded to fluorine or to the oxygen atom of the $OTeF_5$ ligand to the central carbon or boron atom and are similar for CX_3^+, (0.15 for X = F; 0.19 for X = $OTeF_5$) and for BX_3, they are equal (0.09) for X = F or $OTeF_5$. In both cases, the σ-donation from the

Table 6.11. Calculated[a] Natural Atomic Charges, Mayer Bond Orders, and Mayer Natural Atomic Orbital Valencies for CX_3^+, CX_4, and BX_3 (X = F, Cl, Br, I)

CX_3^+ (D_{3h})		F	Cl	Br	I
natural Charge (q)	C (X)	1.37 (–0.12)	–0.09 (0.36)	–0.45 (0.48)	–1.10 (0.70)
bond order	C–X (X···X)	0.88 (–0.04)	1.09 (–0.05)	1.04 (–0.05)	0.99 (–0.06)
valency	C (X)	2.64 (0.81)	3.28 (0.99)	3.12 (0.93)	2.97 (0.88)
p_π populations	C (X)	0.59 (1.77)	0.91 (1.65)	1.00 (1.62)	1.13 (1.57)
σ donation (π donation)[b]	C→X (X→C)	0.32 (0.19)	–0.06 (0.31)	–0.15 (0.33)	–0.32 (0.38)
CX_4 (T_d)		F	Cl	Br	I
natural charge (q)	C (X)	1.25 (–0.31)	–0.11 (0.03)	–0.56 (0.14)	–1.19 (0.30)
bond order	C–X (X···X)	0.70 (–0.03)	0.90 (–0.04)	0.83 (–0.04)	0.79 (–0.03)
valency	C (X)	2.82 (0.61)	3.61 (0.79)	3.34 (0.71)	3.16 (0.69)
BX_3 (D_{3h})		F	Cl	Br	I
natural charge (q)	B (X)	1.39 (–0.46)	0.34 (–0.11)	0.06 (–0.02)	–0.49 (0.16)
bond order	B–X (X···X)	0.86 (–0.02)	1.08 (–0.04)	1.09 (–0.04)	1.16 (–0.04)
valency	B (X)	2.58 (0.81)	3.24 (1.00)	3.27 (1.00)	3.47 (1.07)
p_π populations	B (X)	0.32 (1.86)	0.48 (1.79)	0.53 (1.78)	0.63 (1.74)
σ donation (π donation)[b]	B→X (X→B)	0.57 (0.11)	0.27 (0.16)	0.20 (0.18)	0.04 (0.21)

[a] MP2/(SDB-)cc-pVTZ. [b] The value given is per bond; a negative sign indicates donation in reversed order.

Table 6.12. Calculated[a] Natural Atomic Charges, Mayer Bond Orders and Mayer Natural Atomic Orbital Valencies for $C(OTeF_5)_3^+$ and $B(OTeF_5)_3$

$C(OTeF_5)_3^+$ (C_{3h})[b]	charge	valency		bond order
C	1.30	3.04	C–O	1.01
O	−0.86	1.33	Te–O	0.45
Te	4.07	3.19	Te–F_A	0.56
F_A	−0.65	0.53	Te–F_B	0.54
F_B	−0.67	0.49	Te–$F_{B'}$	0.55
$F_{B'}$	−0.66	0.51		
overall $OTeF_5$	−0.10			
p_π populations at C (O)		0.56 (1.80)		
σ donation (π donation)[c]		0.28 (0.19)		
CF_3^+ (D_{3h})	charge	valency		bond order
C	1.57	2.66	C–F	0.89
F	−0.19	0.82		
p_π populations at C (F)		0.46 (1.83)		
σ donation (π donation)[c]		0.34 (0.15)		
$B(OTeF_5)_3$ (C_{3h})[b]	charge	valency		bond order
B	1.45	2.18	B–O	0.73
O	−1.15	1.22	Te–O	0.58
Te	4.08	3.22	Te–F_A	0.53
F_A	−0.68	0.49	Te–F_B	0.52
F_B	−0.68	0.48	Te–$F_{B'}$	0.53
$F_{B'}$	−0.68	0.49		
overall $OTeF_5$	−0.48			
p_π populations at B (O)		0.27 (1.88)		
σ donation (π donation)[c]		0.57 (0.09)		
BF_3 (D_{3h})	charge	valency		bond order
B	1.56	2.53	B–F	0.84
F	−0.52	0.80		
p_π populations at B (F)		0.26 (1.91)		
σ donation (π donation)[c]		0.61 (0.09)		

[a] HF/(SDB-)cc-pVTZ. [b] The symbols, F_A and $F_B/F_{B'}$ denote axial and equatorial fluorine atoms, where F_B and $F_{B'}$ are nonequivalent under C_{3h} symmetry. [c] The value given is per bond; a negative sign indicates donation in reversed order.

carbon or boron atom to the ligand atom decreases when fluorine is replaced by the $OTeF_5$ group. The charge on the carbon atom of $C(OTeF_5)_3^+$ (1.30) is lower than that on the carbon atom of CF_3^+ (1.57), and the overall charge of the $OTeF_5$ group (–0.10) is somewhat lower than that of fluorine in CF_3^+ (–0.12). As expected, the charge on the carbon atom is somewhat less positive in the $OTeF_5$ derivative, which is consistent with the lower electronegativity of the $OTeF_5$ group.[70] In both $C(OTeF_5)_3^+$ and $B(OTeF_5)_3$, the positive charges on the central atom are lower and on the ligand less negative when compared with the atomic charges of CF_3^+ and BF_3, respectively.

(ii) Mayer Bond Orders and Natural Atomic Orbital Valencies for $C(OTeF_5)_3^+$ and $B(OTeF_5)_3$. The B–O bond order and valencies at the boron and oxygen atoms are lower for $B(OTeF_5)_3$ than the corresponding values of $C(OTeF_5)_3^+$, indicating less double bond character. This is consistent with the π donation being lower for B←O (0.09) than for C←O (0.19). At the HF level, the B–F bond order and valencies at boron and fluorine are also lower for BF_3 than the corresponding values for CF_3^+. The difference between the valencies at boron in BF_3 and in $B(OTeF_5)_3$ is 0.35, which is almost the same as the difference between the valencies at carbon in CF_3^+ and in $C(OTeF_5)_3^+$, 0.38. These trends show that $C(OTeF_5)_3^+/CF_3^+$ and $B(OTeF_5)_3/BF_3$ exhibit similar electronic properties.

6.2.5. Chemical Shift and Coupling Constant Trends

The ^{13}C chemical shifts of the CCl_3^+ and CBr_3^+ cations are significantly deshielded with respect to their parent tetrahalomethanes (Table 6.1). The ^{13}C resonance

of CI_3^+ has also been shown to be strongly deshielded with respect to CI_4 (Table 6.13).[186,187] Electronic structure calculations (MP2/(SDB-)cc-pVTZ) reveal that the ^{13}C deshielding that results from carbocation formation, $\Delta\delta(^{13}C)$, parallels the decrease in the natural atomic charge on carbon relative to the carbon charge in the tetrahalide (Table 6.11). This reduction in negative charge (CCl_3^+, 0.10; CBr_3^+, 0.10; CI_3^+, 0.26) does not, however, fully account for the extent of deshielding, $\Delta\delta(^{13}C)$ (CCl_3^+, +140.7 ppm; CBr_3^+, +239.4 ppm; CI_3^+, +389.3 ppm), observed in the ^{13}C NMR spectra. The shielding changes can be rationalized in terms of the paramagnetic shielding contribution (σ^p) to the overall screening of the ^{13}C nucleus (σ) in the Ramsey equation (eq 6.13), where σ^d is the

$$\sigma = \sigma^p + \sigma^d \tag{6.13}$$

diamagnetic shielding contribution. The paramagnetic term in the Ramsey equation is negative and can be interpreted in terms of the atom-in-a-molecule approach as defined in eq 6.14, where μ_o is the magnetic moment for a given nucleus, μ_B is the Bohr magneton,

$$\sigma_p \approx -\left(\frac{\mu_o}{4\pi}\right)\left(\frac{4\mu_B^2}{\Delta E}\right)\left[\left\langle r^{-3}\right\rangle_{np} P_i + \left\langle r^{-3}\right\rangle_{nd} D_i\right] \tag{6.14}$$

ΔE is the mean excitation energy, $\langle r^{-3}\rangle_{np}$ and $\langle r^{-3}\rangle_{nd}$ are the inverse cube roots of the mean expectation values for the p orbital and d orbital distances from the nucleus, and P_i and D_i are the degrees of imbalance of valence electrons in p and d orbitals, respectively. The approach is a one-center approximation, restricted to terms centered on the nucleus

Table 6.13. Experimental and Calculated[a] Chemical Shifts for CX_3^+ and BX_3 (X = F, Cl, Br, I, $OTeF_5$) and CX_4 (X = F, Cl, Br, I)

	^{13}C[b]			^{19}F[c]		
	exptl	6-31G(d)[d,e]	cc-pVTZ[d,e]	exptl	6-31G(d)[d,e]	cc-pVTZ[d,e]
CF_3^+	– (150.7)[f]	155.5	154.5	–	32.1	32.9
CCl_3^+	237.1[d] (236.3)[g]	249.8	254.8			
CBr_3^+	209.7[d] (207)[g]	304.9	312.8			
CI_3^+	97[h] (95)[g]		436.4			

	exptl[d]	(SDB-)cc-pVTZ[d,e]	exptl[d]	(SDB-)cc-pVTZ[d,e]
$C(OTeF_5)_3^+$	168.8	139.5	–57.6 (F_a) –31.6 (F_e)	–132.7 (F_a) –107.3 (F_e)

	exptl	6-31G(d)[d,e]	cc-pVTZ[d,e]	exptl[d]	6-31G(d)[d,e]	cc-pVTZ[d,e]
CF_4	(119.9)[i]	119.6	123	–62.4	–88.8	–76.2
CCl_4	96.4[d]	132.1	137			
CBr_4	–29.7[d]	139.1	142			
CI_4	–292.3[j]	–	93			

	^{11}B[k]			^{19}F[c]		
	exptl[l,m]		(SDB-)cc-pVTZ[d,e]	exptl[m]		(SDB-)cc-pVTZ[d,e]
$B(OTeF_5)_3$	–22.9		75.4	–48.2 (F_a) –44.4 (F_e)		–62.8 (F_a) –53.4 (F_e)

	exptl[n]	6-31G(d)[d,e]	cc-pVTZ[d,e]	exptl	6-31G(d)[d,e]	cc-pVTZ[d,e]
BF_3	10.0	30.8	24.0	–126.8[o]	–132.5	–125.6
BCl_3	46.5	73.1	68.8			
BBr_3	38.7	92.8	73.1			
BI_3	–7.9		117.8			

[a] Chemical shifts were calculated at the B3LYP/6-311G(d)//HF/6-31G(d) and B3LYP/(SDB-)cc-pVTZ//HF/(SDB-)cc-pVTZ levels for CX_3^+, CX_4 and BX_3, and at the B3LYP/(SDB-)cc-pVTZ//HF/(SDB-)cc-pVTZ level for $C(OTeF_5)_3^+$ and $B(OTeF_5)_3$. [b] Referenced to TMS. [c] Referenced to $CFCl_3$. [d] Present work. [e] The predicted chemical shifts reported here have been obtained by subtracting their absolute values from that of their respective reference compound, i.e., TMS (^{13}C), 180.9969 ppm (T_d, 6-311G*) and 181.2543 ppm (T_d, (SDB-)cc-pVTZ); $CFCl_3$ (^{19}F), 167.9485 ppm (C_{3v}, 6-311G*) and 183.9397 ppm (C_{3v}, (SDB-)cc-pVTZ); $F_3BO(C_2H_5)_2$ (^{11}B), 123.7710 ppm (C_{3v}, 6-311G*) and 116.3587 ppm (C_{3v}, cc-pVTZ). [f] From ref 187. [g] From ref 186. [h] From ref 101. [i] ^{13}C From ref 70. [j] From ref 253. [k] referenced to $B(OCH_3)_3$. [l] The ^{11}B chemical shift quoted in the literature (ref 109) was referenced to $B(OCH_3)_3$ and converted to the ^{11}B chemical shift referenced to $F_3BO(C_2H_5)_2$ by subtraction of 18.3 ppm from the chemical shift referenced to $B(OCH_3)_3$. [m] From ref 109. [n] The ^{11}B spectra were recorded in methyl cyclohexane at 33.5 °C (ref 254). [o] ^{19}F from ref 255.

in question. As the bond length contracts in going from the neutral halide (Table 6.8) to the cation (Table 6.9), the mean expectation value of the inverse cube of the p orbital radius in eq 6.14 is expected to increase. The bond length contraction and concomitant increase in $\langle r^{-3} \rangle_{np}$ results in a more negative paramagnetic contribution to the overall nuclear magnetic shielding term, and, in turn, to a high-frequency ^{13}C chemical shift. Similar trends are also noted for the isoelectronic boron trihalides, BX_3,[254] and the tetrahaloborates, BX_4^- (X = F, Cl, Br, I).[256]

There are significant discrepancies between the experimental ^{11}B and ^{13}C NMR chemical shifts of BX_3 and CX_3^+ and those calculated by the GIAO method (B3LYP/(SDB-)cc-pVTZ) for the heavier halides (Table 6.13). The calculated ^{11}B and ^{13}C NMR chemical shifts show monotonic increases from BCl_3 to BI_3 and from CCl_3^+ to CI_3^+ (inverse halogen effects), which contrast with the observed trends of decreasing chemical shift upon descending group 17 (Table 6.13). The calculated chemical shift trends arise from larger paramagnetic contributions expected for increasingly more covalent interactions between the central atom and the halogen atom upon descending group 17. The discrepancies between the calculated and experimental chemical shifts, however, result from neglect of the effect of spin-orbit (SO) coupling on the overall nuclear shielding, which is not taken into account by the original Ramsey equation.[257] Spin-orbit coupling causes a triplet excitation on the heavy atom, which, in turn, is transmitted to a neighboring atom through the bond. As such, inclusion of the SO-correction increases the shielding calculated for boron and carbon bonded to bromine or iodine, and results in good agreement with observed ^{11}B and ^{13}C NMR chemical shifts for

the BX_3[258] and CX_3^+ [211] series as previously shown. Although plots of ^{11}B and ^{13}C chemical shifts versus halogen electronegativity for BX_4,[256] BX_3,[256] CX_4,[259] and CX_3^+ [187] are near linear for X = Cl, Br and I, it has been pointed out that such trends are fortuitous, and are, in fact, attributable to the SO coupling term.[211] The ^{11}B chemical shift of BF_3 and the predicted ^{13}C chemical shift of CF_3^+ cannot be understood in terms of the high electronegativity of fluorine, nor can they be understood in terms of the traditional notion that high shielding arises from p(π) back donation to the boron[260,261] or carbon[186] atoms from the fluorine atoms. Electronic structure calculations, however, reveal that the p(π) back bonding components in BF_3 and CF_3^+ are weakest among their respective trihalide series (Table 6.11). Thus, the increased shieldings experienced by the boron and carbon nuclei are actually the normal behavior and arise from the highly ionic characters of the B–F and C–F bonds, which lead to large ΔE values and smaller paramagnetic contributions to their respective nuclear shieldings (eq 6.14).[211,258]

The ^{13}C chemical shift of $C(OTeF_5)_3^+$ (168.8 ppm) is in good agreement with values reported for other peroxygen-substituted carbocations ($C(OH)_3^+$, 166.8 ppm;[193] $C(OCH_3)(OH)_2^+$, 164.1 ppm[192]). The carbon deshielding relative to that of $C(OTeF_5)_4$ ($\Delta\delta(^{13}C)$, 53.0 ppm) is consistent with cation formation, and follows the trend predicted for CF_3^+/CF_4 ($\Delta\delta(^{13}C)$, 30.8 ppm). This result indicates that the C–O bonding in $C(OTeF_5)_3^+$ is highly ionic, as expected from the estimated high electronegativity of the $OTeF_5$ group (3.87),[70] leading to a small paramagnetic contribution to the overall nuclear shielding and, thus, to a relatively shielded ^{13}C chemical shift. This ionic character is supported by electronic structure calculations (HF/(SDB-)cc-pVTZ; vide supra) which

show that the charge on the carbon of the $C(OTeF_5)_3^+$ cation (+1.30) is nearly equal to that of CF_3^+ (+1.37), which is consistent with the ^{13}C NMR empirically predicted (150.7 ppm)[187] and computed (154.5 ppm; this work) chemical shifts for the CF_3^+ cation.

The ^{13}C resonance of the $CBr(OTeF_5)_2^+$ cation was observed at 187.6 ppm, but that of $CBr_2(OTeF_5)^+$ was not observed. The chemical shift of the $CBr_2(OTeF_5)^+$ cation was predicted from pairwise additivity relationships (eq 6.15),[256,262] where $\eta_{i,j}$ is a

$$\delta = \Sigma\eta_{i,j} \tag{6.15}$$

parameter associated with the carbon substituents *i* and *j* and independent of all other substituents. The pairwise additivity parameters $\eta_{Br,Br}$ (69.9 ppm), $\eta_{OTeF_5,OTeF_5}$ (56.3 ppm), and $\eta_{Br,OTeF_5}$ (65.6 ppm) were evaluated from the experimental chemical shifts of CBr_3^+, $CBr(OTeF_5)_2^+$, and $C(OTeF_5)_3^+$. In this way, the chemical shift of $CBr_2(OTeF_5)^+$ is predicted to be 201.1 ppm from eq 6.16.

$$\delta(^{13}C) = \eta_{Br,Br} + 2\eta_{Br,OTeF_5} \tag{6.16}$$

The ^{19}F NMR data for $CBr_n(OTeF_5)_{3-n}^+$ are provided in Table 6.1. Previous attempts have been made to explain the ^{19}F NMR trends observed for the $OTeF_5$ group in different chemical environments.[213,263] The trends observed in the present study are in good agreement with the previously noted trends in ^{19}F chemical shift and $^2J(^{19}F_B-^{19}F_A)$, however, some notable differences occur for $OTeF_5$ bound to carbocation centers: (1)

The ^{19}F chemical shifts of the equatorial fluorine environments of $CBr_n(OTeF_5)_{3-n}^+$ have a substantially larger chemical shift range (–31.6 to –19.9 ppm) than the axial fluorine environments (–61.3 to –57.6 ppm), contrasting with the ranges observed for neutral ($^{19}F_B$, –56.6 to –36.7 ppm; $^{19}F_A$, –54.6 to –27.8 ppm) $OTeF_5$-substituted compounds.[263] (2) The $^2J(^{19}F_B–^{19}F_A)$ values range from 156 to 164 Hz, which is significantly smaller than the previously observed range for neutral and anionic species (175–195 Hz).[263] Moreover, the decrease in coupling in going from the neutral species to the cation also holds for $BrOTeF_5$ (180 Hz) and the $Br(OTeF_5)_2^+$ cation (164 Hz). (3) The $^1J(^{19}F_A–^{123,125}Te)$ and $^1J(^{19}F_B–^{123,125}Te)$ couplings were found to increase substantially in going from $C(OTeF_5)_4$ to $C(OTeF_5)_3^+$, from $CBr(OTeF_5)_2^+$ to $CBr_2(OTeF_5)^+$, and from $Br(OTeF_5)$ to $Br(OTeF_5)_2^+$ (Table 6.1). Furthermore, the magnitude of the coupling was found to increase to a greater extent on going from $C(OTeF_5)_3^+$ to $CBr_2(OTeF_5)^+$. Although there are no other systematic studies involving $OTeF_5$ ligands bound to a cation center, these observations are consistent with cation formation, and the trends across the $CBr_n(OTeF_5)_{3-n}^+$ series can be correlated to increasing covalent character of the C–O bond with increasing bromine substitution.

6.3. Conclusions

The present study provides a new oxidative route to carbocations and the first solid state characterization of the previously reported CCl_3^+ and CBr_3^+ cations as well as the novel $C(OTeF_5)_3^+$ cation. The cations have been stabilized as salts of the preformed oxidatively resistant and weakly coordinating $Sb(OTeF_5)_6^-$ anion, which avoids the use of

more strongly coordinating anions derived from strong Lewis acid ligand acceptors, such as SbF_5. Despite their anticipated high electrophilicity, these salts are stable at room temperature. In addition, the $CBr(OTeF_5)_2^+$ and $Br(OTeF_5)_2^+$ cations and $C(OTeF_5)_4$ have been characterized by ^{13}C and/or ^{19}F NMR spectroscopy. NMR spectroscopy has also been used to monitor carbocation formation, ligand substitution by means of redox elimination and decomposition pathways in these systems.

X-ray crystallographic studies show, in all cases, that the carbocation center is planar in the absence of symmetry constraints imposed by the crystal lattice. Despite the strong Lewis acidities predicted for perhalomethyl cations, the CCl_3^+ and CBr_3^+ cations are well isolated in their respective crystal lattices and possess only long secondary C···F contacts to fluorine atoms of the $Sb(OTeF_5)_6^-$ anion that do not significantly exceed the sum of the van der Waals radii of carbon and fluorine. Secondary X···F and X···O (X = Cl, Br) contacts that are close to the sums of the van der Waals radii of the halogen and an oxygen atom of co-crystallized SO_2ClF or a fluorine atom of the anion exist for CCl_3^+ and CBr_3^+ that are in accord with the calculated positive charges on the halogen atoms of both cations.

Computational studies reproduce the experimental metric parameters of CCl_3^+, CBr_3^+ and $C(OTeF_5)_3^+$, and the vibrational frequencies of CCl_3^+ and CBr_3^+, and have been extended to their $OTeF_5$ derivatives.

Contrasting with the CCl_3^+ and CBr_3^+ cations, the $C(OTeF_5)_3^+$ cation possesses two short C···O contacts to the oxygen atoms of two weakly basic, co-crystallized SO_2ClF molecules, which is consistent with the high positive charge on carbon predicted by

electron structure calculations and which approximates that of the highly Lewis acidic CF_3^+ cation.

Natural orbital analyses were performed using HF or MP2 densities with the NBO program (versions 3.1 and 5.0).[126,127] The use of pseudopotential basis set instead of an all-electron basis set was tested and the overall results did not differ significantly, as pointed out previously.[264]

CHAPTER 7

CARBOCATION SYNTHESIS BY USE OF THE NOBLE-GAS OXIDANT, $[XeOTeF_5][Sb(OTeF_5)_6]$: CFX_2^+ (X = Cl, Br) CATIONS AND EVIDENCE FOR CF_3^+

7.1 Introduction

Unlike the CX_3^+ (X = Cl, Br, I, $OTeF_5$) cations (see Chapter 6), considerably less is known about the mixed, fluorine-containing halomethyl cations. The mixed, fluorine-containing chloromethyl cations, $CFCl_2^+$ and CF_2Cl^+, have been observed in the gas phase by mass spectrometry and photoelectron coincidence spectroscopy,[265-269] and have been generated by matrix radiolysis and photoionization of $CFCl_3$ ($CFCl_2^+$)[270] and CF_2Cl_2 (CF_2Cl^+)[271] when condensed with argon at 15 K. Both cations were characterized by infrared spectroscopy, but the assignments of the complex mixture of cationic and radical chlorofluorocarbon species were not corroborated by other means. In another matrix-isolation study, it was claimed that the $CFCl_2^+\cdots Cl^-$ ion pair was generated by irradiation of $CFCl_3$ with γ-rays generated at 77 K using a ^{60}Co source, followed by irradiation with a xenon lamp using a cutoff of 900 nm.[272] The proposed ion pair was characterized by UV-visible absorption spectrophotometry. Similarly, while the mixed bromofluoromethyl cations have been observed in the gas phase,[265,268] persistent $CFBr_2^+$ [273,274] and CF_2Br^+ [273] cations have only been observed by IR spectroscopy of both the natural abundance and ^{13}C-enriched cations when generated by matrix photoionization and radiolysis of $CFBr_3$ and CF_2Br_2, respectively, when condensed with argon at 15 K.

The difficulties encountered in the isolation of fluorine-containing methyl cations is apparent from the paucity of crystal structures that have been determined for these systems, i.e., $[F_2C–S–CF–S]^+$,[195] $[(CH_3)_2CF]^+$,[196] $[(m\text{-}CF_3C_6H_4)(C_6H_5)CF]^+$,[196] and $[CH_3OCHF]^+$.[197] The fluorine-containing perhalomethyl cations are expected to be among the strongest, if not the strongest, known electrophiles.

To date there have been no syntheses of long-lived fluorine-containing, perhalomethyl cations. Among the objectives of the present work are to provide a viable synthetic route to and spectroscopic data for long-lived, mixed fluorine-containing perhalomethyl cations, CFX_2^+ (X = Cl, Br), as well as evidence for complexes of the CF_3^+ cation, in SO_2ClF solution. The present Chapter also details the solid-state characterization of $[CFCl_2][Sb(OTeF_5)_6]$ (Raman spectroscopy) and computational studies relating to $CF_nX_{3-n}^+$ (n = 0–3; X = Cl, Br). The crystal structure of $[SbBr_4][Sb(OTeF_5)_6]\cdot SO_2ClF$, a decomposition product of the $[CFBr_2][Sb(OTeF_5)_6]$ salt, has also been determined by single crystal X-ray diffraction.

7.2. Results and Discussion

7.2.1. Reactions of $CFCl_3$, CF_2Cl_2, and CF_3Cl with $[XeOTeF_5][Sb(OTeF_5)_6]$ and Solution Characterization by ^{13}C and ^{19}F NMR Spectroscopy

The products of the reactions described below were initially characterized in SO_2ClF solution by ^{13}C and ^{19}F NMR spectroscopy, and their NMR parameters are provided in Table 7.1. The ^{19}F NMR spectrum of the $CFCl_2^+$ cation is provided in Figure 7.1.

Table 7.1. ^{13}C and ^{19}F NMR Parameters[a] for Products[b] Resulting from Reactions of $[XeOTeF_5][Sb(OTeF_5)_6]$ with $CFCl_3$, CF_2Cl_2, CF_2Br_2, and CF_3Br

Species	chemical shift (δ), ppm[c]				coupling constant, Hz[c]		
	^{13}C[d]	$^{19}F_C$	$^{19}F_A$	$^{19}F_B$	$^1J(^{13}C-^{19}F_C)$	$^2J(^{19}F_A-^{19}F_B)$	$^4J(^{13}F_C-^{19}F_B)$[d]
$CFCl_2^+$	214.3	168.6			429		
$FClCOTeF_5^+$	90.0	175.4			399	157	9.7
$CFCl_3$	117.1	–1.1			335		
CF_3Cl	125.9	–20.5			308		
$CFBr_2^+$	208.4	207.9			471		
$CFBr_3$[f]	49.5	7			372		
CF_3Br	112.4	–19.1			320		
$F_3CBrOTeF_5^+$	119.4	–48.6	–58.1	–19.6	289	163	n.o.
$F_2BrCOTeF_5$	n.o.	–12.0	–44.6	–48.1	323	177	4.3
CF_4	119.9	–62.5			263		
F_3COTeF_5	119.2	–51.5	–43.8	–49.7	267	180	3.8

Species	isotopic shift, ppm	
	$^1\Delta^{19}F(^{13/12}C)$[e]	$^2\Delta^{19}F(^{37/35}Cl)$
$CFCl_2^+$	–0.1890	–0.0137
$FClCOTeF_5^+$	–0.1749	–0.0099
$CFCl_3$	–0.2036	–0.0079
CF_3Cl	–0.1780	–0.0069
$CFBr_2^+$	–0.1864	
$CFBr_3$[f]	N/A	
CF_3Br	–0.1478	
$F_3CBrOTeF_5^+$	–0.1730	
$F_2BrCOTeF_5$	–0.1595	
CF_4	–0.1230	
F_3COTeF_5	–0.1317	

Table 7.1. (continued...)

[a] Nuclear magnetic resonance spectra were obtained for SO_2ClF solutions at –80 °C. [b] The NMR parameters for CCl_3^+ and CBr_3^+ are given in Table 6.1. [c] The symbols, F_C, F_{eq}, and F_{ax}, denote fluorine bonded to carbon, equatorial fluorine atoms, and axial fluorine atoms, respectively. [d] Not available. [f] Taken from ref 275.

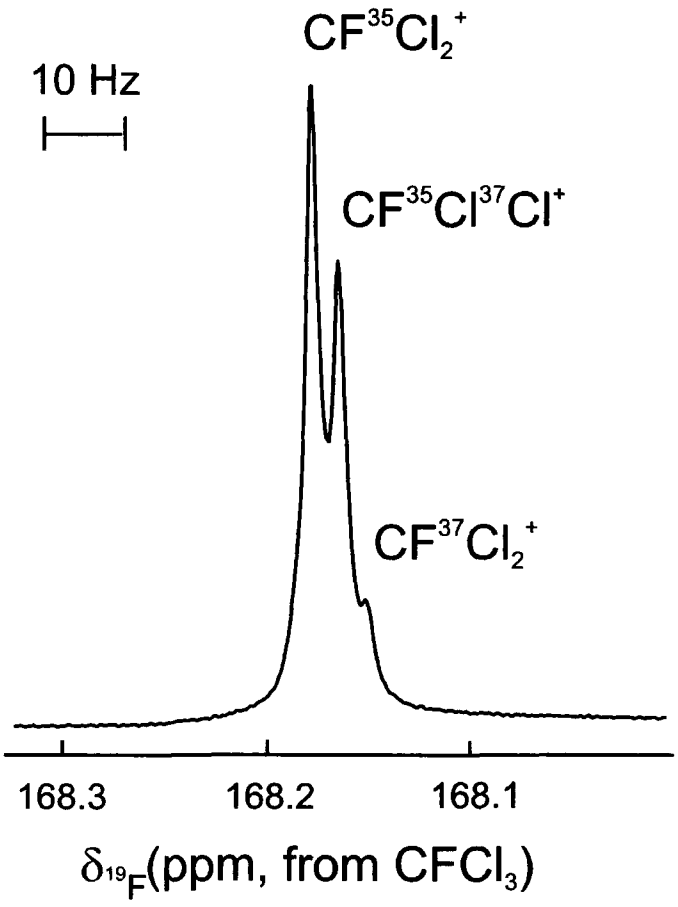

Figure 7.1. The ^{19}F NMR spectrum (470.665 MHz) of $CFCl_2^+$ generated by the reaction of $CFCl_3$ with $[XeOTeF_5][Sb(OTeF_5)_6]$ and recorded at –80 °C in SO_2ClF solvent. The intensity ratio for the three isotopomers was found to be 100 : 73 : 19 (calculated, 100 : 65: 10).

The chlorofluorocarbons (CFCs) $CFCl_3$ (Freon-11) and CF_2Cl_2 (Freon-12) were oxidized, albeit more slowly than CCl_4,[80] by $[XeOTeF_5][Sb(OTeF_5)_6]$ in SO_2ClF at −78 °C, while CF_3Cl (Freon-13) was not oxidized at temperatures approaching room temperature. The $CFCl_2^+$ cation has been synthesized according to eq 7.1 and characterized by ^{13}C and

$$CFCl_3 + [XeOTeF_5][Sb(OTeF_5)_6] \longrightarrow [CFCl_2][Sb(OTeF_5)_6] + ClOTeF_5 + Xe \quad (7.1)$$

^{19}F NMR spectroscopy, and appears to be stable indefinitely at −80 °C. The ^{19}F (168.6 ppm) and ^{13}C (214.3 ppm) chemical shifts are significantly deshielded with respect to those of its parent, $CFCl_3$ (Table 7.1). The large increase in the $^1J(^{19}F-^{13}C)$ coupling in going from $CFCl_3$ (335 Hz) to $CFCl_2^+$ (429 Hz) is consistent with the increase in s-character in going from sp^3-hybridization to sp^2-hybridization at the carbon center. The $CFCl_2^+$ cation was unambiguously established by observation of the secondary isotope shift on the ^{19}F resonance arising from ^{35}Cl and ^{37}Cl, which gives three peaks in the correct intensity ratios corresponding to the isotopomers $FC^{35}Cl_2^+$ (100), $FC^{35}Cl^{37}Cl^+$ (73), and $FC^{37}Cl_2^+$ (19), in agreement with the calculated values of 100 : 65 : 10. The discrepancy between the experimental and calculated intensity ratios is due to the partial overlap of the isotopomer peaks in the ^{19}F NMR spectrum (Figure 7.1).

It was shown by ^{13}C and ^{19}F NMR spectroscopy that the $CFCl_2^+$ cation undergoes ligand exchange with excess $CFCl_3$ at −50 °C over a period of several hours to give $[CCl_3][Sb(OTeF_5)_6]$ and CF_2Cl_2 (eq 7.2). Furthermore, the highly electrophilic $CFCl_2^+$

cation and $ClOTeF_5$ react, with redox elimination of chlorine, to give the $CFCl(OTeF_5)^+$ cation (eq 7.3), which has also been unambiguously characterized by ^{13}C and ^{19}F NMR

$$CFCl_3 + [CFCl_2][Sb(OTeF_5)_6] \longrightarrow [CCl_3][Sb(OTeF_5)_6] + CF_2Cl_2 \quad (7.2)$$

$$[CFCl_2][Sb(OTeF_5)_6] + ClOTeF_5 \longrightarrow$$

$$[CFCl(OTeF_5)][Sb(OTeF_5)_6] + Cl_2 \quad (7.3)$$

spectroscopy (Table 7.1).

The reaction of CF_2Cl_2 and $[XeOTeF_5][Sb(OTeF_5)_6]$ at −78 °C in SO_2ClF has also been studied by NMR spectroscopy (eq 7.4). It is proposed that the CF_2Cl^+ cation is

$$CF_2Cl_2 + [XeOTeF_5][Sb(OTeF_5)_6] \longrightarrow$$

$$[CF_2Cl][Sb(OTeF_5)_6] + ClOTeF_5 + Xe \quad (7.4)$$

generated, but is not observed because it rapidly undergoes halogen exchange reactions to generate $CFCl_2^+$, CCl_3^+, $CFCl_3$, and CF_3Cl according to eq 7.5–7.7, which were all

$$CF_2Cl^+ + CF_2Cl_2 \longrightarrow CFCl_2^+ + CF_3Cl \quad (7.5)$$

$$CFCl_2^+ + CF_2Cl_2 \longrightarrow CF_2Cl^+ + CFCl_3 \quad (7.6)$$

$$CF_2Cl^+ + CFCl_3 \longrightarrow CCl_3^+ + CF_3Cl \quad (7.7)$$

observed by ^{13}C and/or ^{19}F NMR spectroscopy. This result is not unexpected because CF_2Cl^+ is destabilized with respect to $CFCl_2^+$ and CCl_3^+ by virtue of the greater inductive effect of fluorine[196] (see Section 7.2.5).

7.2.2. Reactions of CF_2Br_2 and CF_3Br with $[XeOTeF_5][Sb(OTeF_5)_6]$ and Solution Characterization by ^{13}C and ^{19}F NMR Spectroscopy

The products of the reactions described below were initially characterized in SO_2ClF solution by ^{13}C and ^{19}F NMR spectroscopy, and their NMR parameters are provided in Table 7.1.

Generation of the bromine analogue of the $CFCl_2^+$ cation, $CFBr_2^+$, has proven more difficult because halogen exchange is more facile in the case of bromine, and because the product, $BrOTeF_5$, is more reactive towards the $CFBr_2^+$ cation with respect to redox elimination of Br_2. Thus, it is proposed that the reaction of CF_2Br_2 with $[XeOTeF_5][Sb(OTeF_5)_6]$ in SO_2ClF at −78 °C initially yields CF_2Br^+, which rapidly undergoes halogen exchange with CF_2Br_2 to give $CFBr_2^+$, CBr_3^+, and CF_3Br (eq 7.8–7.10). Although the reactivity of CF_2Br^+ has precluded its direct detection by NMR

$$CF_2Br_2 + [XeOTeF_5][Sb(OTeF_5)_6] \longrightarrow [CF_2Br][Sb(OTeF_5)_6] + BrOTeF_5 + Xe \quad (7.8)$$

$$CF_2Br^+ + CF_2Br_2 \longrightarrow CFBr_2^+ + CF_3Br \quad (7.9)$$

$$CFBr_2^+ + CF_2Br_2 \longrightarrow CBr_3^+ + CF_3Br \quad (7.10)$$

spectroscopy, the $CFBr_2^+$ cation persists for several hours at −80 °C. As with $CFCl_2^+$, the ^{19}F (207.9 ppm) and the ^{13}C (208.4 ppm) chemical shifts are significantly deshielded with respect to those of its parent, $CFBr_3$ (Table 7.1), with a $^1J(^{19}F–^{13}C)$ coupling (471 Hz) that is again indicative of an sp^2-hybridized carbon center. Attempts to grow crystals of

$[CFBr_2][Sb(OTeF_5)_6]$ at −50 °C over several hours yielded $[SbBr_4][Sb(OTeF_5)_6]$ instead (see Section 7.3).

The ^{19}F NMR spectrum also showed that $BrOTeF_5$ was not present in solution, but reacted with both CF_3Br and CF_2Br_2 to generate F_3COTeF_5 and $F_2BrCOTeF_5$. Although the former is known,[276] the latter represents the first example of a mixed bromofluoro-teflate of carbon.

Attempts to generate persistent CF_3^+ in solution failed, likely because of its extremely high electrophilicity. The reaction between CF_3Br and $[XeOTeF_5][Sb(OTeF_5)_6]$ presumably generates incipient $[CF_3][Sb(OTeF_5)_6]$, which then abstracts F^- or $OTeF_5^-$ to give CF_4 and F_3COTeF_5, respectively (eq 7.11 and 7.12). The

$$[CF_3][Sb(OTeF_5)_6] \longrightarrow CF_4 + Sb(OTeF_5)_5(OTeF_4) \quad (7.11)$$

$$[CF_3][Sb(OTeF_5)_6] \longrightarrow F_3COTeF_5 + Sb(OTeF_5)_5 \quad (7.12)$$

Latter were observed by ^{13}C and ^{19}F NMR spectroscopy. The resulting neutral antimony species are, themselves, unstable, as previously noted (see Chapter 6).

Indirect evidence for CF_3^+ as a reactive intermediate is also indicated by the formation of the $F_3CBrOTeF_5^+$ cation (eq 7.13) which has been characterized by ^{13}C and

$$[CF_3][Sb(OTeF_5)_6] + BrOTeF_5 \longrightarrow [F_3CBrOTeF_5][Sb(OTeF_5)_6] \quad (7.13)$$

^{19}F NMR spectroscopy (Table 7.1).

7.2.3. X-ray Crystal Structure of $[SbBr_4][Sb(OTeF_5)_6]\cdot SO_2ClF$

Details of data collection parameters and other crystallographic information are provided in Table 7.2. Bond lengths and bond angles for the salt, as well as closest contacts between the cation and anion, are listed in Table 7.3. One $OTeF_5$ group of the anion was positionally disordered about the equatorial fluorines, and was modeled accordingly (Figure 7.2). Only data from the non-disordered $OTeF_5$ groups are cited in Table 7.3.

Attempts to grow crystals of $[CFBr_2][Sb(OTeF_5)_6]$ at −50 °C over several hours instead yielded crystals of $[SbBr_4][Sb(OTeF_5)_6]\cdot SO_2ClF$ by the following proposed reaction pathway (eq 7.14–7.17):

$$CFBr_2^+ + Sb(OTeF_5)_6^- \longrightarrow F_2BrCOTeF_5 + Sb(OTeF_5)_5 \quad (7.14)$$

$$Sb(OTeF_5)_5 \longrightarrow Sb(OTeF_5)_3 + O_2(TeF_5)_2 \quad (7.15)$$

$$CFBr_2^+ + BrOTeF_5 \longrightarrow BrFCOTeF_5^+ + Br_2 \quad (7.16)$$

$$2Sb(OTeF_5)_3 + 2Br_2 \longrightarrow [SbBr_4][Sb(OTeF_5)_6] \quad (7.17)$$

The species, $Sb(OTeF_5)_5$, is known to be unstable (also see Chapter 6).[110,216] The salt, $[SbBr_4][Sb(OTeF_5)_6]\cdot SO_2ClF$, was characterized by single crystal X-ray diffraction, and the geometric parameters determined for the cation were in excellent agreement with those obtained from the crystal structure of $[SbBr_4][Sb(OTeF_5)_6]$.[79] The geometric parameters of the single molecule of co-crystallized SO_2ClF were also found to be in good agreement with those previously determined structures for SO_2ClF in structures where it does not does not significantly interact with the cation, such as

Table 7.2. Crystallographic Data for $[SbBr_4][Sb(OTeF_5)_6]\cdot SO_2ClF$

chem formula	$O_8F_{31}SClBr_4Sb_2Te_6$
space group	$P2_1/c$
a (Å)	13.2515(4)
b (Å)	15.4225(4)
c (Å)	19.0892(5)
α (deg)	90
β (deg)	106.886(2)
γ (deg)	90
V (Å^3)	3733.1(2)
molecules/unit cell	4
mol wt (g mol^{-1})	2113.20
calcd density (g cm^{-3})	3.760
T (°C)	−173
μ (mm^{-1})	10.64
R_1 [a]	0.0413
wR_2 [b]	0.0705

[a] R_1 is defined as $\Sigma||F_o|-|F_c||/\Sigma|F_o|$ for $I > 2\sigma(I)$. [b] wR_2 is defined as $[\Sigma[w(F_o^2 - F_c^2)^2]/\Sigma w(F_o^2)^2]^{1/2}$ for $I > 2\sigma(I)$.

Table 7.3. Experimental[a] Geometric Parameters for $[SbBr_4][Sb(OTeF_5)_6]\cdot SO_2ClF$ and Calculated[b] Geometric Parameters for the $SbBr_4^+$ cation

		bond lengths (Å)		
Sb(1)–Br(1)	2.3859(5)	[2.4016]	Sb–O	1.946(3)–1.954(3)
Sb(1)–Br(2)	2.3904(6)		O–Te	1.833(3)–1.850(3)
Sb(1)–Br(3)	2.3844(6)		Te–F_{ax}	1.823(3)–1.834(2)
Sb(1)–Br(4)	2.3848(5)		Te–F_{eq}	1.817(3)–1.835(3)
S(1)–Cl(1)	1.969(2)		S(1)–F(40)	1.524(3)
S(1)–O(40)	1.405(4)		S(1)–O(41)	1.398(4)
		bond angles (deg)		
Br(1)–Sb(1)–Br(2)	112.97(2)	[109.47]	Sb–O–Te	138.4(2)–141.0(2)
Br(1)–Sb(1)–Br(3)	109.56(2)		O–Te–F_{ax}	176.6(1)–177.8(1)
Br(1)–Sb(1)–Br(4)	106.16(2)		O–Te–F_{eq}	89.3(1)–95.2(1)
Br(2)–Sb(1)–Br(3)	107.25(2)		O–S–O	122.1(3)
Br(2)–Sb(1)–Br(4)	112.55(2)		O–S–Cl (×2)	110.1(2), 109.25(2)
Br(3)–Sb(1)–Br(4)	108.26(2)		O–S–F (×2)	108.0(2), 105.7(2)
			F–S–Cl	99.2(1)
		contacts (Å)		
Sb(1)—F(15)	3.299(2)		Sb(1)—F(29A)	3.479(8)
Sb(1)—F(22A)	3.460(3)		Sb(1)—O(40)	3.254(4)

[a] Values for the $OTeF_5$ groups were taken from the five non-disordered groups. [b] Values in square brackets were calculated at the SVWN/aug-cc-pVTZ(-PP) level of theory with T_d symmetry.

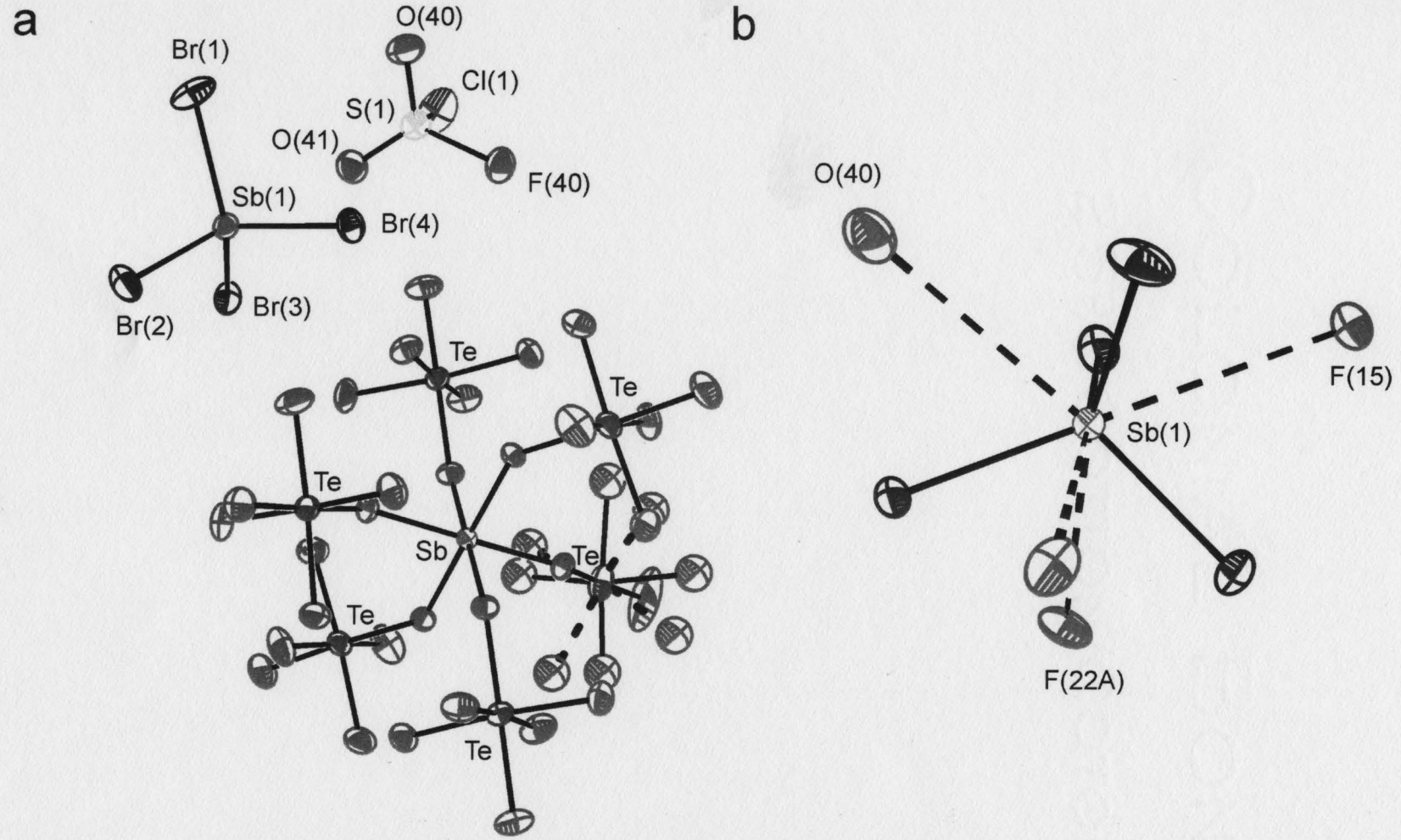

Figure 7.2. Crystal structure of (a) $[SbBr_4][Sb(OTeF_5)_6]\cdot SO_2ClF$ and (b) the closest contacts to Sb(1); thermal ellipsoids are shown at the 50% probability level. The dashed lines indicate the second orientation for the single disordered $OTeF_5$ group. The numbering scheme corresponds to that given in Table 7.3.

$[CBr_3][Sb(OTeF_5)_6]\cdot SO_2ClF$ and the single uncoordinated SO_2ClF molecule in $[C(OTeF_5)_3][Sb(OTeF_5)_6]\cdot 3SO_2ClF$ (see Chapter 6). The presence of the SO_2ClF molecule in the crystal lattice allows for more efficient packing, and is therefore not twinned like the previous structure.[79] As a result, the structural solution for $[SbBr_4][Sb(OTeF_5)_6]\cdot SO_2ClF$ is more precise, with the error on the Sb–Br bond lengths being approximately one half to one quarter of those previously reported. The major difference between the two structures is the number of long contacts and their arrangement about the central antimony atom. Although the current structure possesses three long Sb···F contacts to fluorine atoms, as with the previous structure, ranging from 3.299(2)–3.479(8) Å (van der Waals radii, 3.56 Å),[26] there is a fourth Sb···O contact of 3.254(4) Å (van der Waals radii, 3.61 Å[26]) to SO_2ClF. The four contacts are arranged in a distorted tetrahedral arrangement, and are trans to the Sb–Br bonds, providing distorted cubic coordination about the antimony atom (Figure 7.2).

Electronic structure calculations have been carried out for the $SbBr_4^+$ cation at the SVWN/aug-cc-pVTZ(-PP) level of theory and show that the cation possesses T_d symmetry in the gas phase. The calculated Sb–Br bond length (2.4016 Å) is slightly longer than the average experimental bond length of 2.386(1) Å. The experimental bond angles, which in some cases differ from the ideal tetrahedral angle by more than $\pm\sigma$, average to 109.46(5)° (calculated, 109.47°). The difference in bond angles in the crystal structure is likely the result of long contacts between the fluorine atoms of the anion and the oxygen atom of SO_2ClF (vide supra).

7.2.4. Raman Spectroscopy

The vibrational modes of the $CFCl_2^+$ cation were assigned under C_{2v} symmetry and belong to the irreducible representation $3A_1 + B_1 + 2B_2$. A total of 6 fundamental bands are expected, of which all are infrared and Raman active. The vibrational frequencies were calculated using DFT (SVWN) and MP2 methods and the cc-pVTZ basis set. Assignments were made by comparison with the calculated frequencies and Raman intensities, which are in agreement with the experimental values (Table 7.4).

The low-temperature, solid-state Raman spectrum of the products from the reaction of $CFCl_3$ with $[XeOTeF_5][Sb(OTeF_5)_6]$ displayed large numbers of bands that could be assigned to the $Sb(OTeF_5)_6^-$ anion. The frequency assignments for the $Sb(OTeF_5)_6^-$ anion were made by comparison with those of $[N(CH_3)_4][Sb(OTeF_5)_6]$,[35] $[SbX_4][Sb(OTeF_5)_6]$,[79] and $[XeOTeF_5][Sb(OTeF_5)_6]\cdot SO_2ClF$.[140] Five new bands were observed in the Raman spectrum ($\nu_1(A_1)$, not observed; $\nu_5(B_2)$, 1223.7 cm^{-1}; $\nu_2(A_1)$, 649.3 cm^{-1}; $\nu_4(B_1)$, 617.8 cm^{-1}; $\nu_6(B_2)$, 448.4 cm^{-1}; $\nu_3(A_1)$, 337.3 cm^{-1}) which were assigned, with the aid of electronic structure calculations, to $CFCl_2^+$ and which are in good agreement with the calculated values (Table 7.4). The high-resolution Raman spectrum of $[CFCl_2][Sb(OTeF_5)_6]$ reveals that the $\nu_2(A_1)$ band is split into two components (Table 7.4) that arise from the isotopomers $CF^{35}Cl_2^+$ and $CF^{35}Cl^{37}Cl^+$. The third isotopomeric peak arising from $CF^{37}Cl_2^+$ could not be observed because of its low intensity. The intensities of the observed isotopomer bands are in excellent agreement with the intensities calculated from the chlorine natural abundances ($CF^{35}Cl_2^+$, 100; $CF^{35}Cl^{37}Cl^+$, 65; $CF^{37}Cl_2^+$, 10). The isotopic splitting, $\Delta\nu(^{37/35}Cl)$, of 5.0 cm^{-1} is in good

Table 7.4. Experimental and Calculated Frequencies (cm^{-1}), Raman Intensities[a] and Assignments[b] for $CFCl_2^+$

	$CFCl_2^+$						
		SVWN/cc-pVTZ			MP2/cc-pVTZ		
assgnt	exptl	$CF^{35}Cl_2^+$	$CF^{35}Cl^{37}Cl$	$CF^{37}Cl_2^+$	$CF^{35}Cl_2^+$	$CF^{35}Cl^{37}Cl$	$CF^{37}Cl_2^+$
$\nu_1(A_1)$, ν(C–F)	n.o.[c]	1391.3(1)	1391.1(1)	1391.0(1)	1409.0(4)	1408.9(4)	1408.7(4)
$\nu_2(A_1)$, $\nu_s(CCl_2)$	649.3(100)[d]	661.5(12)	656.3(11)	650.9(11)	678.1(12)	672.7(12)	667.2(11)
$\nu_3(A_1)$, $\delta(CCl_2)$	337.3(54)	325.4(4)	322.2(4)	319.0	338.2(4)	334.9(4)	331.6(4)
$\nu_4(B_1)$, $\delta(CCl_2F)$ o.o.p.	617.8(11)	588.4(<1)	588.0(<1)	587.5(<1)	617.7(1)	617.2(1)	616.7(1)
$\nu_5(B_2)$, $\nu_{as}(CCl_2)$	1223.7(9)	1155.7(1)	1153.6(1)	1151.4(1)	1191.5(<1)	1189.4(<1)	1187.2(<1)
$\nu_6(B_2)$, $\rho_r(CCl_2)$	448.4(29)	440.8(2)	438.4(2)	436.1(2)	455.2(2)	452.7(2)	450.2(2)

[a] Values in parentheses denote experimental relative Raman intensities or calculated Raman intensities ($Å^4$ amu^{-1}). [b] Frequencies have been calculated and assigned for C_{2v} symmetry. [c] Not observed. [d] The $\nu_2(A_1)$ band is split as a result of the mass effect of the ^{35}Cl and ^{37}Cl isotopes: 649.3(100) ($CF^{35}Cl_2^+$) and 644.3(68) ($CF^{35}Cl^{37}Cl^+$) cm^{-1}. The band arising from $CF^{37}Cl_2^+$ was obscured by bands attributed to the $Sb(OTeF_5)_6^-$ anion.

agreement with the calculated splitting (SVWN, 5.3 cm^{-1}; MP2, 5.4 cm^{-1}) and with that measured for CCl_3^+ (5.0–5.3 cm^{-1}). The formally Raman-active $\nu_1(A_1)$ mode was not observed, in accord with the low Raman intensity that was calculated for this band.

7.2.5. Computational Results

Although quantum mechanical ab initio calculations abound for CX_3^+ (X = F, Cl, Br, I; see Chapter 6), there have been no computational studies of the mixed fluorohalomethyl cations and their neutral progenitors. The series of both mixed chlorofluoro- and bromofluoromethyl cations, as well as $XOTeF_5$ (X = Cl, Br) and $XeOTeF_5^+$, have been optimized using the MP2 method with the all-electron correlation consistent cc-pVTZ basis sets for all atoms other than bromine, tellurium, and xenon, for which pseudopotentials were used (SDB-cc-pVTZ). Energies for the MP2-optimized structures were performed, followed by a natural bond orbital (NBO) analysis using the MP2 method.

7.2.5.1. Calculated Charge Distributions and Bonding in $CF_nX_{3-n}^+$ (X = Cl, Br; n = 1–3)

Several prior studies have assessed the bonding and relative stabilities of the CX_3^+ (X = F, Cl, Br, and I) cations in terms of relative degrees of σ and p(π) donation from the halogen atom to the carbon center.[196,199,207] The Natural Bond Orbital (NBO) analyses have shown that the σ effect is strongly withdrawing in the case of fluorine and weakly donating in the cases of chlorine, bromine, and iodine (I > Br > Cl), with the p(π) back-

donation trend following the order I > Br > Cl > F and that these trends were mirrored by the NBO charge analyses.

Figure 7.3 provides analogous assessments of charge distributions and σ and p(π) donation for the mixed chlorofluoro- and bromofluoro- trihalomethyl cations with CF_3^+, CCl_3^+, and CBr_3^+ included for comparison. The individual σ- and π- components are relatively constant throughout the series. The C–F σ-contribution is withdrawing but opposite to the C–F p(π) contribution which, like all C–X contributions, are donating with respect to carbon. In all cases the π-donation, which increases along the series F < Cl < Br < I, serves to stabilize the positive carbon center and dominates the σ-contribution, which also increases in the same direction for Cl, Br, and I. With the exception of negative charges on the fluorine ligands, the halogen ligands are always positively charged and the charge on carbon becomes significantly more positive with each additional fluorine ligand that is added.

Based on calculated carbon charges, the $CFCl_2^+$ and $CFBr_2^+$ cations are, thus far, the most electrophilic trihalomethyl cations that have been shown to persist either in solution ($CFCl_2^+$ and $CFBr_2^+$) or in the solid state ($CFCl_2^+$). Although rapid halogen exchange involving the more electrophilic CF_2Cl^+ and CF_2Br^+ cations may preclude their isolation, the isolation and characterization of a stable salt of the SO_2ClF-solvated $C(OTeF_5)_3^+$ cation, which has a carbon charge and σ- and π-components, in the absence of solvation, that are similar to those of CF_3^+, suggests that CF_3^+ may still be attainable as a persistent entity, albeit solvated in the condensed state.

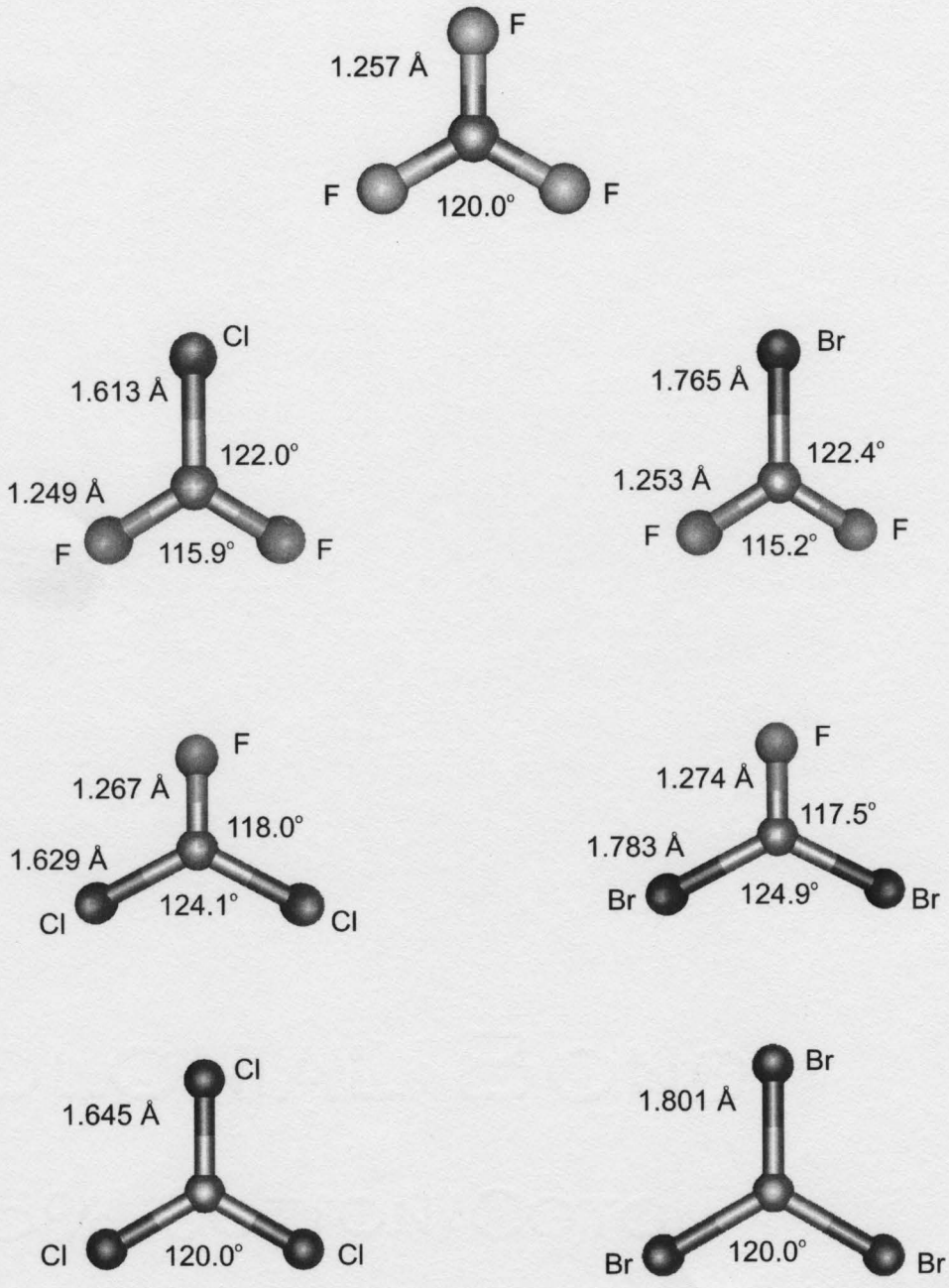

Figure 7.3a. Calculated geometries for $CF_nX_{3-n}^+$ (n = 0–3, X = Cl, Br; MP2/cc-pVTZ).

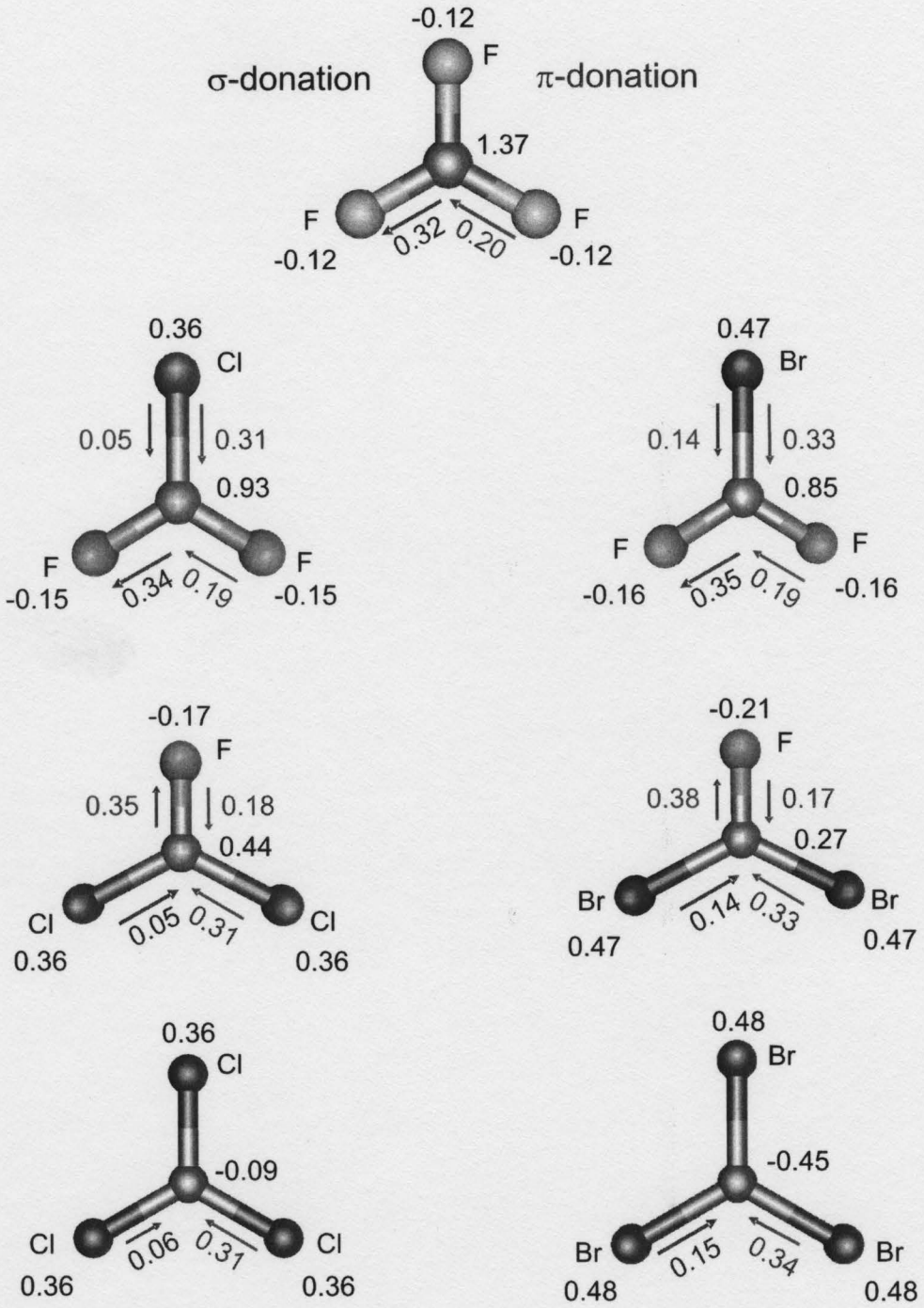

Figure 7.3b. Calculated natural (NBO) charges for $CF_nX_{3-n}^+$ (n = 0–3, X = Cl, Br; MP2/cc-pVTZ//MP2/cc-pVTZ).

7.2.5.2. Gas-Phase Thermodynamics of Reactions of $XeOTeF_5^+$ with CF_nX_{4-n} (X = Cl, Br; n = 0–3)

The calculated standard gas-phase enthalpies (ΔH^o) and Gibbs free energies (ΔG^o) corresponding to eq 7.18 are given in Scheme 7.1. The spontaneity with which

$$CF_nX_{4-n} + [XeOTeF_5][Sb(OTeF_5)_6] \longrightarrow [CF_nX_{3-n}][Sb(OTeF_5)_6] + XOTeF_5 + Xe \quad (7.18)$$

CF_nCl_{4-n} and CF_nBr_{4-n} (n = 0–3) are oxidized decreases dramatically with each successive addition of a fluorine ligand. This trend is in agreement with the experimental findings. For example, CF_3Cl and $[XeOTeF_5][Sb(OTeF_5)_6]$ are unreactive at temperatures as high as 0 °C in SO_2ClF solvent, with $\Delta H^o = -5.4$ and $\Delta G^o = -34.1$ kJ mol^{-1} indicating that the reaction is only slightly favored in the gas phase at 298.15 K. In contrast, the corresponding reaction with CCl_4 occurs rapidly at −78 °C in SO_2ClF solvent,[82] with $\Delta H^o = -158.4$ and $\Delta G^o = -191.9$ kJ mol^{-1}. Standard heats of reaction leading to the formation of the $CF_nBr_{3-n}^+$ cations are 55–65 kJ mol^{-1} more favorable than their $CF_nCl_{3-n}^+$ analogues, in accord with the anticipated relative ease of oxidation of a bromine ligand versus a chlorine ligand.

7.3. Conclusions

The present study provides the first viable synthetic routes to the long-lived $CFCl_2^+$ and $CFBr_2^+$ cations and to their solution characterizations, as well as that of

			ΔH^o	ΔG^o
$CCl_4 + XeOTeF_5^+$	⟶	$CCl_3^+ + ClOTeF_5 + Xe$	−158.4	−191.9
$CFCl_3 + XeOTeF_5^+$	⟶	$CFCl_2^+ + ClOTeF_5 + Xe$	−121.3	−153.0
$CF_2Cl_2 + XeOTeF_5^+$	⟶	$CF_2Cl^+ + ClOTeF_5 + Xe$	−73.3	−106.5
$CF_3Cl + XeOTeF_5^+$	⟶	$CF_3^+ + ClOTeF_5 + Xe$	−5.4	−34.1
$CBr_4 + XeOTeF_5^+$	⟶	$CBr_3^+ + BrOTeF_5 + Xe$	−223.2	−263.3
$CFBr_3 + XeOTeF_5^+$	⟶	$CFBr_2^+ + BrOTeF_5 + Xe$	−188.3	−220.1
$CF_2Br_2 + XeOTeF_5^+$	⟶	$CF_2Br^+ + BrOTeF_5 + Xe$	−140.1	−173.2
$CF_3Br + XeOTeF_5^+$	⟶	$CF_3^+ + BrOTeF_5 + Xe$	−61.1	−89.6

Scheme 7.1. Gas-phase values of ΔH^o and ΔG^o (kJ mol^{-1}) for the reactions of $XeOTeF_5^+$ with CF_nX_{4-n} (X = Cl, Br; n = 0–3; MP2/cc-pVTZ).

$CFCl_2^+$ in the solid state. As well, NMR spectroscopic evidence for the CF_3^+ as an intermediate species has been obtained in solution as the adducted CF_3^+ cation, $F_3C–Br–OTeF_5^+$. The cations have been stabilized as salts of the preformed, oxidatively resistant, and weakly coordinating $Sb(OTeF_5)_6^-$ anion. Both cations differ from their CX_3^+ counterparts (X = Cl, Br) in that they do not show appreciable stability even at temperatures as low as –60 °C, owing to their high electrophilicity. In addition, the $CFClOTeF_5^+$ cation and $F_2BrCOTeF_5$ have been characterized by ^{13}C and ^{19}F NMR spectroscopy. NMR spectroscopy has also been used to monitor the formations and decompositions of the $CFCl_2^+$ and $CFBr_2^+$ cations in solution.

An attempted X-ray crystallographic study of the $CFBr_2^+$ cation yielded the $SbBr_4^+$ cation, which was isolated as the $[SbBr_4][Sb(OTeF_5)_6]\cdot SO_2ClF$ salt. The crystal structure is of better precision than that previously published, and the formation of this salt provides valuable insight into the decomposition pathway for the $CFBr_2^+$ cation.

Computational studies reproduce the vibrational frequencies observed for the $CFCl_2^+$ cation, and the NBO analyses show that the positive charge on carbon for $CF_nX_{3-n}^+$ increases significantly with increasing fluorine substitution. The values of ΔH° and ΔG° calculated for the gas phase follow the experimental trends, and are consistent with the inability to generate CF_3^+ from CF_3Cl, as CF_3Cl is inert to oxidation by the $XeOTeF_5^+$ cation.

CHAPTER 8

SYNTHESIS AND STRUCTURAL CHARACTERIZATION OF $C(OTeF_5)_4$, AND A COMPARATIVE STRUCTURAL STUDY OF THE ISOELECTRONIC $B(OTeF_5)_4^-$ ANION

8.1. Introduction

Although organic examples of orthocarbonates ($C(OR)_4$) abound,[277,278] very few C–O bonded tetrakis-compounds containing inorganic ligands are known; namely $C(OSO_2F)_4$,[279] $C(OCF_3)_4$,[280,281] and $C(OSeF_5)_4$.[282] Although the chemistry of the $OSeF_5$ and $OTeF_5$ ligands are similar, no detailed study of the $OTeF_5$ analogue, $C(OTeF_5)_4$, has appeared in the literature. Prior to this study, the only fully $OTeF_5$-substituted derivatives of the row 2 elements that have been structurally characterized are $B(OTeF_5)_3$,[109,221] $B(OTeF_5)_4^-$,[111,283,284] $O(TeF_5)_2$,[285-287] $(OTeF_5)_2$,[31,288] and $FOTeF_5$.[289,290] The complete $CH_n(OSeF_5)_{4-n}$ (n = 0–3) series has been synthesized by reaction of the corresponding chlorohydrocarbon with $Hg(OSeF_5)_2$ in n-C_6F_{14} and characterized by infrared and Raman spectroscopy, NMR spectroscopy, and mass spectrometry.[282] No crystal structure is available for $C(OSeF_5)_4$, but unit cell parameters have been reported.[282] Although several mono-substituted alkyl $OTeF_5$ derivatives, $ROTeF_5$, have been prepared by reaction of TeF_6 with ROH (R = Me, Et, Pr, $CHMe_2$, Bu, CHMeEt, CH_2CHMe_2),[291] the isolation and full structural characterization of $C(OTeF_5)_4$ has not been reported.

More recently, $C(OTeF_5)_4$ has been generated and characterized in SO_2ClF solution by ^{13}C and ^{19}F NMR spectroscopy for comparison with the NMR parameters of the $C(OTeF_5)_3^+$ cation (see Chapter 6).[80] This chapter provides the detailed synthesis and

solution multi-NMR and solid state characterizations of $C(OTeF_5)_4$ by X-ray crystallography and Raman spectroscopy, and a study of its decomposition in CH_3CN. The $[N(CH_3)_4][B(OTeF_5)_4]$ salt has been synthesized, and its crystal structure and Raman spectrum have been acquired for comparison of the geometrical parameters of $B(OTeF_5)_4^-$ with those of isoelectronic $C(OTeF_5)_4$. Electronic structure calculations for both $C(OTeF_5)_4$ and the $B(OTeF_5)_4^-$ anion were carried out using density functional theory (DFT) methods to obtain the energy-minimized gas-phase structures for comparison with their solid-state geometries, and to assist in the assignments of their Raman spectra.

8.2. Results and Discussion

8.2.1. Synthesis of $C(OTeF_5)_4$ and Solution Characterization by ^{13}C, ^{19}F, and ^{125}Te NMR Spectroscopy

The reaction of stoichiometric amounts of $BrOTeF_5$ and CBr_4 in SO_2ClF solution gave nearly quantitative yields of $C(OTeF_5)_4$ with the elimination of Br_2 according to eq 8.1. Solvent and Br_2 were removed under dynamic vacuum between –78 and 0 °C,

$$CBr_4 + 4\,BrOTeF_5 \longrightarrow C(OTeF_5)_4 + 4\,Br_2 \qquad (8.1)$$

yielding colorless, microcrystalline $C(OTeF_5)_4$ which is stable indefinitely at room temperature.

The full solution NMR characterization of $C(OTeF_5)_4$ in SO_2ClF solution at 30 °C by ^{13}C, ^{19}F, and ^{125}Te NMR spectroscopy relies upon 99% ^{13}C-enrichment and, in

particular, on the ^{13}C NMR spectrum of $^{13}C(OTeF_5)_4$ (Figure 8.1a). The ^{13}C resonance of $C(OTeF_5)_4$ is a singlet at 115.6 ppm that is accompanied by ^{123}Te ($^2J(^{13}C–^{123}Te)$, 54.7 Hz) and ^{125}Te ($^2J(^{13}C–^{125}Te)$, 64.5 Hz) satellites. The ^{13}C environment is significantly more shielded relative to that of the $C(OTeF_5)_3^+$ cation (168.8 ppm).[80] Separate integrations of ^{123}Te (0.87% natural abundance) and ^{125}Te (6.99% natural abundance) satellites were not possible as a result of peak overlap ($\Delta\nu_{1/2} \approx 3$ Hz), thus, the weaker ^{123}Te satellites are not fully resolved and appear as shoulders on the ^{125}Te satellites. Because ^{123}Te and ^{125}Te are spin-½ nuclei of low abundance, only a superposition of subspectra arising from the most abundant isotopomers, $^{13}C(O^0TeF_5)_4$ (singlet), $^{13}C(O^{123/125}TeF_5)(O^0TeF_5)_3$ (doublet), and $^{13}C(O^{125}TeF_5)_2(O^0TeF_5)_2$ (triplet), where ^0Te represents all spinless isotopes of tellurium, was observed. Taking into account the natural isotopic abundances, multiplicities, and statistical distributions of tellurium isotopomers[292] among four sites, the experimental combined $^{123/125}Te$ integrated satellite peak/central peak area ratios (0.0116:0.1696:1.0000:0.1687:0.0126) in the ^{13}C NMR spectrum confirm the presence of four equivalent tellurium atoms when compared with their calculated relative intensity ratios (3×10^{-6}:0.0003:0.0107:0.1678:1.0000:0.1678: 0.0107:0.0003:3×10^{-6}).

The ^{125}Te NMR spectrum of 99% ^{13}C-enriched $C(OTeF_5)_4$ (Figure 8.1b) consists of a well-resolved binomial doublet of doublets of quintets ($\delta(^{125}Te)$, 547.6 ppm) arising from $^2J(^{125}Te–^{13}C) = 65.8$ Hz, $^1J(^{125}Te–^{19}F_A) = 3650$ Hz, and $^1J(^{125}Te–^{19}F_B) = 3756$ Hz.

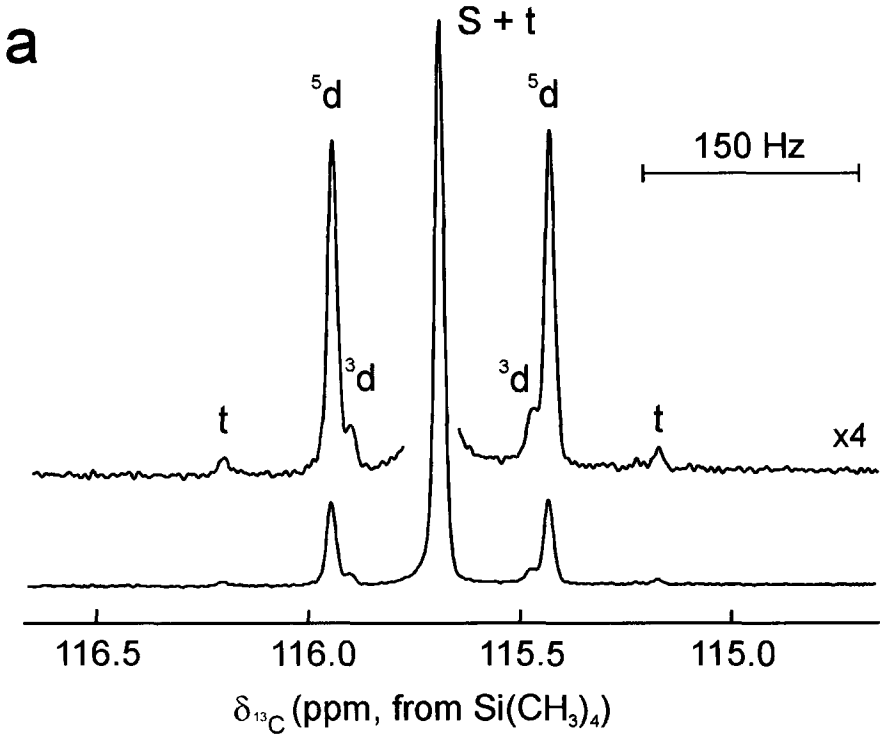
a
S + t
^{5}d
^{5}d
150 Hz
^{3}d
^{3}d
t
t
x4
116.5
116.0
115.5
115.0
$\delta_{^{13}C}$ (ppm, from Si(CH$_3$)$_4$)

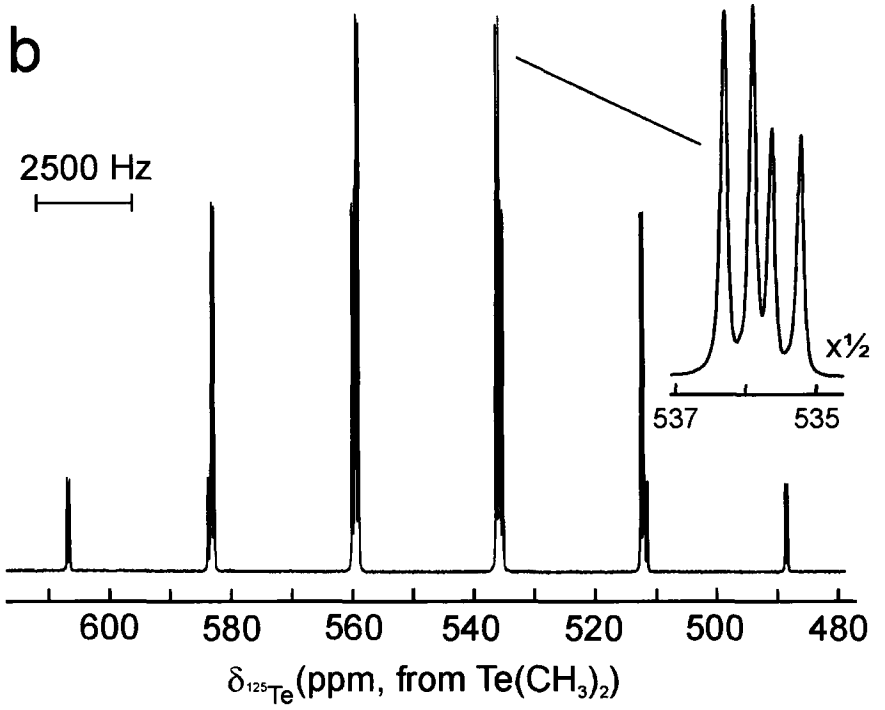
b
2500 Hz
x½
537
535
600
580
560
540
520
500
480
$\delta_{^{125}Te}$(ppm, from Te(CH$_3$)$_2$)

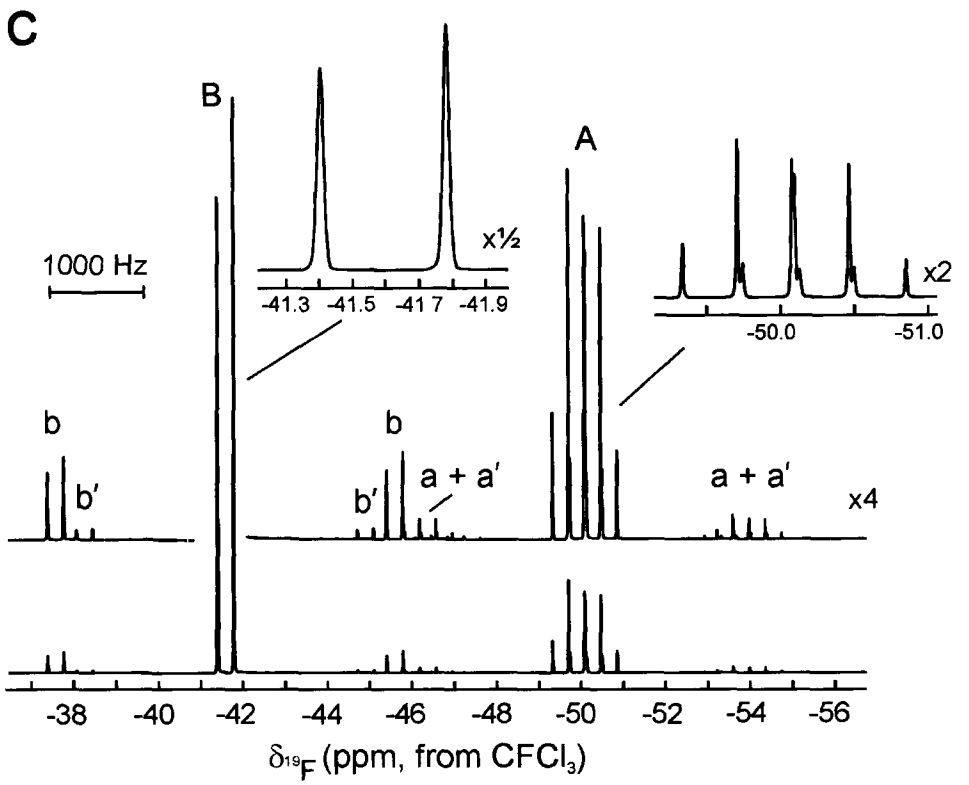
C
B
A
1000 Hz
x½
-41.3 -41.5 -41.7 -41.9
x2
-50.0 -51.0
b
b′
b
b′
a + a′
a + a′
x4
-38 -40 -42 -44 -46 -48 -50 -52 -54 -56
δ19F (ppm, from CFCl3)

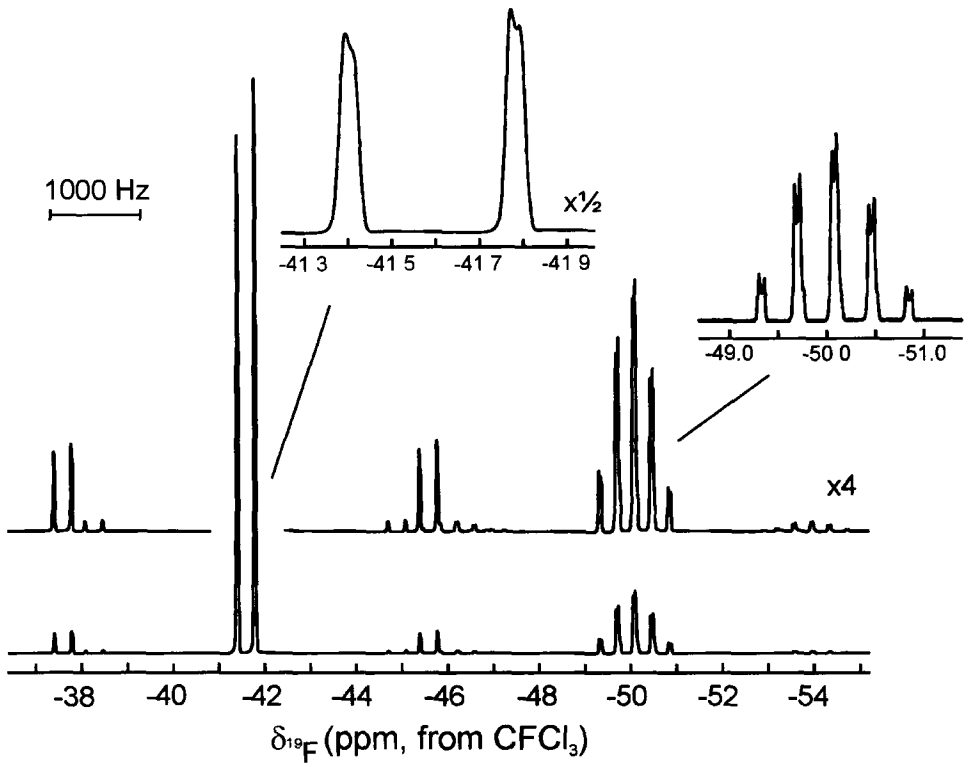
1000 Hz
x½
-41 3 -41 5 -41 7 -41 9
-49.0 -50 0 -51.0
x4
-38 -40 -42 -44 -46 -48 -50 -52 -54
δ19F (ppm, from CFCl3)

Figure 8.1. The NMR spectra of $C(OTeF_5)_4$ recorded in SO_2ClF solution at 30 °C: (a) The ^{13}C NMR spectrum (150.903 MHz) of 99% ^{13}C-enriched $C(OTeF_5)_4$. Natural abundance tellurium isotopomer contributions correspond to S (singlet; $^{13}C(O^{0}TeF_5)_4$, where ^{0}Te are spinless tellurium isotopes) and satellites denoted by $^{3/5}d$ (doublet; $^{13}C(O^{123/125}TeF_5)(O^{0}TeF_5)_3$] and t [triplet; $C(O^{125}TeF_5)_2(O^{0}TeF_5)_2$). (b) The ^{125}Te NMR (157.869 MHz) spectrum of 99% ^{13}C-enriched $C(OTeF_5)_4$; the inset is an expansion of the two most intense lines of the doublet of quintets. (c) The ^{19}F NMR spectra (470.592 MHz) of natural abundance $C(OTeF_5)_4$ (top trace) and 99% ^{13}C-enriched $C(OTeF_5)_4$ (bottom trace). The equatorial and axial fluorine environments of the AB_4 spin systems are denoted by B and A, respectively. Tellurium satellites are denoted by lower case letters, i.e., a and b (^{125}Te); a′ and b′ (^{123}Te).

The ^{125}Te chemical shift is in good agreement with published values of other $OTeF_5$ compounds.[35,140,293,294]

The ^{19}F NMR spectrum of the natural abundance $C(OTeF_5)_4$ (Figure 8.1c) consists of an AB_4 pattern with accompanying ^{123}Te and ^{125}Te satellites and agrees well with previously reported parameters.[80] The NMR spectrum of 99% ^{13}C-enriched $C(OTeF_5)_4$ ($\delta(^{19}F_B)$, –41.6 ppm; $\delta(^{19}F_A)$, –50.1 ppm; $^2J(^{19}F_A–^{19}F_B)$, 180 Hz; Figure 8.1c) shows further splitting of the A part of the spectrum arising from $^3J(^{19}F_A–^{13}C) = 24.5$ Hz, and of the B_4 part arising from $^3J(^{19}F_B–^{13}C) = 12.1$ Hz.

The behavior of $C(OTeF_5)_4$ in CH_3CN is in marked contrast with its behavior in the less basic solvent, SO_2ClF, where it is stable indefinitely at 30 °C. In an attempt to obtain a long-acquisition-time ^{13}C NMR spectrum of ^{13}C-enriched $C(OTeF_5)_4$ in CH_3CN at 30 °C, only CO_2 was observed. A study of the decomposition of $C(OTeF_5)_4$ in CH_3CN at –40 °C by ^{13}C and ^{19}F NMR spectroscopy revealed that during dissolution at 10 °C, followed by immediate quenching of the reaction at –40 °C and recording the NMR spectra at this temperature, $C(OTeF_5)_4$ reacts to form $O(TeF_5)_2$ and CO_2 (Scheme 8.1).

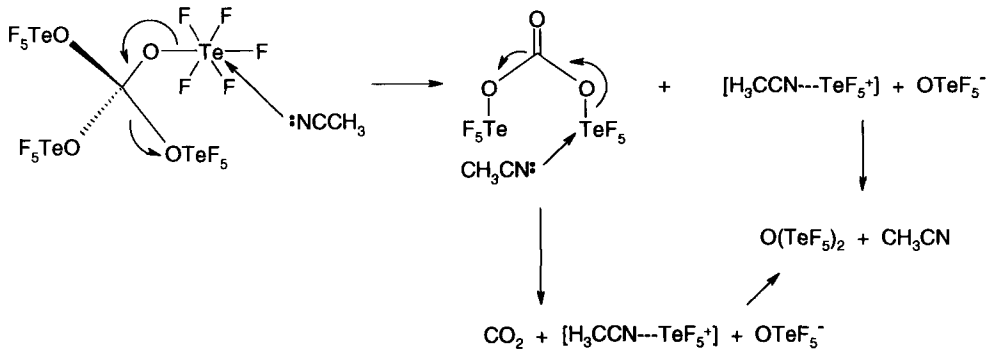

Scheme 8.1. Proposed reaction pathway for the decomposition of $C(OTeF_5)_4$ at 10 °C.

The NMR parameters of $O(TeF_5)_2$ ($\delta(^{19}F_A)$, –47.0 ppm; $\delta(^{19}F_B)$, –37.1; $^2J(^{19}F_A–^{19}F_B)$, 182 Hz)[77] and CO_2 ($\delta(^{13}C)$, 126.0 ppm)[215] were in good agreement with the previously reported values. The proposed decomposition pathway is supported by tentative evidence for the reactive intermediate, $O{=}C(OTeF_5)_2$ (mol% composition: 4.2% $O{=}C(OTeF_5)_2$, 49.5% $C(OTeF_5)_4$, 46.3% $O(TeF_5)_2$). Only the B_4 part of the spectrum of $O{=}C(OTeF_5)_2$ was observed ($\delta(^{19}F_B)$, –40.0 ppm) whereas the A part of the spectrum was obscured by the A parts of the more intense $C(OTeF_5)_4$ and $O(TeF_5)_2$ spectra. Further warming resulted in complete conversion of $C(OTeF_5)_4$ to $O(TeF_5)_2$ and CO_2. The decomposition of $O{=}C(OTeF_5)_2$ to CO_2 and $O(TeF_5)_2$ is supported by the analogous decomposition pathway established for $C(OSO_2F)_4$ which gives rise to CO_2 and $S_2O_5F_2$.[295] Under natural abundance conditions, the ^{13}C NMR spectrum of $O{=}C(OTeF_5)_2$ could not be observed presumably because of its low concentration and the long relaxation time associated with a fully oxygen-substituted carbon species.

The proposed decomposition pathway for $C(OTeF_5)_4$ has features in common with the reaction of CH_3CN with $Nb(OTeF_5)_6^-$, which yields $NbO(OTeF_5)_4(NCCH_3)^-$ and has been observed by ^{19}F NMR spectroscopy.[296] Both reactions lead to intramolecular elimination of $O(TeF_5)_2$ and are apparently initiated by nitrogen coordination of CH_3CN. In the latter case, the seven-coordinate complex anion intermediate, $Nb(OTeF_5)_6(CH_3CN)^-$, is presumably formed, whereas the reaction of $C(OTeF_5)_4$ is unlikely to proceed by S_N2 attack of CH_3CN at the carbon atom of $C(OTeF_5)_4$. Rather, solvent coordination to the tellurium atom of an $OTeF_5$ ligand may occur, which results in expansion of the tellurium valence shell to seven, followed by intramolecular $O(TeF_5)_2$

elimination and $O{=}C(OTeF_5)_2$ formation. Nucleophilic attack of tellurium by CH_3CN may be facilitated by solvent complexation with one or more fluorines of the $OTeF_5$ group, which would build up positive charge on tellurium, thus activating it for attack by CH_3CN.

8.2.2. Differential Scanning Calorimetry (DSC)

During the course of the X-ray crystal structure determination of $C(OTeF_5)_4$, it was found that crystals grown at room temperature by sublimation quickly powdered when handled at or below −100 °C. The phase transition temperature, determined by DSC, showed that an exothermic transition took place at −51.2 °C, releasing 5.73 kJ mol^{-1} of energy. Consequently, X-ray data were collected at −30 °C, which is well above the phase transition temperature. An endothermic phase transition, corresponding to the melting point, occurred at 33.6 °C (heat of fusion, 9.70 kJ mol^{-1}). A second cycle was performed but showed no transitions, consistent with decomposition and/or reaction with the aluminium sample container between the melting point and 125 °C.

8.2.3. X-ray Crystal Structures of $C(OTeF_5)_4$ and $[N(CH_3)_4][B(OTeF_5)_4]$

Details of data collection parameters and other crystallographic information are provided in Table 8.1. Bond lengths, bond angles, torsion angles, and O···O contact distances are listed in Tables 8.2 and 8.3. In order to compare the symmetries for $E(OTeF_5)_4^{-/0}$ (E = B, C), the geometric parameters of the $B(OTeF_5)_4^-$ anion were determined for $[N(CH_3)_4][B(OTeF_5)_4]$ with the view to obtain a structure in which the

Table 8.1. Crystallographic Data for $C(OTeF_5)_4$ and $B(OTeF_5)_4^-$

chem formula	$CO_4F_{20}Te_4$	$H_{12}BC_4NO_4F_{20}Te_4$
space group	*Pc* (No. 7)	C_2 (No. 5)
a (Å)	9.9176(4)	17.9521(10)
b (Å)	17.9965(6)	7.7195(1)
c (Å)	20.9666(8)	16.6623(10)
β (deg)	92.445(2)	94.963(2)
V (Å^3)	3738.8(3)	2300.4(4)
molecules/unit cell	8	4
mol wt (g mol^{-1})	966.38	1039.32
calcd density (g cm^{-3})	3.434	3.001
T (^{o}C)	-30	-170
μ (mm^{-1})	7.18	5.20
R_1 [a]	0.0530	0.0259
wR_2 [b]	0.0944	0.0419

[a] R_1 is defined as $\Sigma||F_o|-|F_c||/\Sigma|F_o|$ for $I > 2\sigma(I)$. [b] wR_2 is defined as $[\Sigma[w(F_o^2 - F_c^2)^2]/\Sigma w(F_o^2)^2]^{1/2}$ for $I > 2\sigma(I)$.

Table 8.2. Experimental[a] and Calculated[b] Geometrical Parameters for $C(OTeF_5)_4$ and $B(OTeF_5)_4^-$

$C(OTeF_5)_4$	exptl (C_1) [ave]	calcd (C_1)	calcd (S_4)
	ΔE (kJ mol^{-1})		
	0.00 C(4) −39 99 C(2) −92 27 C(1)	−173.42	−173 32
	bond lengths (Å)		
C–O	1.35(2) – 1 42(2) [1 38(3)]	1.376 – 1 377 [1.377]	1 376
O–Te	1.85(1) – 1.92(1) [1.89(2)]	1.925 – 1 925 [1 925]	1.925
Te–F	1.74(1) – 1.88(1) [1.80(3)]	1.840 – 1.850 [1.844]	1.839 – 1.850
	bond angles (deg)		
O–C–O (× 2)[d]	110(2) – 116(1) [113(2)]	112.9, 113.0 [113 0]	113.0
O–C–O (× 4)[d]	105(1) – 111(1) [108(2)]	107 7 – 107.8 [107.8]	107.8
C–O–Te	127(1) – 131(1) [129(1)]	123.8 – 123.8 [123 8]	123.7
O–Te–F_a	170 8(7) – 177.7(6) [175(2)]	176.4 – 178 7 [177.6]	176.1
O–Te–F_e	83.9(7) – 96.7(7) [90(4)]	85 8 – 93 7 [90.1]	85.8 – 93.7
	torsion angle (deg)[e]		
Te–O–C–O (x 4)	155(1) – 174(1) [168(5)] 29(3) – 55(2) [46(7)] 63(2) – 87(2) [73(7)]	169.3 – 169.7 [169 5] 47 2 – 47.5 [47.4] 71 4 – 71 7 [71.6]	169.3 47 0 71.9
	O···O (Å)[d,f]		
aa (× 2)	2.28(2) – 2.33(2) [2 31(3)]	2 294, 2.296 [2.295]	2 294
ac (× 4)	2.16(2) – 2.27(2) [2 23(3)]	2.223 – 2.224 [2.224]	2 224

Table 8.2. (continued...)

$B(OTeF_5)_4^-$	exptl (C_1) [ave]	calcd (C_1)	calcd (S_4) (one imag. freq.)[c]	calcd (S_4)
		ΔE (kJ mol^{-1})		
	0.00	−28.99	−31 31	−31 13
		bond lengths (Å)		
B–O	1.463(5) – 1 476(5) [1.471(6)]	1.455 – 1.457 [1.456]	1.456	1.457
O–Te	1.828(2) – 1.834(2) [1.831(3)]	1.857 – 1.858 [1.858]	1.857	1.855
Te–F	1.821(3) – 1.844(2) [1.830(6)]	1.854 – 1.861 [1 857]	1 855 – 1 860	1.854 – 1.860
		bond angles (deg)		
O–B–O (× 2)[d]	113.7(3), 113.8(3) [113.8(7)]	113 3, 115.0 [114.2]	111.5	109.5
O–B–O (× 4)[d]	106.8(3) - 107.9(3) [107.4(5)]	106.6 – 107.7 [107.2]	108.4	109.4
B–O–Te	128.2(2) – 131.6(2) [130(2)]	124.9 – 128.8 [126.9]	126.2	127.8
O–Te–F_a	173.6(1) – 177.1(1) [176(2)]	176.7 – 178 8 [177 9]	176.4	176.3
O–Te–F_e	89.0(1) – 96.0(1) [93(2)]	89.4 – 96.2 [93 0]	89.7 – 95 7	90.0 – 95.9
		torsion angle (deg)[e]		
Te–O–B–O (× 4)	170.4(2) – 179.7(2) [174(4)]	173.7 – 179 4 [176.6]	151.2	135.3
	47.3(4) – 57 9(4) [52(5)]	49 7 – 58.7 [54 2]	29.9	15 2
	61.1(4) – 71 3(4) [67(5)]	60 0 – 68.6 [64 3]	89.4	104 8
		O···O (Å)[d,f]		
aa (× 2)	2.460(4), 2.470(4) [2.465(8)]	1 435, 2 454 [2 445]	2.408	2.386
ac (× 4)	2.366(4) – 2.376(4) [2.371(5)]	2.335 – 2.352 [2 344]	2.363	2 378

Table 8.2. (continued...)

[a] The quoted geometrical parameters are for the non-disordered $C(OTeF_5)_4$ molecules. [b] SVWN/(SDB-)cc-pVTZ. [c] The geometrical parameters correspond to the optimized S_4 geometry having the lowest energy. [d] The distinction between the two sets of O–C–O angles and O···O contacts were initially made for each molecule. The values given correspond to the ranges of each set of angles/contacts. [e] The full list of Te–O–C/B–O torsion angles is given in Table 8.3. [f] The symbols *ac* and *aa* refer to the O···O contact distances for $A(OX)_4$-type molecules of S_4 symmetry as defined in ref 297.

Table 8.3. Experimental (C_1) and Calculated (C_1 and S_4)[a] Te–O–C/B–O Torsion Angles (deg) for $C(OTeF_5)_4$ and $B(OTeF_5)_4^-$

$C(OTeF_5)_4$[b]					$B(OTeF_5)_4^-$			
exptl (C_1)	exptl (C_1)	exptl (C_1)	calcd (C_1)	calcd (S_4)	exptl (C_1)	calcd (C_1)	calcd (S_4)[c]	calcd (S_4)
78.0	77.5	86.6	71.7	71.9	71.3	68.6	89.4	104.8
74.7	76. 2	75.0	71.6		70.4	68.6		
72.0	70.7	67.4	71.5		64.1	60.0		
63.5	65.8	66.4	71.4		61.1	60.0		
55.0	51.8	52.3	47.5	47.0	47.3	49.7	29.9	15.2
45.2	45.5	51.0	47.4		48.5	49.8		
43.8	44.8	49.3	47.3		54.0	58.7		
42.2	44.4	28.8	47.2		57.9	58.7		
174.4	171.2	174.0	107.8	169.3	179.7	179.4	151.2	135.3
169.9	168.4	169.4	169.7		176.6	179.3		
169.7	168.3	169.0	169.6		171.2	173.7		
163.5	165.1	155.3	169.5		170.4	173.7		

[a] SVWN/(SDB-)cc-pVTZ. [b] The quoted torsion angles are for the non-disordered $C(OTeF_5)_4$ molecules. [c] Calculated S_4 geometry with one imaginary frequency.

cation-anion interactions would be minimized so that the anion closely approximates the calculated gas-phase geometry (see Section 8.2.5).

The symmetries of $C(OTeF_5)_4$ and $B(OTeF_5)_4^-$ are not constrained by the crystal symmetries, with all atoms on general positions. The unit cell of $C(OTeF_5)_4$ contains eight molecules that are generated from four crystallographically independent molecules which all occupy C_1 sites. Three of the crystallographically independent molecules are ordered and the remaining molecule is affected by a 60:40 positional disorder (see Figure 8.2). Only the geometric parameters of the three unique, ordered molecules are considered in the ensuing discussion. There are eleven F···F contact distances near or below the sum of the van der Waals radii (2.94 Å)[26] in $C(OTeF_5)_4$. These range from 2.81(2) to 2.99(2) Å and are in accord with well isolated molecules. The structure of $[N(CH_3)_4][B(OTeF_5)_4]$ is well-ordered. The $B(OTeF_5)_4^-$ anion has seven unique long H···F contacts, ranging from 2.47–2.65 Å, that are at or near the sum of the hydrogen and fluorine van der Waals radii (2.67 Å),[26] consistent with a well-isolated anion.

8.2.3.1. Bond Lengths and Bond Angles

The $C(OTeF_5)_4$ molecule (Figure 8.3a) possesses C–O bond lengths (1.35(2)–1.42(2) Å) that are, on average, longer than those reported for the $C(OTeF_5)_3^+$ cation (1.258(15)–1.313(16) Å),[80] and in accord with the expectation that the C–O bonds of the cation will be more covalent. In contrast, the average C–O bond lengths of $C(OTeF_5)_4$ are shorter than those of the isoelectronic $B(OTeF_5)_4^-$ anion (Figure 8.3b, 1.465(5)–1.476(5) Å), which, because of its formal negative charge, is expected to

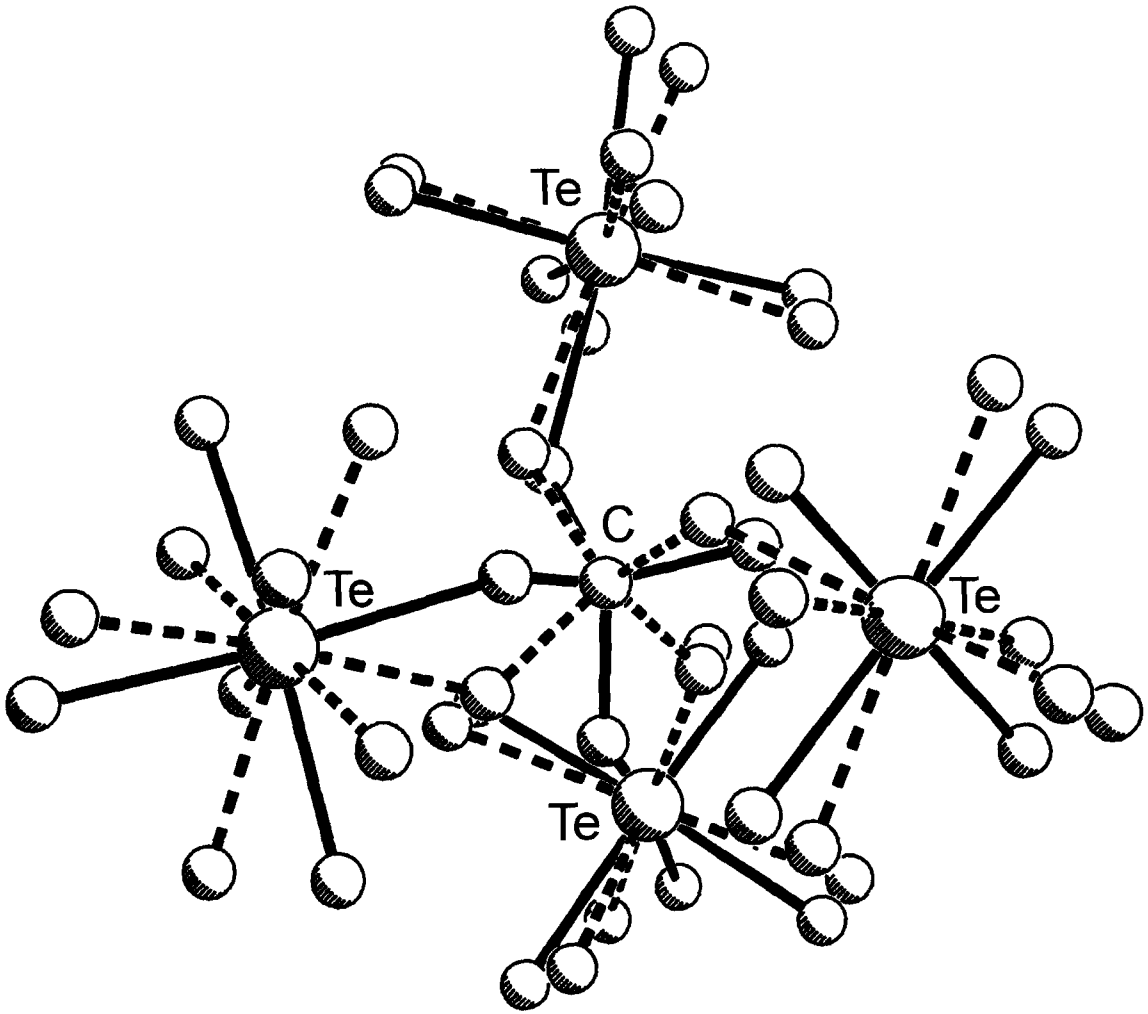

Figure 8.2. The two different orientations of the disordered molecule in the unit cell of $C(OTeF_5)_4$.

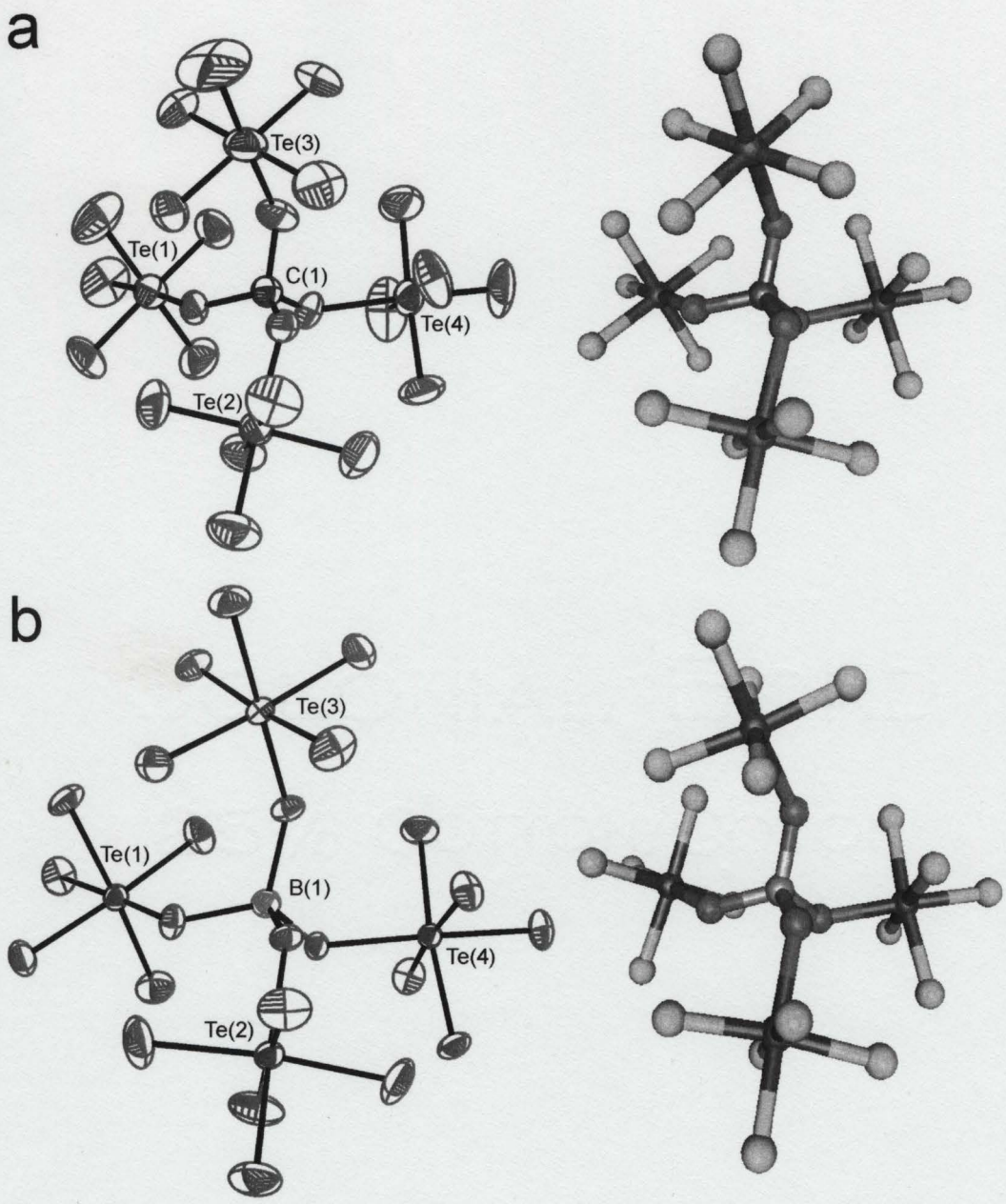

Figure 8.3. X-ray crystal structures of $C(OTeF_5)_4$ and $B(OTeF_5)_4^-$; thermal ellipsoids are shown at the 50% probability level; (a) a view of an ordered $C(OTeF_5)_4$ molecule (left) and the calculated geometry of the $C(OTeF_5)_4$ molecule (right), (b) a view of the $B(OTeF_5)_4^-$ anion (left) and the calculated geometry of the $B(OTeF_5)_4^-$ anion (right).

possess B–O bonds that are more polar than the C–O bonds of its carbon analogue. The decrease in E–O (E = B, C) bond length upon increasing net positive charge is paralleled by an increase in the Te–O bond lengths ($B(OTeF_5)_3$, 1.874(6) Å, $C(OTeF_5)_3^+$, 1.974(8)–1.988(7) Å; $B(OTeF_5)_4^-$, 1.828(2)–1.835(3), $C(OTeF_5)_4$, 1.85(1)–1.92(1) Å). These trends are reproduced by the calculated geometries and NBO analyses (see Section 8.2.5). The Te–F (1.74(1)–1.88(1) Å) bond lengths are in good agreement with those of $B(OTeF_5)_4^-$ (1.819(3)–1.841(2) Å) and those of previously determined $B(OTeF_5)_4^-$ structures.[111,283,284,298,299]

8.2.3.2. Molecular Symmetries

(i) Background. Ligand close packing (LCP) considerations have shown that $A(OX)_4$ systems possess either S_4 or D_{2d} symmetries, depending on the effective radii of the oxygen ligand atoms.[297] Because the A–O–X angles are bent, the LCP approach for this class of molecules is based upon an electron density distribution around oxygen that is not axially symmetric, with the oxygen atom having different ligand radii in different directions. These radii are denoted as *c*, the ligand radius opposite the O–X bond, and *a*, the two ligand radii on either side of the O–X bond. These radii represent the interligand O···O contact distances which can be associated with D_{2d} or S_4 symmetry.[297] Using LCP criteria, an $A(OX)_4$ molecule having S_4 symmetry will have two *a*···*a* and four *a*···*c* interligand contact distances (hereafter denoted as *aa* and *ac*, where $aa > ac$[297]), which is differentiated from D_{2d} symmetry by four *aa* and two *cc* contact distances. Although the

ligand-ligand contact distances are reflected in the O–A–O angles, the latter are not explicitly discussed.[297]

Previously reported structures of well-isolated $B(OTeF_5)_4^-$ anions[111,284,298,299] have been described as having approximate S_4 symmetry.[298] It was noted that for $B(OTeF_5)_4^-$ to possess rigorous local S_4 symmetry (the fluorine atoms were ignored as they are in the present discussion), one set of four Te–O–B–O torsion angles must be 180°, while the other two sets of four torsion angles must be equal in magnitude, but opposite in sign.[298] In fact, these criteria describe a structure possessing local D_{2d} symmetry. Electronic structure calculations in the present work show that the energy-minimized geometries of $E(OTeF_5)_4^{0/-}$ (E = C, B) possess S_4 symmetry without meeting these criteria (see Section 8.2.5).

(ii) Experimental Geometries. In the present study, the O–B–O bond angles of $B(OTeF_5)_4^-$ (Table 8.2) possess precisions sufficient to differentiate tetrahedral from non-tetrahedral angles. The average angles were 113.8(7)° for two angles and 107.4(5)° for four angles. In the case of $C(OTeF_5)_4$, the O–C–O angles do not differ from the ideal tetrahedral angle by more than ±3σ, with averages of 113(2)° for two angles and 108(2)° for four angles. On the basis of O–E–O angle considerations alone, both $E(OTeF_5)_4^{-/0}$ species have local symmetries that are closer to S_4 than to D_{2d} symmetry. Taking into account intramolecular O···O contact distances as per the LCP approach,[297] the $B(OTeF_5)_4^-$ anion and $C(OTeF_5)_4$ have two *aa* (2.465(8) and 2.31(3) Å) and four *ac* (2.371(5) and 2.23(3) Å) contacts, respectively, which are indicative of local S_4

symmetry for both species. A comparative study and fuller discussion of the symmetries of $E(OTeF_5)_4^{-/0}$ are provided in Section 8.2.5, where the experimental structures are also shown to possess S_4 symmetry based on their experimental and calculated Te–O–E–O torsion angles (Table 8.2).

8.2.4. Raman Spectra of $C(OTeF_5)_4$ and $B(OTeF_5)_4^-$

The low-temperature Raman spectra of natural abundance and ^{13}C-enriched $C(OTeF_5)_4$ and that of $[N(CH_3)_4][B(OTeF_5)_4]$ are shown in Figures 8.4 and 8.5. The experimental and calculated frequencies are summarized in Tables 8.4 and 8.5 for $C(OTeF_5)_4$ and $B(OTeF_5)_4^-$, respectively. The vibrational modes of $C(OTeF_5)_4$ and $B(OTeF_5)_4^-$ were assigned under S_4 symmetry and belong to the irreducible representation $\Gamma = 20A + 21B + 20E$, with all 81 modes Raman active and the B and E modes infrared active. The low-temperature, solid-state Raman spectra of $^{12/13}C(OTeF_5)_4$ and $B(OTeF_5)_4^-$ displayed bands that agree with, and could be readily assigned to, their $OTeF_5$ groups by comparison with the calculated frequencies and the published frequencies of other $OTeF_5$ derivatives,[35,140,293,294] thus requiring no further comment.

Bands associated with the CO_4 moiety were assigned in the natural abundance spectrum of $C(OTeF_5)_4$ to 1078.5, 1084.0 cm^{-1} (E, ν(CO – CO)); 1063.5, 1070.5 cm^{-1} (B, $\nu(CO_2 - CO_2)$); and 1023.2 cm^{-1} (A, $\nu(CO_4 - 4TeO)$), which are in good agreement with their respective calculated frequencies (SVWN; 1096.6, 1082.7, and 1010.0 cm^{-1}). Upon ^{13}C isotopic enrichment, the ν(CO – CO) and $\nu(CO_2 - CO_2)$ bands exhibited isotopic shifts to lower frequency of 29.5, 31.1 cm^{-1} (calcd., 29.7 cm^{-1}) and 25.6, 24.8

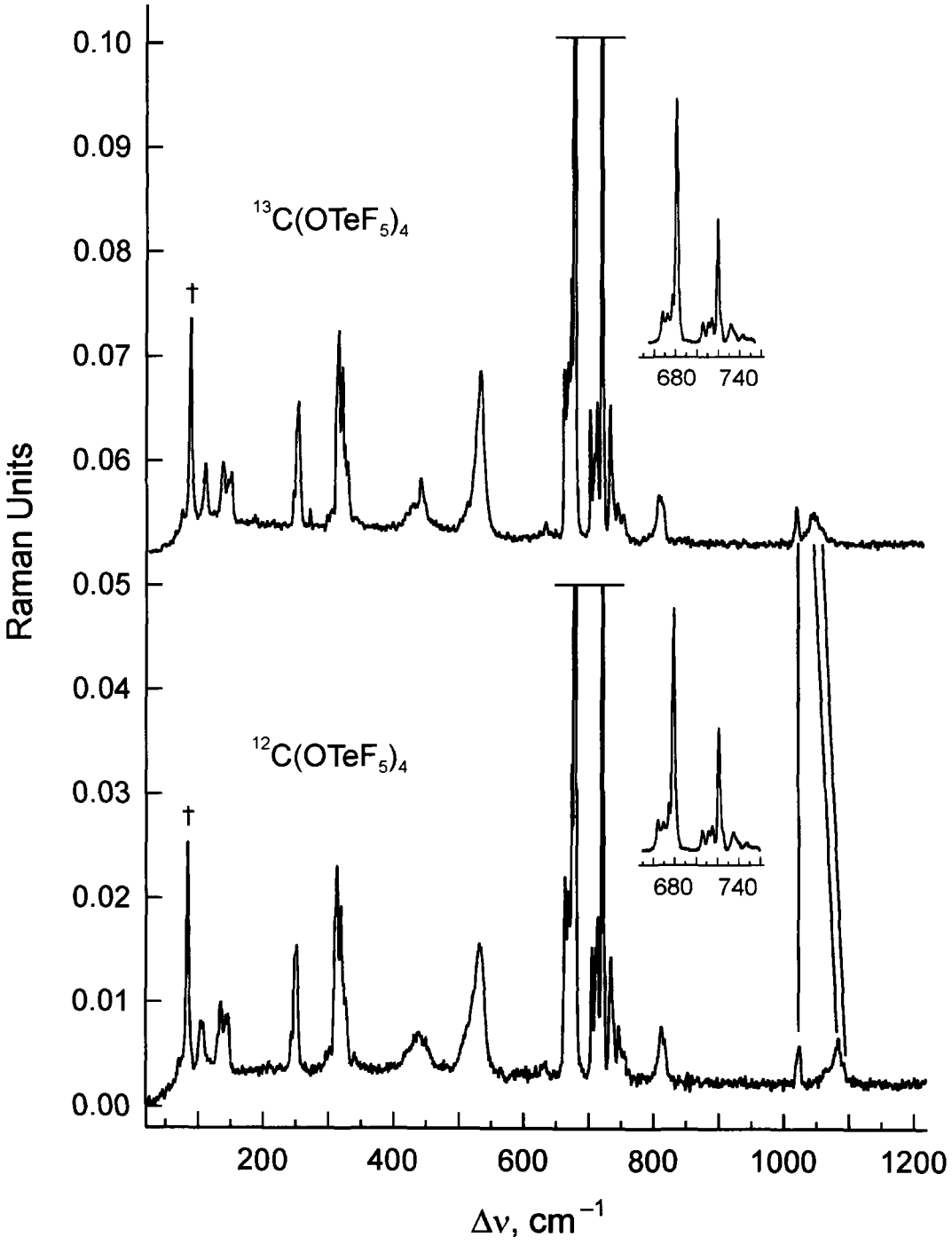

Figure 8.4. Raman spectra of natural abundance and ^{13}C-enriched (99%) $C(OTeF_5)_4$ recorded at −160 °C using 1064-nm excitation. Lines indicate modes that shift upon $^{12/13}C$ substitution. The dagger (†) denotes an instrumental artifact.

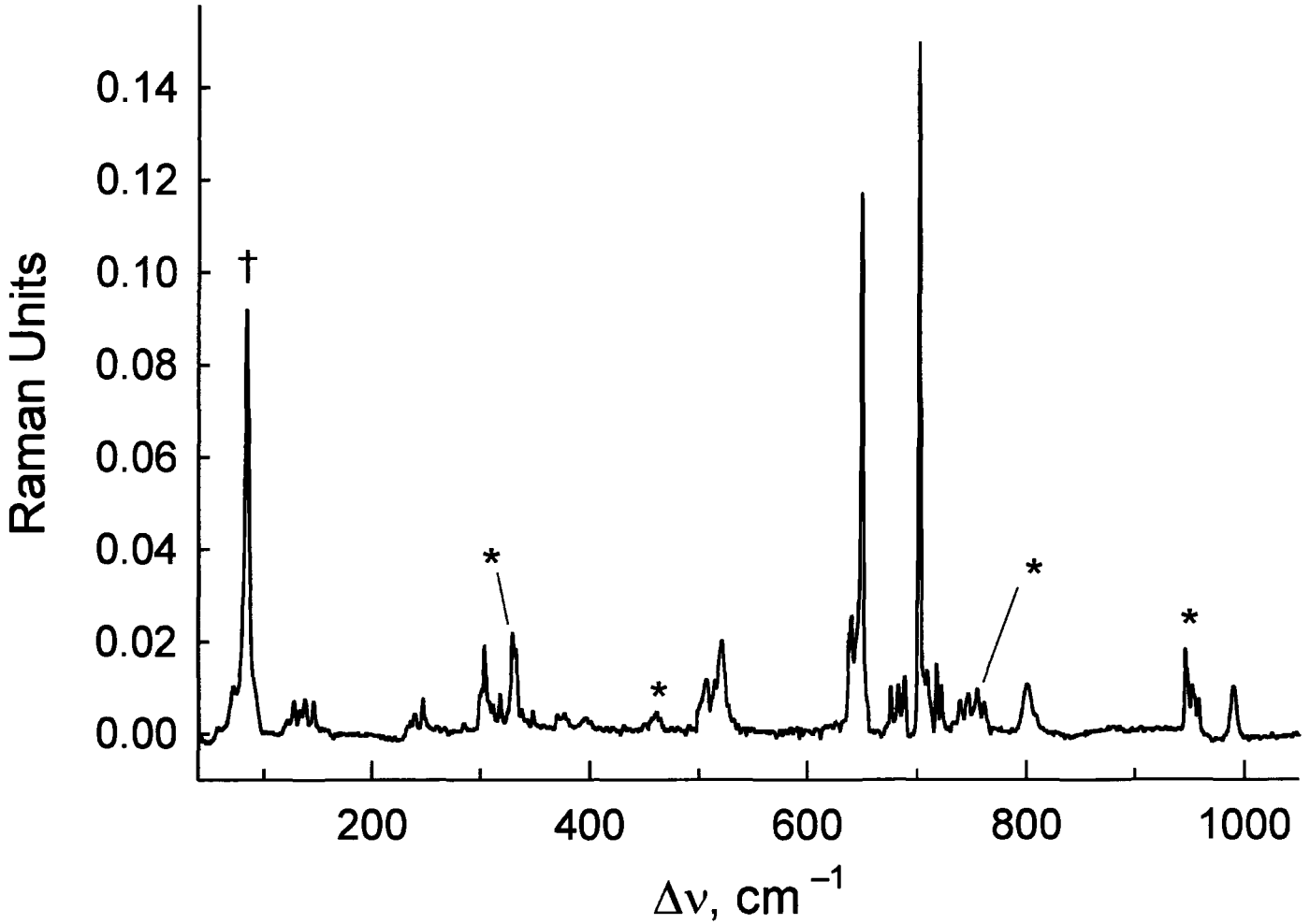

Figure 8.5. Raman spectrum of $[N(CH_3)_4][B(OTeF_5)_4]$ recorded at −160 °C using 1064-nm excitation. Asterisks (*) denote $N(CH_3)_4^+$ cation bands and the dagger (†) denotes an instrumental artifact.

Table 8.4. Experimental and Calculated Vibrational Frequencies[a] for $^{12/13}C(OTeF_5)_4$

$^{12}C(OTeF_5)_4$		$^{13}C(OTeF_5)_4$		
exptl[b]	calcd (S_4)[c]	exptl	calcd (S_4)[c]	assgnts (S_4)[d]
1084.0(2) 1078 5 sh	1096.6(15)	1052 9(<1) 1049.0(<1) 1045.7(<1)	1066.1(14)	E, ν(CO – CO)
1070.5(<1) 1063 5 sh	1082.7(8)	1037.9(1) 1033.9(2)	1053.8(8)	B, $\nu(CO_2 - CO_2)$
1023 2(2)	1010.0(31)	1021.6(2)	1009.0(31)	A, $\nu(CO_4 - 4TeO)$
813.5(3)	793.6(16)	811.7(3)	792 5(16)	E, ν(2TeO – 2TeO)
755 9(1)	741 1(2)	755 6(2)	739 6(1)	B, $\nu[2(TeO - TeF_a) + 2(TeF_a - TeO) + 4(TeF_{e\,trans} - TeF_{e\,trans})]_{small}$
747.3(2)	731 5(1) 731.1(1) 730.4(2)	748.7(2) 746.9 sh	730 9(1) 730.6(1) 730.3(2)	B, $\delta(CO_2 - CO_2) + \nu[(2(TeO - TeF_a) + 2(TeF_a - TeO) + 4(TeF_{e\,trans} - TeF_{e\,trans})]$ E, $\nu[4(TeF_{e\,trans} - TeF_{e\,trans})] + \delta(CO_2 - CO_2)_{small}$ A, $\nu[4(TeF_{e\,trans} - TeF_{e\,trans})]$
736.8 sh 734.7(6)	728.3(2) 725.0(6) 720.1(<1)	737.3 sh 734.7(5)	728.1(2) 724.9(6) 719.9(<1)	B, $\delta(CO_2 - CO_2)_{small} + \nu[4(TeF_{e\,trans} - TeF_{e\,trans})]$ A, $\nu[4(TeF_{e\,trans} - TeF_{e\,trans})]$ E, $\nu[2(TeF_{e\,trans} - TeF_{e\,trans}) + 2(TeF_{2e\,cis} - TeF_{2e\,cis})]$
721.0(44)	707.9(21)	718.8(50) 714.2(8)	708.0(20)	A, $\nu(4TeF_a)$
714.5(10) 710.8(6)	699.2(6)	708.9(7)	699.1(6)	E, $\nu(2TeF_a - 2TeF_a)$
705.3(9)	691.3(10)	703.5(7)	690.2(10)	B, $\delta(CO_2 - CO_2) + \nu(2TeF_a - 2TeF_a)$
678.2(100)	659.2 (91)	677.8(100)	659 2(91)	A, $\nu(4TeF_{4e})$
668.3(11) 663.8(11)	657.5 (2) 653.7(4) 651 3(5) 650 5(7) 649.6(2)	667.2(13) 663 9(12)	657.8(2) 653 7(4) 651.2(4) 650.3(7) 649.4(2)	B, $\delta(4COTe) + \nu(2TeF_{4e} - 2TeF_{4e})$ B, $\nu[4(TeF_{2e\,trans} - TeF_{2e\,trans})]$ E, $\nu[(2TeF_{2e\,trans} - 2TeF_{2e\,trans})]$ A, $\nu[4(TeF_{2e\,trans} - TeF_{2e\,trans})]$ E, $\nu[(TeF_{4e} - TeF_{4e}) + 2(TeF_{2e\,trans} - TeF_{2e\,trans})]$
632.7(<1)	640.4(3)	632.3(<1)	640 9(3)	B, $\delta(2COTe - 2COTe) + \nu(4TeF_{4e})$
533 0(11) 512 0 sh	539.9(56)	538.1(11)	543.3(56)	A, δ(4COTe)

Table 8.4. (continued...)

442.1(2)	444.3(5)	441.5(1)	446.1(5)	A, ρ_t(4COTe)
428.4(3)	429.7(2)	428.2(4) 422.0 sh	429 1(2)	E, $\rho_w(CO_2)$
338 7(<1)	360 9(<1)		361.0(<1)	B, $\rho_w(CO_4)$
324 3(9)	325.8(<1)	329.6 sh 325.4(6)	327.1(<1)	A, $\rho_r(CO_2 - CO_2) + \delta(2TeF_{4e\ umbrella} - 2TeF_{4e\ umbrella})$
319 6(14) 313.3(16) 302. 3(1)	306.6(1) 305.9(1) 303 4(2) 302.1(<1) 300.0(1) 299.2(1) 298.2(<1) 296.1(<1)	319.3(13) 312.6(11) 302.1(1)	307.4(1) 307 0(1) 304.0(2) 302.9(<1) 300.7(1) 299.2(1) 298.4(<1) 297.1(<1)	strongly coupled deformation and torsion modes involving both $OTeF_5$ and COTe moieties
268.7(<1)	291.5(1) 285.7(2) 284.1(<1) 281.7(1)	269.0(1)	292 8(1) 285 7(2) 284.0(<1) 282.1(<1)	
251.7(11) 248 6(11) 243.8 sh	236.3(<1) 234.1(2) 233.9(<1) 232.6(2) 230.4(<1)	251.7(7) 247.2(8)	236.5(<1) 234.7(2) 233.9(<1) 233.0(2) 231 7(<1)	

Table 8.4. (continued...)

184.5(<1)	200 5(<1)	185.5(<1)	202.4(<1)	strongly coupled deformations and torsion modes involving both $OTeF_5$ and COTe moieties
	194.0(<1)		196.6(<1)	
	193 4(<1)		196.1(<1)	
	189 5(<1)		191 6(<1)	
145 2(4)	133.9(1)	145.5(5)	134.3(1)	
142.3(4)	129.7(<1)	140.6(4)	131.0(<1)	
135.0(4)	127.8(1)	133 8(4)	130.5(<1)	
	123.4(<1)		124.3(1)	
	119.9(<1)		120.9(<1)	
107 6(1)	98.1(1)	107 6(5)	99.7(1)	
	93.0(<1)		97 4(<1)	
	46.6(<1)		46.9(<1)	
	38.5(<1)		38.9(<1)	
	33.2(<1)		36.9(<1)	
	32.0(<1)		32.9(<1)	
	27.1(<1)		27.0(<1)	
	22.4(<1)		25.4(<1)	
	17.0(<1)		24.7(<1)	

[a] Frequencies are given in cm^{-1}. [b] Values in parentheses denote experimental relative Raman intensities. The abbreviation denotes a shoulder (sh). [c] SVWN/(SDB-)cc-pVTZ. Raman intensities (in $Å^4$ amu^{-1}) are given in parentheses. [d] The abbreviations denote stretch (ν), bend (δ), twist (ρ_t), wag (ρ_w), and rock (ρ_r). Bond elongations and angle openings are denoted by plus (+) signs and bond contractions and angle closings are denoted by minus (−) signs. The notations, F_a and F_e, refer to the axial fluorine atom and the four equatorial fluorine atoms of the $OTeF_5$ group; the notations TeF_{2e} and TeF_{4e} indicate that 2 or 4, respectively, Te–F_e bond stretching motions are in phase. The notations, $F_{e\ trans}$ and $F_{e\ cis}$, indicate that the fluorine atoms are trans or cis to each other.

Table 8.5. Experimental and Calculated Vibrational Frequencies[a] for $E(OTeF_5)_4^{-/0}$ (E = B, C)[c]

$^{12}C(OTeF_5)_4$		$B(OTeF_5)_4^-$			
	calcd (S_4)[c]	exptl[b,d]	calcd (S_4)[c]		assgnts (S_4)[c]
1084(2) 1078 sh	1097(15)	989(7), br	1026(6)	1065[690]	E, ν(EO – EO)
1070(<1) 1064 sh	1083(8)	989(7), br	1019(8)	1040[459]	B, $\nu(EO_2 - EO_2)$
1023(2)	1010(31)	958(4) 951(7)	981(80)	968[0]	A, $\nu(EO_4 - 4TeO)$
813 5(3)	794(16)	800(7)	787(15)	781[<1]	E, ν(2TeO – 2TeO)
756(1)	741(2)	761(4)	774(8)	785[54]	B, $\nu[2(TeO - TeF_a) + 2(TeF_a - TeO) + 4(TeF_{e\,trans} - TeF_{e\,trans})]_{small}$
747.3(2)	731(1)	754(7)	708(1)	709[225]	E, $\nu[4(TeF_{e\,trans} - TeF_{e\,trans})] + \delta(EO_2 - EO_2)_{small}$
	732(1)	746(5)	710(2)	710[322]	B, $\delta(EO_2 - EO_2) + \nu[(2(TeO - TeF_a) + 2(TeF_a - TeO) + 4(TeF_{e\,trans} - TeF_{e\,trans})]$
	730(2)	738(4)	704(4)	706[0]	A, $\nu[4(TeF_{e\,trans} - TeF_{e\,trans})]$
736 8 sh 734.7(6)	728(2) 725(6) 720(<1)	721(7) 718(11)	707(2) 696(9) 698(<1)	707[90] 700[0] 699[38]	B, $\delta(EO_2 - EO_2)_{small} + \nu[4(TeF_{e\,trans} - TeF_{e\,trans})]$ A, $\nu[4(TeF_{e\,trans} - TeF_{e\,trans})]$ E, $\nu[2(TeF_{e\,trans} - TeF_{e\,trans}) + 2(TeF_{2e\,cis} - TeF_{2e\,cis})]$
721 0(44)	708(21)	709 sh 702(100)	675(60)	677[0]	A, $\nu(4TeF_a)$
714.5(10) 711(6)	699(6)	688(8) 682(7)	660(6)	662[155]	E, $\nu(2TeF_a - 2TeF_a)$
705(9)	691(10)	675(7)	659(17)	659[63]	B, $\delta(EO_2 - EO_2) + \nu(2TeF_a - 2TeF_a)$
678(100)	659(91)	649(78) 646 sh	636(63)	636[0]	A, $\nu(4TeF_{4e})$

Table 8.5. (continued...)

668(11) 664(11)	658(2) 654(4) 651(5) 651(7) 650(2)	640(18)	627(1) 632(4) 630(<1) 629(7) 628(2)	628[1] 633[3] 631[1] 629[0] 628[<1]	B, δ(4EOTe) + ν(2TeF$_{4e}$ – 2TeF$_{4e}$) B, ν[4(TeF$_{2e\ trans}$ – TeF$_{2e\ trans}$)] E, ν[(2TeF$_{2e\ trans}$ – 2TeF$_{2e\ trans}$)] A, ν[4(TeF$_{2e\ trans}$ – TeF$_{2e\ trans}$)] E, ν[(TeF$_{4e}$ – TeF$_{4e}$) + 2(TeF$_{2e\ trans}$ – TeF$_{2e\ trans}$)]
633(<1)	640(3)	461(3)	479(12)	516[<<1]	B, δ(2EOTe – 2EOTe) + ν(4TeF$_{4e}$)
533(11) 512 sh	540(56)	521(13) 514 sh 506(8) 500 sh	524(39)	522[0]	A, δ(4EOTe)
442(2)	444(5)	333(10)	353(3)	383[0]	A, ρ_t(4EOTe)
428(3)	430(2)	396(3) 375(3) 370 sh 348(3) 333(13)	457(<1)	446[71]	E, ρ_w(EO$_2$)
339(<1)	361(<1)	311 sh	317(6)	331[157]	B, ρ_w(EO$_4$)
324(9)	326(<1)	318(6)	323(<1)	329[0]	A, ρ_r(EO$_2$ – EO$_2$) + δ(2TeF$_{4e\ umbrella}$ – 2TeF$_{4e\ umbrella}$)
320(14) 313(16) 302(1)	307(1) 306(1) 303(2) 302(<1) 300(1) 299(1) 298(<1) 296(<1)	304(14) 299 sh	315(1) 313(3) 312(<1) 310(18) 310(<1) 306(<1) 307(<1) 307(<1)	315[23] 314[21] 313[0] 311[7] 309[18] 306[0] 308[56] 306[137]	strongly coupled deformations and torsion modes involving both OTeF$_5$ and EOTe moieties

Table 8.5. (continued...)

269(<1)	292(1)	284 (1)	291(4)	295[26]	strongly coupled deformations and torsion modes involving both $OTeF_5$ and EOTe moieties
	286(2)		279(<1)	278[<1]	
	284(<1)		276(<1)	277[0]	
	282(1)		276(<1)	277[<1]	
252(11) 249(11) 244 sh	236(<1)	248 sh 246(5) 236(3) 233(3)	234(<1)	234[0]	
	234(<1)		231(<1)	230[8]	
	234(2)		228(1)	228[2]	
	233(2)		220(<1)	222[0]	
	230(<1)		211(<1)	217[4]	
184(<1)	200(<1)		204(<1)	202[<1]	
	194(<1)		200(<1)	199[0]	
	193(<1)		200(<1)	199[<<1]	
	190(<1)		189(<1)	189[<1]	
145(4) 142(4) 135(4)	134(1)	145(4) 138(4) 136 sh 127(4) 126 sh	135(1)	133[0]	
	130(<1)		131(<1)	130[<<1]	
	128(1)		126(<1)	124[0]	
	123(<1)		124(<1)	121[<1]	
	120(<1)		105(<1)	108[<1]	
108(1)	98(1)		93(<1)	87[0]	
	93(<1)		96(<1)	92[<1]	
	47(<1)		47(<1)	37[<1]	
	39(<1)		36(<1)	35[0]	
	33(<1)		42(<1)	35[<1]	
	32(<1)		41(<1)	33[<1]	
	27(<1)		28(<1)	10[<1]	
	22(<1)		28(<1)	9[<1]	
	17(<1)		8(<1)	-9[0]	

Table 8.5. (continued...)

[a] Frequencies are given in cm^{-1}. [b] Values in parentheses denote experimental uncorrected relative Raman intensities. The abbreviation denotes a shoulder (sh). [c] SVWN/(SDB-)cc-pVTZ. Raman intensities (in $Å^4$ amu^{-1}) are given in parentheses. [d] The abbreviations denote stretch (ν), bend (δ), twist (ρ_t), wag (ρ_w), and rock (ρ_r). Bond elongations and angle openings are denoted by plus (+) signs and bond contractions and angle closings are denoted by minus (−) signs. The notations, F_a and F_e, refer to the axial fluorine atom and the four equatorial fluorine atoms of the $OTeF_5$ group; the notations TeF_{2e} and TeF_{4e} indicate that 2 or 4, respectively, Te–F_e bond stretching motions are in phase. The notations, $F_{e\ trans}$ and $F_{e\ cis}$, indicate that the fluorine atoms are trans or cis to each other.

cm^{-1} (calcd., 28.9 cm^{-1}), respectively. In contrast, $\nu(CO_4 - 4TeO)$ shifted by only 1.6 cm^{-1} (calcd., 1.0 cm^{-1}), which is consistent with the near-zero displacement of the carbon atom in the latter mode. The vibrational frequencies of $C(OTeF_5)_4$ are higher than those of $B(OTeF_5)_4^-$; the B–O stretching frequencies occur at 989 cm^{-1}, which is broad (E, $\nu(BO - BO)$ and B, $\nu(BO_2 - BO_2)$) and at 951, 958 cm^{-1} (A, $\nu(BO_4 - 4TeO)$). The $^{10/11}B$ isotopic shifts were not observed, but have been calculated (Table 8.5). No pure O–C–O or O–B–O bending modes are predicted by computational methods, rather, they are strongly coupled to TeO and TeF stretching modes and have not been explicitly assigned in Tables 8.4 and 8.5.

8.2.5. Computational Results

The geometric parameters and vibrational frequencies (see Section 8.2.4) were calculated using DFT (SVWN) methods for both $C(OTeF_5)_4$ and $B(OTeF_5)_4^-$. All-electron correlation consistent (cc-pVTZ) basis sets were used for all atoms other than tellurium, for which a semi-relativistic large core pseudopotential (SDB-cc-pVTZ) basis set was used. Natural bond orbital (NBO) analyses were carried out on the DFT-optimized geometries at the HF level of theory. Total energies for experimental geometries were derived from single-point calculations.

8.2.5.1. Geometries

The initial $C(OTeF_5)_4$ and $B(OTeF_5)_4^-$ geometries used in the optimization were very close to square planar about the central E atom with all E–O–Te angles close to

linear and $OTeF_5$ groups pseudo-octahedral with two Te-F_e bonds and the Te-F_a bond of each $OTeF_5$ being essentially coplanar with the EO_4 moiety. The starting geometry had C_1 symmetry and the initial calculations were done at the HF level using the (SDB-)cc-pVTZ basis set which gave two local minima. As indicated by the three groups of Te–O–E–O dihedral bond angles (vide infra), the calculated geometries were close to S_4 symmetry (Figure 8.6). Both systems were then optimized at the SVWN level at C_1 symmetry, resulting in all frequencies real for both systems. All geometrical parameters, including the Te–O–E–O torsion angles, are comparable to the experimental values. Using the coordinates from the latter calculations, both systems were optimized at the SVWN level at S_4 symmetry resulting in all frequencies real for $C(OTeF_5)_4$ and one imaginary frequency for $B(OTeF_5)_4^-$. While the Te–O–C–O angles were similar to those under C_1 symmetry, the Te–O–B–O angles had changed significantly. In an attempt to obtain all frequencies real for $B(OTeF_5)_4^-$ at the SVWN level, a further geometry optimization was carried out starting from the optimized S_4 (SVWN) geometry of $C(OTeF_5)_4$ and produced an energy-minimized S_4 geometry with all frequencies real and Te–O–B–O dihedral bond angles that differed from those obtained previously for S_4 (one imaginary frequency) and C_1 symmetries.

The calculated bond lengths and bond angles associated with the C_1 and S_4 energy-minimized (SVWN/(SDB-)cc-pVTZ) geometries of $C(OTeF_5)_4$ and $B(OTeF_5)_4^-$ all fall within the range of the experimentally determined values, with the exception of the calculated C–O–Te angles which were ca. 5° smaller. The calculated Te–O–C–O

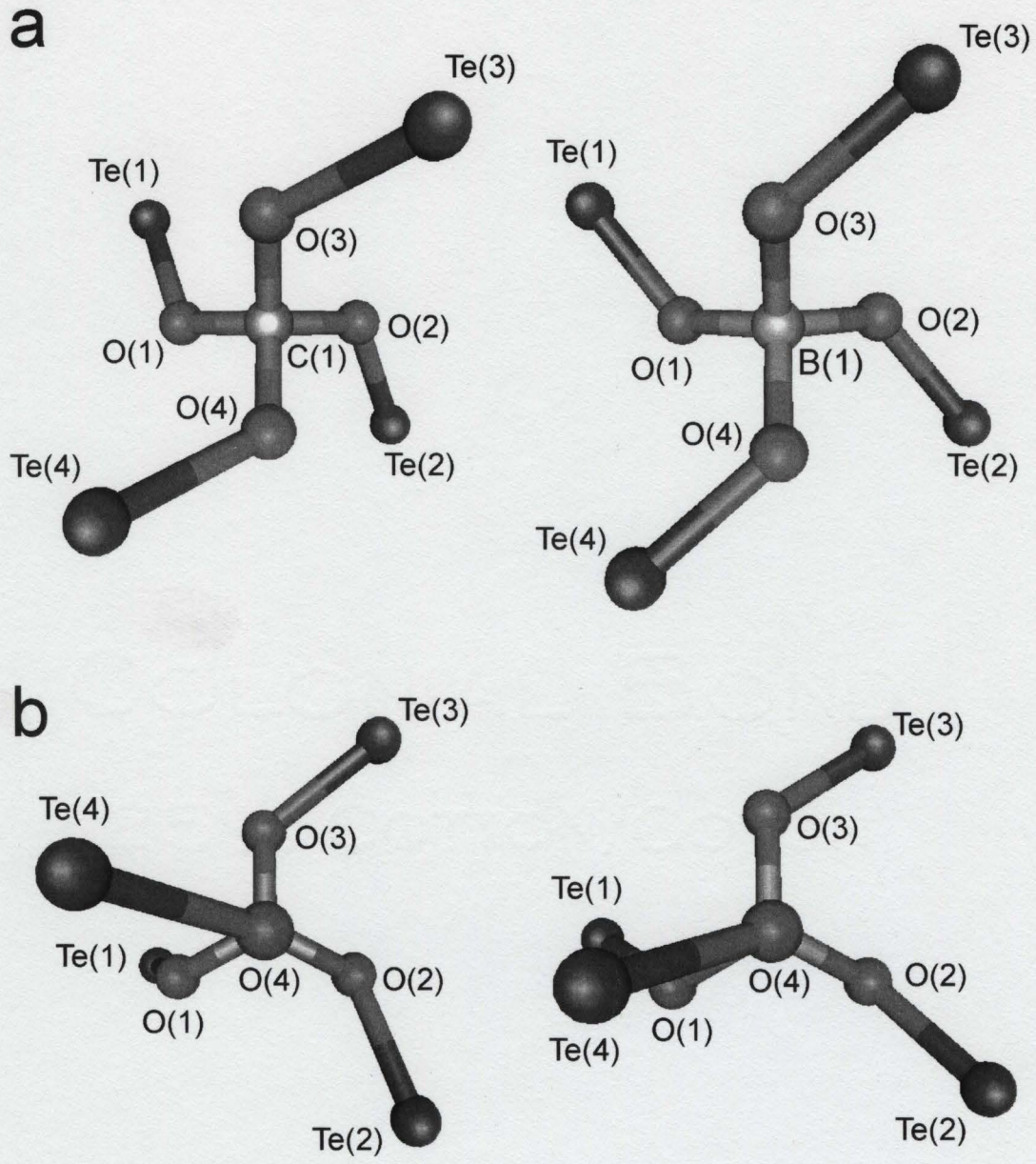

Figure 8.6. Calculated local geometries (S_4 symmetry) for the $E(OTe)_4$ moieties of $E(OTeF_5)_4^{0/-}$ (E = C, B) species (a) looking down the collinear S_4- and C_2-axes, and (b) looking along the E(1)–O(4) bond.

torsion angles for both C_1 and S_4 symmetries of $C(OTeF_5)_4$ are similar to the experimental torsion angles, and are consistent with $C(OTeF_5)_4$ being well isolated in the structure (see Section 8.2.3). In contrast, the Te–O–B–O torsion angles of $B(OTeF_5)_4^-$ vary significantly. The C_1-structure is only slightly higher in energy than the S_4-structure, but the Te–O–B–O torsion angles are in better agreement with the experimental values. This suggests that the solid-state geometry of $B(OTeF_5)_4^-$, because of its ionic nature, is more susceptible to crystal packing effects than the carbon analogue. When the largest set of calculated Te–O–B–O torsion angles decrease, S_4 symmetry is maintained by concomitant increases in the intermediate set of angles and decreases in the smallest set of angles (Tables 8.2 and 8.3).

8.2.5.2. Natural Bond Orbital (NBO) Analyses

Natural atomic charges, Mayer natural atomic orbital valencies, and natural atomic orbital bond orders between atoms in $C(OTeF_5)_4$ and $B(OTeF_5)_4^-$, calculated at the HF level of theory, are given in Table 8.6.

(i) Natural Atomic Charges for $C(OTeF_5)_4$ and $B(OTeF_5)_4^-$. The NBO analyses for $C(OTeF_5)_4$ and $B(OTeF_5)_4^-$ were carried out at the HF/(SDB-)cc-pVTZ level of theory so that the results could be compared with previous calculations for $C(OTeF_5)_3^+$ and $B(OTeF_5)_3$ (also see Chapter 6).[80] The positive charge on the carbon atom of $C(OTeF_5)_4$ (1.20) is lower than that of $C(OTeF_5)_3^+$ (1.30), with the boron analogues exhibiting

Table 8.6. Calculated[a,b] Natural Bond Orbital (NBO) Charges, Valencies, and Bond Orders for $C(OTeF_5)_4$ and $B(OTeF_5)_4^-$

	$C(OTeF_5)_4$ (S_4)		$B(OTeF_5)_4^-$ (S_4)[c]			$C(OTeF_5)_4$ (S_4)	$B(OTeF_5)_4^-$ (S_4)[c]
	charge	valency	charge	valency		bond order	bond order
E	1.199	3.264	1.046	2.684	E–O	0.910	0.658
O	–0.946	1.163	–1.000	1.225	O–Te	0.498	0.655
Te	3.965	3.039	3.547	3.237	Te–F_A	0.500	0.511
F_A	–0.660	0.471	–0.613	0.470	Te–F_B	0.487	0.508
F_B	–0.666	0.454	–0.615	0.468	Te–$F_{B'}$	0.491	0.509
$F_{B'}$	–0.662	0.453	–0.606	0.470	Te–$F_{B''}$	0.482	0.504
$F_{B''}$	–0.665	0.449	–0.610	0.469	Te–$F_{B'''}$	0.490	0.511
$F_{B'''}$	–0.666	0.459	–0.614	0.473			
overall $OTeF_5$	–0.300		–0.511				

[a] SVWN/(SDB-)cc-pVTZ//HF/(SDB-)cc-pVTZ. [b] The symbols F_A and $F_B/F_{B'}/F_{B''}/F_{B'''}$ denote axial and equatorial fluorine atoms, where $F_B/F_{B'}/F_{B''}/F_{B'''}$ are nonequivalent under S_4 symmetry. [c] The geometrical parameters correspond to the optimized S_4 geometry having the lowest energy.

parallel behavior, i.e., $B(OTeF_5)_4^-$ (1.25) and $B(OTeF_5)_3$ (1.45). The higher boron charges of $B(OTeF_5)_3$ and $B(OTeF_5)_4^-$ relative to the carbon charges of their carbon analogues reflect the higher electronegativity of carbon. As a result of the lower electronegativity of boron and higher net negative charges of $B(OTeF_5)_3$ and $B(OTeF_5)_4^-$, the charge separations between the central atom and the ligands are greater for the boron analogues. Thus, the total charge on a $OTeF_5$ group of $B(OTeF_5)_4^-$ (–0.56) is more negative than that of $C(OTeF_5)_4$ (–0.30) with a parallel trend for $B(OTeF_5)_3$ (–0.48) and $C(OTeF_5)_3^+$ (–0.10). The charge separations are indicative of the greater polarity of the B–O bonds when compared with those of their carbon analogues.

(ii) Bond Orders and Valencies for $C(OTeF_5)_4$ and $B(OTeF_5)_4^-$. The C–O bond order for $C(OTeF_5)_4$ (0.91) is significantly higher than that of $B(OTeF_5)_4^-$ (0.62), and, again, reflects the greater polarities of the B–O bonds. The trend is also exhibited by $C(OTeF_5)_3^+$ (1.01) and $B(OTeF_5)_3$ (0.73) (also see Chapter 6).[80] The bond order differences in going from $E(OTeF_5)_3^{0/+}$ to $E(OTeF_5)_4^{-/0}$ are 0.11/0.10, which reflect the differences in E ← O π donation in going from trigonal planar to tetrahedral local geometries. The valencies at E are also consistent with the greater polarities of the B–O bonds in $B(OTeF_5)_4^-$ (2.68) when compared with $C(OTeF_5)_4$ (3.26), with parallel behavior exhibited by $B(OTeF_5)_3$ (2.18) and $C(OTeF_5)_3^+$ (3.04).[80]

8.3 Conclusions

The present study provides a synthetic route to $C(OTeF_5)_4$ and describes its structural characterization in solution and in the solid state. In contrast with the room temperature stability of $C(OTeF_5)_4$ in SO_2ClF, dissolution of $C(OTeF_5)_4$ in CH_3CN results in rapid decomposition of $C(OTeF_5)_4$ at 10 °C to give CO_2 and $O(TeF_5)_2$, with the reaction likely proceeding through the reactive intermediate, $O{=}C(OTeF_5)_2$. With the availability of a more precise crystal structure for $B(OTeF_5)_4^-$, determined in the course of the present work, and that of $C(OTeF_5)_4$, it has proven possible to assess the local symmetries of $E(OTeF_5)_4^{0/-}$ by LCP predictions and by comparisons of Te–O–E–O torsion angles. Both approaches established that the geometries of $C(OTeF_5)_4$ and $B(OTeF_5)_4^-$ are best represented by S_4 rather than by C_1 or D_{2d} symmetries. Electronic structure calculations accurately reproduced the experimental geometric parameters and are in accord with assignments of the experimental symmetries to S_4. They have also aided in the vibrational assignments of $E(OTeF_5)_4^{0/-}$, and reproduce the $^{12/13}C$ isotopic shifts associated with the vibrational frequencies of the CO_4 moiety of $C(OTeF_5)_4$.

CHAPTER 9

CONCLUSIONS AND DIRECTIONS FOR FUTURE WORK

9.1. Conclusions

The chemistry of Xe(II) has been significantly extended to include the first known neutral oxide fluoride, $O(XeF)_2$, which has been synthesized and definitively characterized in CH_3CN solution at –40 °C by ^{17}O, ^{19}F, and ^{129}Xe NMR spectroscopy, and in the solid state by low-temperature Raman spectroscopy. This discovery also completes the list of known neutral oxide fluorides of Xe(II), Xe(IV), Xe(VI), and Xe(VIII) (see Table 1.1).

As well, the first nitrate derivative of a noble-gas element, $FXeONO_2$, has been synthesized and fully characterized in solution by ^{14}N, ^{19}F, and ^{129}Xe NMR spectroscopy and in the solid state by low-temperature Raman spectroscopy and single crystal X-ray diffraction. The compound is a colorless solide that decomposes above 0 °C. An early report[99] of the syntheses of $FXeONO_2$ and $Xe(ONO_2)_2$ could not be substantiated because no spectroscopic or other characterization of these compounds was attempted in the prior work. Moreover, the physical properties and stability of $FXeONO_2$ prepared in the present work do not agree with with those described in the earlier work.

The syntheses of $O(XeF)_2$ and $FXeONO_2$ demonstrate the synthetic utility of the $FXeOXeFXeF^+$ cation, or more specifically, its ability to insert the FXeO moiety into X–F (X = Xe(II), N(V)) bonds to give FXeO–R-type linkages, which could not be obtained by metathesis reactions with strong monoprotic acids.

The salt, $[XeOTeF_5][Sb(OTeF_5)_6]\cdot SO_2ClF$, has now been fully characterized in SO_2ClF solution by NMR spectroscopy and in the solid state by low-temperature Raman spectroscopy and single crystal X-ray diffraction. Unlike $[XeOTeF_5][AsF_6]$ and $[XeOSeF_5][AsF_6]$, and fluorine analogues, $[XeF][MF_6]$ (M = As, Sb, Bi, Nb, Ta, Ru, Ir, Os, Au), the $XeOTeF_5^+$ cation in $[XeOTeF_5][Sb(OTeF_5)_6]\cdot SO_2ClF$ is devoid of interactions with the anion and only a very weak interaction with the co-crystallized SO_2ClF molecule exists. The relative "nakedness" of the cation in this structure renders it a strong Lewis acid and a potent oxidizer; the latter property has been expoited to generate perhalogenated carbocations cations (vide infra).

The $[XeOTeF_5][Sb(OTeF_5)_6]$ salt has been shown to oxidatively remove a halogen bound to carbon, generating the $[CX_3][Sb(OTeF_5)_6]$ (X = Cl, Br, $OTeF_5$) and $[CFX_2][Sb(OTeF_5)_6]$ (X = Cl, Br) salts. The former salts have been characterized for the first time in the solid state by X-ray crystallography, while evidence for the CFX_2^+ cations has been obtained in solution by ^{13}C and ^{19}F NMR spectroscopy. This synthetic approach has also led to the first syntheses of the $F_3C–Br–OTeF_5^+$, $ClFCOTeF_5^+$, $CBr(OTeF_5)_2^+$, $CBr_2OTeF_5^+$, and $Br(OTeF_5)_2^+$ cations, as well as neutral $F_2BrCOTeF_5$. The CFX_2^+ cations are the first examples of long-lived perhalomethyl cations that contain fluorine, and, as such, are among the strongest electrophiles known. The neutral pentafluoroorthotellurate of carbon, $C(OTeF_5)_4$, which arose as a side product from the reaction of CBr_4 with $[XeOTeF_5][Sb(OTeF_5)_6]$, has now been prepared in bulk and fully characterized in solution by NMR spectroscopy, and in the solid state by Raman spectroscopy and X-ray crystallography. The experimental and calculated gas-phase

geometric parameters and symmetries of $C(OTeF_5)_4$ have also been compared with those of the isoelectronic $B(OTeF_5)_4^-$ anion.

9.2. Directions for Future Work

The synthetic utility of the $FXeOXeFXeF^+$ cation in generating new neutral Xe(II) compounds affords the possibility of synthesizing other neutral Xe(II) derivatives bound to an oxygen-linked ligand. A moderate to strong fluoride ion donor should displace $Xe_2F_3^+$ according to eq 9.1. Preliminary work has shown that ClO_2F reacts

$$FXeOXeFXeF^+ + RF \longrightarrow FXeO\text{–}R + Xe_2F_3^+ \qquad (9.1)$$

to form $FXeOClO_2$ according to eq 9.2,[300] and has been characterized by low-temperature

$$[Xe_3OF_3][AsF_6] + 2ClO_2F \longrightarrow FXeOClO_2 + 2XeF_2 + [ClO_2][AsF_6] \qquad (9.2)$$

Raman spectroscopy and by ^{19}F and ^{129}Xe NMR spectroscopy. Other possible fluoride ion donors include, ClO_3F, BrO_3F, and POF_3 to give $FXeOClO_3$, $FXeOBrO_3$, and $FXeOP(O)F_2$, respectively.

Another possibility is to further exploit the lability of the weak bond between the $FXeOXe^+$ and XeF_2 in the $FXeOXeFXeF^+$ cation to synthesize adducts of the $FXeOXe^+$ cation with various oxidatively resistant nitrogen bases. For example, preliminary work has shown that $N{\equiv}SF_3$ will displace XeF_2 in NSF_3 solution to give $FXeOXe{---}N{\equiv}SF_3^+$ according to eq 9.3,[301] which has been verified in the solid state by low-temperature

$$FXeOXeFXeF^+ + N{\equiv}SF_3 \longrightarrow FXeOXe{-}{-}{-}N{\equiv}SF_3^+ + XeF_2 \qquad (9.3)$$

Raman spectroscopy of the natural abundance and ^{18}O-enriched $[FXeOXe{-}{-}{-}N{\equiv}SF_3][AsF_6]$ salt. Other oxidatively resistant nitrogen bases that could be considered for such a study include CH_3CN, C_5F_5N, *o*-, *p*-$C_4F_4N_2$, and *s*-$C_3F_3N_3$, which have all been found to form stable adducts with XeF^+.

Although CFX_2^+ (X = Cl, Br) have been characterized by ^{13}C and ^{19}F NMR spectroscopy and Raman spectroscopy, in the case of $CFCl_2^+$, no structural information has been obtained by single-crystal X-ray diffraction. While $CFBr_2^+$ was unattainable (see Chapter 7), the $CFCl_2^+$ cation demonstrates sufficient stability in SO_2ClF solution at low temperatures to allow for crystal growth, though all attempts thus far have failed in spite of its documented stability in the solid state by Raman spectroscopy. Another approach to attaining a structure of a fluorine-containing carbocation would be to replace a halogen ligand with a more stabilizing ligand, such as $OTeF_5$. In a manner similar to the preparation of $C(OTeF_5)_4$ (see Chapter 8), $CFBr_2^+$ could be reacted with two equivalents of $BrOTeF_5$ to give the $CF(OTeF_5)_2^+$ cation according to eq 9.4.

$$CFBr_2^+ + 2BrOTeF_5 \longrightarrow CF(OTeF_5)_2^+ + 2Br_2 \qquad (9.4)$$

The demonstrated of the synthetic utility of $[XeOTeF_5][Sb(OTeF_5)_6]{\cdot}SO_2ClF$ for the oxidative removal of a halogen bound to carbon may provide a means to generate cations of groups 14 and 16. More specifically, silyl cations are of considerable interest because π-back donation is reduced as a result of poor overlap between filled 2p orbitals

of the carbon ligand atoms and the vacant 3p orbital of silicon. Consequently, they are much more difficult to stabilize.[302] Only the $[Mes_3Si][B(C_5F_5)_4]$ salt has been prepared where bulky 1,3,5-trimethylphenyl (mesityl, Mes) groups prevent coordination,[302] resulting in a silyl cation that is free of interactions with the anion and the solvent, which has been studied by ^{29}Si NMR spectroscopy and by X-ray crystallography.

The syntheses of sterically unhindered silyl cation salts containing weakly coordinating anions may prove possible using the oxidative approaches described in Chapters 6 and 7. The preparation of perhalogenated silyl cations have been attempted according to eq 9.5 in SO_2ClF solvent. Among the perhalocations, $SiCl_3^+$ should provide

$$SiCl_4 + [XeOTeF_5][Sb(OChF_5)_6] \longrightarrow [SiCl_3][Sb(OTeF_5)_6] + ClOTeF_5 + Xe \quad (9.5)$$

the most favorable π stabilization of the positive charge on silicon. Preliminary ^{29}Si NMR studies, however, show that the silicon nucleus is very shielded relative to that of $SiMes_3^+$, indicating strong coordination to the solvent, anion, and/or $ClOTeF_5$.[303] Further study of products from the reaction of $SiCl_4$ with $[XeOTeF_5][Sb(OChF_5)_6]$, such as Raman spectroscopy and single crystal X-ray diffraction, needs to be done in order to understand the nature of this adduct.

Apart from $SiCl_3^+$, the trimethylsilylium ion has yet to be isolated. The proposed synthesis of this cation is given by eq 9.6. It is possible, based on the experiences of Lambert,[304] that the silyl cation may interact with an oxygen lone pair of $ClOChF_5$ to form an adduct with $ClOChF_5$ (eq 9.7). Indeed, as with $SiCl_3^+$, the ^{29}Si NMR

$$SiMe_3Cl + [XeOChF_5][Sb(OChF_5)_6] \longrightarrow [SiMe_3][Sb(OChF_5)_6] + XOChF_5 + Xe \quad (9.6)$$

$$SiMe_3^+ + XOChF_5 \longrightarrow Me_3SiO(X)ChF_5^+ \quad (9.7)$$

spectrum of the reaction mixture shows that the $SiMe_3^+$ cation is strongly coordinated in SO_2ClF solution.[303] A singlet was observed that has been tentatively assigned to the silyl cation $Si(OSiMe_3)_2(OTeF_5)^+$, which has been characterized by single-crystal X-ray diffraction.[303] Further study must be done in order to follow the decomposition of $SiMe_3^+$ to $Si(OSiMe_3)_2(OTeF_5)^+$ by NMR spectroscopy, as well as to try and crystallize any intermediate silyl cations.

There are no examples of perfluorinated cations of the chalcogens in their highest oxidation state, +6. Although the trigonal pyramidal $Ch'F_3^+$ (Ch′ = S,[305] Se,[306,307] Te[308]) cations have been obtained by fluoride ion abstraction from the corresponding tetrafluorides, the hexafluorides do not behave as fluoride ion donors towards strong Lewis acids such as AsF_5 and SbF_5.[309] Attempts should be made to synthesize salts of the trigonal bipyramidal $Ch'F_5^+$ cations by oxidation of $Ch'F_5X$ (X = Cl, Br; except in the case of SeF_5Br, which is unknown)[310-314] in SO_2ClF and/or SO_2F_2 according to eq 9.8. Although preliminary work

$$Ch'F_5X + [XeOChF_5][M(OChF_5)_6] \longrightarrow [Ch'F_5][M(OChF_5)_6] + XOChF_5 + Xe \quad (9.8)$$

(Ch′ = S, Se, Te; Ch = Se or Te; M = As or Sb)

demonstrated that the reaction of SF_5Br with $[XeOTeF_5][M(OTeF_5)_6]$ gave SF_6 as the major product, with F^- abstraction from $Sb(OTeF_5)_6^-$. It should, however still be possible to generate SeF_5^+ and TeF_5^+, as the Ch–F bonds (Ch = Se, Te) are weaker than that of sulfur, making fluoride abstraction from the anion less likely.

Although $Te(OTeF_5)_4$ is known,[293,315] the sulfur and selenium analogues have not been prepared. The derivative series should be completed by synthesizing $S(OChF_5)_4$ and $Se(OChF_5)_4$ according to eq 9.9 and 9.10. It has been shown that $Xe(OTeF_5)_2$ oxidizes

$$3Ch'F_4 + 4B(OChF_5)_3 \longrightarrow 3Ch'(OChF_5)_4 + 4BF_3 \quad (Ch' = S, Se) \qquad (9.9)$$

$$Ch'Cl_4 + 4ClOChF_5 \longrightarrow Ch'(OChF_5)_4 + 4Cl_2 \qquad (9.10)$$

$Te(OTeF_6)_4$ to $Te(OTeF_6)_6$.[315] Oxidative addition of $OChF_5$ to $Ch'(OChF_5)_4$ using $[XeOChF_5][M(OChF_5)_6]$ to give the pentakis-cations (eq 9.11) should be attempted.

$$[XeOChF_5][M(OChF_5)_6] + Ch'(OChF_5)_4 \longrightarrow [Ch'(OChF_5)_5][M(OChF_5)_6] + Xe \qquad (9.11)$$

References

1. Bartlett, N. *Proc. Chem. Soc.* **1962**, 218.
2. Graham, L.; Graudejus, O.; Jha, N. K.; Bartlett, N. *Coord. Chem. Rev.* **2000,** *197*, 321-334.
3. Hoppe, R.; Dähne, W.; Mattauch, H.; Rödder, K. M. *Angew. Chem., Int. Ed. Engl.* **1962,** *1*, 599.
4. Peacock, R. D.; Selig, H. *J. Am. Chem. Soc.* **1964,** *86*, 3895.
5. Gillespie, R. J.; Schrobilgen, G. J. *Inorg. Chem.* **1976,** *15*, 22-31.
6. Frlec, B.; Holloway, J. H. *Inorg. Chem.* **1976,** *15*, 1263-1270.
7. Stein, L. *Inorg. Chem.* **1984,** *23*, 3670-3671.
8. Khriachtchev, L.; Pettersson, M.; Runeberg, N.; Lundell, J.; Räsänen, M. *Nature* **2000,** *406*, 874-876.
9. Runeberg, N.; Pettersson, M.; Khriachtchev, L.; Lundell, J.; Räsänen, M. *J. Chem. Phys.* **2001,** *114*, 836-841.
10. Selig, H.; Holloway, J. H. In *Topics in Current Chemistry*; Boschke, F. L., Ed.; Springer-Verlag: Berlin, 1984; Vol. 124, pp 33-90.
11. Holloway, J. H. *J. Fluorine Chem.* **1986,** *33*, 149-157.
12. Holloway, J. H.; Hope, E. G. *Adv. Inorg. Chem.* **1998,** *46*, 51-100.
13. Schrobilgen, G. J. In *Synthetic Fluorine Chemistry*; Olah, G. A.; Prakash, G. K. S.; Chambers, R. D., Eds.; John Wiley & Sons, Inc.: New York, 1999; pp 31-42.
14. Gerken, M.; Schrobilgen, G. J. *Coord. Chem. Rev.* **2000,** *197*, 335-395.
15. Brel, V. K.; Pirkuliev, N. S.; Zefirov, N. S. *Russ. Chem. Rev.* **2001,** *70*, 231-264.
16. Lehmann, J. F.; Mercier, H. P. A.; Schrobilgen, G. J. *Coord. Chem. Rev.* **2002,** *233-234*, 1-39.
17. Laszlo, P.; Schrobilgen, G. J. *Angew. Chem., Int. Ed. Engl.* **1988,** *27*, 479-489.
18. Ball, P., *Elegant Solutions: Ten Beautiful Experiments in Chemistry*, The Royal Society of Chemistry: Cambridge, UK, 2005, Chapter 8.
19. Malm, J. G.; Selig, H. H.; Jortner, J.; Rice, S. A. *Chem. Rev.* **1965,** *65*, 199-236.
20. Falconer, W. E.; Sunder, W. A. *J. Inorg. Nucl. Chem.* **1967,** *29*, 1380-1381.
21. Berry, R. S.; Reimann, C. W. *J. Chem. Phys.* **1963,** *38*, 1540-1543.
22. Sladky, F. O.; Bulliner, P. A.; Bartlett, N.; DeBoer, B. G.; Zalkin, A. *Chem. Comm.* **1968**, 1048-1049.
23. Fir, B. A.; Gerken, M.; Pointner, B. E.; Mercier, H. P. A.; Dixon, D. A.; Schrobilgen, G. J. *J. Fluorine Chem.* **2000,** *105*, 159-167.
24. Bartlett, N. *Endeavour* **1972,** *31*, 107-112.
25. Zalkin, A.; Ward, D. L.; Biagioni, R. N.; Templeton, D. H.; Bartlett, N. *Inorg. Chem.* **1978,** *17*, 1318-1322.
26. Bondi, A. *J. Phys. Chem.* **1964,** *68*, 441-451.
27. Bartlett, N.; Wechsberg, M.; Jones, G. R.; Burbank, R. D. *Inorg. Chem.* **1972,** *11*, 1124-1127.
28. Wechsberg, M.; Bulliner, P. A.; Sladky, F. O.; Mews, R.; Bartlett, N. *Inorg. Chem.* **1972,** *11*, 3063-3070.
29. Sladky, F. O. *Monatsh. Chem.* **1970,** *101*, 1559-1570.

30. Sladky, F. O. *Monatsh. Chem.* **1970,** *101*, 1571-1577.
31. Seppelt, K.; Nothe, D. *Inorg. Chem.* **1973,** *12*, 2727-2730.
32. Naumann, D.; Tyrra, W.; Gnann, R.; Pfolk, D. *J. Chem. Soc., Chem. Commun.* **1994**, 2651-2653.
33. Musher, J. I. *J. Am. Chem. Soc.* **1968,** *90*, 7371-7372.
34. Sawyer, J. F.; Schrobilgen, G. J.; Sutherland, S. J. *J. Chem. Soc., Chem. Commun.* **1982**, 210-211.
35. Mercier, H. P. A.; Sanders, J. C. P.; Schrobilgen, G. J. *J. Am. Chem. Soc.* **1994,** *116*, 2921-2937.
36. Frohn, H.-J.; Jakobs, S.; Henkel, G. *Angew. Chem., Int. Ed. Engl.* **1989,** *28*, 1506-1507.
37. Syvret, R. G.; Schrobilgen, G. J. *Inorg. Chem.* **1989,** *28*, 1564-1573.
38. Eisenberg, M.; DesMarteau, D. D. *Inorg. Chem.* **1972,** *11*, 1901-1904.
39. Burns, J. H.; Ellison, R. D.; Levy, H. *Acta. Crystallogr.* **1965,** *18*, 11.
40. Bartlett, N.; Wechsberg, M. *Z. Anorg. Allg. Chem.* **1971,** *385*, 5-17.
41. Burbank, R. D.; Jones, G. R.; Bartlett, N. *Inorg. Chem.* **1970,** *9*, 2264-2268.
42. Bartlett, N.; Žemva, B.; Jesih, A.; Templeton, D. H.; Zalkin, A.; Cheetham, A. K. *J. Am. Chem. Soc.* **1987,** *109*, 7420.
43. Holloway, J. H.; Schrobilgen, G. J. *Inorg. Chem.* **1981,** *20*, 3363-3368.
44. Holloway, J. H.; Schrobilgen, G. J. *Inorg. Chem.* **1980,** *19*, 2632-2640.
45. Tramšek, M.; Lork, E.; Mews, R.; Žemva, B. *J. Solid State Chem.* **2001,** *162*, 243-249.
46. Benkič, P.; Tramšek, M.; Žemva, B. *Solid State Sciences* **2002,** *4*, 9-14.
47. Benkič, P.; Tramšek, M.; Žemva, B. *Solid State Sciences* **2002,** *4*, 1425-1434.
48. Turicnik, A.; Benkič, P.; Žemva, B. *Inorg. Chem.* **2002,** *41*, 5521-5524.
49. Tramšek, M.; Benkič, P.; Turicnik, A.; Tavcar, G.; Žemva, B. *J. Fluorine Chem.* **2002,** *114*, 143-148.
50. Tramšek, M.; Benkič, P.; Žemva, B. *Inorg. Chem.* **2004,** *43*, 699-703.
51. Tavcar, G.; Benkič, P.; Žemva, B. *Inorg. Chem.* **2004,** *43*, 1452-1457.
52. Tramšek, M.; Benkič, P.; Žemva, B. *Angew. Chem., Int. Ed. Engl.* **2004,** *43*, 3456-3458.
53. Tsao, P.; Cobb, C. C.; Claassen, H. H. *J. Chem. Phys.* **1971,** *54*, 5247-5253.
54. Ogden, J. S.; Turner, J. J. *Chem. Comm.* **1966**, 693-694.
55. Jacob, E.; Opferkuch, R. *Angew. Chem., Int. Ed. Engl.* **1976,** *15*, 158-159.
56. Chernick, C. L.; Claassen, H. H.; Malm, J. G.; Plurien, P. L. In *Noble Gas Compounds*; Hyman, H. H., Ed.; University of Chicago Press: Chicago, IL, 1963; p 287.
57. Smith, D. F. *Science* **1963,** *140*, 899-900.
58. Seppelt, K.; Rupp, H. H. *Z. Anorg. Allg. Chem.* **1974,** *409*, 331-337.
59. Jacob, E. *Z. Naturforsch., B: Chem. Sci.* **1980,** *35*, 1088-1095.
60. Schumacher, G. A.; Schrobilgen, G. J. *Inorg. Chem.* **1984,** *23*, 2923-2929.
61. Christe, K. O.; Wilson, W. W. *Inorg. Chem.* **1988,** *27*, 1296-1297.
62. Christe, K. O.; Wilson, W. W. *Inorg. Chem.* **1988,** *27*, 3763-3768.
63. Nielsen, J. B.; Kinkead, S. A.; Eller, P. G. *Inorg. Chem.* **1990,** *29*, 3621-3622.

64. Gillespie, R. J.; Schrobilgen, G. J. *J. Chem. Soc., Chem. Commun.* **1977**, 595-597.
65. Gillespie, R. J.; Schrobilgen, G. J. *Inorg. Chem.* **1974,** *13*, 2370-2374.
66. Brock, D. S.; Bilir, V.; Mercier, H. P. A.; Schrobilgen, G. J. *J. Am. Chem. Soc.* **2007,** *129*, 3598-3611.
67. Gerken, M.; Pointner, B. E.; Schrobilgen, G. J.; Mercier, H. P. A.; Moran, M. D.; Boatz, J. A.; Hoge, B.; Christe, K. O., in preparation.
68. Gunn, S. R. *J. Am. Chem. Soc.* **1965,** *87*, 2290-2291.
69. Lentz, D.; Seppelt, K. *Angew. Chem., Int. Ed. Engl.* **1978,** *17*, 355-356.
70. Birchall, T.; Myers, R. D.; de Waard, H.; Schrobilgen, G. J. *Inorg. Chem.* **1982,** *21*, 1068-1073.
71. Sladky, F. O. *Monatsh. Chem.* **1970,** *101*, 1578-1582.
72. Sladky, F. O. *Angew. Chem., Int. Ed. Engl.* **1970,** *9*, 375-376.
73. Lentz, D.; Seppelt, K. *Angew. Chem., Int. Ed. Engl.* **1978,** *17*, 356-361.
74. Lentz, D.; Seppelt, K. *Angew. Chem., Int. Ed. Engl.* **1979,** *18*, 66-67.
75. Fir, B. A.; Mercier, H. P. A.; Sanders, J. C. P.; Dixon, D. A.; Schrobilgen, G. J. *J. Fluorine Chem.* **2001,** *110*, 89-107.
76. Keller, N.; Schrobilgen, G. J. *Inorg. Chem.* **1981,** *20*, 2118-2129.
77. Sanders, J. C. P.; Schrobilgen, G. J. *J. Chem. Soc., Chem. Commun.* **1989**, 1576-1578.
78. Elliott, H. S. A.; Lehmann, J. F.; Schrobilgen, G. J., unpublished results.
79. Casteel, W. J., Jr.; Kolb, P.; LeBlond, N.; Mercier, H. P. A.; Schrobilgen, G. J. *Inorg. Chem.* **1996,** *35*, 929-942.
80. Mercier, H. P. A.; Moran, M. D.; Schrobilgen, G. J.; Steinberg, C.; Suontamo, R. J. *J. Am. Chem. Soc.* **2004,** *126*, 5533-5548.
81. Minkwitz, R.; Bäck, B. In *Inorganic Fluorine Chemistry, Toward the 21st Century*; Thrasher, J. S.; Strauss, S. H., Eds.; American Chemical Society; Washington, DC, 1994; Volume 555, Chapter 6, pp 90-103.
82. Minkwitz, R.; Molsbeck, W. *Z. Anorg. Allg. Chem.* **1992,** *607*, 175-176.
83. Minkwitz, R.; Bernstein, D.; Preut, H.; Sartori, P. *Inorg. Chem.* **1991,** *30*, 2157-2161.
84. Clegg, M. J.; Downs, A. J. *J. Fluorine Chem.* **1989,** *45*, 13.
85. Hartl, H.; Nowicki, J.; Minkwitz, R. *Angew. Chem., Int. Ed. Engl.* **1991,** *30*, 328-329.
86. Stein, L. *J. Fluorine Chem.* **1982,** *20*, 65-74.
87. Brown, D. R.; Clegg, M. J.; Downs, A. J.; Fowler, R. C.; Minihan, A. R.; Norris, J. R.; Stein, L. *Inorg. Chem.* **1992,** *31*, 5041-5052.
88. Drews, T.; Seppelt, K. *Angew. Chem., Int. Ed. Engl.* **1997,** *36*, 273-274.
89. Frohn, H.-J.; Klose, A.; Henkel, G. *GIT Fachz. Lab.* **1993,** *37*, 752-755.
90. Frohn, H.-J.; Klose, A.; Henkel, G. In *11th Winter Fluorine Conference*; St. Petersburg, FL, January 1993; Paper 58.
91. Minkwitz, R.; Nowicki, G. *Angew. Chem., Int. Ed. Engl.* **1990,** *29*, 688-689.
92. Frohn, H.-J.; Klose, A.; Schroer, T.; Henkel, G.; Buss, V.; Opitz, D.; Vahrenhorst, R. *Inorg. Chem.* **1998,** *37*, 4884-4890.
93. Frohn, H.-J.; Klose, A., unpublished results.

94. Christe, K. O.; Wilson, W. W.; Wilson, R. D. *Inorg. Chem.* **1984,** *23*, 2058-2063.
95. Gillespie, R. J.; Schrobilgen, G. J. *J. Chem. Soc., Chem. Commun.* **1974**, 90-92.
96. Gillespie, R. J.; Schrobilgen, G. J. *Inorg. Chem.* **1974,** *13*, 1230-1235.
97. LeBlond, N.; Schrobilgen, G. J. *Chem. Commun.* **1996**, 2479-2480.
98. LeBlond, N.; Mercier, H. P. A.; Dixon, D. A.; Schrobilgen, G. J. *Inorg. Chem.* **2000,** *39*, 4494-4509.
99. Eisenberg, M.; DesMarteau, D. D. *Inorg. Nuc. Chem. Lett.* **1970,** *6*, 29-34.
100. Zefirov, N. S.; Gakh, A. A.; Zhdankin, V. V.; Stang, P. J. *J. Org. Chem.* **1991,** *56*, 1416-1418.
101. Krossing, I.; Bihlmeier, A.; Raabe, I.; Trapp, N. *Angew. Chem., Int. Ed. Engl.* **2003,** *42*, 1531-1534.
102. Winfield, J. M. *J. Fluorine Chem.* **1984,** *25*, 91-98.
103. Aynsley, E. E.; Hetherington, G.; Robinson, P. L. *J. Chem. Soc.* **1954**, 1119-1124.
104. Mercier, H. P. A.; Sanders, J. C. P.; Schrobilgen, G. J.; Tsai, S. S. *Inorg. Chem.* **1993,** *32*, 386-393.
105. Emara, A. A. A.; Lehmann, J. F.; Schrobilgen, G. J. *J. Fluorine Chem.* **2005,** *126*, 1373-1376.
106. Schenk, P. W. In *Handbook of Preparative Inorganic Chemistry*; Brauer, G., Ed.; Academic Press: New York, 1963; Vol. 1, pp 489-491.
107. Christe, K. O.; Schack, C. J.; Wilson, R. D. *Inorg. Chem.* **1975,** *14*, 2224-2230.
108. Koppe, K., Ph.D. Thesis, Universität Duisburg-Essen, Duisburg, Germany: 2005.
109. Kropshofer, H.; Leitzke, O.; Peringer, P.; Sladky, F. O. *Chem. Ber.* **1981,** *114*, 2644-2648.
110. Lentz, D.; Seppelt, K. *Z. Anorg. Allg. Chem.* **1983,** *502*, 83-88.
111. Noirot, M. D.; Anderson, O. P.; Strauss, S. H. *Inorg. Chem.* **1987,** *26*, 2216-2223.
112. Vonnegut, B.; Warren, B. E. *J. Am. Chem. Soc.* **1936,** *58*, 2459-2461.
113. Powell, B. M.; Heal, K. M.; Torrie, B. H. *Mol. Phys.* **1984,** *53*, 929-939.
114. *SMART*, release 5.054; Siemens Energy and Automation Inc.: Madison, WI, 1999.
115. *SAINT+*, release 6.01; Siemens Energy and Automation Inc.: Madison, WI, 1999.
116. *APEX2*, release 2.0-2; Bruker AXS Inc.: Madison, WI, 2005.
117. Sheldrick, G. M. *SADABS (Siemens Area Detector Absorption Corrections)*, version 2.03; Siemens Analytical X-ray Instruments Inc.: Madison, WI, 1999.
118. Sheldrick, G. M. *SADABS (Siemens Area Detector Absorption Corrections)*, version 2.10; Siemens Analytical X-ray Instruments, Inc.: Madison, WI, 2004.
119. Sheldrick, G. M. *SHELXTL*, release 5.1; Siemens Analytical X-ray Instruments, Inc.: Madison, WI, 1998.
120. Sheldrick, G. M. *SHELXTL*, reslease 6.14; Siemens Analytical X-ray Instruments, Inc.: Madison, WI, 2000-2003.
121. Bain, A. *MEXICO*, release 3.0; McMaster University: Hamilton, Ontario, Canada, 2002.
122. Frisch, M. J.; Trucks, G. W.; Schlegel, H. B.; Scuseria, G. E.; Robb, M. A.; Cheeseman, J. R.; Zakrzewski, V. G.; Montgomery, J. A. J.; Burant, J. C.; Dapprich, S.; Millam, J. M.; Daniels, A. D.; Kudin, K. N.; Strain, M. C.; Farkas, O.; Tomasi, J.; Barone, V.; Cossi, M.; Cammi, R.; Mennucci, B.; Pomelli, C.;

Adamo, C.; Clifford, S.; Ochterski, J.; Petersson, G. A.; Ayala, P. Y.; Cui, Q.; Morokuma, K.; Salvador, P.; Dannenberg, J. J.; Malick, D. K.; Rabuck, A. D.; Raghavachari, K.; Foresman, J. B.; Cioslowski, J.; Ortiz, J. V.; Baboul, A. G.; Stefanov, B. B.; Liu, G.; Liashenko, A.; Piskorz, P.; Komaromi, I.; Gomperts, R.; Martin, R. L.; Fox, D. J.; Keith, T.; Al-Laham, M. A.; Peng, C. Y.; Nanayakkara, A.; Challacombe, M.; Gill, P. M. W.; Johnson, B.; Chen, W.; Wong, M. W.; Andres, J. L.; Gonzalez, C.; Head-Gordon, M.; Replogle, E. S.; Pople, J. A. *Gaussian 98*, Revision A.11; Gaussian, Inc.: Pittsburgh, PA, 2001.

123. Frisch, M. J.; Trucks, G. W.; Schlegel, H. B.; Scuseria, G. E.; Robb, M. A.; Cheeseman, J. R.; Montgomery, J. A. J.; Vreven, T.; Kudin, K. N.; Burant, J. C.; Millam, J. M.; Iyengar, S. S.; Tomasi, J.; Barone, V.; Mennucci, B.; Cossi, M.; Scalmani, G.; Rega, N.; Petersson, G. A.; Nakatsuji, H.; Hada, M.; Ehara, M.; Toyota, K.; Fukuda, R.; Hasegawa, J.; Ishida, M.; Nakajima, T.; Honda, Y.; Kitao, O.; Nakai, H.; Klene, M.; Li, X.; Knox, J. E.; Hratchian, H. P.; Cross, J. B.; Adamo, C.; Jaramillo, J.; Gomperts, R.; Stratmann, R. E.; Yazyev, O.; Austin, A. J.; Cammi, R.; Pomelli, C.; Ochterski, J. W.; Ayala, P. Y.; Morokuma, K.; Voth, G. A.; Salvador, P.; Dannenberg, J. J.; Zakrzewski, V. G.; Dapprich, S.; Daniels, A. D.; Strain, M. C.; Farkas, O.; Malick, D. K.; Rabuck, A. D.; Raghavachari, K.; Foresman, J. B.; Ortiz, J. V.; Cui, Q.; Baboul, A. G.; Clifford, S.; Cioslowski, J.; Stefanov, B. B.; Liu, G.; Liashenko, A.; Piskorz, P.; Komaromi, I.; Martin, R. L.; Fox, D. J.; Keith, T.; Al-Laham, M. A.; Peng, C. Y.; Nanayakkara, A.; Challacombe, M.; Gill, P. M. W.; Johnson, B.; Chen, W.; Wong, M. W.; Gonzalez, C.; Pople, J. A. *Gaussian 03*, Revision C.02; Gaussian, Inc.: Pittsburgh, PA, 2003.
124. Reed, A. E.; Weinstock, R. B.; Weinhold, F. *J. Chem. Phys.* **1985,** *83*, 735-746.
125. Reed, A. E.; Curtiss, L. A.; Weinhold, F. *Chem. Rev.* **1988,** *88*, 899-926.
126. Glendening, E. D.; Reed, A. E.; Carpenter, J. E.; Weinhold, F. *NBO*, Version 3.1; Gaussian, Inc.: Pittsburgh, PA, 1990.
127. Glendening, E. D.; Badenhoop, J. K.; Reed, A. E.; Carpenter, J. E.; Bohmann, C. M.; Morales, C. M.; Weinhold, F. *NBO*, Version 5.0; Theroretical Chemistry Institute, University of Wisconsin: Madison, WI, 2001.
128. McWeeny, R. *Phys. Rev.* **1962,** *126*, 1028-1034.
129. Ditchfield, R. *Mol. Phys.* **1974,** *27*, 789-807.
130. Wolinski, K.; Sadlej, A. J. *Mol. Phys.* **1980,** *41*, 1419-1430.
131. Wolinski, K.; Hilton, J. F. *J. Am. Chem. Soc.* **1990,** *112*, 8251-8260.
132. Dennington, R. I.; Keith, T.; Millam, J. M.; Eppinnett, K.; Hovell, W. L.; Gilliland, R. *GaussView*, version 3.07; Semichem, Inc.: Shawnee Mission, KS, 2003.
133. Noury, S.; Krokidis, X.; Fuster, F.; Silvi, B. *TopMod package*, University of Paris VI: Paris, 1998.
134. Dagani, R. *Chem. Eng. News* **2002,** *80*, 27-29.
135. Beattie, I. R. *Progr. Inorg. Chem.* **1963,** *5*, 1-26.
136. Gillespie, R. J.; Netzer, A.; Schrobilgen, G. J. *Inorg. Chem.* **1974,** *13*, 1455-1459.

137. McConnell, H. M.; McLean, A. D.; Reilly, C. A. *J. Chem. Phys.* **1955,** *23*, 1152-1159.
138. Ingman, P.; Jokisaari, J. P.; Sanders, J. C. P.; Schrobilgen, G. J. *Magn. Reson. Chem.* **1994,** *32*, 242-247.
139. Lehmann, J. F.; Dixon, D. A.; Schrobilgen, G. J. *Inorg. Chem.* **2001,** *40*, 3002-3017.
140. Mercier, H. P. A.; Moran, M. D.; Sanders, J. C. P.; Schrobilgen, G. J.; Suontamo, R. J. *Inorg. Chem.* **2005,** *44*, 49-60.
141. Dailey, B. P.; Shoolery, J. N. *J. Am. Chem. Soc.* **1955,** *77*, 3977-3981.
142. Porcham, W.; Engelbrecht, A. *Monatsh. Chem.* **1971,** *102*, 333-349.
143. Kolthoff, I. M.; Willman, A. *J. Am. Chem. Soc.* **1934,** *56*, 1007-1013.
144. Khadzhi-Ogly, M. R.; Yagodovskaya, T. V.; Nekrasov, L. I. *Zh. Fiz. Khim.* **1981,** *55*, 3124-3127.
145. Khadzhi-Ogly, M. R.; Yagodovskaya, T. V.; Nekrasov, L. I. *Zh. Fiz. Khim.* **1982,** *56*, 1807-1809.
146. Wilson, W. W.; Christe, K. O. *Inorg. Chem.* **1987,** *26*, 1631-1633.
147. Bradley, R. S. *Trans. Faraday Soc.* **1956,** *52*, 1255-1259.
148. Wartel, M.; Boughriet, A.; Fischer, J. C. *Anal. Chem. Acta* **1979,** *110*, 211.
149. Schrobilgen, G. J.; Holloway, J. H.; Granger, P.; Brevard, C. *Inorg. Chem.* **1978,** *17*, 980-987.
150. Obermeyer, A.; Borrmann, H.; Simon, A. *J. Am. Chem. Soc.* **1995,** *117*, 7887-7890.
151. Minkwitz, R.; Hertel, T. *Z. Natur.* **1997,** *52b*, 1307-1310.
152. Tramšek, M.; Žemva, B. *J. Fluorine Chem.* **2006,** *127*, 1275-1284.
153. Luzzati, P. V. *Acta. Cryst.* **1951,** *4*, 120-131.
154. Lehmann, J. F., Ph.D. Thesis, McMaster University, Hamilton, Ontario, Canada: 2004.
155. Kvick, Å.; McMullan, R. K.; Newton, M. D. *J. Chem. Phys.* **1982,** *76*, 3754-3761.
156. Guillory, W. A.; Bernstein, M. L. *J. Chem. Phys.* **1975,** *62*, 1058-1060.
157. Redlich, O.; Nielsen, L. E. *J. Am. Chem. Soc.* **1943,** *65*, 654-660.
158. Andrews, B.; Anderson, A. *J. Chem. Phys.* **1981,** *74*, 1534-1537.
159. Gerken, M.; Hazendonk, P.; Nieboer, J.; Schrobilgen, G. J. *J. Fluorine Chem.* **2004,** *125*, 1163-1168.
160. Howarth, O. W. In *Multinuclear Magnetic Resonance*; Mason, J., Ed.; Plenum Press: New York, 1987.
161. Sanders, J. C. P.; Schrobilgen, G. J. In *Proceedings of the NATO Advanced Study Institute on Methodological Approach to Multinuclear NMR in Liquids and Solids - Chemical Applications*; Granger, P.; Harris, R. K., Eds.; Kluwer Academic Publishers; Maratea, Italy, 1988; Vol. 322, pp 172-181.
162. Brownstein, M.; Gillespie, R. J. *J. Am. Chem. Soc.* **1970,** *92*, 2718-2721.
163. Dean, P. A. W.; Gillespie, R. J. *J. Am. Chem. Soc.* **1969,** *91*, 7260-7264.
164. Gerken, M.; Kolb, P.; Wegner, A.; Mercier, H. P. A.; Borrmann, H.; Dixon, D. A.; Schrobilgen, G. J. *Inorg. Chem.* **2000,** *39*, 2813-2824.
165. Drews, T.; Seppelt, K. *Z. Anorg. Allg. Chem.* **1991,** *606*, 201-207.

166. Mootz, D.; Merschenz-Quack, A. *Acta. Crystallogr.* **1988,** *C44*, 924-925.
167. Chen, G. S.; Passmore, J. *J. Chem. Soc., Dalton Trans.* **1979**, 1257-1261.
168. Hoge, B.; Boatz, J. A.; Hegge, J.; Christe, K. O. *Inorg. Chem.* **1999,** *38*, 3143-3149.
169. Christe, K. O.; Gnann, R.; Wagner, R. I.; Wilson, W. W. *Eur. J. Solid State Inorg. Chem.* **1996,** *33*, 865-877.
170. Haase, J.; Winnewisser, M. *Z. Naturforsch., A* **1968,** *23*, 61-64.
171. Craig, N. C.; Futamura, K. *Spectrochim. Acta., Part A* **1989,** *45*, 507-509.
172. Cameron, T. S.; Krossing, I.; Passmore, J. *Inorg. Chem.* **2001,** *40*, 4488-4490.
173. Minkwitz, R.; Molsbeck, W.; Preut, H. *Z. Naturforsch., B: Chem. Sci.* **1989,** *44*, 1581-1583.
174. Savin, A.; Nesper, R.; Wengert, S.; Fässler, T. F. *Angew. Chem., Int. Ed. Engl.* **1997,** *36*, 1808-1832.
175. Olah, G. A.; Rasul, G.; Yudin, A. K.; Burrichter, A.; Prakash, G. K. S.; Chistyakov, A. L.; Stankevich, I. V.; Akhrem, I. S.; Gambaryan, N. P.; Vol'pin, M. E. *J. Am. Chem. Soc.* **1996,** *118*, 1446-1451.
176. Martin, R. H.; Lampe, F. W.; Taft, R. W. *J. Am. Chem. Soc.* **1966,** *88*, 1353-1357.
177. Lias, S. G.; Eyler, J. R.; Ausloos, P. *Int. J. Mass Spectrom. Ion Phys.* **1976,** *19*, 219-239.
178. Jacox, M. E.; Milligan, D. E. *J. Chem. Phys.* **1971,** *54*, 3935-3950.
179. Jacox, M. E. *Chem. Phys.* **1976,** *12*, 51-63.
180. Vančik, H.; Percač, K.; Sunko, D. E. *J. Am. Chem. Soc.* **1990,** *112*, 7418-7419.
181. Abboud, J.-L. M.; Castaño, O.; Herreros, M.; Elguero, J.; Jagerovic, N.; Notario, R.; Sak, K. *Int. J. Mass Spectrom. Ion Processes* **1998,** *175*, 35-40.
182. Prochaska, F. T.; Andrews, L. *J. Am. Chem. Soc.* **1978,** *100*, 2102-2108.
183. Jacox, M. E. *Chem. Phys.* **1984,** *83*, 171-180.
184. Forney, D.; Jacox, M. E.; Irikura, K. K. *J. Chem. Phys.* **1994,** *101*, 8290-8295.
185. Maclagan, R. G. A. R. *J. Mol. Struc. (Theochem)* **1991,** *235*, 21-24.
186. Olah, G. A.; Heiliger, L.; Prakash, G. K. S. *J. Am. Chem. Soc.* **1989,** *111*, 8020-8021.
187. Olah, G. A.; Rasul, G.; Heiliger, L.; Prakash, G. K. S. *J. Am. Chem. Soc.* **1996,** *118*, 3580-3583.
188. Klages, F.; Zange, E. *Chem. Ber.* **1959,** *92*, 1828-1834.
189. Meerwein, H.; Bodenbenner, K.; Borner, P.; Kunert, F.; Wunderlich, H. *Ann.* **1960,** *632*, 38-55.
190. Meerwein, H.; Hederich, V.; Morschel, H.; Wunderlich, H. *Ann.* **1960,** *635*, 1-21.
191. Ramsey, B. G.; Taft, R. W. *J. Am. Chem. Soc.* **1966,** *88*, 3058-3063.
192. Olah, G. A.; White, A. M. *J. Am. Chem. Soc.* **1968,** *90*, 1884-1889.
193. Minkwitz, R.; Schneider, S. *Angew. Chem., Int. Ed. Engl.* **1999,** *38*, 714-715.
194. Laube, T. *Chem. Rev.* **1998,** *98*, 1277-1312.
195. Antel, J.; Klaus, H.; Jones, P. G.; Mews, R.; Sheldrick, G. M.; Waterfeld, A. *Chem. Ber.* **1985,** *118*, 5006-5008.
196. Christe, K. O.; Zhang, X.; Bau, R.; Hegge, J.; Olah, G. A.; Prakash, G. K. S.; Sheehy, J. A. *J. Am. Chem. Soc.* **2000,** *122*, 481-487.

197. Minkwitz, R.; Reinemann, S.; Blecher, O.; Hartl, H.; Brüdgam, I. *Inorg. Chem.* **1999,** *38*, 844-847.
198. Laube, T.; Bannwart, E.; Hollenstein, S. *J. Am. Chem. Soc.* **1993,** *115*, 1731-1733.
199. Christe, K. O.; Hoge, B.; Boatz, J. A.; Prakash, G. K. S.; Olah, G. A.; Sheehy, J. A. *Inorg. Chem.* **1999,** *38*, 3132-3142.
200. Minkwitz, R.; Meckstroth, W.; Preut, H. *Z. Anorg. Allg. Chem.* **1992,** *617*, 136-142.
201. Minkwitz, R.; Meckstroth, W.; Preut, H. *Z. Naturforsch., B: Chem. Sci.* **1992,** *48*, 19-22.
202. Jönsson, P.-G.; Olovsson, I. *Acta. Crystallogr.* **1968,** *B24*, 559-564.
203. Kvick, Å.; Jönsson, P.-G.; Olovsson, I. *Inorg. Chem.* **1969,** *8*, 2775-2780.
204. Minkwitz, R.; Schneider, S.; Seifert, M. *Z. Anorg. Allg. Chem.* **1996,** *622*, 1404-1410.
205. Caira, M. R.; De Wet, J. F. *Acta. Crystallogr.* **1981,** *B37*, 709-711.
206. Paulsen, H.; Dammeyer, R. *Chem. Ber.* **1973,** *106*, 2324.
207. Frenking, G.; Fau, S.; Marchand, C. M.; Grützmacher, H. *J. Am. Chem. Soc.* **1997,** *119*, 6648-6655.
208. Robinson, E. A.; Johnson, S. A.; Tang, T.-H.; Gillespie, R. J. *Inorg. Chem.* **1997,** *36*, 3022-3030.
209. Robinson, E. A.; Heard, G. L.; Gillespie, R. J. *J. Mol. Struct.* **1999,** *485-486*, 305-319.
210. Mercier, H. P. A.; Moran, M. D.; Schrobilgen, G. J.; Suontamo, R. J. *J. Fluorine Chem.* **2004,** *125*, 1563-1578.
211. Kaupp, M.; Malkina, O. L.; Malkin, V. G. *Chem. Phys. Lett.* **1997,** *265*, 55-59.
212. Seppelt, K. *Chem. Ber.* **1973,** *106*, 1920-1926.
213. Seppelt, K. *Z. Anorg. Allg. Chem.* **1973,** *399*, 65-72.
214. Gombler, W. *Spectrochim. Acta., Part A* **1981,** *37*, 57-61.
215. Ettinger, R.; Blume, P.; Patterson, A.; Lauterbur, P. C. *J. Mag. Reson.* **1972,** *33*, 1597-1598.
216. Syvret, R. G.; Mitchell, K. M.; Sanders, J. C. P.; Schrobilgen, G. J. *Inorg. Chem.* **1992,** *31*, 3381-3385.
217. Cohen, S.; Powers, R.; Rudman, R. *Acta. Crystallogr.* **1979,** *B35*, 1670-1674.
218. Cockcroft, J. K.; Fitch, A. N. *Z. Kristallogr.* **1994,** *209*, 488-490.
219. More, M.; Baert, F.; Lefebvre, J. *Acta. Crystallogr.* **1977,** *B33*, 3681-3684.
220. Pauling, L., *The Nature of the Chemical Bond*, 3rd ed.; Cornell University Press: Ithaca, New York, 1960, p 260.
221. Sawyer, J. F.; Schrobilgen, G. J. *Acta. Crystallogr.* **1982,** *B38*, 1561-1563.
222. Olah, G. A.; Donovan, D. J.; Lin, H. C. *J. Am. Chem. Soc.* **1976,** *98*, 2661-2663.
223. Calves, J.-Y.; Gillespie, R. J. *J. Am. Chem. Soc.* **1977,** *99*, 1788-1792.
224. Olah, G. A.; Donovan, D. J. *J. Am. Chem. Soc.* **1978,** *100*, 5163.
225. Olah, G. A.; Donovan, D. J. *J. Am. Chem. Soc.* **1978,** *100*, 5163-5169.
226. Vanderryn, J. *J. Chem. Phys.* **1959,** *30*, 331-332.
227. Anderson, T. F.; Lassettre, E. N.; Yost, D. M. *J. Chem. Phys.* **1936,** *4*, 703-707.

228. Clark, R. J. H.; Rippon, D. M. *J. Chem. Soc. D.: Chem. Commun.* **1971**, 1295-1296.
229. Stammreich, H.; Tavares, Y.; Bassi, D. *Spectrochim. Acta.* **1961,** *17*, 661-664.
230. Clark, R. J. H.; Mitchell, P. D. *J. Chem. Phys.* **1972,** *56*, 2225-2232.
231. Shurvell, H. F. *Spectrochim. Acta., Part A* **1971,** *27*, 2375-2383.
232. Reynolds, C. H. *J. Chem. Soc., Chem. Commun.* **1991**, 975-976.
233. Dixon, D. A.; Feller, D.; Sandrone, G. *J. Phys. Chem. A.* **1999,** *103*, 4744-4751.
234. Ricca, A. *J. Phys. Chem. A.* **1999,** *103*, 1876-1879.
235. Hansel, A.; Scheiring, C.; Glantschnig, M.; Lindinger, W.; Ferguson, E. E. *J. Chem. Phys.* **1998,** *109*, 1748-1750.
236. Irikura, K. K. *J. Am. Chem. Soc.* **1999,** *121*, 7689-7695.
237. Basch, H.; Hoz, T.; Hoz, S. *J. Phys. Chem. A.* **1999,** *103*, 6458-6467.
238. Rodriquez, C. F.; Bohme, D. K.; Hopkinson, A. C. *J. Phys. Chem.* **1996,** *100*, 2942-2949.
239. Robles, E. S. J.; Chen, P. *J. Phys. Chem.* **1994,** *98*, 6919-6923.
240. Jonas, V.; Frenking, G.; Reetz, M. T. *J. Am. Chem. Soc.* **1994,** *116*, 8741-8753.
241. Chandrakumar, K. R. S.; Pal, S. *J. Phys. Chem. A.* **2002,** *106*, 11775-11781.
242. Rowsell, B. D.; Gillespie, R. J.; Heard, G. L. *Inorg. Chem.* **1999,** *38*, 4659-4662.
243. Bauschlicher, C. W. J.; Ricca, A. *J. Phys. Chem. A.* **1999,** *103*, 4313-4318.
244. Fau, S.; Frenking, G. *Mol. Phys.* **1999,** *96*, 519-527.
245. Brinck, T.; Murray, J. S.; Politzer, P. *Inorg. Chem.* **1993,** *32*, 2622-2625.
246. Hudgens, J. W.; Johnson, R. D. I.; Tsai, B. P.; Kafafi, S. A. *J. Am. Chem. Soc.* **1990,** *112*, 5763-5772.
247. Tachikawa, H. *J. Phys. Chem. A.* **1997,** *101*, 7454-7459.
248. Jovári, P.; Mészáros, G.; Pusztai, L.; Sváb, E. *J. Chem. Phys.* **2001,** *114*, 8082-8090.
249. Pohl, S. *Z. Kristallogr.* **1982,** *159*, 211-216.
250. Lévy, H.; Brockway, L. O. *J. Am. Chem. Soc.* **1937,** *59*, 2085-2092.
251. Spencer, C.; Lipscomb, W. N. *J. Chem. Phys.* **1958,** *28*, 355.
252. Konaka, S.; Ito, T.; Morino, Y. *Bull. Chem. Soc. Japan* **1966,** *39*, 1146-1154.
253. DeMarco, R. A.; Fox, W. B.; Moniz, W. B.; Sojka, S. A. *J. Magn. Reson.* **1975,** *18*, 522-526.
254. Lappert, M. F.; Litzow, M. R.; Pedley, J. B.; Tweedale, A. *J. Chem. Soc. A.* **1971**, 2426-2428.
255. Branchadell, V.; Oliva, A. *J. Mol. Struc. (Theochem)* **1991,** *236*, 75-84.
256. Hartman, J. S.; Schrobilgen, G. J. *Inorg. Chem.* **1972,** *11*, 940-951.
257. Morishima, I.; Endo, K.; Yonezawa, T. *J. Chem. Phys.* **1973,** *59*, 3356-3364.
258. Kaupp, M., *Relativistic Effects on NMR Chemical Shifts*, Elsevier: Amsterdam, 2003/2004, p to be published.
259. Malkin, V. G.; Malkina, O. L.; Salahub, D. R. *Chem. Phys. Lett.* **1996,** *261*, 335-345.
260. Onak, T.; Landesman, H.; Williams, R. E.; Shapiro, I. *J. Phys. Chem.* **1959,** *63*, 1533-1535.
261. Good, C. D.; Ritter, D. M. *J. Am. Chem. Soc.* **1962,** *84*, 1162-1166.

262. Vladimiroff, T.; Malinowski, E. R. *J. Chem. Phys.* **1967,** *46*, 1830-1841.
263. Seppelt, K. *Angew. Chem., Int. Ed. Engl.* **1982,** *21*, 877-888.
264. Simón-Manso, Y.; Fuentealba, P. *J. Mol. Struc. (Theochem)* **2003,** *634*, 89-94.
265. Langford, M. L.; Harris, F. M. *Int. J. Mass Spectrom. Ion Processes* **1990,** *96*, 111-113.
266. Domazou, A. S.; Quadir, M. A.; Buehler, R. E. *J. Phys. Chem.* **1994,** *98*, 2877-2822.
267. Sheng, L.; Qi, F.; Gao, H.; Zhang, Y.; Yu, S.; Li, W.-K. *Int. J. Mass Spectrom. Ion Processes* **1997,** *161*, 151-159.
268. Seccombe, D. P.; Tuckett, R. P.; Fisher, B. O. *J. Chem. Phys.* **2001,** *114*, 4074-4088.
269. Lee, M. S.; Park, M.; Chung, Y. *J. Korean Phys. Soc.* **2003,** *42*, 493-498.
270. Prochaska, F. T.; Andrews, L. *J. Chem. Phys.* **1978,** *68*, 5568-5576.
271. Prochaska, F. T.; Andrews, L. *J. Chem. Phys.* **1978,** *68*, 5577-5586.
272. Truszkowski, S.; Ichikawa, T. *J. Phys. Chem.* **1989,** *93*, 4522-4526.
273. Prochaska, F. T.; Andrews, L. *J. Phys. Chem.* **1978,** *82*, 1731-1742.
274. Keelan, B. W.; Andrews, L. *J. Phys. Chem.* **1979,** *83*, 2488-2496.
275. Muller, N.; Carr, D. T. *J. Phys. Chem.* **1963,** *67*, 112-115.
276. Schack, C. J.; Christe, K. O. *J. Fluorine Chem.* **1990,** *47*, 79-87.
277. Diaper, C. M. *Science of Synthesis* **2005,** *18*, 1203-1282.
278. Lebel, H.; Grenon, M. *Science of Synthesis* **2005,** *22*, 669-747.
279. DesMarteau, D. D. *Inorg. Chem.* **1968,** *7*, 434-437.
280. Adcock, J. L.; Robin, M. L.; Zuberi, S. *J. Fluorine Chem.* **1987,** *37*, 327-336.
281. Lin, W. H.; Clark, W. D.; Lagow, R. J. *J. Org. Chem.* **1989,** *54*, 1990-1992.
282. Huppmann, P.; Lentz, D.; Seppelt, K. *Z. Anorg. Allg. Chem.* **1981,** *472*, 26-32.
283. Hurlburt, P. K.; Anderson, O. P.; Strauss, S. H. *J. Am. Chem. Soc.* **1991,** *113*, 6277-6278.
284. Hurlburt, P. K.; Anderson, O. P.; Strauss, S. H. *Can. J. Chem.* **1992,** *70*, 726-731.
285. Engelbrecht, A.; Loreck, W.; Nehoda, W. *Z. Anorg. Allg. Chem.* **1968,** *360*, 88-96.
286. Buerger, H. *Z. Anorg. Allg. Chem.* **1968,** *360*, 97-103.
287. Oberhammer, H.; Seppelt, K. *Angew. Chem., Int. Ed. Engl.* **1978,** *17*, 69-70.
288. Zylka, P.; Oberhammer, H.; Seppelt, K. *J. Mol. Struc.* **1991,** *243*, 411-418.
289. Schack, C. J.; Wilson, W. W.; Christe, K. O. *Inorg. Chem.* **1983,** *22*, 18-21.
290. Schack, C. J.; Christe, K. O. *Inorg. Chem.* **1984,** *23*, 2922.
291. Fraser, G. W.; Millar, J. B. *J. Chem. Soc., Dalton Trans.* **1974**, 2029-2031.
292. Björgvinsson, M.; Sawyer, J. F.; Schrobilgen, G. J. *Inorg. Chem.* **1987,** *26*, 741-749.
293. Mercier, H. P. A.; Sanders, J. C. P.; Schrobilgen, G. J. *Inorg. Chem.* **1995,** *34*, 5261-5273.
294. Casteel, W. J., Jr.; MacLeod, D. M.; Mercier, H. P. A.; Schrobilgen, G. J. *Inorg. Chem.* **1996,** *35*, 7279-7288.
295. Lustig, M. *Inorg. Chem.* **1965,** *4*, 1828-1830.

296. Van Seggen, D. M.; Hurlburt, P. K.; Anderson, O. P.; Strauss, S. H. *Inorg. Chem.* **1995,** *34*, 3453-3464.
297. Heard, G. L.; Gillespie, R. J.; Rankin, D. W. H. *J. Mol. Struc.* **2000,** *520*, 237-248.
298. Van Seggen, D. M.; Hurlburt, P. K.; Noirot, M. D.; Strauss, S. H. *Inorg. Chem.* **1992,** *31*, 1423-1430.
299. Hurlburt, P. K.; Rack, J. J.; Luck, J. S.; Dec, S. F.; Webb, J. D.; Anderson, O. P.; Strauss, S. H. *J. Am. Chem. Soc.* **1994,** *116*, 10003-10014.
300. Moran, M. D.; Schrobilgen, G. J., unpublished results.
301. Moran, M. D.; Smith, G. L.; Schrobilgen, G. J., unpublished results.
302. Lambert, J. B.; Zhao, Y.; Zhang, M. S. *J. Phys. Org. Chem.* **2001,** *14*, 370-379.
303. Moran, M. D.; Mercier, H. P. A.; Schrobilgen, G. J., unpublished results.
304. Lambert, J. B.; Zhang, S.; Stern, C. L.; Huffman, J. C. *Science* **1993,** *260*, 1917-1918.
305. Azeem, M.; Brownstein, M.; Gillespie, R. J. *Can. J. Chem.* **1969,** *47*, 4159-4167.
306. Edwards, A. J.; Jones, G. R. *J. Chem. Soc. A.* **1970**, 1491-1497.
307. Edwards, A. J.; Jones, G. R. *J. Chem. Soc. A.* **1970**, 1891-1894.
308. Edwards, A. J.; Taylor, P. *J. Chem. Soc., Dalton Trans.* **1973**, 2150-2153.
309. Schrobilgen, G. J., unpublished observations.
310. Jonethal, U.; Kuschel, R.; Seppelt, K. *J. Fluorine Chem.* **1998,** *88*, 3-4.
311. Winter, R.; Terjeson, R. J.; Gard, G. *J. Fluorine Chem.* **1998,** *89*, 105-106.
312. Schack, C. J.; Wilson, R. D.; Hon, J. F. *Inorg. Chem.* **1972,** *11*, 208-209.
313. Murchie, M.; Passmore, J. *Inorg. Synth.* **1986,** *24*, 31-33.
314. Lawlor, L.; Passmore, J. *Inorg. Chem.* **1979,** *18*, 2921-2923.
315. Lentz, D.; Pritzkow, H.; Seppelt, K. *Angew. Chem., Int. Ed. Engl.* **1977,** *16*, 729-730.

Appendix A

DECOMPOSITION OF $O(XeF)_2$

As stated in Chapter 3, the products resulting from the decomposition of $O(XeF)_2$ at 10 °C, and the products from the decomposition of $O(XeF)_2$ in HF at –78 °C, are very similar. Both products were orange, and their Raman spectra (Figure A1 and Table A1) were identical in the region between 550 and 490 cm^{-1}. Although the nature of the products could not be established on the basis of Raman spectroscopy, it is clear that xenon is retained in the products, as evidenced by the intense Xe–F stretching frequencies in the 500–600 cm^{-1} region of the spectra. While it cannot be ruled out that the peak at 430 cm^{-1} arises from residual $O(XeF)_2$ (437/433 cm^{-1}), it is more likely that it belongs to another XeO-bound species. One possibility would be the redox decomposition of $O(XeF)_2$ to give a Xe(IV) compound, $(OXeF_2)_n$, and Xe according to eq A.1.

$$2n\ O(XeF)_2 \longrightarrow (OXeF_2)_n + n\ Xe \qquad (A.1)$$

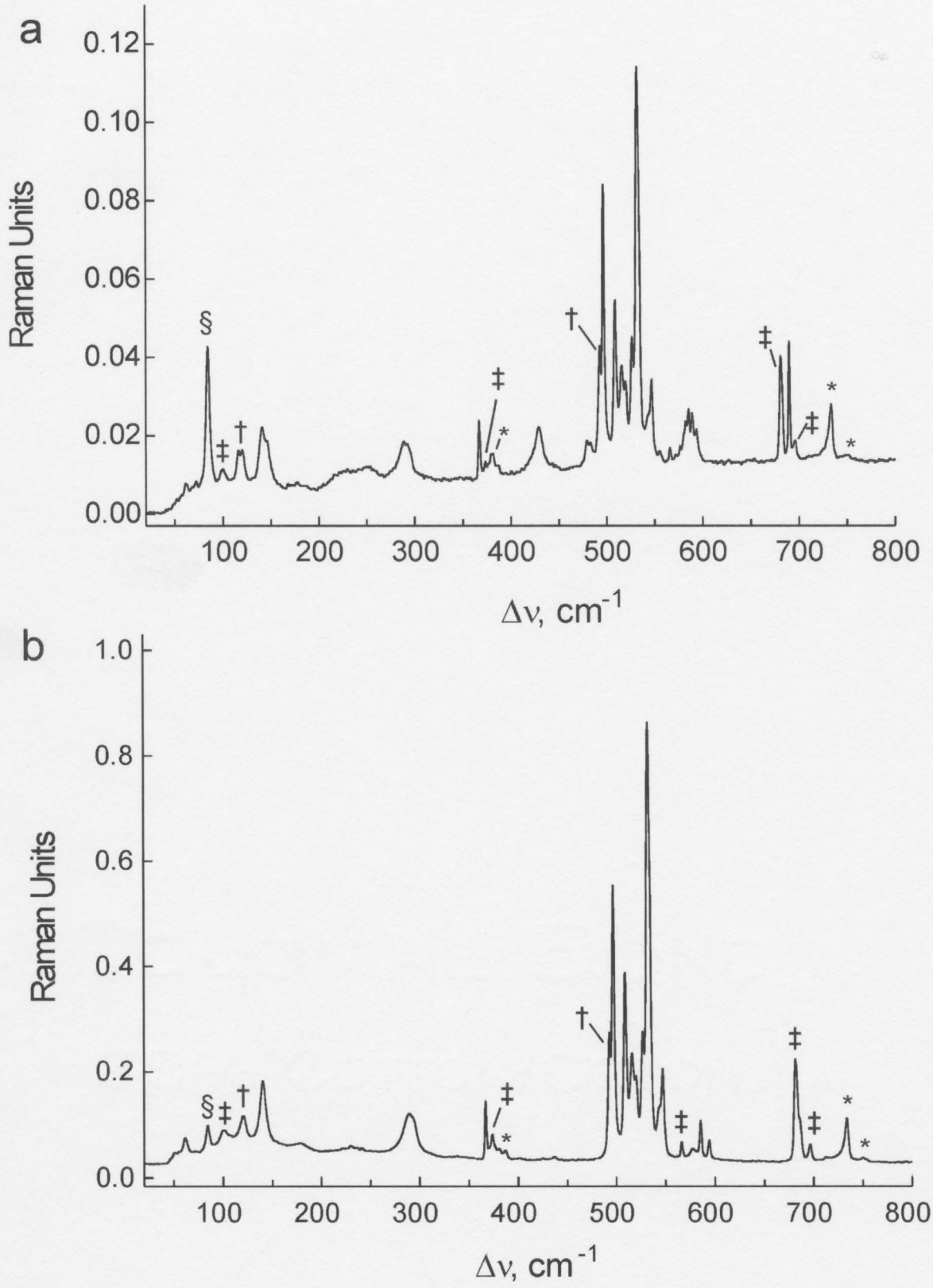
a
Raman Units
0.12
0.10
0.08
0.06
0.04
0.02
0.00
§
‡
†
‡
*
†
‡
‡
*
*
100
200
300
400
500
600
700
800
Δν, cm-1
b
Raman Units
1.0
0.8
0.6
0.4
0.2
0.0
§
‡
†
‡
*
†
‡
‡
‡
*
*
100
200
300
400
500
600
700
800
Δν, cm-1

Figure A.1. Raman spectra of (a) decomposition products of $O(XeF)_2$ in HF at –78 °C (HF removed under dynamic vacuum at –78 °C), and (b) solid products from the decomposition of $O(XeF)_2$ at 10 °C, recorded at –160 °C using 1064-nm excitation. The symbols denote FEP (*), XeF_2 (†), $[NO][AsF_6]$ (‡), and instrument artifact (§).

Table A.1. Experimental Raman Frequencies and Intensities[a] for the Products Resulting from the Decomposition of $O(XeF)_2$

frequencies, cm^{-1}	
$O(XeF)_2$ [b]	$O(XeF)_2$ [c]
686 sh	690(24)
594(5)	593(9)
	589(13)
585(9)	585(14)
	582(11)
	580(5)
578(3)	577(3)
	555(3)
547(22)	547(22)
543 sh	543 sh
532(100)	532(100)
527(31)	527(33)
520(20)	520(22)
516(26)	516(25)
509(44)	509(42)
493(31)	493(31)
	483(6)
	479(6)
436(<1)	429(11)
367(15)	367(15)
290(13)	289(11)
	250 br
	226 br
179 br	179 br
	146 sh
140(20)	141(15)
	71(2)
62(6)	61(4)

[a] Raman intensities (in $Å^4$ amu^{-1}) are given in parentheses. [b] Decomposition products (10 °C) [c] Decomposition in HF solvent at –78 °C.